UNVERSIDADE DE SÃO PAULO
INSTITUTO DE QUÍMICA DE SÃO CARLOS
PROGRAMA DE PÓS-GRADUAÇÃO EM QUÍMICA

Isabela Alteia Mattioli

Graphene electrical-electrochemical vertical devices: the new generation of *on chip* biosensors

SÃO CARLOS – SP

2022

ISABELA ALTEIA MATTIOLI

Graphene electrical-electrochemical vertical devices: the new generation of *on chip* biosensors

Thesis presented to the São Carlos Institute of Chemistry (IQSC) in partial fulfillment of the requirements for the degree of Doctor in Science.

Concentration area: Analytical and Inorganic Chemistry

Advisor: Prof. Dr. Frank Nelson Crespilho

SÃO CARLOS – SP

2022

Autorizo a reprodução e divulgação total ou parcial deste trabalho, por qualquer meio convencional ou eletrônico para fins de estudo e pesquisa, desde que citada a fonte.

Assinatura: Isabela Alteia Mattioli
Data: 27/01/2022

Ficha Catalográfica elaborada pela Seção de Referência e Atendimento ao Usuário do SBI/IQSC

Mattioli, Isabela Alteia
Graphene electrical-electrochemical vertical devices: the new generation of on chip biosensors / Isabela Alteia Mattioli. — São Carlos, 2022.
150 f.

Tese (Doutorado em Química Analítica e Inorgânica) — Instituto de Química de São Carlos / Universidade de São Paulo, 2022.

Orientador: Prof. Dr. Frank Nelson Crespilho

1. Grafeno. 2. Biossensor. 3. Dispositivo elétrico eletroquímico. 4. DNA. 5. SARS-CoV-2. I. Título.

Wilneide do Carmo Marchi Maiorano - CRB: 3978/8

AKNOWLEDGEMENTS

- To my parents, Carlos and Fatima, for all the support, advice, and for encouraging me to be bold and strong within these years;
- To my brother and sister, Murillo and Marcela, for being present and helping me to overcome all challenges with joy;
- To my boyfriend Luiz Filipe for the true partnership, countless supporting words and for being present in all moments;
- To Professor Dr. Frank Nelson Crespilho for all the scientific discussions, teachings and confidence;
- To all my friends who were present in this journey, for the joyful moments, for all incredible meetings and for helping me to not give up at any time;
- To all my Lab colleagues, for the support, teachings, tips, collaborations, and funny moments;
- To São Carlos Institute of Chemistry (IQSC) for all the infrastructure and facilities;
- To Gislei Ap. A. de Oliveira for all the efficient support with documentation processes;
- To Priscila Cervini and Ana Paula Garcia for all the teachings and support in the beginning of my scientific path;
- To Professor Dr. Nirton Cristi Silva Vieira for helping me in all Graphene Field-Effect Transistors studies and receiving me in UNIFESP, São José dos Campos;
- To Sao Paulo Federal University (UNIFESP) – São José dos Campos for the used infrastructure during my research visit aiming Graphene Field Effect Transistors studies;
- To São Paulo Research Foundation (FAPESP) for the financial support with the scholarship 2018/11071-0;
- To Coordinating Agency for Advanced Training of Graduate Personnel (CAPES) and MeDiCo Network CAPES-Brazil fundings, as well as to National Council for Scientific and Technological Development (CNPq).

EPIGRAPH

Everything has been figured out, except how to live.

Jean-Paul Sartre

ABSTRACT

The COVID-19 pandemic brought the global need to develop new biosensors for practical use, with quick response, sensitivity, and low cost, aiming point-of-care diagnosis and mass monitoring concerning the contamination of a population. In this sense, graphene field effect transistors (GFETs) are among the most promising biodevices due to their sensitivity and rapidness of response. However, the low selectivity inherent to the response mechanism of GFETs and the use of a non-polarizable reference electrode of the $Ag/AgCl_{sat}$ type in its configuration limit its application. In this sense, this Doctorate Thesis presents the development and application of a new type of biosensor based on monolayer graphene, with hybrid detection, where the device uses electrical and electrochemical principles, called Graphene Vertical Electrical-Electrochemical Device (EEVD). EEVD was designed so that an electrode formed by the heterojunction of a graphene layer/adsorbed redox probe is exposed to the electrolyte and, as a result, small variations caused by the presence of analytes at the electrode/electrolyte interface change the charge density near the graphene K point of first Brillouin zone. This perturbation alters the Dirac point and causes energy dispersion, resulting in different values of capacitance and potential of the interface, which are strongly correlated to the presence of the analyte. Furthermore, it was observed that faradaic processes can occur in the orthonormal plane of graphene in the presence of a redox probe coupled by van der Waals interactions, intensifying the interface perturbation by the presence of the analyte in the electrolyte, making EEVD more sensitive when compared to GFET. As a proof of concept, a EEVD based on the graphene/ferrocene heterojunction was used for single-stranded DNA detection, obtaining a limit of detection (LOD) of zeptomolar magnitude order (10^{-21} mol L^{-1}). Because it has a total negative charge, DNA changes the capacitance of the interface formed by the heterojunction, and varies its open circuit potential (OCP), which in turn responds linearly to alterations of DNA concentrations. Therefore, EEVD was applied as an immunosensor for the diagnosis of COVID-19. For this, ferrocene was replaced by the neutral red redox probe modified with Spike protein receptor binding domain (RBD) of SARS-CoV-2. In this configuration, the biosensor requires 40 μL of serum sample from a patient infected with COVID-19, and it is possible to detect IgG antibodies produced in response to COVID-19 infection with an LOD of 1.0 pg mL^{-1}. Finally, an EEVD-type biosensor was developed for antigen detection (SARS-CoV-2 virus) in saliva samples, with a LOD of 2.86 fmol L^{-1}, indicating the suitability of the biosensor for the diagnosis of COVID-19 in early stage. Both the immunosensor and the antigen biosensor for the diagnosis of COVID-19 were validated in real samples and using validation parameters from ANVISA and ABRAMED.

Keywords: graphene, biosensor; DNA; electrical device; electrochemical device; SARS-CoV-2

RESUMO

A pandemia de COVID-19 trouxe a necessidade global de desenvolvimento de novos biossensores de uso prático, com rápida reposta, sensíveis e de baixo custo, visando o diagnóstico no ponto de atendimento e monitoramento em massa da contaminação da população. Nesse sentido, os transistores de efeito de campo de grafeno (GFETs) estão entre os biodispositivos mais promissores devido à sensibilidade e rapidez de resposta. Entretanto, a baixa seletividade, inerente ao mecanismo de resposta dos GFETs e o uso de um eletrodo de referência não-polarizável do tipo $Ag/AgCl_{sat}$ em sua configuração limitam a aplicação. Neste sentido, nesta Tese de Doutorado apresentam-se o desenvolvimento e a aplicação de um novo tipo de biossensor a base de grafeno monocamada, com detecção híbrida, onde o dispositivo usa princípios elétricos e eletroquímicos, denominado Dispositivo Elétrico-Eletroquímico Vertical de Grafeno (DEEV). O DEEV foi projetado para que um eletrodo formado pela heterojunção de camada grafeno/sonda redox adsorvida fique exposta ao eletrólito e, com isso, pequenas mudanças causadas por analitos na interface eletrodo/eletrólito altere a densidade de carga próxima ao ponto K da primeira zona de Brillouin do grafeno. Esta perturbação altera o ponto de Dirac e causa dispersão de energia, resultando em diferentes valores de capacitância e potencial da interface, que são fortemente correlacionadas à presença do analito. Além disso, foi observado que processos faradaicos podem ocorrer no plano ortonormal do grafeno na presença de uma sonda redox acoplada por interações de van der Waals, intensificando a perturbação da interface pela presença do analito no eletrólito, tornando o DEEV mais sensível quando comparado ao GFET. Como prova de conceito, utilizou-se um DEEV baseado na heterojunção grafeno/ferroceno para detecção de DNA em fita única, obtendo-se um limite de detecção (LOD) na ordem de zeptomolar (10^{-21} mol L^{-1}). Por ter carga total negativa, o DNA altera a capacitância da interface formada pela heterojunção, alterando também o potencial de circuito aberto (OCP), que por sua vez, responde às mudanças de concentrações de DNA. Por conseguinte, o DEEV foi aplicado como um imunossensor para diagnóstico de COVID-19. Para isso, substituiu-se o ferroceno pela sonda redox *neutral red* modificada com os domínios RBD da proteína Spike do SARS-CoV-2. Nesta configuração, o biossensor requer 40 μL de amostra de soro de um paciente infectado com COVID-19, sendo possível detectar anticorpos IgG produzidos em resposta à infecção por COVID-19 com LOD de 1,0 pg mL^{-1}. Por fim, desenvolveu-se um biossensor do tipo DEEV para detecção de antígeno (vírus SARS-CoV-2) em amostras de saliva, com LOD de 2,86 fmol L^{-1}, indicando a adequação do biossensor para o diagnóstico de COVID-19 em estágio inicial. Tanto o imunossensor, quanto o biossensor de antígeno para diagnóstico de COVID-19, foram validados em amostras reais e utilizando parâmetros de validação da ANVISA e ABRAMED.

Palavras-chave: grafeno, biossensor; DNA; dispositivo elétrico; dispositivo eletroquímico; SARS-CoV-2

LIST OF ABBREVIATIONS

AuNP – Gold nanoparticles

BS – Bovine Serum

BSA – Bovine Serum Albumin

CE - Counter-Electrode

CPE – Constant Phase Element

CVD – Carbon Vapor Deposition

DC – Direct current

DLS – Dynamic Light Scattering

EE – Electrical-Electrochemical

EIS – Electrochemical Impedance Spectroscopy

EEVD – Electrical Electrochemical Vertical Device

Fc - Ferrocene

G – Monolayer graphene

GFET – Graphene Field-Effect Transistors

IgG – Immunoglobulin G

LFD – Lateral Flow Devices

LOD – Limit of Detection

OCP – Open Circuit Potential

PBS – Phosphate Buffer Saline

PNR – Poly-Neutral Red

POC – Point of Care

RE – Reference Electrode

RBD – Receptor Binding Domain of Spike Protein

S – Spike Protein

SD – Standard Deviation

S1 – Subunit 1 of Spike Protein

ssDNA – Single-stranded DNA

WE – Working Electrode

LIST OF FIGURES

INTRODUCTION

Figure 1 – Schematic representation of biosensing signal transducing...........................17

Chapter I - On the Challenges for the Diagnosis of SARS-CoV-2 Based on a Review of Current Methodologies

Figure 1 - (A) Representation of CoV structure containing its spike glycoprotein (S), envelope protein (E), nucleocapsid protein (N), transmembrane glycoprotein (M), and its RNA viral genome. (B) Genome structure of SARS-CoV, MERS-CoV, and SARS-CoV-2 and encoded proteins...25

Figure 2 - SARS-CoV-2 most appropriate detection methods along the course of infection. This figure is an illustrative scheme and it should be mentioned that discrepancies exist in the literature, especially for the tails of the curves. We decided to keep the qualitative character until more data are collected and a consensus is stablished on the time dependences...26

Figure 3 - (A) Schematic representation of RT-PCR procedure to detect viral RNA through DNA amplification and detection...28

Figure 4 - Sensitivity susceptibility to the primer gene for LAMP analyses. (A,B) RT-LAMP sensitivity toward ORF1ab gene targeting for SARS-CoV-2 detection based on ORF1ab-4 primer; (D,E) sensitivity of the proposed RT-PCR assay for SARS-CoV-2 S protein targeting using primer set S-123; (C,F) Conventional PCR assay sensitivity concerning both ORF1ab and S genes targeting for SARS-CoV-2 detection................29

Figure 5 - Brief description of operation modes of both (A) sandwich and (B) indirect ELISA assays for detecting SARS-CoV-2 antigens..32

Figure 6 - (A) Schematic representation of operation principles of CLIA assays. (B) IgG and IgM antibody quantification through CLIA assays versus days of infection by SARS-CoV-2..33

Figure 7 - Representation of a typical LFD assay that can be employed for SARS-CoV-2 testing. The design of commercial assays is the same as that represented above. The device comprises a sample pad in which IgM and IgG antibodies are immobilized. The conjugate pad contains gold nanoparticles (AuNP) conjugated to a SARS-CoV-2 antigen. In test lines, anti-human IgG and anti-human IgM are immobilized to interact with IgG-AuNP-antigen and IgM-AuNP antigen complex. The control line contains nonhuman reactive anti-IgG or anti-IgM. The absorbent pad is useful for maintaining sample flow through the strip..34

Figure 8 - (A) Application of GFET-based electrical immunosensor with SARS-CoV-2 S protein antibodies immobilized onto graphene surface. The device was employed for SARS-CoV-2 detection in clinical samples from COVID-19 infected patients. (B) Schematic representation of GFET immunosensor for RBD of S1 subunit. V_{ref} shift due to antibodies immobilization in comparison to the bare graphene surface.....................35

Figure 9 - (a) LSPR response versus RdRp of SARS-CoV-2 concentration; (b) zoom of low-concentration region of LSPR biosensor responses for different RdRp oligos concentrations; (c) LSPR biosensor response for detection of other viruses, such as

ORF1ab and E protein from SARS-CoV- 2 and RdRp from SARS-CoV; (d) comparison of LSPR biosensor response in single-analyte samples and mixture of several sequences.....37

Chapter II - Problems of Interpreting Diagnostic Tests for SARS-CoV-2: Analytical Chemistry Concerns

Figure 1 - Steps involved in the development of a testing method for COVID-19 diagnosis. The TT to be employed is part of the entire method, although the main source of testing errors is not related to its execution. During the technique validation, it is fundamental to determine the assay reproducibility, sensitivity, LOD, and standard deviations through a statistical treatment of the results.....49

Chapter III - Highly sensitive interfaces of graphene electrical-electrochemical vertical devices for on drop atto-molar DNA detection

Figure 1 - EEVD preparation and operation schematics. A) EEVD device preparation description. Steps 1 and 2 correspond to graphene wet transfer methodology. After subsequent thermal annealing for formation of graphene on the SiO_2/Si interface, Step 3 presents an optical micrograph of graphene on SiO_2/Si. Step 4 depicts a typical pristine graphene electrochemical response in a 0.10 mol L^{-1} phosphate buffer solution (pH 7.2). Step 5 illustrates ferrocene in ethanol (5.0 mg mL^{-1}) drop casting and adsorption on graphene, forming a graphene-fc vdW heterojunction. Step 6 illustrates a typical final cyclic voltammogram obtained for graphene-fc in a 0.10 mol L^{-1} phosphate buffer solution (pH 7.2) after removal of excess ferrocene. B) Schematic representation of the working principles of an EEVD with the proposed graphene-fc heterojunction. C) Schematic representation of a GFET's working principles for comparison purposes with Fig. 1B. D) Representation of ssDNA quantification with our EEVD graphene-fc devices through interfacial potential (E_{int}) variations.....54

Figure 2 - EEVD electrical-electrochemical performance. A) Schematic of GFET setup with graphene-fc interface. The represented setup is also valid for the bare graphene interface; B) Representative schematic of EEVD configuration with graphene-fc interface. This setup is also valid for the bare graphene interface; C) Output curves of bare graphene EEVDs in a 0.1 mol L^{-1} phosphate buffer solution (PBS) (pH 7.2) under (black) short-circuit conditions at 5 mV s^{-1} and (blue) field-effect conditions with V_g = 0 V (*vs.* $Ag/AgCl_{sat}$); D) Output curves of graphene-fc EEVDs in a 0.1 mol L^{-1} phosphate buffer (pH 7.2) under (black) short-circuit conditions at 5 mV s^{-1} and (blue) field-effect conditions with V_g = 0 V (*vs.* $Ag/AgCl_{sat}$); E) Leakage current plot for graphene (black) and graphene-fc (red) interfaces in 0.01 mol L^{-1} PBS (pH 7.4) under V_{ds} = 0.01 V using $Ag/AgCl_{sat}$ as the gate electrode; F) Transfer curves (under field-effect) obtained using graphene (black) and graphene-fc (red) in 0.01 mol L^{-1} PBS (pH 7.4). All experiments used V_{ds} = 0.01 V; G) Short-circuit profiles after direct inversion of current signals with bare graphene (black) and graphene-fc (red) heterojunctions in a 0.10 mol L^{-1} phosphate buffer solution (pH 7.2).....55

Figure 3 - ssDNA adsorption based on graphene-fc characterization A) Schematic representation of graphene-fc heterojunctions formed by van der Waals adsorption of ferrocene and ssDNA adsorption and its *n* doping on graphene; B) Nyquist plots for bare graphene (black), graphene-fc (red), graphene-fc-ssDNA (green) interfaces from

1.10^5 Hz to 0.1 Hz, under the OCP potential of each surface (OCP ~ 0.13 V), in a 0.10 mol L^{-1} phosphate buffer solution (pH 7.2) and potential amplitude of 0.005 V; C) Impedance modulus *vs.* applied frequency logarithm plot for bare graphene (black, onset frequency ~ 4.6 Hz), graphene-fc (red) and graphene-fc-ssDNA (green, onset frequency ~ 7.4 Hz); D) Raman spectra for graphene (black), graphene-fc (red), and graphene-fc-ssDNA (green) surfaces; E) Close-ups of D band; G band, and 2D band shifts obtained for each interface......58

Figure 4 - ssDNA on drop detection A) Schematic representation of ssDNA adsorption onto EEVDs using a graphene-fc vdW heterojunction; B) Photograph of EEVD analysis on a drop setup during ssDNA detection; C) I_{ds} *vs.* V_{ds} plots of graphene-fc EEVDs under adsorption of ssDNA in a 1 amol L^{-1} – 1 μmol L^{-1} concentration range; D) Variation of OCP potential as a function of ssDNA adsorption in a 1.0 amol L^{-1} – 1μmol L^{-1} concentration range (in 0.10 mol L^{-1} phosphate buffer solution: pH 7.2) for graphene-fc EEVD with n = 3......59

Figure S1 - Cyclic voltammetry of bare graphene devices in 0.10 mol L^{-1} HCl for electrochemical removal of Cu residues at 1st cycle (black), 3rd cycle (red) and 16th cycle (blue). ν = 100 mV s^{-1}......63

Figure S2 – A) Raman spectra for monolayer graphene on Si/SiO_2 after EEVD's confection collected at basal plane (black line) and edge (red line) of graphene; B) AFM micrograph obtained for graphene on Si/SiO_2 at its basal plane; C) graphene sheet thickness plot collected by AFM tip on contact mode operation......64

Figure S3 - I_{ds} *vs.* V_{ds} plots for A) bare graphene, under V_g = 0, 0.1, 0.15, 0.2, 0.25, 0.3, 0.35, 0.4 and 0.45 V. Gray dashed line correspond to a no electrolyte and no gate voltage applied measurement; B) graphene-fc under V_g = -0.2, -0.1, 0, 0.1 and 0.2 V; C) Expanded red-circled region on Figure S2A for better observing I_{ds} variations as a function of different V_g. All voltages applied *vs.* $Ag/AgCl_{sat}$ as electrolyte-gated electrode. Experiments carried out in 0.01 mol L^{-1} phosphate buffer pH 7.4......67

Figure S4 - Bare graphene-SiO_2 transfer curve from -0.3 V to 0.5 V in 0.01 mol L^{-1} PBS under V_{ds} = 0.01 V......68

Figure S5 - Output curves of bare graphene EEVDs in 0.1 mol L-1 phosphate buffer pH 7.2 taken in short circuit conditions with different scan rates: a) 5 mV s^{-1}; b) 10 mV s^{-1} and c) 25 mV s^{-1}......69

Figure S6 - Cyclic voltammetry of adsorbed ferrocene onto graphene in A) 0.10 mol L^{-1} KCl (30th scan), scan rate = 25 mV s^{-1}; B) Cyclic voltammogram of bare graphene (black) and adsorbed ferrocene (red) 0.10 mol L^{-1} phosphate buffer pH 7.2, (3rd scan), ν = 25 mV s^{-1}......71

Figure S7 - Short-circuit transfer curves for EEVD with graphene-fc interface in 0.10 mol L^{-1} phosphate buffer pH 7.2 from 0 to 0.6 V (*vs.* $Ag/AgCl_{sat}$) and from 0.6 V to 0 V (*vs.* $Ag/AgCl_{sat}$), at 5 mV s^{-1}......72

Figure S8 - I_{ds} *vs.* V_{ds} curves In short-circuit conditions for bare graphene on SiO_2 (black; gray dots), graphene-fc (red; red dots). Dotted curves correspond to the non-modified ones while solid curves correspond to signal modified ones, as presented in Figure 2G of the main text......73

Figure S9 - Equivalent circuit simulated for graphene-fc and graphene-fc-ssDNA heterojunctions..77

Chapter IV - Graphene-based hybrid electrical-electrochemical point-of-care device for serologic COVID-19 diagnosis

Figure 1 – G-PNR EEVDs. A) Optical image of a pristine graphene EEVD after confection; B) Raman spectrum for pristine graphene EEVD (graphene on Si/SiO$_2$); C) Cyclic voltammograms of PNR electropolymerization under Ar atmosphere in a graphene large area (~0.1 cm^2) 2D electrode in PBS (0.01 mol L^{-1}, pH 7.4), KNO$_3$ (0.5 mol L^{-1}), and neutral red monomer (2.0 mmol L^{-1}), from – 1.0 V to +1.0 V (*vs.* Ag/AgCl$_{sat}$) for 2 scans and from – 1.0 V to + 0.5 V (*vs.* Ag/AgCl$_{sat}$) for 15 scans; n = 50 mV s^{-1}; D) Cyclic voltammograms of graphene interface in bare PBS (0.01 mol L^{-1}, pH 7.4) before PNR functionalization (black) and after PNR functionalization (red), leading to G-PNR interface; E) Schematic representation of hybrid EE experiments with graphene-based EEVDs; F) Pristine graphene (black) and G-PNR (red) EE I_{ds} *vs.* V_{ds} curves in PBS (0.01 mol L^{-1}, pH 7.4)..86

Figure 2 - AuNP/RBD characterization and adsorption onto G-PNR. A) TEM micrograph of AuNP/RBD bioconjugate; B) Schematic representation on AuNP/RBD immobilization methodology onto G-PNR; C) Optical image of G-PNR-AuNP/RBD surface in thin layer Au substrate; D) 2D chemical mapping of AuNP/RBD distribution onto G-PNR by proteinaceous RBD amide-I band monitoring; E) The respective 3D chemical mapping..87

Figure 3 - Electrochemical and EE studies for IgG interaction with G-PNR-AuNP/RBD surface. A) Cyclic voltammograms for bare graphene (black), G-PNR (red), G-PNR-AuNP/RBD (cyan) and G-PNR-AuNP/RBD after interaction with human IgG (1.0 mg mL^{-1}) (orange) in PBS (0.01 mol L^{-1}, pH 7.4), n = 50 mV s^{-1}; B) Hybrid I_{ds} *vs.* V_{ds} EE curves for bare graphene (black), G-PNR (red), G-PNR-AuNP/RBD (cyan) and G-PNR-AuNP/RBD after interaction with human IgG (1.0 mg mL^{-1}) (orange) in PBS (0.01 mol L^{-1}, pH 7.4), n = 5 mV s^{-1}; C) Nyquist plots for bare graphene (black), G-PNR (red), G-PNR-AuNP/RBD (cyan) and G-PNR-AuNP/RBD after interaction with human IgG (1.0 mg mL^{-1}) (orange) interfaces in PBS (0.01 mol L^{-1}, pH 7.4), from 1×10^5 to 0.1 Hz, amplitude = 5 mV and DC$_{pot}$ = OCP of each interface; D) Respective impedance modulus plots for each interface of item C)..87

Figure 4 - IgG detections for COVID-19 diagnosis through EEVD. A) Schematic representation of G-PNR-AuNP/RBD interface detecting IgG antibodies; B) Calibration curve for IgG detections from 1.0 pg mL^{-1} to 1.0 mg mL^{-1} concentrations in PBS (0.01 mol L^{-1}, pH 7.4) as support electrolyte by hybrid I_{ds} *vs.* V_{ds} EE experiments at 5 mV s^{-1}; C) Distribution of OCP displacement values for n = 9 for positive and negative IgG detections in diluted patient serum samples by G-PNR-AuNP/RBD EEVD; D) Analysis via ELISA dimerized intact RBD in samples from 20 positive and negative patients…89

Figure S1 - Pristine graphene EEVD confection. Schematic representation of the steps involved on the monolayer graphene EEVD confection by wet graphene transfer procedure, mediated by polystyrene polymer..94

Figure S2 - Pristine graphene EEVD. Photograph of pristine graphene EEVD ready-to-use..95

Figure S3 - E-etching of Cu residues. Cyclic voltammograms of Cu residues removal of EEVD graphene surface after wet transfer procedure in 0.1 mol L^{-1} HCl, n = 100 mV s^{-1}. The color scale varies from clearer pink to darker pink, between 1st, 3rd, 5th, 10th and 15th scans..96

Figure S4 – Optical images of PNR polymerization. Optical image of large area pristine graphene 2D electrode (A) before and (B) after PNR electropolymerization................97

Figure S5 - Raman spectra of graphene and G-PNR electrode surfaces. Comparison between graphene and G-PNR after PNR electropolymerization..................................98

Figure S6 - EIS G-PNR characterization. A) Nyquist plots obtained by EIS for bare graphene (black) and G-PNR (red) EEVD interfaces in a non-electroactive reaction medium (0.01 mol L^{-1} PBS pH 7.4), from 1×10^5 to 0.1 Hz under DC_{pot} = each interface OCP potential, variating with 5 mV of amplitude. B) Impedance modulus curves for graphene (black) and G-PNR (red) interfaces in 0.01 mol L^{-1} PBS pH 7.4, from 1×10^5 to 0.1 Hz, amplitude = 5 mV and DC_{pot} = OCP of each interface.....................................99

Figure S7 - Equivalent circuits. Equivalent circuits for A) graphene and B) G-PNR interfaces after best electrochemical circuit fitting on NOVA software.......................100

Figure S8 – Bioconjugates UV-Vis spectra. UV-Vis spectra for individual steps of BSA and protein additions for A) AuNP/RBD bioconjugates for the following involved reagents: AuNP (—), PBS + borate buffer (—), PBS + BSA protein (—), PBS + RBD protein (—) and the final AuNP/RBD bioconjugate (—)...101

Figure S9 – TEM micrograph for bare AuNP. A) TEM micrograph for bare AuNP colloidal suspension; B) AuNP diameter distribution obtained from TEM micrograph in A), average diameter of (15.3 ± 1.9) nm...102

Figure S10 – Possible interferents in IgG detection in human sera samples. Experiments were performed in 0.01 mol L^{-1} PBS pH 7.4 as support electrolyte with 1.0 µg mL^{-1} human IgM, BSA and bilirubin oxidase, respectively..103

Chapter V - Interfacial SARS-CoV-2 RBD femtomolar detections through graphene electrical-electrochemical vertical devices in serum and saliva

Figure 1 – Successive cyclic voltammograms obtained for pristine monolayer graphene cycling in 0.1 mol L^{-1} HCl, from -1.0 to 1.0 V (*vs.* $Ag/AgCl_{sat}$), 16 scans, $\nu = 100$ mV s^{-1}..113

Figure 2 – A) Optical image of monolayer graphene deposited onto EEVD channel on Si/SiO_2 substrate; B) Raman spectrum of monolayer graphene device showed in Figure 1A presenting typical graphene bands at 1328 (D band), 1595 (G band) and 2652 cm^{-1} (2D band); C) Schematic representation of EEVD's hybrid electrical-electrochemical working principles and Equations 1 and 2 representation...114

Figure 3 – A) Cyclic voltammograms obtained during the PNR electrodeposition from -1.0 to 1.2 V (*vs.* $Ag/AgCl_{sat}$), 2 scans and from -1.0 to 0.5 V, 15 scans, $\nu = 50$ mV s^{-1}; B) Cyclic voltammograms for bare graphene surface (black) and G-PNR surface after electrodeposition (red) in 0.01 mol L^{-1} PBS pH 7.4; C) Nyquist plots for bare graphene surface (black) and G-PNR surface after electrodeposition (red) in 0.01 mol L^{-1} PBS, pH 7.4, obtained from 1×10^5 to 0.1 Hz, DC_{pot} = OCP with 5.0 mV amplitude, with the

resultant equivalent circuit for G-PNR in the inset figure. D) Best electrochemical circuit fit for EEVD's bare graphene surface using NOVA software..117

Figure 4 – A) UV-Vis spectra obtained for each step of AuNP/IgG bioconjugate synthesis; B) Schematic representation of AuNP/IgG immobilization onto G-PNR EEVD..........118

Figure 5 – UV-Vis IgG spectrum in 0.01 mol L^{-1} PBS pH 8..118

Figure 6 – DLS size distribution by intensity of A) AuNP; B) AuNP/IgG bioconjugate..119

Figure 7 – A) Optical image of G-PNR surface onto Au substrate; B) 2D chemical mapping showing the distribution of PNR typical bands (SEELAJAROEN et al., 2019)..120

Figure 8 – A) Optical image of G-PNR interface with immobilized AuNP/IgG bioconjugate in an Au substrate; B) 2D and C) 3D chemical map of immobilized AuNP/IgG onto G-PNR based on amide I (1652 cm^{-1}) and amide II (1570 cm^{-1}) bands of the antibody..120

Figure 9 – Optical images collected for each surface analyzed by Raman mapping: A) bare graphene, B) G-PNR and C) G-PNR-AuNP/IgG..121

Figure 10 – 2D and 3D Raman mapping by D (Red color) and G (Green color) graphene bands integration for A), B) and C) bare graphene surface; D), E) and F) G-PNR and G), H) and I) G-PNR-AuNP/IgG surface. All 3D plots are normalized by highest band intensity of each surface..123

Figure 11 – A) Hybrid EE I_{ds} vs. (V_{ds} – V_{OCP}) curves for graphene (black), G-PNR-AuNP/IgG (green) and G-PNR-AuNP/IgG (pink) after interaction with 1.0 µg mL^{-1} RBD for 10 minutes and B) EIS Nyquist plots for graphene (black), G-PNR-AuNP/IgG (green) and G-PNR-AuNP/IgG (pink) after interaction with 1.0 µg mL^{-1} RBD for 10 minutes collected from 1×10^{5} Hz to 0.1 Hz with direct-current potential, DC_{pot}, equal to OCP, amplitude of 5 mV. All plots obtained in 0.01 mol L^{-1} PBS, pH 7.4............................125

Figure 12 - Cyclic voltammogram of graphene (black), G-PNR (red) and G-PNR-AuNP/IgG (green) obtained from -1.0 to 1.0 V (*vs.* Ag/AgCl$_{sat}$), ν = 50 mV s^{-1}, in 0.01 mol L^{-1} PBS, pH 7.4..126

Figure 13 – A) Schematic representation of RBD detection in a 40 µL drop by interaction with IgG in G-PNR-AuNP/IgG surface by hybrid EE methodology; B) Calibration curve for RBD detections from 10^{-12} to 10^{-7} g mL^{-1} concentrations (n = 3) in 0.01 mol L^{-1} PBS, pH 7,4; C) Positive (green) and negative (red) RBD detections in spiked bovine fetal serum (left, n = 20); and positive (blue) and negative (pink) RBD detections for spiked synthetic saliva (right, n = 30)..128

APPENDIX

Figure 1 – A) Schematic representation of an EEVD; B) Optical image of EEVD channel with monolayer graphene deposited onto Si/SiO_2..142

LIST OF TABLES

INTRODUCTION

Table 1 – Examples of works reported in literature for a variety of biosensing devices based on different detection strategies..18

Chapter I - On the Challenges for the Diagnosis of SARS-CoV-2 Based on a Review of Current Methodologies

Table 1 - Various Types of RT-PCR Protocols for SARS-CoV-2 Detection in the Literature ……………………………………………………………………………….29

Table 2 - Types of Commercial and Developed ELISA and CLIA Immunoassays Based on IgG and IgM Antigenic Activity Towards SARS-CoV-2 Proteins…………….........33

Table 3 - Commercial and Recent LFDs for COVID-19 Diagnosis…………….........35

Chapter III - Highly sensitive interfaces of graphene electrical-electrochemical vertical devices for on drop atto-molar DNA detection

Table S1 - Field effect parameters evaluated for bare graphene interface, graphene-fc and graphene-fc-ssDNA heterojunctions..75

Table S2 - Raman spectroscopy parameters obtained using a 633 nm laser for pristine graphene, graphene-fc and graphene-fc-ssDNA interfaces..79

Chapter IV - Graphene-based hybrid electrical-electrochemical point-of-care device for serologic COVID-19 diagnosis

Table 1 - Comparison of several serological detection methods of IgG antibodies produced in response to SARS-CoV-2 infection..89

Chapter V - Interfacial SARS-CoV-2 RBD femtomolar detections through graphene electrical-electrochemical vertical devices in serum and saliva

Table 1 – Comparison between different detection methodologies for RBD/Spike S1 protein quantification aiming COVID-19 diagnosis...130

TABLE OF CONTENTS

INTRODUCTION...17
PRESENTATION OF THE CHAPTERS...21
CHAPTER I - On the Challenges for the Diagnosis of SARS-CoV-2 Based on a Review of Current Methodologies..23
CHAPTER II - Problems of Interpreting Diagnostic Tests for SARS-CoV-2: Analytical Chemistry Concerns..47
CHAPTER III - Highly sensitive interfaces of graphene electrical-electrochemical vertical devices for on drop atto-molar DNA detection...51
CHAPTER IV - Graphene-based hybrid electrical-electrochemical point-of-care device for serologic COVID-19 diagnosis...82
CHAPTER V - Interfacial SARS-CoV-2 RBD femtomolar detections through graphene electrical-electrochemical vertical devices in serum and saliva..............103
1. Introduction...106
2. Objectives 107
3. Methods..108
  3.1 Reagents and materials...108
  3.2 Samples preparation...108
  3.3 AuNP synthesis...109
  3.4 Bioconjugate synthesis..109
  3.5 Micro-FTIR experiments..109
  3.6 UV-Vis measurements 110
  3.7 Dynamic Light Scattering (DLS) measurements 110
  3.8 EEVDs confection...110
  3.9 EEVD modification...111
  3.10 Raman Spectroscopy..111
  3.11 Electrical-Electrochemical measurements 111
  3.12 Analytical quantifications by EEVDs...112
4. Results and discussion..113
  4.1 Graphene EEVD working features...113
  4.2 Non-covalent modification of EEVD interface with PNR and AuNP/IgG bioconjugate...116
  4.3 Hybrid electrical electrochemical studies...124
  4.4 Viral detections through RBD quantifications...................................126
5. Conclusions 131
6. References...132
REFERENCES 138
APPENDIX...142
ANNEX...146

INTRODUCTION

As the global population grows, human needs become more complex. As a consequence, the demand on food quality monitoring, environmental screening, self-healthcare through telemedicine, mass-testing of infection diseases and pathogens detection become more evident and required to provide better life quality. To fulfill these needs, biosensing devices have been studied since their first development the 60's (VIGNESHVAR et al., 2016) and are continuously improved as technology and research evolve. By definition, a biosensor is an analytical device composed by a signal transducer interface containing a biological modifier responsible for biorecognition of the analyte of interest (Figure 1). This biorecognition is made in relation to the analyte concentration in the system medium. Based on these principles, research community have developed a large variety of biosensors that employ different detection methodologies based on distinct chemical phenomena for signal transducing, as: surface plasmon resonance, (LEE et al., 2015) electrochemistry, (ZHAN et al., 2016) exploration of electric nanomaterial properties, (MARTÍNEZ-DOMINGO et al., 2020) immunochromatography, (BAKER et al., 2020) chemiluminescence (NIRALA et al., 2020), impedance (EISSA et al., 2015) and others. A few examples are presented in Table 1.

Figure 1 – Schematic representation of biosensing signal transducing

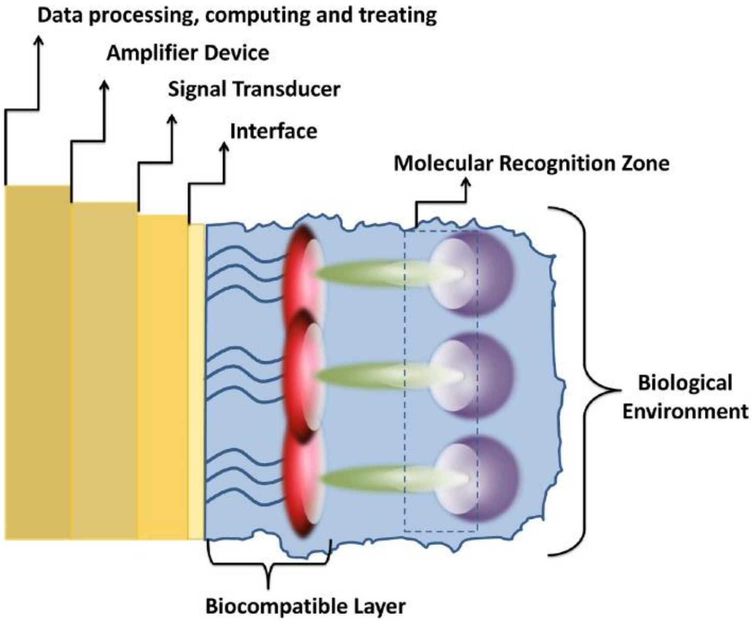

Source: reprinted from (OLIVEIRA et al., 2014)

Table 1 – Examples of works reported in literature for a variety of biosensing devices based on different detection strategies.

Detection principle	**Analyte of interest**	**Type of device**	**Reference**
Electrical	Heart failure brain natriuretic peptide	Field effect transistor	(LEI et al., 2017)
Electrical	Alzheimer disease biomarker	Field effect transistor	(PARK et al., 2020)
Surface plasmon coupled chemiluminescence	Mycotoxins	Silver nanoparticles modified platform	(JIANG et al., 2020a)
Surface plasmon resonance with interferometry	Lung cancer biomarker	Anodic aluminium chip	(LEE et al., 2015)
Photothermal and surface plasmon resonance	SARS-CoV-2 genetic material	Gold nanoislands in an Au film	(QIU et al., 2020)
Electrical pulse induced-electrochemical	Hepatitis E virus	Graphene quantum dots and Au-PANI nanowires	(CHOWDHURY et al., 2019)
Electrochemical	Influenza virus	Paper-based	(DEVARAKONDA et al., 2017)
Immunochromatography	COVID-19 IgG antibodies	Paper based lateral flow device	(CHEN et al., 2020)
Impedance	DNA	CVD graphene film	(BENVIDI et al., 2018)

Source: own author

Among all these techniques, electrical and electrochemical ones present some advantages, as: rapidness of response, easiness of operation of the developed devices, possibility of application in miniaturized Point-of-Care (POC) devices for local and just-in-time monitoring of analytes of interest, facility of device manufacturing without extensive and onerous preparation steps, robustness, remarkable sensitivity and selectivity, capacity of reaching extremely low Limits of Detection (LODs). (SIQUEIRA JR et al., 2013; HAMMOND et al., 2016) Moreover, the availability of miniaturized versions of the equipment required for electrochemical and electrical analyzes have increased over the past years, proportioning facility of POC detections performance by these devices.

These features are interesting for fulfilling some of the most prominent needs of human global community nowadays. As an example, it can be cited the need for mass testing of a population aiming controlling and monitoring of infectious diseases. This can be clearly illustrated by the intense research on alternative biosensors that have been being developed for research community during COVID-19 pandemics outbreak. (AYDIN; AYDIN; SEZGINTÜRK, 2021; MOJSOSKA et al., 2021; SHAO et al., 2021; ZHAO et al., 2021) The application of electrical and electrochemical wearable biosensors for self-healthcare and body monitoring have also attracted much attention from technological and medical community, as it allows the spread of telemedicine practices around the world, (AJAMI; TEIMOURI, 2015) especially in the COVID-19 pandemics context. (KICHLOO et al., 2020; LUKAS et al., 2020) Therefore, it has become noticeable that electrical and electrochemical biosensing devices are considered one of the most promising alternative technologies that can be explored for COVID-19 pandemics controlling. (JIANG et al., 2020b)

In this context, literature presents a large number of reports on how these devices have been applied for diagnosis and infection monitoring in a community. For example, Shao and collaborators developed a single-walled carbon nanotube field effect transistor for the rapid detection of SARS-CoV-2 viral antigens through S protein and N protein monitoring. This electrical-based device was capable of returning a binary positive or negative response for viral infection with LODs of an order of magnitude of fg mL^{-1} for both target proteinaceous analytes. (SHAO et al., 2021) This is of great interest and usefulness for mass testing purposes of infections at early stage. Li and collaborators also studied the application of electrical based devices for viral SARS-CoV-2 detections. However, the quantification of viral genetic material (RNA) was explored by using a graphene field effect transistor for detections in throat swab and human serum samples, that could be made with LODs of fmol L^{-1} of order of magnitude, evidencing the high sensitivity that this sort of device can achieve. (LI et al., 2021) On the other hand, electrochemical biosensors have also been studied for COVID-19 analytical applications. As example, Chaibun and co-authors developed a rapid electrochemical device based on isothermal rolling amplification, allowing the detection of S and N protein copies in clinical samples. Studies carried out with these samples showed a concordance of 100% with qRT-PCR results, proving the device as a highly selective alternative device for these quantifications. (CHAIBUN et al., 2021) Ali Ehsan and collaborators also explored electrochemistry towards COVID-19 detections. They developed a graphene-based screen printed electrode on paper substrates for Spike protein detections. IgG antibodies produced in response to SARS-CoV-2 infection were immobilized onto the electrode surface, leading to a label free device, capable of reaching a Limit of Quantification (LOQ) of fg mL^{-1} order of magnitude. (EHSAN; KHAN; REHMAN, 2021)

Despite of the remarkably promising results reached by electrochemical devices applied for COVID-19 infections, it is known that the sensitivity and LOD reached by this sort of device are not as promising as the reached parameters by electrical-based devices without further modifications, and, in many cases, depends on the extensive functionalization of electrode surface and monitoring of faradaic processes involving the target analyte or another label. Moreover, when COVID-19 quantifications are targeted, these difficulties can be intensified by the absence of redox co-factors in most of SARS-CoV-2 genes (as S and N proteins, for example), as well as in the IgG and IgM antibodies produced as a response for the viral infection. Thus, monitoring such kind of process by electrochemical detection techniques can be struggling. However, electrical based field effect transistors also present is disadvantages. As it frequently involves the sweeping of a gate voltage V_g versus I_{DS} measurement, (REDDY et al., 2012) a gate electrode is always required, and it frequently consists of an Ag/AgCl$_{\mathrm{sat}}$ electrode. It is known that this kind of electrode is non-polarizable due to its internal chemical equilibrium (BARD; FAULKNER, 2001) and therefore, any external polarization on it disbalance its intrinsic potential. As a consequence, potential readings in field-effect quantifications can be dubious. Another problem related to field effect transistors (Especially the graphene-based ones) comes from its highly sensitive interface and poor selectivity. The adsorption of every component from the analyte medium (electrolyte ions, water molecules, interferants and other compounds) lead to interfacial doping in some extent and consequently, Dirac potential shifts can be observed. (SIQUEIRA JR et al., 2013) To overcome this problem, interfacial functionalization is required, and depending on the strategy adopted, this device preparation step can take a long time. This can be a serious challenge to be avoided for the application of these biosensors in COVID-19 detections, as they required a robust result response that can affect public health status. Therefore, developing a biosensing device that can combine the most remarkable advantages of both electrical and electrochemical detection mechanisms and overcome the challenges involved in these two techniques is of great importance for biosensing research community, especially those involved in COVID-19 detections.

PRESENTATION OF THE CHAPTERS

This Thesis is divided into five different chapters, which are closely correlated to the major objective of developing a new generation of graphene-based biosensors. Chapter I, intitled *"On the Challenges for the Diagnosis of SARS-CoV-2 Based on a Review of Current Methodologies"*[*] gives an introduction on the COVID-19 pandemics outbreak and its implications not only in biosensing research field, but also in medical diagnosis and assays development. It also acts as a general introduction to the problematics that this Thesis aims to solve. A careful bibliographic revision of some of the most prominent COVID-19 detection technologies has been made, and insights regarding possible improvements were also given by the authors. Chapter II, intitled *"Problems of Interpreting Diagnostic Tests for SARS-CoV-2: Analytical Chemistry Concerns"*[†] carries a brief discussion on COVID-19 tests interpretations. The importance of correct analytical parameters evaluation and its implications on tests results was pointed out by the authors. Besides, differences between sensitivity and LOD, two frequently misinterpreted analytical parameters, were presented. In Chapter III, intitled *"Highly sensitive interfaces of graphene electrical-electrochemical vertical devices for on drop atto-molar DNA detection"*[‡] , turn, an unprecedent graphene-based biosensing technology was developed aiming highly sensitive biosensing detections in a miniaturized configuration, which can be used for POC diagnosis purposes. The developed device has its working principles based on hybrid electrical and electrochemical detection, allowing higher sensitivity, robustness, and reproducibility in comparison to other electrical detection methodologies. A proof-of-concept of the successful development of the proposed device, named Electrical Electrochemical Vertical Device (EEVD) was carried out with single-stranded DNA detections within a micro to atto-molar concentration range, with a LOD of 10^{-21} order of magnitude.

---

[*] MATTIOLI, I. A. et al. On the Challenges for the Diagnosis of SARS-CoV-2 Based on a Review of Current Methodologies. **ACS Sensors**, v. 5, n. 12, p. 3655–3677, 2020.

[†] MATTIOLI, I. A.; CRESPILHO, F. N. Problems of interpreting diagnostic tests for SARS-CoV-2: Analytical chemistry concerns. **Anais da Academia Brasileira de Ciencias**, v. 92, n. 4, p. 1–3, 2020

[‡] MATTIOLI, I. A. et al. Highly sensitive interfaces of graphene electrical-electrochemical vertical devices for on drop atto-molar DNA detection. **Biosensors and Bioelectronics**, v. 175, p. 112851, 2021.

Sequentially, EEVDs were applied for COVID-19 related detections and proved as interesting alternative biosensors for POC purposes, presented in Chapters IV and V. Both developed biosensors were built based on non-covalent interactions between graphene with its modifiers, for improvement of selectivity and sensitivity. Firstly, Chapter IV, intitled *"Graphene-based hybrid electrical-electrochemical point-of-care device for serologic COVID-19 diagnosis"*[§] presents the application of EEVDs for the serologic detection of IgG antibodies produced in response to SARS-CoV-2 infection, with a LOD of 1.0 pg mL^{-1} achieved. In Chapter V, intitled *"Interfacial SARS-CoV-2 RBD femtomolar detections through graphene electrical-electrochemical vertical devices in serum and saliva",* EEVDs were used for sensitive SARS-CoV-2 viral detections through RBD monitoring, with an LOD of 2.86 fmol L^{-1}. Moreover, apart from the detection studies, a careful characterization study by Raman Spectroscopy, Micro-FTIR, UV-Vis and Electrochemical techniques were presented for both EEVDs presented in Chapters IV and V, in order to provide essential information for better understanding the fundamental features of the proposed biosensing devices.

[§] MATTIOLI, I. A. et al. Graphene-Based Hybrid Electrical-Electrochemical Point-of-Care Device for Serologic COVID-19 Diagnosis. **Biosensors and Bioelectronics**, v. 199, p. 113866, 2022.

CHAPTER I - On the Challenges for the Diagnosis of SARS-CoV-2 Based on a Review of Current Methodologies

Author Contributions: <u>Isabela A. Mattioli:</u> conceived the project, performed bibliographic revision, endorsed discussion regarding the collected data, wrote and revised the manuscript; <u>Ayaz Hassan:</u> performed bibliographic revision, endorsed discussion regarding the collected data, wrote and revised the manuscript; <u>Osvaldo N. Oliveira Jr:</u> revised and corrected the manuscript; and <u>Frank N. Crespilho:</u> conceived the project, wrote, revised and corrected the manuscript.

In this article, a careful and deep discussion was made regarding the COVID-19 pandemics outbreak and its consequences for biosensing research field, as well as for the emerging need of mass-testing by POC devices. SARS-CoV-2 structural details were presented and discussed and comments on the differences between genetic and serologic detections for COVID-19 diagnosis. The strengths and limitations of a variety of employed techniques towards viral, genetic and serologic COVID-19 diagnosis (*i.e.* CRISPR, RT-PCR, Imunoassays, ELISA, LAMP, electrochemical, electrical and optical ones) were pointed out and, their respective performances were compared. Finally, authors insights on future possibilities for the development of new biosensing technologies were also presented.

ACS SENSORS

pubs.acs.org/acssensors Review

On the Challenges for the Diagnosis of SARS-CoV-2 Based on a Review of Current Methodologies

Isabela A. Mattioli, Ayaz Hassan, Osvaldo N. Oliveira, Jr., and Frank N. Crespilho*

Cite This: *ACS Sens.* 2020, 5, 3655–3677

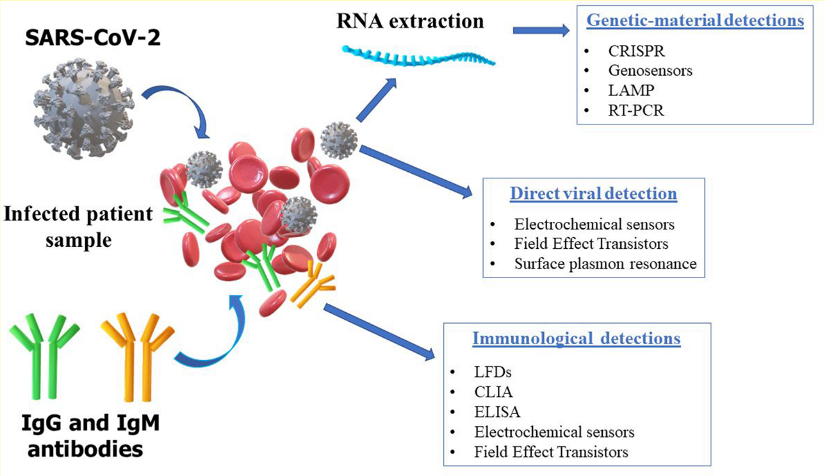

ABSTRACT: Diagnosis of COVID-19 has been challenging owing to the need for mass testing and for combining distinct types of detection to cover the different stages of the infection. In this review, we have surveyed the most used methodologies for diagnosis of COVID-19, which can be basically categorized into genetic-material detection and immunoassays. Detection of genetic material with real-time polymerase chain reaction (RT-PCR) and similar techniques has been achieved with high accuracy, but these methods are expensive and require time-consuming protocols which are not widely available, especially in less developed countries. Immunoassays for detecting a few antibodies, on the other hand, have been used for rapid, less expensive tests, but their accuracy in diagnosing infected individuals has been limited. We have therefore discussed the strengths and limitations of all of these methodologies, particularly in light of the required combination of tests owing to the long incubation periods. We identified the bottlenecks that prevented mass testing in many countries, and proposed strategies for further action, which are mostly associated with materials science and chemistry. Of special relevance are the methodologies which can be integrated into point-of-care (POC) devices and the use of artificial intelligence that do not require products from a well-developed biotech industry.

KEYWORDS: *SARS-CoV-2, point-of-care, COVID-19 diagnosis, biosensors, lateral flow devices, RT-PCR, surface plasmon resonance, nanoparticles*

The COVID-19 pandemic has shown the relevance of developing new tools for diagnosis, especially with low-cost technologies that permit rapid assays within the so-called *point-of-care* (POC) diagnosis paradigm.[1] The existence of well-established diagnostic methodologies for detecting viral genetic material[2,3] and human antibodies using rapid tests[4,5] has made it possible to achieve a relatively early detection of COVID-19 infection, in some cases with high accuracy. This has been instrumental for governments and societies to take proper actions to control spread and minimize the overall damage. Indeed, mass testing has been recommended from the early days of the pandemic by the World Health Organization (WHO)[6] for the surveillance and control of the spread of the disease. There are, however, important challenges to be faced in terms of performance of the diagnostic tools for detecting both genetic material and antibodies, mostly due to the cost and testing speed. Even more importantly, only a few countries could fully benefit from the existing technology, either because

Received: July 7, 2020
Accepted: November 17, 2020
Published: December 3, 2020

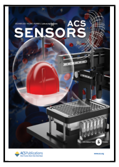

ACS Publications

https://dx.doi.org/10.1021/acssensors.0c01382

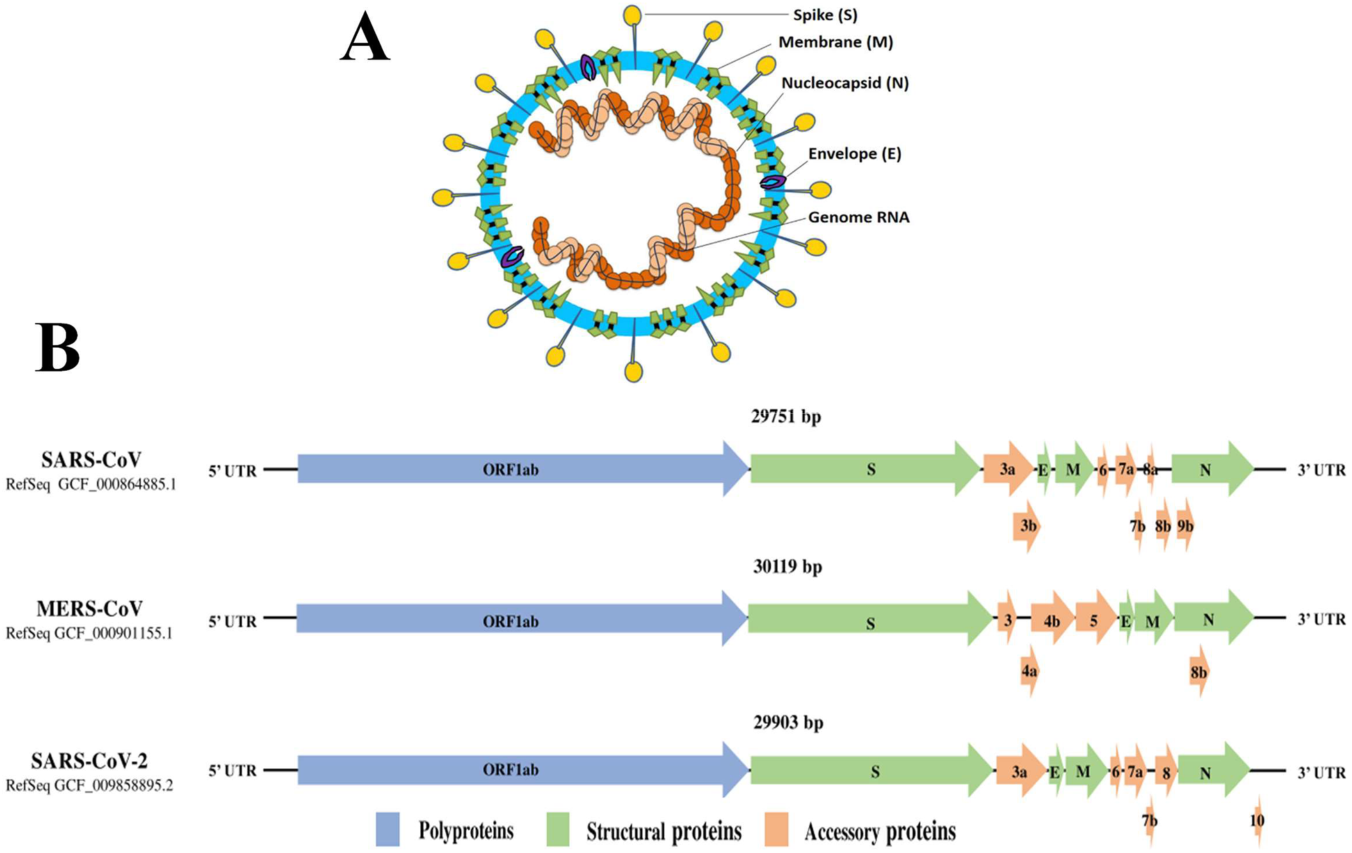

Figure 1. (A) Representation of CoV structure containing its spike glycoprotein (S), envelope protein (E), nucleocapsid protein (N), transmembrane glycoprotein (M), and its RNA viral genome. Reprinted with permission from ref 32. Copyright 2020, John Wiley and Sons. (B) Genome structure of SARS-CoV, MERS-CoV, and SARS-CoV-2 and encoded proteins. Reprinted with permission from ref 22. Copyright 2020, John Wiley and Sons.

the methods are too expensive or not easily deployable in poorer settings. Overcoming these challenges by using efficient and ready-to-use biosensor workflow research products could rapidly address the outbreak, as we shall elaborate upon in this article.

The failure of many countries to implement mass testing during the COVID-19 pandemic has highlighted the need for extra efforts and investments in the research and technology development of disease diagnosis. This is crucial to guarantee the security of humanity in general and of nations in view of possible outbreak of other pandemics. Here, we propose three different strategies to be adopted by governments and the scientific community for future epidemics to ensure protection of the population: (i) dissemination of plants in the biotechnology industry or at least ensure means to adequately supply the diagnostic tools to all countries, (ii) development of low-cost alternatives for the detection of genetic materials and immunoassays, particularly within the paradigm of POC diagnosis, and (iii) development of diagnostic strategies based on pattern recognition methods, as this minimizes the limitations brought by the lack of biotechnology industry. To achieve these goals, we suggest readaptation of existing methodologies for the diagnosis of COVID-19. This will make it possible to monitor current and future infectious diseases and place humankind in better shape to combat upcoming outbreaks of pathogenic diseases.

In this review, we mainly focus on the genosensing and immunosensing technologies which could be adapted to COVID-19 diagnosis, in addition to the molecular diagnosis and diagnosis exploiting pattern recognition. Attempts are made to provide a comprehensive review of the possibilities for diagnosis through illustration of the potential of such technologies. This review article is organized as follows. First, we comment on the structure, receptors, and possible targets of SARS-CoV-2 since an effective diagnosis requires understanding of the molecular machinery of the pathogens. The SARS-CoV-2 Diagnosis section introduces a brief discussion of the different detection techniques employed for COVID-19, with emphasis on the need to leverage distinct types of detection. An overview is presented of the challenges in detecting SARS-CoV-2 with nucleic acids-based and immuno-based techniques in the next two sections. Before concluding, we discuss emerging technologies that hold promise for the near future in the section Emerging Strategies for Diagnosis of COVID-19.

STRUCTURE OF SARS-COV-2

Coronaviruses (CoVs) belong to the *Coronaviridae* family of enveloped positive-stranded RNA viruses that exhibit the largest RNA genome of all known viruses. This family is divided into four main genera: alpha, beta, gamma, and delta-CoVs.[7,8] CoVs can be hosted by birds (gamma, delta-CoVs) or mammals (alpha, beta-CoVs), causing intestinal and respiratory illnesses.[8,9] Before the emergence of the severe acute respiratory syndrome coronavirus (SARS-CoV-2) in the outbreak of Covid-19 in December, 2019,[10] only six CoV

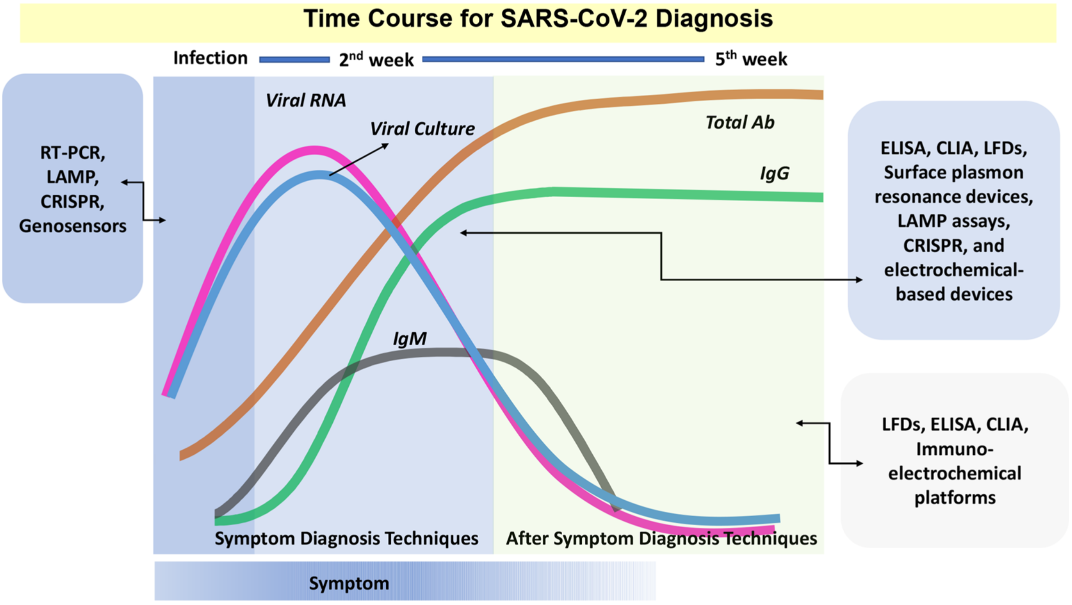

Figure 2. SARS-CoV-2 most appropriate detection methods along the course of infection. This figure is an illustrative scheme and it should be mentioned that discrepancies exist in the literature, especially for the tails of the curves. We decided to keep the qualitative character until more data are collected and a consensus is established on the time dependences.

species were known to infect humans. Four of these, i.e., HCoV-NL63, HCoV-HKU1, HCoV-OC43, and HCoV-229E, are related to mild respiratory infections,[8,11] while SARS-CoV and MERS-CoV cause severe respiratory illnesses. SARS-CoV caused an endemic in 2002−2003 in Guangang, China, and MERS-CoV emerged in Saudi Arabia in 2012.[8,11] Both SARS-CoV and MERS-CoV spread to several countries, infecting thousands of individuals with respiratory and neurological diseases with a high mortality rate.[12] The recent seventh member, SARS-CoV-2, is highly pathogenic. The disease it causes, referred to as COVID-19, is much more infectious and has spread to more than 200 countries in a time span of less than six months. Although the elderly are the most severely affected, with up to 50% of fatalities, a large number of hospitalizations have occurred for adult healthy patients with 2−11% fatality rate.[13] As of 14th October, 2020, more than 38 million people were infected by SARS-CoV-2 with at least one million deaths confirmed.[14]

The severity of the COVID-19 outbreak has led to a global mobilization by the pharmaceutical industry, governments, and academia to develop efficient diagnostics for mass testing, create a safe vaccine, and investigate treatments based on already approved medications.[15,16] In all of these endeavors, structural studies of SARS-CoV-2 are proving essential.[17−21] All CoVs exhibit similar structures with their genomes arranged in a similar fashion, as illustrated in Figure 1A. The viral genome and the nucleocapsid protein (N) are complexed to form a helical case within the hemagglutinin−esterase viral membrane (this latter is only present in some beta-CoVs). The viral gene also encodes a spike protein (S), nucleocapsid (N), internal protein (I), small membrane envelope protein (E), and a membrane protein (M).[7] In addition, a 5′-untranslated region (UTR), a 3′ UTR, nonstructural open reading frames (ORFs), and a conserved replicase domain (ORF1ab) (Figure 1B) exist in the viral genome.[22] The spike protein of SARS-CoV-2 is divided into the subunits S1 and S2, with a functional polybasic furin cleavage at the S1−S2 boundary, which can improve infection in host cells.[11,23] The spike protein receptor binding domain (RBD) localized in S1[24] has six amino acids (N501, L455, Q493, F486, S494, and Y505)[11] that are essential for binding on human ACE2 (Angiotensin-Converting Enzyme 2) receptors.[19] Among these six amino acids, five differ from SARS-CoV to SARS-CoV-2.[11] This interaction between the spike protein RBD and ACE2 receptors, which is crucial for the high contamination rate of SARS-CoV-2 in comparison to other human CoVs, has been studied in detail,[18,19,25−27] and is a potential therapeutic target. The SARS-CoV-2 spike protein may be useful for neutralization immunoassays[28] and a target for POC tests. The remaining structural proteins, N, E, and M, are mostly involved in the regulatory functions, RNA synthesis, protective function against the host immune system, and viral pathogenesis. These are more conserved proteins as compared to the S among the several human CoVs known so far. Moreover, structural similarities in SARS-CoV, MERS-CoV, and SARS-CoV-2 open the possibility for application or adaptation of existing diagnosis technologies and efficient treatment of COVID-19. On the other hand, SARS-CoV-2 exhibits a diverse gene position and has the chance of continued variation in the genome sequence due to the pandemic-scale spread of the disease.[29,30] Previous studies on several genomic sequences of SARS-CoV-2 revealed approximately 4% genomic mutation of total 220 strains analyzed,[31] suggesting the coexistence of different strains, which might be a new challenge for several diagnostic methods.

■ SARS-COV-2 DIAGNOSIS

SARS-CoV-2 has a unique biological characteristic, which brings several challenges to the health systems globally, and resulted in a poor response to contain the pathogenic disease. After the genetic sequence of the virus was known, the disease could be diagnosed with molecular testing based on viral RNA, such as reverse trancriptase polymerase chain reaction (RT-PCR), which are laboratory based and required skilled persons for operating sophisticated equipment. Therefore, mass testing could not be performed in the beginning of the pandemic due to the unavailability of testing facilities to the general public. Thanks to the research and development efforts of the clinical laboratory and academic researchers, several new and modified diagnostic tools were developed to make them available at varied locations. Indeed, today several types of diagnostic tools are available for detecting SARS-CoV-2.

Detection of SARS-CoV-2 has been made with various analytical techniques, either through quantification of nucleic acids or by measuring the immunoresponse of infected humans via antibody detection. The genetic-based techniques comprise RT-PCR, LAMP (Loop-Mediated Isothermal Amplification), CRISPR (Clustered Regularly Interspaced Short Palindromic Repeats), and genosensors, while immuno-based assays are mainly made with LFDs (Lateral Flow Devices), CLIA (Chemiluminescent Immunoassays), ELISA (Enzyme-Linked Immunosorbent Assays), and immunosensors. Detection in genosensors and immunosensors can be done with electrochemical and/or electrical measurements, as will be further discussed in the last two sections of this article. Even though the techniques mentioned are effective and sensitive, their sensitivity has been influenced by the choice of the principle of detection, viral load, and specific immuno-response of individuals. Indeed, one of the major challenges in the diagnosis of COVID-19 is the need to employ more than one detection strategy owing to the long incubation period of the virus. In addition to detecting genetic material of SARS-CoV-2, which can be performed at any stage, detection of antibodies through serological immunosensing needs to be carried out at different time points after infection. Figure 2 shows a schematic timeline with the most appropriate detection methods along the course of infection.

The profiles for IgG and IgM antibodies of SARS-CoV-2 have been discussed in a few works in the literature.[33,34] They are similar to the ones obtained for SARS-CoV infection, although the time dependences are significantly different.[35,36] For SARS-CoV infections, IgM peaks after 3 weeks from the onset of symptoms, while IgG peaks in the fifth week after onset of symptoms.[35] In the case of SARS-CoV-2, the viral load peaks in approximately 5−7 days after the onset of symptoms. IgG and IgM antibodies have different profiles. The IgM level in the organism peaks within ~14 days after the onset of symptoms and rapidly decreases in the third week of infection.[34] IgG, however, peaks between the second and third week of infection. Differently from IgM, the IgG level in the infected organism remains high until the fifth week of infection.

In the first days of infection, detection of COVID-19 is mainly performed by quantification of the SARS-CoV-2 viral load. Therefore, genetic-based techniques such as RT-PCR, LAMP, CRISPR, and genosensors are the most indicated (Figure 2, dark blue region, left). The peak of SARS-CoV-2 viral load coincides with the beginning of the immunoresponse to the disease through IgM and IgG production (middle region of Figure 2). In this case, in addition to detection of SARS-CoV-2 genetic material through LAMP, RT-PCR, CRISPR, and genosensors, immunological assays with high sensitivity can be applied for IgG and IgM, including CLIA, ELISA, LFDs, and immunosensors. After the third week of infection, IgG load reaches its maximum in the infected organism as the SARS-CoV-2 viral load remarkably decays. Hence, genetic-based techniques are no longer effective, and detection of SARS-CoV-2 is performed through IgG and IgM quantifications by CLIA, ELISA, LFDs, and electrochemical and electrical immunosensors (Figure 2, soft-blue region, right).

Immunoassays are cost-effective, sensitive, rapid, and selective, but they involve rigorous washing steps which affect automatization.[37] The genetic material-based techniques frequently exhibit improved sensitivity and selectivity in comparison to immunological assays.[37] This is a key advantage for detection of SARS-CoV-2, a virus with high structural similarity to SARS-CoV.[18] Nevertheless, detecting nucleic acids often requires time-consuming analyses and highly skilled operators,[37] being thus disadvantageous for mass testing in a pandemic outbreak. Therefore, there are challenges to be addressed in both types of detection for reaching an effective diagnosis, as will be further discussed in this review paper. Most of the techniques mentioned in this review have already been employed for SARS-CoV and/or MERS-CoV, including RT-PCR,[38] ELISA,[39] LAMP,[40] CLIA,[41] LFDs,[42] immunosensors,[43] and genosensors.[44] Some have been implemented in POC devices for several pathologies, including LFDs,[45,46] CLIA assays,[47] genosensors,[48] electrochemical immunosensors,[43,49] and field-effect transistor devices.[50] Herein, we will discuss important perspectives for adapting these existing technologies for COVID-19 detection.

From the need of different types of diagnostics, one may list the types of materials for the sensing units or test kits, most of which are products of the biotech industry. For detection of genetic material, the kits must contain DNA sequences (primers) which will function as biorecognition elements for different target genes responsible for proteins of the virus, such as ORF1ab, N protein, and S protein, for example. These are the cases of RT-PCR and LAMP assays. The primers are normally immobilized onto different materials depending on the technique and type of assay.[51,52] As usual in any development of a diagnostic tool, the sensing platform is first validated with standard spiked samples before experiments are done with real samples (i.e., swabs, blood, serum, and plasma samples).[3,53] The primers for RT-PCR and LAMP assays are produced by molecular biology methods. In the immunoassays, the biorecognition elements are frequently proteins (biomarkers) which will bind specifically to antibodies immobilized onto the sensing platform.[24,54,55] These devices can be applied to a large number of samples, as blood, serum, plasma, urine, and saliva. There is a large variety of materials onto which these biorecognition elements can be immobilized, including polystyrene in ELISA assays, magnetic beads in CLIA, and nanomaterials in electrochemical and electrical immunosensors. As in the case of genetic-based platforms, immunosensors are validated in spiked samples prior to real sample analyses.[56] The target antibodies and the biorecognition elements are produced by the biotech industry.

■ GENETIC MATERIAL-BASED DETECTION TECHNIQUES

In genetic material-based techniques, SARS-CoV-2 is detected through quantification of its viral RNA. For RT-PCR and LAMP assays, RNA is quantified after its transcription to DNA. CRISPR assays, on the other hand, are based on Case 13 targeting enzyme activity. In this section, we shall discuss the operation principles of these techniques and their application to SARS-CoV-2. Unfortunately, genosensors for SARS-CoV-2 detections have not been developed yet. Because we believe that integrating genosensors in POC devices is a viable route for mass testing of COVID-19, we shall discuss their earlier use for pathogens such as SARS-CoV.

RT-PCR for SARS-CoV-2 Testing. RT-PCR has been the most used technique for early diagnosis of SARS-CoV-2. RT-PCR, whose scheme to detect mRNA is shown in Figure 3, is already applied to detect several pathogens, including virus and bacteria.[57,58] For COVID-19, this involves detection of the causative virus,[53,59] similarly to its use in other acute respiratory infections. Diagnostics can be made with samples from different parts of the human body, including anal, nasopharyngeal, and oropharyngeal swabs and human fluids such as blood, blood serum, saliva, and urine.[60,61] SARS-CoV-2 could be found in 78% of serum and 50% of plasma samples.[22,62,63] Usually, PCR reactions are applied to DNA amplification and detection by direct reactions with *Taq* polymerase. However, since the genomic material of such viral pathogens as CoVs is RNA, a previous step for viral mRNA conversion to DNA is required. Therefore, the RT-PCR detection mechanism comprises two steps: (1) an RNA-dependent DNA polymerase (reverse-transcriptase) copies mRNA into complementary DNA (cDNA); and (2) *Taq* polymerase is applied to amplify the generated cDNA.[58] Most RT-PCR tests for CoVs are performed with fluorescence measurements and are quantitative, which is why sometimes they are referred to as RT-qPCR. Briefly, cDNA polymerizes with a probe targeted with both fluorescent and quencher labels. After polymerization into double-stranded DNA (ds-DNA), the quencher and fluorescent probes are separated and light emission from the fluorophore is observed upon light excitation.[58]

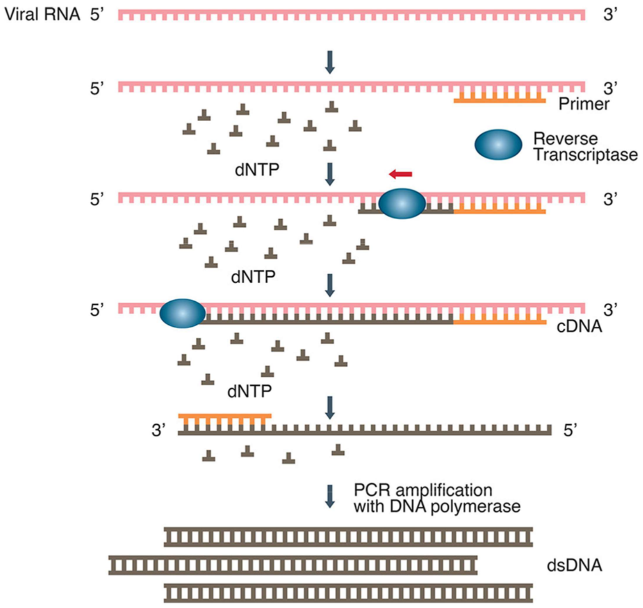

Figure 3. (A) Schematic representation of RT-PCR procedure to detect viral RNA through DNA amplification and detection. Reprinted with permission from ref 70. Copyright 2020, American Chemical Society.

RT-PCR detection is highly reproducible, sensitive, and selective. It is considered the most appropriate method for CoVs detection, including SARS-CoV-2.[58] However, it is time-consuming and expensive, requiring several steps to obtain the viral genome and post-sample treatments in a well-equipped laboratory. These requirements are especially limiting for the needed rapid, low-cost assays for SARS-CoV-2.[58,59,64] Moreover, its reliability for SARS-CoV-2 has been questioned owing to conflicting results depending on the sampling specimens.[65,66] Indeed, false results from RT-PCR analyses were observed for pharyngeal swab specimens from Wuhan hospitals,[67] probably owing to insufficient testing material collected from the patients, laboratory errors, or sample transportation issues.[2] In fact, to improve the reliability of the diagnosis, a recommendation was made to combine RT-PCR results with computer tomography images.[67] Furthermore, variable results from RT-PCR tests involving primers in ORF1ab and N genes were obtained due to variation in RNA sequences.[67] Thus, ORF1ab and N gene were not recommended for RT-PCR testing by institutions throughout the world.[22]

Many efforts have been made to improve RT-PCR in the context of COVID-19 detection. One such example is a high-throughput platform (Cobas 6800) for automated detection, which is helpful to cope with large numbers of samples without any fluctuations in the tests.[68] With this methodology, key steps in SARS-CoV-2 detection were fully automated, including nucleic acids extraction, purification, amplification, and detection. This facilitated sample-handling and data interpretation by people who are not familiar with RT-PCR assays. The samples can be inserted after a rapid processing, reducing the average total time of analysis to less than 30 min (including manual and hands-on steps).[68] Analytical validations regarding inter-run variability, limit of detection (LOD), and cross reactions with other pathogens were performed. For 25 mL of reaction volume, a LOD of 689.3 copies/mL with 95% of detection probability was reached, based on E gene targeting, without false positive results. It should be noted that test validation was made with spiked-in material, and therefore matrix effects from real samples could not be truly investigated.[68] These analytical results were consistent with those obtained by Corman et al., who also used RT-PCR for COVID-19 detection.[53] In this case, however, a workflow was established for situations in which viral genomic material of the virus is absent, which may be an alternative strategy for SARS-CoV-2 testing. The detection mechanisms were based on assays for E and RdRp genes. The latter assay contained specific probes capable of distinguishing SARS-CoV-2 from SARS-CoV, avoiding false positives that could occur due to structural similarities between CoVs. A LOD of 5.2 and 3.8 copies/reaction was obtained for E gene and RdRp, respectively. There was no cross reactivity with other human CoVs, 229E, KHU1, NL63, OC43, and MERS-CoV, showing the specificity of the assays.[53] To reduce the costs of RT-PCR assays, a new protocol was proposed for SARS-CoV-2 negative diagnostics with pharyngeal samples of asymptomatic volunteers with Trizol-RNA purification.[69] Although 3 of 12 volunteers involved in the work had to be retested, the accuracy and sensitivity limit reached with a known lentivirus was of 1−10 virus particles. These results were obtained after a primer validation step for RdRp, N, S and E genes, which is essential for a new RT-PCR assay. The time of analysis was 4 h, and the cost was estimated at less than US$ 15 per sample.[69] Hence, the issues to address for large-scale application of this protocol include the long time for analysis and the inaccuracy for detecting positive cases of SARS-CoV-2.

RT-PCR was also employed as the main diagnostic tool during MERS-CoV and SARS-CoV endemics,[71,72] and there-

Table 1. Various Types of RT-PCR Protocols for SARS-CoV-2 Detection in the Literature

gene target[a]	positive rate for SARS-CoV-2	LOD (95% of detection probability)	type of samples	ref
RdRp, N, E	55%	Not informed	Faecal samples	74
ORF1ab, NP	40.98% (ORF1ab) and 39.80% (NP)	Not informed	Nasal and pharyngeal swabs, bronchoalveolar lavage fluid, sputum	64
Nsp2 protein	39%	1.8 $TCID_{50}$/mL	Urine, rectal swabs, RTS	75
E-Gene-LDT	Not informed	95.55 copies/mL	Oropharyngeal, nasopharyngeal swabs	3
Not informed	3.33%	Not informed	Tears, conjunctival secretions, sputum	76
E	Not informed	27.6−32.2 (Ct, positive samples)	Oropharyngeal swabs	74
E, S	Not informed (single patient study)	Not informed	Semen, urine	77
RdRp helicase, S, N	28.2% for RdRp helicase, 43.6 for negative RdRd-P2, 24.2% RTS and 8.5% NRTS	11.2 copies/reaction for all genes	RTS, NRTS	78
CD4+, T lymphocytes, CRP, ESR, PCT	16.7% (stool), 6.9% (urine), 21.8 (oropharyngeal, feces)	Not informed	oropharyngeal swab, stool, urine, feces, and serum samples	61

[a] ESR: Erythrocyte sedimentation rate. CRP: C-reactive protein. PCT: ProcalcitoninCD4+: Cluster of differentiation 4. NP: nucleocapsid protein. RTS: Respiratory tract specimens. NRTS: nonrespiratory tract specimens. $TCID_{50}$: 50% tissue culture infective dose. Ct: Threshold cycle.

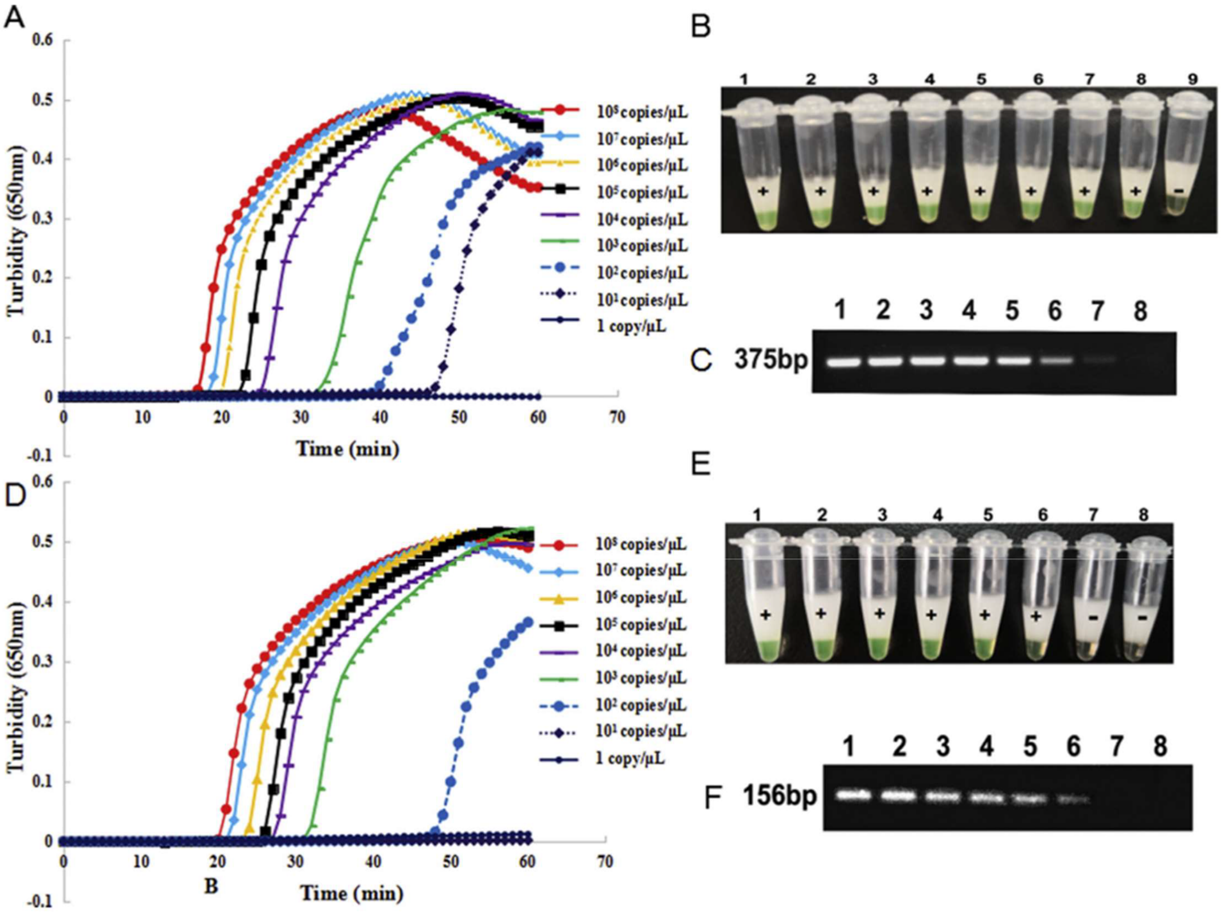

Figure 4. Sensitivity susceptibility to the primer gene for LAMP analyses. (A,B) RT-LAMP sensitivity toward ORF1ab gene targeting for SARS-CoV-2 detection based on ORF1ab-4 primer; (D,E) sensitivity of the proposed RT-PCR assay for SARS-CoV-2 S protein targeting using primer set S-123; (C,F) Conventional PCR assay sensitivity concerning both ORF1ab and S genes targeting for SARS-CoV-2 detection. Reprinted with permission from ref 81. Copyright 2020, Elsevier Publisher.

fore was successfully adapted to SARS-CoV-2. For example, the protocol for MERS-CoV detection based on N gene targeting may complement other gene targeting,[73] such as upstream MERS-CoV E gene (upE).[22,73] A remarkable specificity was achieved, which was confirmed by the lack of false positive amplifications with other human CoVs. Although satisfactory analytical results were obtained, this study was limited by the low amount of available real samples, and therefore the latter data reflect mock specimens spiked with the virus. Furthermore, storage conditions, handling, and collection for all the spiked samples were not patterned, leading to the lack of reliability of the results.[73] Hence, a stricter sample preparation protocol must be adopted if one decides to apply these assays for SARS-CoV-2 detection. In fact, important parameters optimized for other CoVs cannot be reproduced for a successful analysis of SARS-CoV-2 infections.[22] On the other hand, interference from other pathogens, e.g., other CoVs, may appear in case of simultaneous presence of these viruses in the sample. For instance, peaks of viral load for SARS-CoV, MERS-CoV, and SARS-CoV-2 are different. SARS-CoV and MERS-CoV viral load peaks were observed during the second week of infection, while the SARS-CoV-2 viral peak occurs in the first week of infection. Another important aspect concerns sampling specimens for RT-PCR analyses of viral RNA, which cannot be the same for the latter CoVs: SARS-CoV and MERS-CoV presented a positive rate of infection of approximately 100% for LRT (lower respiratory tract) specimens. SARS-CoV-2, in its turn, was more detectable (higher positive rate for RNA) with URT (upper respiratory tract) specimens.[22] This suggested that CoVs have different viral kinetics depending on the sampling specimens, and therefore, this is a new parameter to be optimized in RT-PCR. Nucleic acids testing by RT-PCR in blood samples has been effective to monitor SARS-CoV and MERS-CoV,[63,72] with the high viral load associated with the severe disease stage in the latter endemics.

Table 1 lists some RT-PCR assays for SARS-CoV-2 detection with figures of merit (as LOD), or from initial clinical studies. In this table, the positive rate found for SARS-CoV-2 with each assay was also reported. The positive rate should be interpreted as the rate of effective viral RNA detection with the respective RT-PCR assay and the chosen sample specimen.

Loop-Mediated Isothermal Amplification (LAMP) Assays. LAMP is a recent nucleic acid amplification technique, alternative to RT-PCR, which is based on a set of four designed primers and a strand displacement of active DNA polymerase. It is able to produce DNA targets (up to 10^9) in less than one hour under isothermal conditions (~63 °C).[79,80] LAMP assays have high specificity, sensitivity, simplicity of operation, and short time of analyses,[79] being more sensitive, stable, and resistant to inhibitors than PCR assays. This allows application with minimal sample preparation and less extensive nucleic acid extraction.[79] Because it is performed at a fixed temperature, its application in a POC assay for SARS-CoV-2 detection has been recommended.[58]

Similar to RT-PCR, RT-LAMP employs RNA transcription into DNA with DNA polymerase, but the selectivity is higher owing to the larger number of primers. RT-LAMP was applied to MERS-CoV with selectivity in the presence of similar CoVs,[40] and has been adapted to the diagnosis of COVID-19. In-house and commercial RT-LAMP assays reported for SARS-CoV-2 are based on primers for different genes, such as ORF1ab,[80−82] E protein,[80] S protein,[81−83] RdRp,[82] Nsp3,[83] ORF8,[83] ORF1a,[84] and N protein.[82−84]

To provide quick diagnosis, colorimetric detections were adopted.[83,84] RT-LAMP has been much less used than RT-PCR, but its sensitivity and reliability have been comparable to those of RT-PCR[80,82,84] In the study by Park et al., however, the LOD (100 copies per reaction) was not sufficient to detect COVID-19 in infected patients, which was attributed to the inadequate choice of target sequences based on SARS-CoV criteria.[83] Therefore, the correct choice of primers to be used in RT-LAMP assays seems to interfere not only on selectivity of the assay, but also on its ability to detect SARS-CoV-2 genetic material at trace levels. Yan and co-workers demonstrated that the accuracy may depend on SARS-CoV-2 mutations on the primer sequence of the target gene, as shown in Figure 4.[81] In fact, this limitation is also present in other genetic material-based assays, including RT-PCR.[85] Since RT-LAMP depends on using different primers and only shows optimum results at high temperatures, its application is limited and quite challenging under ordinary conditions. Besides, LAMP assays are not as useful as RT-PCR for mass testing because of the need of sophisticated (and, thus, expensive) thermal cycling equipment.[84] Another challenge faced by scaling-up RT-LAMP assays regards the need of genetic primers for the nucleic acid amplification reactions, which are expensive and nontrivial reagents to be obtained and cannot be stocked for a long time.

CRISPR-Based Biosensing Strategies. CRISPR-Cas (clustered regularly interspaced short palindromic repeats-CRISPR-associated) is a powerful analytical tool to modify genomes and gene functions.[86−88] A recent discovery of Cas13 as an RNA targeting enzyme in CRISPR-Cas has sparked excitement for next-generation biosensors with higher specificity, sensitivity, and rapid detection of nucleic acids.[86] Cas13 is an RNA-guided RNase capable of producing multiple cleavages in the nonspecific target single-strand RNA (ss-RNA).[89] To make it target specific, a CRISPR RNA (crRNA) is needed, and the resulting Cas13-crRNA complex has a higher target specificity for being guided to a RNA sequence of interest.[90] Thus, RNA sensing of Cas13 with nonspecific endonuclease activity is used as a detection strategy, where this enzyme modified with an RNA guide sequence is activated after combining with the specific target.

A fluorescent signal is produced as the activated enzyme interacts with a fluorophore quencher, which indicates the presence of RNA or DNA with high sensitivity and selectivity, up to fmol L^{-1}.[91] The collateral activity of the CRISPR Case family, particularly Cas13, is a triggered cleavage process with self-amplification ability, thus making the system highly sensitive and selective to detect nucleic acids.[88] In addition to the fluorescently labeled based detection, other strategies include visual detection of liquid−liquid phase separation in turbid solutions and lateral flow detection with antigen-labeled reporters.[92,93] The CRISPR/Cas13 biosensing technology has been used to detect ss-RNAs level of Zika virus,[94] dengue virus,[95] and micro-RNA (mi-RNA) in serum samples of brain-tumor patients.[96] In the latter investigation, an integrated low-cost, portable CRISPR/Cas13a biosensor was used to measure the electrochemical signal from miR-19b (brain tumor marker) with detection limit of 10 pmol L^{-1} within a total processing time of less than 4 h.[96] The technique can therefore be fast and low-cost, and does not require sophisticated laboratory equipment.

The sensitivity of the CRISPR/Cas13 method can be enhanced by introducing an isothermal preamplification step in a platform referred to as SHERLOCK (Specific High Sensitivity Enzymatic Reporter UnLOCKing).[97] This system uses recombinase polymerase amplification (RPA) of RNA or DNA and depends upon the introduction of T7 promotor (RNA polymerase), enabling RNA transcription followed by detection with Cas13. A protocol using SHERLOCK technology has been published to detect target RNA sequences with synthetic S and ORF1ab genes of SARS-CoV-2.[98] RNA sequences at concentrations as low as 20 amol L^{-1} were detected using lateral flow detection readout. The CRISPR/Cas13a assay has been reported with faster analyses than RT-PCR.[99] It can also be used as a benchmark for further advancements to provide a rapid, easy-to-handle, and sensitive system for mass testing.

One of the most prominent challenges for the application of CRISPR-based strategies is the noticeably high complexity of the technique. It requires an expert team and nontrivial reagents. Other difficulties include lack of standardization of tests, sequence limitations, and limited literature in CRISPR assays. Moreover, an additional step of DNA amplification is often needed to lower the LOD.[100] Owing to these characteristics, CRISPR technologies are less economically viable than RT-PCR and LAMP assays.

Genosensors. Genosensors are a useful, cost-effective alternative to RT-PCR for detecting viral RNA fragments of specific sequences. Similar to RT-PCR, genosensing is based on nucleic acid testing via hybridization between a probe, usually a single strand oligonucleotide, and a complementary DNA or RNA.[101] Upon hybridization of the probe immobilized on the sensor surface, a fluorescent, electrical, or electrochemical signal is produced, thus allowing the biorecognition of the target RNA. In contrast to RT-PCR, the genosensing approach is free from amplification and separation steps, making it simple and easy to handle. It has been used in food analysis[102] and environmental control,[103] but only recently in POC diagnosis.[101,104,105] Indeed, there is a demand for further developments of commercial products for mass testing, which may explain why genosensors for SARS-CoV-2 have not been reported yet. Because genosensors usually involve immobilization of specific probes for hybridization, these devices are of significant selectivity and rarely affected by interferents. This is relevant for the detection of SARS-CoV-2 in the presence of other CoVs, for example.

The prospects of employing genosensing assays for COVID-19 diagnosis are nevertheless promising because related technologies can be adapted. For instance, a genosensor device with a sandwich assay detected the Zika virus in samples of infected individuals, including saliva, serum, and urine in the presence of 1000-fold higher concentrations of dengue and chikungunya homologues.[106] A miniaturized gold-based genosensor platform detected SARS-CoV with an electrochemical technique with an LOD of 6 pmol L^{-1}.[44] The genosensor was sufficiently selective to distinguish 2-base and 1-base mismatches between complementary and unpaired hybrids.[44,107] Both genosensors detailed in refs 44 and 107 contained biotin-labeled probes. For the SARS-CoV genosensor, optimized performance was reached with a judicious choice of matrices and approaches to immobilize the complementary strand to a 30-mer sequence that encodes specific SARS-CoV regions.[44] It is in this aspect that materials chemistry and materials science may play a crucial role, since behind the simplicity of the genosensing methodology is the background knowledge acquired over decades of combining nanomaterials and biomolecules for sensing and biosensing (for a detailed review, see ref 108).[108] Many are the examples of successful results with genosensors depending on leveraging nanomaterials for matrices and principles of detection.[109] In the detection of a cancer biomarker, for instance, the organization of self-assembled monolayers was crucial to allow for distinguishing cell lines of neck and head cancer.[110] For SARS-CoV-2 genetic material detection, a supersandwich-type genosensing device was developed for early detection of viral RNA without amplification steps. The LOD reached of 200 copies/mL was claimed as the lowest in the literature up to the present day.[111] The detection assay allows the monitoring of the results through a smartphone. The development of these types of genosensing devices allow diagnosis with high sensitivity, which is suitable for mass-testing. On the other hand, the extensive preparation steps of the electrode and long incubation times can be considered time-consuming.

Therefore, this dependence on genosensor constituent materials should be considered for adapting current methodologies for COVID-19 diagnosis. While this dependence also applies to immunosensors, as discussed in the next section, the demand for rapid testing with genetic materials is a more urgent one while the COVID-19 pandemic lasts. On the other hand, despite its great selectivity, sensitivity, and other advantages, the scaling-up of genosensing technologies for quick mass COVID-19 technologies may face a number of challenges. As an example, the preparation of genosensing devices usually requires a long time and expensive reagents that cannot be stored at room temperature. Moreover, genosensing devices also demand non-ordinary transport conditions and normally present short shelf-lives.

In summary, the genetic materials-based diagnostics are rapid, sensitive, and specific and can enable the quantitative detection of SARS-CoV-2 RNA and hence early and large-scale detection of SARS-CoV-2. Nevertheless, their testing procedures are complex, in addition to their high cost and slow delivery to the end users. For example, building a RT-PCR processing lab may cost up to 15,000 USD to produce RT-PCR kits of 100 USD each,[1] in addition to the high ratio of false positive and false negative results, which occurs most routinely in these diagnostics tests.

■ IMMUNO-BASED TECHNIQUES

In this section, operation principles and the applicability of immunologically based techniques, such as ELISA, CLIA, and Lateral Flow assays, will be described in the SARS-CoV-2 detection scenario. We will first discuss the use of POC assays for COVID-19 diagnosis, and highlight some of the challenges inherent in these assays. Some important aspects of immunology toward SARS-CoV-2 proteins will be discussed. As we did for genetic material-based techniques, perspectives will also be presented of the use of nanomaterials to improve performance. Emerging immunosensors for SARS-CoV-2 detections will be mentioned, in addition to existing immunosensors developed for other CoVs.

Point-of-care (POC) immunodevices provide a useful platform for SARS-CoV-2 detection. Most POC devices have used immunological testing mechanisms, since tests of nucleic acids (such as viral RNA, for example) in these platforms are not straightforward.[112] It should be noted, however, that electrochemical and impedimetric genosensors are now also considered for POC purposes[48,113] as we discussed previously. POCs have been used for real-time identification of CoVs and other pathogenic diseases,[114] including SARS-CoV and MERS-CoV.[42,115,116] A successful detection of CoVs requires a suitable target protein and its corresponding antibody. For SARS-CoV-2, the most studied protein is the S protein with 24.5% non-conserved amino acid sequence of SARS-CoV. Distinguishing between SARS-CoV and SARS-CoV-2 was possible owing to these divergences in amino acid sequences, especially the antigenicity differences in RBD attributed to the low similarity in the non-conserved amino acid sequences.[117] SARS-CoV-2 S protein is not inhibited by polyclonal anti-SARS-CoV S1 antibodies T62.[117,118] Despite the differences in amino acid sequences, cross-reactivity between SARS-CoV, MERS-CoV, and SARS-CoV-2 S proteins antibodies is still possible in immunoassays. Indeed, SARS-CoV specific antibodies, such as the CR3022 human monoclonal antibody, bind to SARS-CoV-2 RBDs.[119] Furthermore, polyclonal goat antibodies anti-MHV S AO4 could be used to detect three CoVs S proteins. This suggested the existence of a conserved epitope in SARS-CoV, MERS-CoVs, and SARS-CoV-2.[118] The selective detection of these viruses using goat anti-MHV S antibodies AO4 by POC assays is not possible. Consequently, to avoid cross-reactivity and improve selectivity for COVID-19 diagnosis, specific recombinant antigens are needed. Therefore, some of the immunoassays for other CoVs based on S proteins should be carefully reviewed and readapted for SARS-CoV-2 diagnosis. An alternative protein that can be used for SARS-CoV-2 detections is N protein. There is evidence that SARS-CoV-2 may be detected through its N protein target alone or combined to S protein in different POCs.[1,120,121] Detection through N proteins already proved to be effective in immunoassays for MERS-CoV and SARS-CoV.[116,122]

Large-scale COVID-19 diagnosis in real blood samples has been made by targeting S protein with IgG and IgM antibodies in POC assays.[5] IgM and IgG sero conversion occurs simultaneously or sequentially in SARS-CoV-2 infected humans.[33] IgG reaches its maximum level in human blood after 17−19 days from the onset of symptoms, while IgM reaches its peak within 20−22 days after this onset.[33] IgM and IgG activity involves SARS-CoV-2 S and N proteins,[123] as confirmed by measuring their binding kinetics to S and N proteins.[124] Most intensive care unit (ICU) patients had higher concentrations of S and/or N IgG antibodies, probably due to the longer-term viral infection. Detection of N protein-based IgM and IgG was more efficient for early identification of the infection, owing to the immunogenicity and intracellular accumulation before virus packaging (i.e., virus assembly).[124] Some of these tests were less sensitive than S protein counterparts.[121] Another important aspect of N and S proteins regards their cross reactivity. Some degree of cross reactivity of SARS-CoV N and S protein was observed for positive COVID-19 serum samples regarding IgM and IgG responses.[33] A combined detection of N and S proteins by their IgM and IgG appears to increase the SARS-CoV-2 detection rate in early infections (up to 75% of patients).[33,124] Another antibody employed for SARS-CoV-2 detections in POC immunoassays is IgA, which can target the S protein RBD in immunoassays.[125,126] Its kinetic response in COVID-19 patients, however, remains unknown.[126] The concentration of IgA peaks during the third week of infection, being more persistent than IgM.[127] Therefore, different POC assays exist for CoVs immunological testing (including SARS-CoV-2) with IgM, IgG, and IgA antigen−antibody interactions.[125−130]

In contrast to the genetic material-based techniques, the immunosensing diagnostic tools could provide cost-effective diagnosis at primary health care units. Except for a few of these methods, such as ELISA which requires large readout devices, anticoagulants, and trained personnel, the majority of them do not need expensive laboratory infrastructure and a lot of reagents.[131] Therefore, they can be easily implemented outside a laboratory. Although we could not find the price of single immunosensing devices in the literature, they are considered less expensive due to their simple assay protocols. These protocols include three or four steps: sample injection, reaction, visualization/interpretation of the results. Therefore, they are economically much more viable than molecular or nucleic acids-based techniques.

Enzyme-Linked Immunosorbent Assays (ELISA). ELISA assays are popular immunoassays[132] to detect pathogens via quantification of antibodies[133] made to interact with antigens adsorbed on a solid support, e.g., polystyrene.[133] In an ELISA assay, the sample is first incubated in a polystyrene tube coated with the antigen. Then, enzyme-labeled Ig antibodies are added to the tube. After antigen−antibody interactions and washing steps, the remaining enzyme provides a quantification of the specific antibody in the serum sample. Antibodies can also be detected by other similar ELISA strategies, in three different assays (competitive, inhibition, and double-antibody).[133]

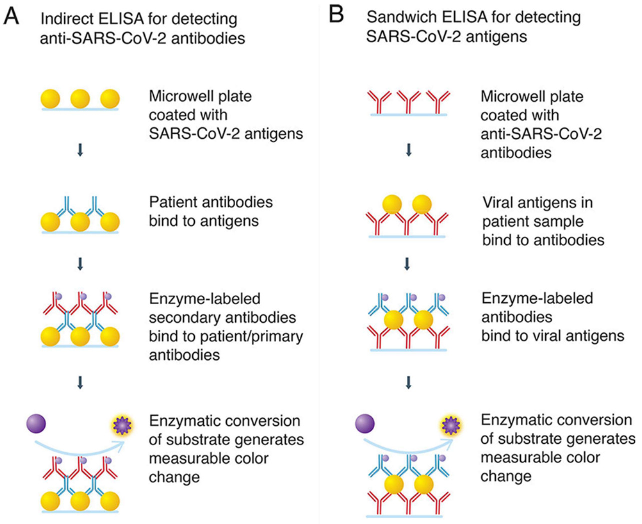

Figure 5. Brief description of operation modes of both (A) sandwich and (B) indirect ELISA assays for detecting SARS-CoV-2 antigens. Reprinted with permission from ref 70. Copyright 2020, American Chemical Society.

ELISA assays for SARS-CoV-2 have been developed for direct (sandwich) or indirect IgG and IgM detection,[121,134−136] this latter also called as capture or sandwich approach. Figure 5 shows a detailed comparison of these two methodologies.[57] Competitive ELISA is based upon the competitive binding of the sample analyte and a reference to the limited quantity of the adsorbed antibody.[133] This latter approach is only adopted for small peptides containing a single recognizable binding epitope. For example, Liu and co-workers observed that ELISA assays for IgM detection of S protein of SARS-CoV-2 are more sensitive than for the N proteins.[134] The sensitivity in IgG detection, on the other hand, was similar for S and N proteins. Therefore, the assays can be employed as a complementary test to RT-PCR, particularly for serum samples of COVID-19 patients after 10 days post-disease onset.[134] The main advantages of ELISA assays, especially for COVID-19 diagnosis, are the high sensitivity, uniform testing for a wide range of patients, speed, and simplicity of operation.[136] However, when direct antibody screening is employed to improve simplicity and rapidness of analyses, false positive results may be recorded. This is frequently related to interference factors. As an example, Wang and co-workers stated that interference in ELISA assays for IgM detections occurs.[137] It was found that rheumatoid factors at mid-to-high levels can lead to false positive IgM results. These data were obtained through urea dissociation tests.[137] Indirect antigen or

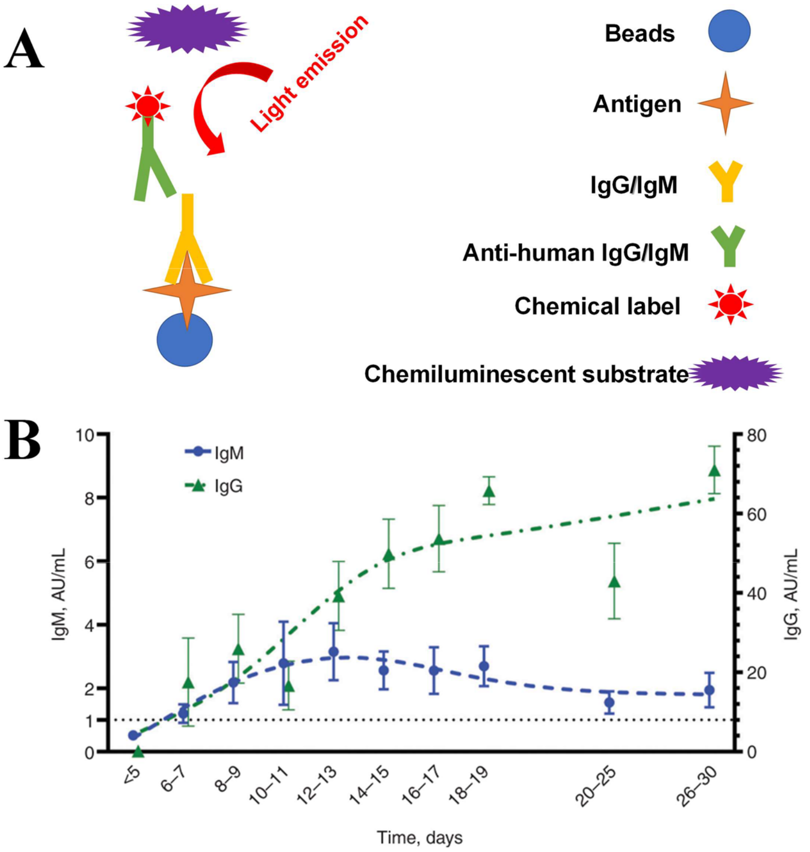

Figure 6. (A) Schematic representation of operation principles of CLIA assays. (B) IgG and IgM antibody quantification through CLIA assays versus days of infection by SARS-CoV-2. Reprinted with permission from ref 140. Copyright 2020, Walter de Gruyter GmbH &Co. KG.

Table 2. Types of Commercial and Developed ELISA and CLIA Immunoassays Based on IgG and IgM Antigenic Activity Towards SARS-CoV-2 Proteins

immunoassay/ test name	target	antibody	sensitivity	LOD	cutoff	ref
ELISA	SARS-CoV-2 S1 subunit of S protein	IgG/IgA	Not informed	Not informed	1.1 kAU/L (IgG, IgA)	127
ELISA	S and N recombinant SARS-CoV-2 proteins and HRP-conjugated antigen	Ab/IgG/IgM	89.6–100 (Ab), 54.1–79.8% (IgG), 73.3–94.3% (IgM)	Not informed	Not informed	152
rN and rS based ELISA	SARS-CoV-2 recombinant S and N proteins	IgG/IgM	74.3% (IgG), 77.1% (IgM)	Not informed	Not informed	134
ELISA HB300E analyzer	SARS-CoV-2 S and N proteins	IgG/IgM	33.3%	Not informed	Not informed	153
ELISA Euroimmun	Recombinant S1 structural SARS-CoV-2 protein	IgG/IgA	84%	Not informed	Not informed	125
CLIA Maglumi	SARS-CoV-2 recombinant antigen labeled with ABEI	IgG/IgM	64.3%	Not informed	Not informed	125
CLIA iFlash 1800 Analyzer	N and S SARS-CoV-2 proteins	IgG/IgM	73.3% (IgM); 83.3% (IgG)	Not informed	7.1 AU/mL (IgG); 10 AU/mL (IgM)	120
CLIA iFlash 300 analyzer	N and S SARS-CoV-2 proteins	IgG/IgM	Not informed	Not informed	Not informed	154
CLIA Axceed 260 analyzer	N and S SARS-CoV-2 proteins	IgG/IgM	Not informed	Not informed	Not informed	155

antibody screening, on the other hand, may be affected by nonspecific immobilizations.[138] Besides these challenges, cross-reactivity between SARS-CoV-2 and SARS-CoV can also happen, specifically with the EUROIMMUN ELISA assay for IgG detections.[139] Interference from other matrix components, such as hemoglobin, triglycerides, and bilirubin, was also evaluated, with no significant interference on the assay result.[139]

Chemiluminescent Assays (CLIA). Strategies using antibodies include chemiluminescent immunoassays (CLIA) described in Figure 6A.[140] CLIA are attractive due to possible automation, high specificity, low level of interferences, high stability of conjugates and reagents, reduced incubation time, compatibility with immunological assays protocols, and wide dynamic range.[141] Validation of CLIA assays is frequently performed by comparing with results from ELISA. The large-scale application of CLIA is hampered, however, owing to limited test panels, high costs, and nonlinear response to the analyte concentration due to complex chemical reactions.[138] In CLIA assays, a luminescent label acts as indicator of the chemical reaction in a direct or indirect methodology. For direct methods, acridinium and ruthenium esters are luminophores, while enzymatic markers (alkaline phosphatases, horseradish peroxidase with luminol, and AMPPD) are applied for indirect methods.[138] Antibodies may be labeled with different types of materials, including nanomaterials that possess increased surface electron density and surface area. This leads to signal amplification,[56,142] as illustrated with the use of gold nanoparticles,[56,143] magnetite nanoparticles,[56,144] and Au−Ag alloy nanoparticles.[145]

As occurs with ELISA assays, hemoglobin, triglycerides, bilirubin, and rheumatoid factor are matrix compounds which can interfere on CLIA results.[146] In addition, because CLIA is an immunoassay, other compounds such as autoantibodies, endogenous compounds, and human anti-animal antibodies can also interfere and lead to false results. A detailed review on interference in imunoassays is given in ref 147.

Detection of SARS-CoV-2 using CLIA has been mostly performed by targeting N and S proteins through IgM and IgG antibodies.[121] CLIA commercial assays had comparable sensitivity with ELISA and LFDs (lateral flow devices) POC devices,[125,148] but less specificity.[121] Montesinos and coworkers compared two automated assays for detecting SARS-CoV-2 in serum samples. Euroimmun IgG/IgA ELISA assays were more sensitive than IgG/IgM Maglumi CLIA assays,[125] consistent with results for other pathogens.[149] The results from a commercial CLIA assay for IgM and IgG are shown in Figure 6B, where the concentration of each antibody was monitored along the course of the infection, starting from the fever onset.[140] Deviations in the results were less than 4% and 6% for IgM and IgG, respectively. The detection of SARS-CoV-2 through fully automated CLIA assays has been reported.[150] The mass application of these automated assays is a challenge for low-budget locations, and there is the possibility of false negative results, especially at early-stage of infections.[150] Therefore, other methodologies are required for the correct management and treatment of patients. Table 2 lists some ELISA and CLIA assays used for SARS-CoV-2 detection. Most of the articles do not present a LOD value or even the obtained cutoff for the studied assay. These latter parameters are essential to evaluate the minimum amount of analyte that can be detected by the assay. This issue is frequently related to misinterpretation of the meaning of sensitivity in the medical area. A thorough discussion of this topic is provided in ref 151.

Lateral Flow Devices (LFDs) for Point-of-Care Testing. POC immunoassays in LFDs provide quick, efficient, and inexpensive testing through immunochromatographic mechanisms. LFDs are paper-based strip devices comprising four main regions: (1) cellulose-based sample pad for sample dropping; (2) conjugate pad, generally made of glass fiber containing the labeled particles (generally colorimetric or fluorescent) conjugated to the analyte receptor; (3) nitrocellulose-based detection pad with test lines, and control lines—test lines contain biomolecules capable of binding to the analyte-label-conjugated particles (if the target analyte is present in the sample); a signal proportional to the analyte concentration is generated, while control lines are used to verify the test operation, capturing labeled-conjugated particles independently of the presence of the analyte; (4) absorption pad, also made of cellulose, which helps induce sample flow through the test strip.[156] The limitations of POCs with LFDs are related to the low sensitivity toward the target analyte and cross-reactivity with other species in the sample matrix. Moreover, the viscosity of the liquid samples needs to be within a certain range, which prevents a wider use of such devices.[156] Interference from matrix blood samples, as discussed in CLIA and ELISA assays, should also be taken into account for LFDs immunoassays. A number of other difficulties may exist for application of LFDs, which include denaturing of immobilized proteins (i.e., antigens), nonspecific adsorption, nanoparticle aggregation, and steric hindrance.[157] The performance of the assays may also depend on the paper used in some LFDs. To exemplify, trapping of biomolecules on paper pores results not only in binding undesired effects, but also in flux rate changes.[157] To cope with these problems, several pretreatments of the pads are carried out.[158] An illustration of a LFD device likely to be used for SARS-CoV-2 is depicted in Figure 7.

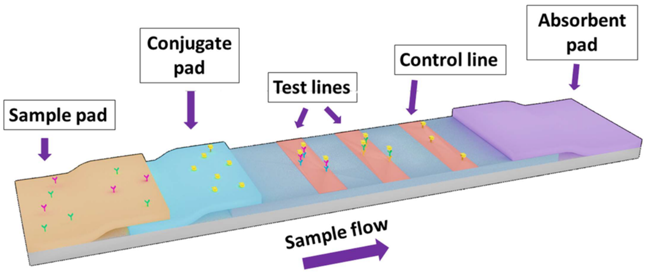

Figure 7. Representation of a typical LFD assay that can be employed for SARS-CoV-2 testing. The design of commercial assays is the same as that represented above. The device comprises a sample pad in which IgM and IgG antibodies are immobilized. The conjugate pad contains gold nanoparticles (AuNP) conjugated to a SARS-CoV-2 antigen. In test lines, anti-human IgG and anti-human IgM are immobilized to interact with IgG-AuNP-antigen and IgM-AuNP-antigen complex. The control line contains nonhuman reactive anti-IgG or anti-IgM. The absorbent pad is useful for maintaining sample flow through the strip.

In spite of these limitations and challenges, LFDs have been applied for COVID-19 diagnosis in human blood and serum samples,[1,4,130,135] in most cases to confirm suspected and asymptomatic cases.[4] In comparison to ELISA and CLIA assays, LFDs diagnostics shows satisfactory sensitivity and accuracy for SARS-CoV-2 detection.[125] The sensitivity with nine commercially available immunochromatographic gold-labeled LFDs for IgM and IgG detections ranged 72.7−100%, with results obtained in less than 20 min.[159] Since LFDs are not quantitative for COVID-19, the sensitivity parameter adopted is different from those used in analytical chemistry. This difference was clarified by Lassaunière et al., who defined sensitivity as "the number of patients which were correctly diagnosed with SARS-CoV-2 infections by the studied POCs after a previous positive SARS-CoV-2 diagnosis by nucleic acids testing with respiratory samples".[130] Most LFD tests for SARS-CoV-2 are based on S or N proteins as antigens, but a large number of commercial LFDs assays do not specify the virus protein chosen as antigen. Although Whitman and collaborators reported the maximum sensitivity in their LFDs detections for COVID-19 diagnosis, they focused on the report of the "positivity" rate obtained, which increased significantly after 2 weeks of disease conditions.[160]

Table 3. Commercial and Recent LFDs for COVID-19 Diagnosis[a]

immunoassay/test name	target	SARS-CoV-2 species	sample	sensitivity	ref
LFD Avioq	IgG/IgM	Recombinant SARS-CoV-2 antigen	Human serum	68.8%	125
LFD/LNPs labeling	IgG	SARS-CoV-2 N protein	Human serum	Not informed	163
LFD	IgG/IgM	RBD of S protein	Blood samples	88.66% (positive results); 90.63% (negative results)	128
LFD	Ab/IgG/IgM	SARS-CoV-2 N and S proteins	Plasma samples	97.5% (Ab); 86.3% (IgG) 88.8% (IgM)	153
LFD AutoBioDiagnostics	IgG/IgM	Not informed	Human serum	93%	130
LFD DynamikerBiotechnology	IgG/IgM	Not informed	Human serum	90%	130
LFD CTK Biotech	IgG/IgM	Not informed	Human serum	90%	130
LFD ArtronLaboratories	IgG/IgM	Not informed	Human serum	83%	130
LFDs (DeepBlue, Bioperfectus, UCP)	IgG/IgM	Not informed	Human serum and plasma samples	84.3−100%	160

[a] LNPs: Lanthanide-doped polystyrene nanoparticles. Ab: Total antibody. RBD: Receptor binding domain.

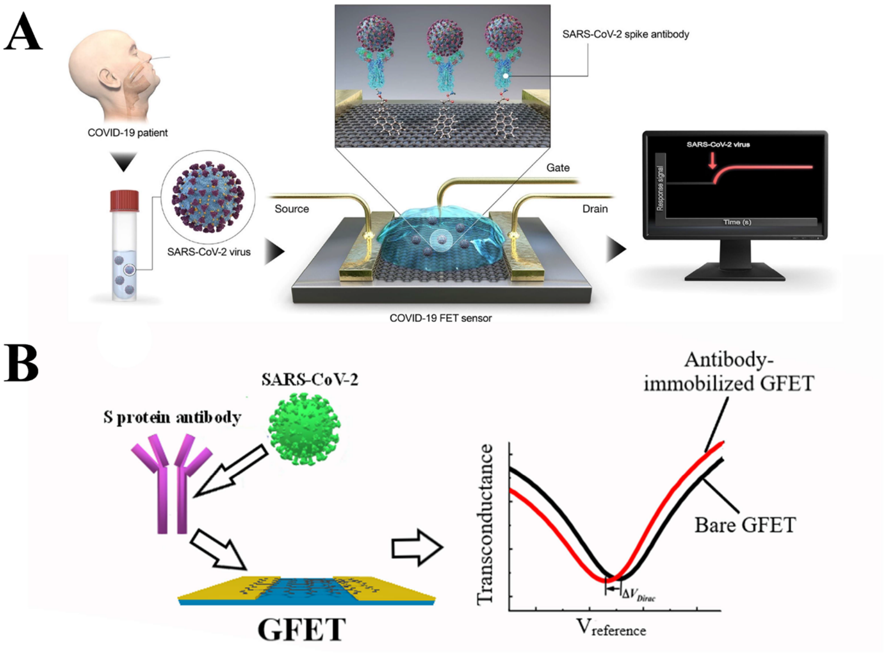

Figure 8. (A) Application of GFET-based electrical immunosensor with SARS-CoV-2 S protein antibodies immobilized onto graphene surface. The device was employed for SARS-CoV-2 detection in clinical samples from COVID-19 infected patients. Reprinted with permission from ref 182. Copyright, 2020, American Chemical Society. (B) Schematic representation of GFET immunosensor for RBD of S1 subunit. V_{ref} shift due to antibodies immobilization in comparison to the bare graphene surface.

Diagnosis of SARS-CoV-2 with LFDs has also benefited from recent advances in incorporation of nanoparticles.[45,161,162] For instance, lanthanide-doped polystyrene nanoparticles were employed instead of conventional AuNP as fluorescent labels for detecting IgG through N protein immobilization.[163] The assay was reproducible (coefficient of variation <15%) with detection results comparable to RT-PCR, showing the suitability for detection of suspicious and asymptomatic COVID-19 cases.[163] However, in contrast to RT-PCR assays, LFDs assays are limited at the onset of infection, because production of IgG and IgM antibodies has not yet begun.

Colloidal gold nanoparticles were studied by Huang and co-workers on a simple and easy-to-handle LFD platform to detect SARS-CoV-2 N protein using an anti-human IgM−colloidal gold nanoparticle conjugate. Despite the similarity between these assays and the commercial LFDs for SARS-CoV-2 detection, selectivity and sensitivity achieved were satisfactory and up to 90% in both cases.[164] However, this research is at an early stage of development. Indeed, there is no report of a well-established methodology using these innovative LFDs for COVID-19 diagnosis. This highlights another important challenge for the use of LFDs: the successful establishment of novel nanobiointerfaces for the development of new LFDs within an acceptable time frame. A possible alternative is to employ nanomaterials for antibody conjugates and colorimetric responses on test strips, which could be viable for COVID-19 diagnosis.

Some of LFDs for SARS-CoV-2 immunodetection are summarized in Table 3.

Electrochemical and Field-Effect Transistor-Based Immunosensors as Point-of-Care Devices. Electrochemical and electrical immunosensors have been incorporated into POC devices for many pathogens and analytes,[165−170] particularly with incorporation of nanomaterials (including 2D materials).[171−178] Electrochemical immunosensors have indeed been used for MERS-CoV,[43] but surprisingly, we have been able to find only one example for SARS-CoV-2, with the eCoVSens platform. A fluorine-doped indium−tin oxide electrode was modified with gold nanoparticles and COVID-19 monoclonal antibodies for detecting the S1 domain of S protein.[179] Spiked samples were analyzed within 10−30 s, and the LODs of 90 and 120 fmol L^{-1} were reached.

Among the immunosensors containing nanomaterials, of special relevance are the graphene field-effect transistors (GFETs) in which biosensing exploits changes in the electrical properties of the interface induced by analyte approximation and/or adsorption.[172,180,181] High performance is expected owing to the high basal plane conductivity of graphene, and its dependence on surface changes.[173,182] The first GFET developed to detect SARS-CoV-2 is illustrated in Figure 8A.[182] Antibodies for the S protein were immobilized through 1-pyrenebutanoic acid and succinimidyl ester probe linkers. Detection was made by measuring the drain current with clinical samples prepared from nasopharyngeal swabs, under a constant bias of 10 mV.[182] The device was capable of distinguishing infected from noninfected samples, with a detection limit of 0.42×10^2 copies/mL.[182] The LODs for other samples tested were 1 fg/mL, 100 fg/mL, and 16 pfu/mL in phosphate buffer saline, clinical transport medium, and culture medium, respectively.[182] Another GFET immunosensor applied to SARS-CoV-2[24] had antibodies from SARS-CoV S1 subunit immobilized onto graphene, as illustrated in Figure 8B. Using changes in the liquid gate voltage (V_{ref}), detection of RBD (Receptor Binding Domain of S1 subunit) of S protein could be achieved with a LOD of 0.2 pmol L^{-1} with a measuring time of only 2 min, according to Figure 8B.[24] The ACE2 enzyme could also be detected with S1 spike protein by monitoring the V_{ref} changes. This latter immunosensor is interesting for quantifications of infected cells, since ACE2, a human integral membrane protein, acts as receptor for SARS-CoV-2 binding and subsequent infection.[26] Considering the strategies involving different targets for detection published so far for SARS-CoV-2, we believe that monitoring real-time ACE2-spike S1 protein interactions is useful for evaluating *in vivo* infections.

In spite of being promising, electrochemical and electrical immunosensors frequently face selectivity as the main challenge for their validation. This is normally addressed with functionalization strategies, as mentioned above related to specific antibodies for COVID-19 early and sensitive diagnosis. However, the need of additional preparation steps for functionalization and biomolecules incubation frequently increases the biosensor fabrication time, making them more expensive than other immunosensing devices.

On the other hand, the adoption of functionalization strategies for selectivity improvement is also useful for minimizing interference effects. These methodologies are known for their significant efficiency, and consequently, they are adopted not only in biosensing technologies, but also in a wider range of detection through electrochemical methods. For instance, a gold microelectrode presented remarkable anti-interference activity toward As^{3+} detections by using amino-functionalized graphene oxide as modifying agent.[183] For SARS-CoV-2 diagnosis, interference from other CoVs with similar structures as well as other compounds from the sample matrix may be avoided by functionalizing the electrochemical device with recombinant antigens or their specific antibodies. This was the case of detection of SARS-CoV-2 S1 subunit antibodies using recombinant antigens on gold micropillar electrodes decorated with graphene oxide.[184] The LOD was 1 pmol L^{-1} with a detection time of 11.5 s with a smartphone-based interface,[184] but these devices may not be suitable for mass-testing because of the target analyte chosen by the authors: specific antibodies for S1 subunit proteins of SARS-CoV-2, which are not produced by a human infected organism. Instead, perhaps an electrochemical sensing platform for detecting IgG and IgM antibodies may be a more efficient strategy.

■ EMERGING STRATEGIES FOR DIAGNOSIS OF COVID-19

In this section, we wish to emphasize that the diagnosis of COVID-19 can be improved and extended if sensing strategies are explored, which can lead to low-cost methodologies for mass tests and/or increased accuracy. There are several such strategies, but for the sake of conciseness, we shall illustrate only three types: paper-based biosensing, plasmonic-enhanced biosensing, and use of pattern recognition methods (which may incorporate machine learning). All of these three strategies can be utilized not only for immunosensing and genosensing but also with alternative principles of detection in which specific biorecognition is not required.

Paper-Based Biosensors. Paper-based biodevices (PBBs) are simple, inexpensive, and robust alternatives to assays, as has been proven for diagnosis of infectious diseases.[185−187] These are miniaturized POC devices[188] made of porous cellulose capable of storing the reagents, and the reaction with the analyte being detected either visually by a color contrast through fluorescent/colorimetric dyes or via spectroscopic measurements.[189] In order to be sensitive and selective for a given disease, these devices have biorecognition elements immobilized, such as enzymes, antibodies, and aptamers.[190−193] The whole detection process is performed on a single strip of nonexpensive paper, without requiring additional instrumentation and multiple processing steps. This feature has been exploited in immunosensors[54,194,195] and in genosensors with nanomaterials such as reduced graphene oxide−gold nanocomposites[113] and bimetallic nanostructures.[48] For genosensors, sensitivity and accuracy for the diagnosis of malaria were higher than with RT-PCR.[196] PBBs are also useful for multiplex POC devices for sensitive, high quality diagnostics of biomarkers of several diseases.[186]

PBBs have been used to detect diseases within a label-free detection scheme in which a biorecognition element is not required. A PBB with oxidized paper was capable of detecting an abnormal level of human serum albumin (HSA) in urine samples via colorimetry, which is associated with a disease referred to as proteinuria/microalbuminuria.[197] Detection was made possible, in spite of the absence of a biorecognition element, owing to covalent bonding to the protein, as confirmed by micro-FTIR spectroscopy.

In spite of their advantages, PBBs have not been reported so far for SARS-CoV-2 diagnosis, probably because mass-testing in official centers of COVID-19 diagnosis is challenging. First, as already mentioned in the LFDs section, paper-based devices may be limited owing to their complexity.[158] Problems may arise from trapping of biomolecules, thus causing a decrease in binding effectiveness and requiring adequate preconditioning of the paper matrix.[157,158] Second, automated methods to fabricate paper-based devices need to be developed. This can be done with such techniques as inkjet printing, PDMS

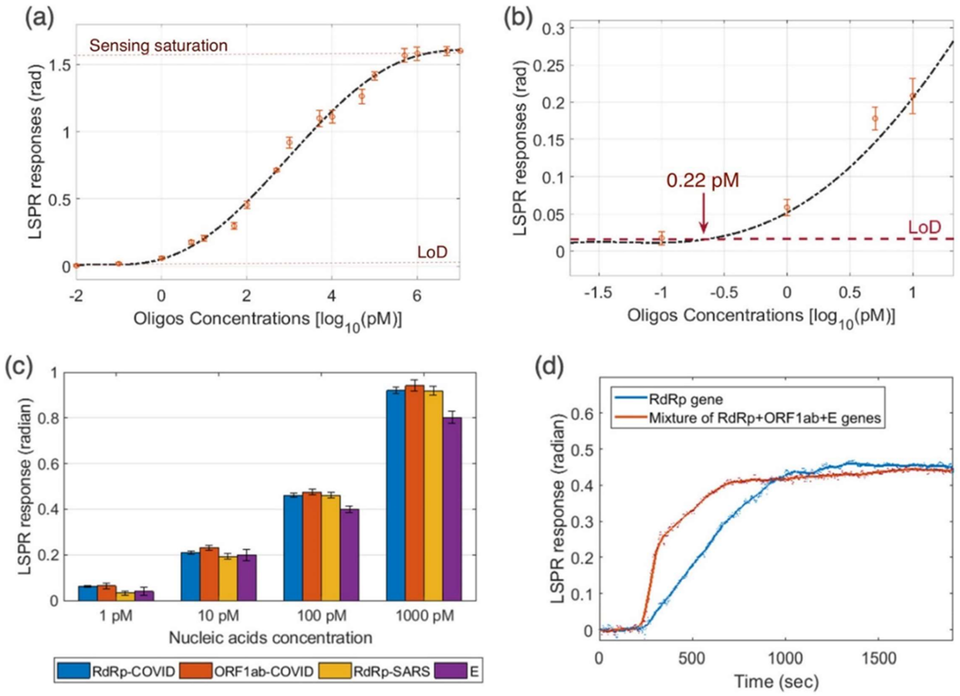

Figure 9. (a) LSPR response versus RdRp of SARS-CoV-2 concentration; (b) zoom of low-concentration region of LSPR biosensor responses for different RdRp oligos concentrations; (c) LSPR biosensor response for detection of other viruses, such as ORF1ab and E protein from SARS-CoV-2 and RdRp from SARS-CoV; (d) comparison of LSPR biosensor response in single-analyte samples and mixture of several sequences. Reprinted with permission from ref 215. Copyright 2020, American Chemical Society.

plotting, laser cutting, and photolithography. However, in addition to the expensive equipment required, preparation takes several steps and resolution is low.[198] Therefore, the scaling-up of PBBs may be less advantageous than expected, especially in the context of COVID-19 pandemics, which requires fast and effective strategies.

Plasmonic-Based Biosensors. Plasmonic effects have been exploited for biosensing with various principles of detection (for a focused review, see ref 199),[199] including surface plasmon resonance (SPR)[200−202] and localized surface plasmon resonance (LSPR).[203−205] LSPR, in particular, is promising owing to the enhanced electromagnetic field in the neighborhood of the nanostructures, which imparts higher sensitivity[206] as demonstrated in LFD assays where the colorimetric signal of gold nanoparticles was amplified upon laser excitation. Another advantage is the possibility of using laser-reader systems with the standard LFDs architecture and operation mode.[206] One should emphasize that LSPR can be useful for investigating interaction mechanisms during infection by SARS-CoV-2, including protein interactions with human receptors believed to be essential for the virus maintenance in human cells. Indeed, SPR can provide experimental evidence of phenomena related to docking studies.[207−210] Another advantage of LSPR biosensors is the cost of commercialization, as for example a home-built LSPR system based on white-light extinction would cost ∼$25,000 or less.[211] Compared with other more sophisticated LSPR equipment, this is a lower-cost possibility.

When plasmonic and thermal effects are combined, the sensitivity of the biosensing device for detecting nucleic acids can be increased considerably.[212] The “thermoplasmonic” effect arises from the nonradiative relaxation of absorbed light in nanomaterials, thus generating an excessive localized heat energy that can be harnessed as a local heating source for controlled thermal processes.[213] This provides a rapid alternative methodology for identifying DNA sequences and mutations.[214] A similar methodology was adopted in dual-function biosensors for SARS-CoV-2 detection[215] in synthetic viral oligonucleotide sequences identical to the one used in ref 53. The AuNIs (Au nanoislands) sensing chip functionalized with synthetic receptor oligonucleotide (RdRp SARS-CoV-2-C) was implemented into an LSPR detection system. Hybridization was ∼8 times faster with the thermoplasmonic effect when RdRp SARS-CoV-2 genes were injected into the sensing chamber. The evaluation of this dual-plasmonic device for viral nucleic acids detection based on LSPR responses is illustrated in Figure 9. It should be noted that nonspecific binding of mismatching sequences was prevented, which demonstrates the impact of localized heating on the hybridization kinetics. Various challenges must be addressed to apply LSPR biosensor to COVID-19, including the difficulties in preparing robust, reproducible substrates. Furthermore, the devices should ideally be reusable and easy to functionalize and clean after analysis.[211]

Artificial Intelligence Based Methods. The sensing strategies mentioned so far are all based on detecting specific targets requiring genetic sequence probes, proteins, and protein subunits. Because a considerable amount of data is generated, especially to account for the variability of the biological samples, statistical and computational methods can be utilized for the diagnosis, including machine learning, Internet of Things (IoT), deep learning, and other artificial intelligence (AI) approaches.[216−221] AI can also be employed during COVID-19 pandemics for the development of personalized medicine.[222] For example, Prasad and coworkers[223] developed a guide for reinforced learning algorithms to determine extubation time for each patient. The course of the treatment, evolution of symptoms, and day-to-day updates of the recuperation of patients can also be monitored through artificial intelligence algorithms.[224] Another prospective application of artificial intelligence is in the development of safe vaccines and pursuing therapeutic drugs.[225] Although artificial intelligence methodologies seem useful and efficient, several issues must be tackled for its widespread implementation. These include a speedy data collection, storage, and analysis, which requires specialized people and data centers. This may be difficult for some developing countries severely affected by SARS-CoV-2.

Perhaps the most important breakthrough will be reached when various types of data are integrated into a single system. This could be realized with computer-assisted diagnosis systems, as discussed in reviews dedicated to the use of Big Data concepts and computational methods in processing sensing data.[226−228] IoT approaches are also useful for online data collection from sensing devices and interpretation of these data, as well as orienting medical decisions based on Big Data analysis models.[221] The framework of these computer-assisted systems is entirely generic and can be applied to any type of task involving diagnosis, monitoring, or surveillance. More specifically for COVID-19, one may envisage a diagnosis strategy considering reports of symptoms, analysis of health parameters, and data from sensors which do not need to be specific for SARS-CoV-2 (i.e., sensors other than the immunosensors and genosensors discussed here). Hence, a somewhat accurate diagnosis could be achieved even if no specific tests are available. An added advantage would arise from feeding the results from a large number of people into a surveillance system to monitor the disease spread, which could be performed in a seamless manner in a computer system.

■ CONCLUSIONS

Herein we have described the main strategies employed so far in SARS-CoV-2 diagnosis, which are basically categorized into methods to detect genetic material of the virus and immunoassays. Special emphasis was given to identifying the strengths and limitations of these methodologies. In particular, we elaborated upon the limitations in connection with the difficulties in performing mass testing in many countries, from which we identified three major challenges: (i) employ genosensors in POC devices to replace the sophisticated methods used (RP-PCR, LAMP, CRISPR) in detecting genetic material, since this is critical to diagnose individuals with no symptoms; (ii) improve the accuracy of the diagnosis based on immunoassays, which is by no means straightforward because distinct types of antibodies may be needed to detect owing to the time dependence of their concentrations along the infection course; (iii) use pattern recognition methods that do not require biotech products and the test kits, which is essential in poorer places.

For all the challenges above, we envisage that new developments will be required in materials, especially nanomaterials. From our survey, we noted that the main emphasis has been placed on the definition of target biomolecules, but strategies to enhance performance using nanomaterials have been limited. For detection of genetic material, for instance, developing low-cost alternatives to the expensive methods should be prioritized, and this depends on novel uses of nanomaterials. One should aim at POC devices which can fulfill all the stringent requirements of low-cost, rapid tests and easy deployment in any setting. Also relevant to the chemistry and materials community is the possible extension of well-established electrochemical, electrical, and plasmonic effects to diagnosis of SARS-CoV-2. In this review, we have mentioned a few examples in which graphene and metallic nanoparticles were incorporated into the sensing devices, and we can foresee that much more can be done by exploiting the whole portfolio of biosensing strategies in which nanomaterials are used.

■ AUTHOR INFORMATION

Corresponding Author

Frank N. Crespilho − *São Carlos Institute of Chemistry, University of São Paulo, São Carlos 13560-970, São Paulo, Brazil;* orcid.org/0000-0003-4830-652X;
Email: frankcrespilho@iqsc.usp.br

Authors

Isabela A. Mattioli − *São Carlos Institute of Chemistry, University of São Paulo, São Carlos 13560-970, São Paulo, Brazil;* orcid.org/0000-0002-1646-3996
Ayaz Hassan − *São Carlos Institute of Chemistry, University of São Paulo, São Carlos 13560-970, São Paulo, Brazil;* orcid.org/0000-0003-3842-5883
Osvaldo N. Oliveira, Jr. − *São Carlos Institute of Physics, University of São Paulo, São Carlos 13560-590, São Paulo, Brazil;* orcid.org/0000-0002-5399-5860

Complete contact information is available at:
https://pubs.acs.org/10.1021/acssensors.0c01382

Notes

The authors declare no competing financial interest.

■ ACKNOWLEDGMENTS

The authors gratefully acknowledge the São Paulo Research Foundation (FAPESP) for the financial support of the research projects under the grant numbers: 19/15333-1, 19/12053-8, 18/11071-0, and 18/22214-6. Coordinating Agency for Advanced Training of Graduate Personnel (CAPES), MeDiCo Network CAPES-Brazil grant number: 88881.504532/2020-01 and for PNPD program, grant number: 88887.358060/2019-00. National Council of Scientific and Technological Development (CNPq) project number 305486/2019-5.

■ VOCABULARY

Biosensors: Biosensors are devices thar are able to transduce a biological event into a measurable analytical signal. Proteins, biological structures and microorganisms can be detected through biosensing strategies.

Antibody: An antibody is a protein produced by the immunological system for the defense of their host organism from external pathogens. They do it with high specificity, by binding to specific parts of the targets.

Point-of-care devices: These are devices that enable medical diagnosis at the time and place of patient care. They are suitable for quick and mass testing, without long sample preparation steps and reactions.

Genosensors: A genosensor is a specific type of biosensor dedicated to the detection of DNA (i.e., genetic material). The event that enables detection consists of hybridization of DNA specific probes that are complementary to the DNA (or RNA) target sequence to be detected.

Electrochemical sensors: Devices that can give information on the composition of a system based on electron-transfer reactions into a sensing transducer (electrodes). The signal obtained can be used for quantification and other analytical purposes.

Analytical chemistry: A branch of chemistry dedicated to the determination of composition of matter and its quantification. In many cases, analytical chemistry deals with these issues through the development of robust instrumentation, implementation of statistics and innovative sensing strategies.

■ REFERENCES

(1) Sheridan, C. Fast, Portable Tests Come Online to Curb Coronavirus Pandemic. *Nat. Biotechnol.* **2020**, *38*, 515.

(2) Li, Y.; Yao, L.; Li, J.; Chen, L.; Song, Y.; Cai, Z.; Yang, C. Stability Issues of RT-PCR Testing of SARS-CoV-2 for Hospitalized Patients Clinically Diagnosed with COVID-19. *J. Med. Virol.* **2020**, *92*, 903.

(3) Nörz, D.; Fischer, N.; Schultze, A.; Kluge, S.; Mayer-Runge, U.; Aepfelbacher, M.; Pfefferle, S.; Lütgehetmann, M. Clinical Evaluation of a SARS-CoV-2 RT-PCR Assay on a Fully Automated System for Rapid on-Demand Testing in the Hospital Setting. *J. Clin. Virol.* **2020**, *128*, 104390.

(4) Abbasi, J. The Promise and Peril of Antibody Testing for COVID-19. *JAMA - J. Am. Med. Assoc.* **2020**, *323*, 1881.

(5) Li, Z.; Yi, Y.; Luo, X.; Xiong, N.; Liu, Y.; Li, S.; Sun, R.; Wang, Y.; Hu, B.; Chen, W.; Zhang, Y.; Wang, J.; Huang, B.; Lin, Y.; Yang, J.; Cai, W.; Wang, X.; Cheng, J.; Chen, Z.; Sun, K.; Pan, W.; Zhan, Z.; Chen, L.; Ye, F. Development and Clinical Application of A Rapid IgM-IgG Combined Antibody Test for SARS-CoV-2 Infection Diagnosis. *J. Med. Virol.* **2020**, *92*, 1518.

(6) *Strategic Preparedness and Response Plan on COVID-19*; World Health Organization, 2020; p 20.

(7) Weiss, S. R.; Leibowitz, J. L. *Coronavirus Pathogenesis*, 1st ed.; Elsevier Inc., 2011; Vol *81*. DOI: 10.1016/B978-0-12-385885-6.00009-2.

(8) Corman, V. M.; Muth, D.; Niemeyer, D.; Drosten, C. Hosts and Sources of Endemic Human Coronaviruses. *Adv. Virus Res.* **2018**, *100*, 163−188.

(9) Cui, J.; Li, F.; Shi, Z. L. Origin and Evolution of Pathogenic Coronaviruses. *Nat. Rev. Microbiol.* **2019**, *17* (3), 181−192.

(10) Wu, F.; Zhao, S.; Yu, B.; Chen, Y. M.; Wang, W.; Song, Z. G.; Hu, Y.; Tao, Z. W.; Tian, J. H.; Pei, Y. Y.; Yuan, M. L.; Zhang, Y. L.; Dai, F. H.; Liu, Y.; Wang, Q. M.; Zheng, J. J.; Xu, L.; Holmes, E. C.; Zhang, Y. Z. A New Coronavirus Associated with Human Respiratory Disease in China. *Nature* **2020**, *579* (7798), 265−269.

(11) Andersen, K. G.; Rambaut, A.; Lipkin, W. I.; Holmes, E. C.; Garry, R. F. The Proximal Origin of SARS-CoV-2. *Nat. Med.* **2020**, *26* (April), 450−452.

(12) Mahase, E. Coronavirus Covid-19 Has Killed More People than SARS and MERS Combined, despite Lower Case Fatality Rate. *BMJ.* **2020**, *368*, m641.

(13) Singhal, T. A Review of Coronavirus Disease-2019 (COVID-19). *Indian J. Pediatr.* **2020**, *87* (4), 281−286.

(14) *Weekly Epidemiological Update*; October 2020. DOI: 10.30895/2312-7821-2020-8-1-3-8.

(15) Amanat, F.; Krammer, F. SARS-CoV-2 Vaccines: Status Report. *Immunity* **2020**, *52* (4), 583−589.

(16) Elfiky, A. A. Ribavirin, Remdesivir, Sofosbuvir, Galidesivir, and Tenofovir against SARS-CoV-2 RNA Dependent RNA Polymerase (RdRp): A Molecular Docking Study. *Life Sci.* **2020**, *253*, 117592.

(17) Walls, A. C.; Park, Y. J.; Tortorici, M. A.; Wall, A.; McGuire, A. T.; Veesler, D. Structure, Function, and Antigenicity of the SARS-CoV-2 Spike Glycoprotein. *Cell* **2020**, *181* (2), 281−292.

(18) Lan, J.; Ge, J.; Yu, J.; Shan, S.; Zhou, H.; Fan, S.; Zhang, Q.; Shi, X.; Wang, Q.; Zhang, L.; Wang, X. Structure of the SARS-CoV-2 Spike Receptor-Binding Domain Bound to the ACE2 Receptor. *Nature* **2020**, *581*, 215.

(19) Yan, R.; Zhang, Y.; Li, Y.; Xia, L.; Guo, Y.; Zhou, Q. Structural Basis for the Recognition of SARS-CoV-2 by Full-Length Human ACE2. *Science (Washington, DC, U. S.)* **2020**, *367* (6485), 1444−1448.

(20) Tahir ul Qamar, M.; Alqahtani, S. M.; Alamri, M. A.; Chen, L.-L. Structural Basis of SARS-CoV-2 3CLpro and Anti-COVID-19 Drug Discovery from Medicinal Plants. *J. Pharm. Anal.* **2020**, *10*, 313.

(21) Lung, J.; Lin, Y.-S.; Yang, Y.-H.; Chou, Y.-L.; Shu, L.-H.; Cheng, Y.-C.; Te Liu, H.; Wu, C.-Y. The Potential Chemical Structure of Anti-SARS-CoV-2 RNA-Dependent RNA Polymerase. *J. Med. Virol.* **2020**, *92*, 693.

(22) Yan, Y.; Chang, L.; Wang, L. Laboratory Testing of SARS-CoV, MERS-CoV, and SARS-CoV-2 (2019-nCoV): Current Status, Challenges, and Countermeasures. *Rev. Med. Virol.* **2020**, *30* (March), 1−14.

(23) Xu, R.; Cui, B.; Duan, X.; Zhang, P.; Zhou, X.; Yuan, Q. Saliva: Potential Diagnostic Value and Transmission of 2019-NCoV. *Int. J. Oral Sci.* **2020**, *12* (1), 1 DOI: 10.1038/s41368-020-0080-z.

(24) Zhang, X.; Qi, Q.; Jing, Q.; Ao, S.; Zhang, Z.; Ding, M.; Wu, M.; Liu, K.; Wang, W.; Ling, Y.; Zhang, Z.; Fu, W. Electrical Probing of COVID-19 Spike Protein Receptor Binding Domain via a Graphene Field-Effect Transistor. *arXiv [phys]* **2020**, 2003.12529.

(25) Zhang, H.; Penninger, J. M.; Li, Y.; Zhong, N.; Slutsky, A. S. Angiotensin-Converting Enzyme 2 (ACE2) as a SARS-CoV-2 Receptor: Molecular Mechanisms and Potential Therapeutic Target. *Intensive Care Med.* **2020**, *46* (4), 586−590.

(26) Hoffmann, M.; Kleine-Weber, H.; Schroeder, S.; Krüger, N.; Herrler, T.; Erichsen, S.; Schiergens, T. S.; Herrler, G.; Wu, N. H.; Nitsche, A.; Müller, M. A.; Drosten, C.; Pöhlmann, S. SARS-CoV-2 Cell Entry Depends on ACE2 and TMPRSS2 and Is Blocked by a Clinically Proven Protease Inhibitor. *Cell* **2020**, *181* (2), 271−280.

(27) Li, R.; Qiao, S.; Zhang, G. Analysis of Angiotensin-Converting Enzyme 2 (ACE2) from Different Species Sheds Some Light on Cross-Species Receptor Usage of a Novel Coronavirus 2019-NCoV. *J. Infect.* **2020**, *80* (4), 469−496.

(28) Nie, J.; Li, Q.; Wu, J.; Zhao, C.; Hao, H.; Liu, H.; Zhang, L.; Nie, L.; Qin, H.; Wang, M.; Lu, Q.; Li, X.; Sun, Q.; Liu, J.; Fan, C.; Huang, W.; Xu, M.; Wang, Y. Establishment and Validation of a Pseudovirus Neutralization Assay for SARS-CoV-2. *Emerging Microbes Infect.* **2020**, *9* (1), 680−686.

(29) Afzal, A. Molecular Diagnostic Technologies for COVID-19: Limitations and Challenges. *J. Adv. Res.* **2020**, *26*, 149.

(30) Phan, T. Genetic Diversity and Evolution of SARS-CoV-2. *Infect., Genet. Evol.* **2020**, *81*, 104260.

(31) Pachetti, M.; Marini, B.; Benedetti, F.; Giudici, F.; Mauro, E.; Storici, P.; Masciovecchio, C.; Angeletti, S.; Ciccozzi, M.; Gallo, R. C.; Zella, D.; Ippodrino, R. Emerging SARS-CoV-2 Mutation Hot Spots Include a Novel RNA-Dependent-RNA Polymerase Variant. *J. Transl. Med.* **2020**, *18* (1), 1−9.

(32) Li, G.; Fan, Y.; Lai, Y.; Han, T.; Li, Z.; Zhou, P.; Pan, P.; Wang, W.; Hu, D.; Liu, X.; Zhang, Q.; Wu, J. Coronavirus Infections and Immune Responses. *J. Med. Virol.* **2020**, *92* (4), 424−432.

(33) Long, Q.; Liu, B.-Z.; Deng, H.-J.; Wu, G.-C.; Deng, K.; Chen, Y.; Liao, P.; Qiu, J.; Lin, Y.; Cai, X.; Wang, D.-Q.; Hu, Y.; Ren, J.; Tang, N.; Xu, Y.; Yu, L.; Mo, Z.; Gong, F.; Zhang, X.-L.; Tian, W.; Hu, L.; Zhang, X.; Xiang, J.; Du, H.; Liu, H.; Lang, C.; Luo, X.; Wu, S.; Cui, X.; Zhou, Z.; Zhu, M.; Wang, J.; Xue, C.; Li, X.-F.; Wang, L.; Li, Z.; Wang, K.; Niu, C.; Yang, Q.-J.; Tang, X.-J.; Zhang, Y.; Liu, X.-M.; Li, J.-J.; Zhang, D.-C.; Zhang, F.; Liu, P.; Yuan, J.; Li, Q.; Hu, J.-L.; Chen, J.; Huang, A.-L. Antibody Responses to SARS-CoV-2 in Patients with COVID-19. *Nat. Med.* **2020**, *26*, 845.

(34) Sethuraman, N.; Jeremiah, S. S.; Ryo, A. Interpreting Diagnostic Tests for SARS-CoV-2. *JAMA - J. Am. Med. Assoc.* **2020**, *323*, 2249.

(35) Li, G.; Chen, X.; Xu, A. Profile of Specific Antibodies to the SARS-Associated Coronavirus. *N. Engl. J. Med.* **2003**, *349* (5), 508−509.

(36) Woo, P. C. Y.; Lau, S. K. P.; Wong, B. H. L.; Chan, K. H.; Chu, C. M.; Tsoi, H. W.; Huang, Y.; Peiris, J. S. M.; Yuen, K. Y. Longitudinal Profile of Immunoglobulin G (IgG), IgM, and IgA Antibodies against the Severe Acute Respiratory Syndrome (SARS) Coronavirus Nucleocapsid Protein in Patients with Pneumonia Due to the SARS Coronavirus. *Clin. Diagn. Lab. Immunol.* **2004**, *11* (4), 665−668.

(37) Liébana, S.; Brandão, D.; Alegret, S.; Pividori, M. I. Electrochemical Immunosensors, Genosensors and Phagosensors for Salmonella Detection. *Anal. Methods* **2014**, *6* (22), 8858−8873.

(38) Zhang, L.; Hao, M.; Zhang, K.; Zhang, R.; Lin, G.; Jia, T.; Zhang, D.; Chang, L.; Xie, J.; Li, J. External Quality Assessment for the Molecular Detection of MERS-CoV in China. *J. Clin. Virol.* **2016**, *75*, 5−9.

(39) Huang, J. C.; Chang, Y. F.; Chen, K. H.; Su, L. C.; Lee, C. W.; Chen, C. C.; Chen, Y. M. A.; Chou, C. Detection of Severe Acute Respiratory Syndrome (SARS) Coronavirus Nucleocapsid Protein in Human Serum Using a Localized Surface Plasmon Coupled Fluorescence Fiber-Optic Biosensor. *Biosens. Bioelectron.* **2009**, *25* (2), 320−325.

(40) Shirato, K.; Yano, T.; Senba, S.; Akachi, S.; Kobayashi, T.; Nishinaka, T.; Notomi, T.; Matsuyama, S. Detection of Middle East Respiratory Syndrome Coronavirus Using Reverse Transcription Loop-Mediated Isothermal Amplification (RT-LAMP). *Virol. J.* **2014**, *11* (39), 1−11.

(41) Kumar, V.; Shin, J. S.; Shie, J.-J.; Ku, K. B.; Kim, C.; Go, Y. Y.; Huang, K.-F.; Kim, M.; Liang, P.-H. Identification and Evaluation of Potent Middle East Respiratory Syndrome Coronavirus (MERS-CoV) 3CLPro Inhibitors Vathan. *Antiviral Res.* **2017**, *141*, 101−106.

(42) Kogaki, H.; Uchida, Y.; Fujii, N.; Kurano, Y.; Miyake, K.; Kido, Y.; Kariwa, H.; Takashima, I.; Tamashiro, H.; Ling, A. E.; Okada, M. Novel Rapid Immunochromatographic Test Based on an Enzyme Immunoassay for Detecting Nucleocapsid Antigen in SARS-Associated Coronavirus. *J. Clin. Lab. Anal.* **2005**, *19*, 150−159.

(43) Layqah, L. A.; Eissa, S. An Electrochemical Immunosensor for the Corona Virus Associated with the Middle East Respiratory Syndrome Using an Array of Gold Nanoparticle-Modified Carbon Electrodes. *Microchim. Acta* **2019**, *186* (4), 1 DOI: 10.1007/s00604-019-3345-5.

(44) Abad-Valle, P.; Fernández-Abedul, M. T.; Costa-García, A. Genosensor on Gold Films with Enzymatic Electrochemical Detection of a SARS Virus Sequence. *Biosens. Bioelectron.* **2005**, *20* (11), 2251−2260.

(45) Liu, Q.; Cheng, S.; Chen, R.; Ke, J.; Liu, Y.; Li, Y.; Feng, W.; Li, F. Near-Infrared Lanthanide-Doped Nanoparticles for a Low Interference Lateral Flow Immunoassay Test. *ACS Appl. Mater. Interfaces* **2020**, *12* (4), 4358−4365.

(46) Grant, B. D.; Anderson, C. E.; Williford, J. R.; Alonzo, L. F.; Glukhova, V. A.; David, S.; Weigl, B. H.; Nichols, K. P.; Grant, C.; Benjamin, D.; Caitlin, E.; John, R.; Luis, F.; Veronika, A.; Boyle, S.; Lateral, A. S.-C. A. H. A SARS-CoV-2 Coronavirus Antigen-Detecting Half-Strip Lateral Flow Assay Towards the Development of Point of Care Tests Using Commercially Available Reagents. *ChemRxiv* **2020**, 1 DOI: 10.26434/chemrxiv.12250142.v1.

(47) Wang, Y.; Dzakah, E.; Kang, Y.; Cai, Y.; Wu, P.; Tang, B.; Li, R.; He, X. A Sensitive and Rapid Chemiluminescence Immunoassay for Point-of-Care Testing (Poct) of Copeptin in Serum Based on High-Affinity Monoclonal Antibodies via Cytokine-Assisted Immunization. *Int. J. Nanomed.* **2019**, *14*, 4293−4307.

(48) Narang, J.; Singhal, C.; Mathur, A.; Sharma, S.; Singla, V.; Pundir, C. S. Portable Bioactive Paper Based Genosensor Incorporated with Zn-Ag Nanoblooms for Herpes Detection at the Point-of-Care. *Int. J. Biol. Macromol.* **2018**, *107*, 2559−2565.

(49) Chowdhury, A. D.; Takemura, K.; Li, T.-C.; Suzuki, T.; Park, E. Y. Electrical Pulse-Induced Electrochemical Biosensor for Hepatitis E Virus Detection. *Nat. Commun.* **2019**, *10* (1), 4−7.

(50) Gao, A.; Lu, N.; Wang, Y.; Li, T. Robust Ultrasensitive Tunneling-FET Biosensor for Point-of-Care Diagnostics. *Sci. Rep.* **2016**, *6* (March), 1−9.

(51) Kim, J.; Jung, S.; Byoun, M. S.; Yoo, C.; Sim, S. J.; Lim, C. S.; Kim, S. W.; Kim, S. K. Multiplex Real-Time PCR Using Temperature Sensitive Primer-Supplying Hydrogel Particles and Its Application for Malaria Species Identification. *PLoS One* **2018**, *13*, e0190451.

(52) Harikai, N.; Saito, S.; Abe, M.; Kondo, K.; Kitta, K.; Akiyama, H.; Teshima, R.; Kinoshita, K. Real-Time PCR Method Using Capturing Oligo-Immobilized PCR Tubes to Determine the Specific Gene for Soybean and Genetically Modified Soybean in Food Matrices. *Biosci., Biotechnol., Biochem.* **2008**, *72* (11), 2953−2958.

(53) Corman, V. M.; Landt, O.; Kaiser, M.; Molenkamp, R.; Meijer, A.; Chu, D. K. W.; Bleicker, T.; Brünink, S.; Schneider, J.; Schmidt, M. L.; Mulders, D. G. J. C.; Haagmans, B. L.; Van Der Veer, B.; Van Den Brink, S.; Wijsman, L.; Goderski, G.; Romette, J. L.; Ellis, J.; Zambon, M.; Peiris, M.; Goossens, H.; Reusken, C.; Koopmans, M. P. G.; Drosten, C. Detection of 2019 Novel Coronavirus (2019-NCoV) by Real-Time RT-PCR. *Eurosurveillance* **2020**, *25* (3), 1−8.

(54) Prasad, K. S.; Cao, X.; Gao, N.; Jin, Q.; Sanjay, S. T.; Henao-Pabon, G.; Li, X. J. A Low-Cost Nanomaterial-Based Electrochemical Immunosensor on Paper for High-Sensitivity Early Detection of Pancreatic Cancer. *Sens. Actuators, B* **2020**, *305*, 127516.

(55) Cesewski, E.; Johnson, B. N. Electrochemical Biosensors for Pathogen Detection. *Biosens. Bioelectron.* **2020**, *159* (April), 112214.

(56) Du, L.; Ji, W.; Zhang, Y.; Zhang, C.; Liu, G.; Wang, S. Ultrasensitive Detection of 17β-Estradiol Using Gold Nanoparticle-Based Fluorescence Immunoassay. *Analyst* **2015**, *140* (8), 2001.

(57) Freeman, W. M.; Walker, S. J.; Vrana, K. E. Quantitative RT-PCR: Pitfalls and Potential. *BioTechniques* **1999**, *26* (1), 112−125.

(58) Bustin, S. A.; Nolan, T. RT-QPCR Testing of SARS-CoV-2: A Primer. *Int. J. Mol. Sci.* **2020**, *21*, 3004.

(59) Kim, Y. J.; Sung, H.; Ki, C.-S.; Hur, M. COVID-19 Testing in South Korea: Current Status and the Need for Faster Diagnostics. *Ann. Lab. Med.* **2020**, *40* (5), 349−350.

(60) Peng, L.; Liu, J.; Xu, W.; Luo, Q.; Chen, D.; Lei, Z.; Huang, Z.; Li, X.; Keji, D.; Lin, B.; Gao, Z. SARS-CoV-2 Can Be Detected in Urine, Blood, Anal Swabs, and Oropharyngeal Swabs Specimens. *J. Med. Virol.* **2020**, *92*, 1676.

(61) Ling, Y.; Xu, S.; Lin, Y.; Tian, D.; Zhu, Z.; Dai, F.; Wu, F.; Song, Z.; Huang, W.; Chen, J.; Hu, B.; Wang, S.; Mao, E.; Zhu, L.; Zhang, W.; Lu, H. Persistence and Clearance of Viral RNA in 2019 Novel Coronavirus Disease Rehabilitation Patients. *Chin. Med. J. (Engl).* **2020**, *133* (9), 1039−1043.

(62) Hung, I. F. N.; Lau, S. K. P.; Woo, P. C. Y.; Yuen, K. Y. Viral Loads in Clinical Specimens and SARS Manifestations. *Hong Kong Med. J.* **2009**, *15*, 20−22.

(63) Kim, S. Y.; Park, S. J.; Cho, S. Y.; Cha, R. H.; Jee, H. G.; Kim, G.; Shin, H. S.; Kim, Y.; Jung, Y. M.; Yang, J. S.; Kim, S. S.; Cho, S. I.; Kim, M. J.; Lee, J. S.; Lee, S. J.; Seo, S. H.; Park, S. S.; Seong, M. W. Viral RNA in Blood as Indicator of Severe Outcome in Middle East Respiratory Syndrome Coronavirus Infection. *Emerging Infect. Dis.* **2016**, *22* (10), 1813−1816.

(64) Liu, R.; Han, H.; Liu, F.; Lv, Z.; Wu, K.; Liu, Y.; Feng, Y. Positive Rate of RT-PCR Detection of SARS-CoV-2 Infection in 4880 Cases from One Hospital in Wuhan, China, from Jan to Feb 2020. *Clin. Chim. Acta* **2020**, *505* (March), 172−175.

(65) Hase, R.; Kurita, T.; Muranaka, E.; Sasazawa, H.; Mito, H.; Yano, Y. A Case of Imported COVID-19 Diagnosed by PCR-Positive Lower Respiratory Specimen but with PCR-Negative Throat Swabs. *Infect. Dis. (Auckl).* **2020**, *52* (6), 423−426.

(66) Wölfel, R.; Corman, V. M.; Guggemos, W.; Seilmaier, M.; Zange, S.; Müller, M. A.; Niemeyer, D.; Jones, T. C.; Vollmar, P.; Rothe, C.; Hoelscher, M.; Bleicker, T.; Brünink, S.; Schneider, J.; Ehmann, R.; Zwirglmaier, K.; Drosten, C.; Wendtner, C. Virological Assessment of Hospitalized Patients with COVID-2019. *Nature* **2020**, *581*, 465.

(67) Wang, Y.; Kang, H.; Liu, X.; Tong, Z. Combination of RT-qPCR Testing and Clinical Features for Diagnosis of COVID-19 Facilitates Management of SARS-CoV-2 Outbreak. *J. Med. Virol.* **2020**, *92*, 538−539.

(68) Pfefferle, S.; Reucher, S.; Nörz, D.; Lütgehetmann, M. Evaluation of a Quantitative RT-PCR Assay for the Detection of the Emerging Coronavirus SARS-CoV-2 Using a High Throughput System. *Eurosurveillance* **2020**, *25* (9), 1−5.

(69) Won, J.; Lee, S.; Park, M.; Kim, T. Y.; Park, M. G.; Choi, B. Y.; Kim, D.; Chang, H.; Kim, V. N.; Lee, C. J. Development of a Laboratory-Safe and Low-Cost Detection Protocol for SARS-CoV-2 of the Coronavirus Disease 2019 (COVID-19). *Exp. Neurobiol.* **2020**, *29* (2), 107−13.

(70) Carter, L. J.; Garner, L. V.; Smoot, J. W.; Li, Y.; Zhou, Q.; Saveson, C. J.; Sasso, J. M.; Gregg, A. C.; Soares, D. J.; Beskid, T. R.; Jervey, S. R.; Liu, C. Assay Techniques and Test Development for COVID-19 Diagnosis. *ACS Cent. Sci.* **2020**, *6* (5), 591−605.

(71) Al Johani, S.; Hajeer, A. H. MERS-CoV Diagnosis: An Update. *J. Infect. Public Health* **2016**, *9* (3), 216−219.

(72) Poon, L. L. M.; Chan, K. H.; Wong, O. K.; Yam, W. C.; Yuen, K. Y.; Guan, Y.; Lo, Y. M. D.; Peiris, J. S. M. Early Diagnosis of SARS Coronavirus Infection by Real Time RT-PCR. *J. Clin. Virol.* **2003**, *28* (3), 233−238.

(73) Lu, X.; Whitaker, B.; Sakthivel, S. K. K.; Kamili, S.; Rose, L. E.; Lowe, L.; Mohareb, E.; Elassal, E. M.; Al-sanouri, T.; Haddadin, A.; Erdman, D. D. Real-Time Reverse Transcription-Pcr Assay Panel for Middle East Respiratory Syndrome Coronavirus. *J. Clin. Microbiol.* **2014**, *52* (1), 67−75.

(74) Wu, Y.; Guo, C.; Tang, L.; Hong, Z.; Zhou, J.; Dong, X.; Yin, H.; Xiao, Q.; Tang, Y.; Qu, X.; Kuang, L.; Fang, X.; Mishra, N.; Lu, J.; Shan, H.; Jiang, G.; Huang, X. Prolonged Presence of SARS-CoV-2 Viral RNA in Faecal Samples. *Lancet Gastroenterol. Hepatol.* **2020**, *5* (5), 434−435.

(75) Yip, C. C. Y.; Ho, C. C.; Chan, J. F. W.; To, K. K. W.; Chan, H. S. Y.; Wong, S. C. Y.; Leung, K. H.; Fung, A. Y. F.; Ng, A. C. K.; Zou, Z.; Tam, A. R.; Chung, T. W. H.; Chan, K. H.; Hung, I. F. N.; Cheng, V. C. C.; Tsang, O. T. Y.; Tsui, S. K. W.; Yuen, K. Y. Development of a Novel, Genome Subtraction Derived, SARS-CoV-2 Specific COVID-19 Nsp2 Real Time RT-PCR Assay and Its Evaluation Using Clinical Specimens. *Int. J. Mol. Sci.* **2020**, *21* (7), 2574.

(76) Xia, J.; Tong, J.; Liu, M.; Shen, Y.; Guo, D. Evaluation of Coronavirus in Tears and Conjunctival Secretions of Patients with SARS-CoV-2 Infection. *J. Med. Virol.* **2020**, *92*, 589−594.

(77) Paoli, D.; Pallotti, F.; Colangelo, S.; Basilico, F.; Mazzuti, L.; Turriziani, O.; Antonelli, G.; Lenzi, A.; Lombardo, F. Study of SARS-CoV-2 in Semen and Urine Samples of a Volunteer with Positive Naso-Pharyngeal Swab. *J. Endocrinol. Invest.* **2020**, *43*, 1819.

(78) Chan, J. F.-W.; Yip, C. C.-Y.; To, K. K.-W.; Tang, H.-C.; Wong, S. C.-Y.; Leung, K.-H.; Fung, A. Y.-F.; Ng, A. C.-K.; Zou, Z.; Tsoi, H.-W.; Choi, G. K.-Y.; Tam, A. R.; Cheng, V. C.-C.; Chen, K.-H.; Tsang, O. T.-Y.; Yuen, K.-Y Improved Molecular Diagnosis of COVID-19 by the Novel, Highly Sensitive and Specific COVID-19-RdRp/Hel Real-Time Reverse Transcription-Polymerase Chain Reaction Assay Validated in Vitro and with Clinical Specimens. *J. Clin. Microbiol.* **2020**, *58*, 1−29.

(79) Nguyen, T.; Bang, D. D.; Wolff, A. 2019 Novel Coronavirus Disease (COVID-19): Paving the Road for Rapid Detection and Point-of-Care Diagnostics. *Micromachines* **2020**, *11* (3), 306.

(80) Yang, W.; Dang, X.; Wang, Q.; Xu, M.; Zhao, Q.; Zhou, Y.; Zhao, H.; Wang, L.; Xu, Y.; Wang, J.; Han, S.; Wang, M.; Pei, F.; Wang, Y. Rapid Detection of SARS-CoV-2 Using Reverse Transcription RT-LAMP Method. *medRxiv* **2020**, 1 DOI: 10.1101/2020.03.02.20030130.

(81) Yan, C.; Cui, J.; Huang, L.; Du, B.; Chen, L.; Xue, G.; Li, S.; Zhang, W.; Zhao, L.; Sun, Y.; Yao, H.; Li, N.; Zhao, H.; Feng, Y.; Liu, S.; Zhang, Q.; Liu, D.; Yuan, J. Rapid and Visual Detection of 2019 Novel Coronavirus (SARS-CoV-2) by a Reverse Transcription Loop-Mediated Isothermal Amplification Assay. *Clin. Microbiol. Infect.* **2020**, *26*, 773.

(82) Lu, R.; Wu, X.; Wan, Z.; Li, Y.; Zuo, L.; Qin, J.; Jin, X. Development of a Novel Reverse Transcription Loop-Mediated Isothermal Amplification Method for Rapid Detection of SARS-CoV-2. *Virol. Sin.* **2020**, *35*, 344.

(83) Park, G. S.; Ku, K.; Baek, S. H.; Kim, S. J.; Kim, S. Il; Kim, B. T.; Maeng, J. S. Development of Reverse Transcription Loop-Mediated Isothermal Amplification (RT-LAMP) Assays Targeting SARS-CoV-2. *J. Mol. Diagn.* **2020**, *22*, 729.

(84) Zhang, Y.; Odiwuor, N.; Xiong, J.; Sun, L.; Nyaruaba, R. O.; Wei, H.; Tanner, N. A.; Tanner, N. Rapid Molecular Detection of SARS-CoV-2 (COVID-19) Virus RNA Using Colorimetric LAMP. *medRxiv* **2020**, *2*, 1 DOI: 10.1101/2020.02.26.20028373.

(85) Clem, A. L.; Sims, J.; Telang, S.; Eaton, J. W.; Chesney, J. Virus Detection and Identification Using Random Multiplex (RT)-PCR with 3′-Locked Random Primers. *Virol. J.* **2007**, *4*, 65.

(86) Li, Y.; Li, S.; Wang, J.; Liu, G. CRISPR/Cas Systems towards Next-Generation Biosensing. *Trends Biotechnol.* **2019**, *37* (7), 730−743.

(87) Cong, L.; Ran, F. A.; Cox, D.; Lin, S.; Barretto, R.; Habib, N.; Hsu, P. D.; Wu, X.; Jiang, W.; Marraffini, L. A.; Zhang, F. Multiplex Genome Engineering Using CRISPR/Cas Systems. *Science (Washington, DC, U. S.)* **2013**, *339*, 819−824.

(88) Jinek, M.; Chylinski, K.; Fonfara, I.; Hauer, M.; Doudna, J. A.; Charpentier, E. A Programmable Dual-RNA−Guided DNA Endonuclease in Adaptive Bacterial Immunity. *Science (Washington, DC, U. S.)* **2012**, *337*, 816−822.

(89) Zuo, X.; Fan, C.; Chen, H. Y. Biosensing: CRISPR-Powered Diagnostics. *Nat. Biomed. Eng.* **2017**, *1* (6), 1−2.

(90) Gootenberg, J. S.; Abudayyeh, O. O.; Lee, J. W.; Essletzbichler, P.; Dy, A. J.; Joung, J.; Verdine, V.; Donghia, N.; Daringer, N. M.; Freije, C. A.; Myhrvold, C.; Bhattacharyya, R. P.; Livny, J.; Regev, A.; Koonin, E. V.; Hung, D. T.; Sabeti, P. C.; Collins, J. J.; Zhang, F. Nucleic Acid Detection with CRISPR-Cas13a/C2c2. *Science (Washington, DC, U. S.)* **2017**, *356* (6336), 438−442.

(91) O'Connell, M. R. Molecular Mechanisms of RNA Targeting by Cas13-Containing Type VI CRISPR−Cas Systems. *J. Mol. Biol.* **2019**, *431* (1), 66−87.

(92) Dogterom, M.; Idema, T.; Brouns, S. J. J.; Reese, L. CRISPR-Based DNA and RNA Detection with Liquid-Liquid Phase Separation Willem. *BioRxiv* **2019**, 1−19.

(93) Gootenberg, J. S.; Abudayyeh, O. O.; Kellner, M. J.; Joung, J.; Collins, J. J.; Zhang, F. Multiplexed and Portable Nucleic Acid Detection Platform with Cas13, Cas12a and Csm6. *Science (Washington, DC, U. S.)* **2018**, *360* (6387), 439−444.

(94) Myhrvold, C.; Freije, C. A.; Gootenberg, J. S.; Abudayyeh, O. O.; Metsky, H. C.; Durbin, A. F.; Kellner, M. J.; Tan, A. L.; Paul, L. M.; Parham, L. A.; Garcia, K. F.; Barnes, K. G.; Chak, B.; Mondini, A.; Nogueira, M. L.; Isern, S.; Michael, S. F.; Lorenzana, I.; Yozwiak, N. L.; MacInnis, B. L.; Bosch, I.; Gehrke, L.; Zhang, F.; Sabeti, P. C. Field-Deployable Viral Diagnostics Using CRISPR-Cas13. *Science (Washington, DC, U. S.)* **2018**, *360* (6387), 444−448.

(95) Li, H.; Wang, S.; Dong, X.; Li, Q.; Li, M.; Li, J.; Guo, Y.; Jin, X.; Zhou, Y.; Song, H.; Kou, Z. CRISPR-Cas13a Cleavage of Dengue Virus NS3 Gene Efficiently Inhibits Viral Replication. *Mol. Ther.–Nucleic Acids* **2020**, *19* (March), 1460−1469.

(96) Bruch, R.; Baaske, J.; Chatelle, C.; Meirich, M.; Madlener, S.; Weber, W.; Dincer, C.; Urban, G. A. CRISPR/Cas13a-Powered Electrochemical Microfluidic Biosensor for Nucleic Acid Amplification-Free MiRNA Diagnostics. *Adv. Mater.* **2019**, *31* (51), 1905311.

(97) Freije, C. A.; Myhrvold, C.; Boehm, C. K.; Lin, A. E.; Welch, N. L.; Carter, A.; Metsky, H. C.; Luo, C. Y.; Abudayyeh, O. O.; Gootenberg, J. S.; Yozwiak, N. L.; Zhang, F.; Sabeti, P. C. Programmable Inhibition and Detection of RNA Viruses Using Cas13. *Mol. Cell* **2019**, *76* (5), 826−837.

(98) Zhang, F.; Abudayyeh, O. O.; Gootenberg, J. S. A Protocol for Detection of COVID-19 Using CRISPR Diagnostics; *broadinstitute.org*; 2020; https://www.broadinstitute.org/files/publications/special/COVID-19%20detection%20(updated).pdf.

(99) Hou, T.; Zeng, W.; Yang, M.; Chen, W.; Ren, L.; Ai, J.; Wu, J.; Liao, Y.; Gou, X.; Li, Y.; Wang, X.; Su, H.; Gu, B.; Wang, J.; Xu, T. Development and Evaluation of a Rapid CRISPR-Based Diagnostic for COVID-19. *PLoS Pathog.* **2020**, *16* (8), e1008705.

(100) van Dongen, J. E.; Berendsen, J. T. W.; Steenbergen, R. D. M.; Wolthuis, R. M. F.; Eijkel; Jan, C. T.; Segerink, L. I. Point-of-Care CRISPR/Cas Nucleic Acid Detection: Recent Advances, Challenges and Opportunities. *Biosens. Bioelectron.* **2020**, *166*, 112445.

(101) Malecka, K.; Swieton, E.; Verwilst, P.; Stachyra, A.; Sirko, A.; Dehaen, W.; Radecki, J.; Radecka, H. Ultrasensitive Electrochemical Genosensor for Direct Detection of Specific RNA Sequences Derived from Avian Influenza Viruses Present in Biological Samples. *Acta Biochim. Polym.* **2019**, *66* (3), 299−304.

(102) Martín-Fernández, B.; Manzanares-Palenzuela, C. L.; Sánchez-Paniagua López, M.; de-los-Santos-Álvarez, N.; López-Ruiz, B. Electrochemical Genosensors in Food Safety Assessment. *Crit. Rev. Food Sci. Nutr.* **2017**, *57* (13), 2758−2774.

(103) Khanmohammadi, A.; Jalili Ghazizadeh, A.; Hashemi, P.; Afkhami, A.; Arduini, F.; Bagheri, H. An Overview to Electrochemical Biosensors and Sensors for the Detection of Environmental Contaminants. *J. Iran. Chem. Soc.* **2020**, *17*, 2429.

(104) Ozkan-Ariksoysal, D.; Kayran, Y. U.; Yilmaz, F. F.; Ciucu, A. A.; David, I. G.; David, V.; Hosgor-Limoncu, M.; Ozsoz, M. DNA-Wrapped Multi-Walled Carbon Nanotube Modified Electrochemical Biosensor for the Detection of Escherichia Coli from Real Samples. *Talanta* **2017**, *166*, 27−35.

(105) Sadighbayan, D.; Sadighbayan, K.; Khosroushahi, A. Y.; Hasanzadeh, M. Recent Advances on the DNA-Based Electrochemical Biosensing of Cancer Biomarkers: Analytical Approach. *TrAC, Trends Anal. Chem.* **2019**, *119*, 115609.

(106) Alzate, D.; Cajigas, S.; Robledo, S.; Muskus, C.; Orozco, J. Genosensors for Differential Detection of Zika Virus. *Talanta* **2020**, *210*, 120648.

(107) Abad-Valle, P.; Fernández-Abedul, M. T.; Costa-García, A. DNA Single-Base Mismatch Study with an Electrochemical Enzymatic Genosensor. *Biosens. Bioelectron.* **2007**, *22* (8), 1642−1650.

(108) Oliveira, O. N.; Iost, R. M.; Siqueira, J. R.; Crespilho, F. N.; Caseli, L. Nanomaterials for Diagnosis: Challenges and Applications in Smart Devices Based on Molecular Recognition. *ACS Appl. Mater. Interfaces* **2014**, *6* (17), 14745−14766.

(109) Kaushik, M.; Sonia; Mahendru, S.; Tyagi, P.; Kukreti, S. Multiple Dimensions of Functional Relevance of Genosensors. *Integr. Ferroelectr.* **2017**, *185* (1), 134−143.

(110) Carr, O.; Raymundo-Pereira, P. A.; Shimizu, F. M.; Sorroche, B. P.; Melendez, M. E.; de Oliveira Pedro, R.; Miranda, P. B.; Carvalho, A. L.; Reis, R. M.; Arantes, L. M. R. B.; Oliveira, O. N. Genosensor Made with a Self-Assembled Monolayer Matrix to Detect MGMT Gene Methylation in Head and Neck Cancer Cell Lines. *Talanta* **2020**, *210*, 120609.

(111) Zhao, H.; Liu, F.; Xie, W.; Zhou, T.-C.; OuYang, J.; Jin, L.; Li, H.; Zhao, C.-Y.; Zhang, L.; Wei, J.; Zhang, Y.-P.; Li, C.-P. Ultrasensitive Supersandwich-Type Electrochemical Sensor for SARS-CoV-2 from the Infected COVID-19 Patients Using a Smartphone. *Sens. Actuators, B* **2021**, *327*, 128899.

(112) Van Amerongen, A.; Veen, J.; Arends, H. A.; Koets, M. Lateral Flow Immunoassays. In *Handbook of Immunoassay Technologies: Approaches, Performances, and Applications*; 2018; pp 157−182. DOI: 10.1016/B978-0-12-811762-0.00007-4.

(113) Shajaripour Jaberi, S. Y.; Ghaffarinejad, A.; Omidinia, E. An Electrochemical Paper Based Nano-Genosensor Modified with Reduced Graphene Oxide-Gold Nanostructure for Determination of Glycated Hemoglobin in Blood. *Anal. Chim. Acta* **2019**, *1078*, 42−52.

(114) Vashist, S. K. Point-of-Care Diagnostics: Recent Advances and Trends. *Biosensors* **2017**, *7* (4), 62.

(115) Hoy, C. F. O.; Kushiro, K.; Yamaoka, Y.; Ryo, A.; Takai, M. Rapid Multiplex Microfiber-Based Immunoassay for Anti-MERS-CoV Antibody Detection. *Sens. Bio-Sensing Res.* **2019**, *26*, 100304.

(116) Trivedi, S. U.; Miao, C.; Sanchez, J. E.; Caidi, H.; Tamin, A.; Haynes, L.; Thornburg, N. J. Development and Evaluation of a Multiplexed Immunoassay for Simultaneous Detection of Serum IgG Antibodies to Six Human Coronaviruses. *Sci. Rep.* **2019**, *9* (1), 1−8.

(117) Zheng, M.; Song, L. Novel Antibody Epitopes Dominate the Antigenicity of Spike Glycoprotein in SARS-CoV-2 Compared to SARS-CoV. *Cell. Mol. Immunol.* **2020**, *17*, 536.

(118) Ou, X.; Liu, Y.; Lei, X.; Li, P.; Mi, D.; Ren, L.; Guo, L.; Guo, R.; Chen, T.; Hu, J.; Xiang, Z.; Mu, Z.; Chen, X.; Chen, J.; Hu, K.; Jin, Q.; Wang, J.; Qian, Z. Characterization of Spike Glycoprotein of SARS-CoV-2 on Virus Entry and Its Immune Cross-Reactivity with SARS-CoV. *Nat. Commun.* **2020**, *11* (1), 1 DOI: 10.1038/s41467-020-15562-9.

(119) Tian, X.; Li, C.; Huang, A.; Xia, S.; Lu, S.; Shi, Z.; Lu, L.; Jiang, S.; Yang, Z.; Wu, Y.; Ying, T. Potent Binding of 2019 Novel Coronavirus Spike Protein by a SARS Coronavirus-Specific Human Monoclonal Antibody. *Emerging Microbes Infect.* **2020**, *9*, 382−385.

(120) Infantino, M.; Grossi, V.; Lari, B.; Bambi, R.; Perri, A.; Manneschi, M.; Terenzi, G.; Liotti, I.; Ciotta, G.; Taddei, C.; Benucci, M.; Casprini, P.; Veneziani, F.; Fabbri, S.; Pompetti, A.; Manfredi, M. Diagnostic Accuracy of an Automated Chemiluminescent Immunoassay for Anti-SARS-CoV-2 IgM and IgG Antibodies: An Italian Experience. *J. Med. Virol.* **2020**, *92*, 1671.

(121) Kontou, P. I.; Braliou, G. G.; Dimou, N. L.; Nikolopoulos, G.; Bagos, P. G. Antibody Tests in Detecting SARS-CoV-2 Infection: A Meta-Analysis. *Diagnostics* **2020**, *10*, 319.

(122) Flego, M.; Di Bonito, P.; Ascione, A.; Zamboni, S.; Carattoli, A.; Grasso, F.; Cassone, A.; Cianfriglia, M. Generation of Human Antibody Fragments Recognizing Distinct Epitopes of the Nucleocapsid (N) SARS - CoV Protein Using a Phage Display Approach. *BMC Infect. Dis.* **2005**, *5*, 1−8.

(123) Haveri, A.; Smura, T.; Kuivanen, S.; Österlund, P.; Hepojoki, J.; Ikonen, N.; Pitkäpaasi, M.; Blomqvist, S.; Rönkkö, E.; Kantele, A.; Strandin, T.; Kallio-Kokko, H.; Mannonen, L.; Lappalainen, M.; Broas, M.; Jiang, M.; Siira, L.; Salminen, M.; Puumalainen, T.; Sane, J.; Melin, M.; Vapalahti, O.; Savolainen-Kopra, C. Serological and Molecular Findings during SARS-CoV-2 Infection: The First Case Study in Finland, January to February 2020. *Eurosurveillance* **2020**, *25* (11), 1−6.

(124) Sun, B.; Feng, Y.; Mo, X.; Zheng, P.; Wang, Q.; Li, P.; Peng, P.; Liu, X.; Chen, Z.; Huang, H.; Zhang, F.; Luo, W.; Niu, X.; Hu, P.; Wang, L.; Peng, H.; Huang, Z.; Feng, L.; Li, F.; Zhang, F.; Li, F.; Zhong, N.; Chen, L. Kinetics of SARS-CoV-2 Specific IgM and IgG Responses in COVID-19 Patients. *Emerging Microbes Infect.* **2020**, *9*, 940.

(125) Montesinos, I.; Gruson, D.; Kabamba, B.; Dahma, H.; Van Den Wijngaert, S.; Reza, S.; Carbone, V.; Vandenberg, O.; Gulbis, B.; Wolff, F.; Rodriguez-Villalobos, H. Evaluation of Two Automated and Three Rapid Lateral Flow Immunoassays for the Detection of Anti-SARS-CoV-2 Antibodies. *J. Clin. Virol.* **2020**, *128* (April), 104413.

(126) Ma, H.; Zeng, W.; He, H.; Zhao, D.; Yang, Y.; Jiang, D.; Zhou, P.; Qi, Y.; He, W.; Zhao, C.; Yi, R.; Wang, X.; Wang, B.; Xu, Y.; Yang, Y.; Kombe, A. J. K.; Ding, C.; Xie, J.; Gao, Y.; Cheng, L.; Li, Y.; Ma, X.; Jin, T. COVID-19 Diagnosis and Study of Serum SARS-CoV-2 Specific IgA, IgM and IgG by a Quantitative and Sensitive Immunoassay. *medRxiv* **2020**, 1 DOI: 10.1101/2020.04.17.20064907.

(127) Padoan, A.; Sciacovelli, L.; Basso, D.; Negrini, D.; Zuin, S.; Cosma, C.; Faggian, D.; Matricardi, P.; Plebani, M. IgA-Ab Response to Spike Glycoprotein of SARS-CoV-2 in Patients with COVID-19: A Longitudinal Study. *Clin. Chim. Acta* **2020**, *507* (April), 164−166.

(128) Li, Z.; Yi, Y.; Luo, X.; Xiong, N.; Liu, Y.; Li, S.; Sun, R.; Wang, Y.; Hu, B.; Chen, W.; Zhang, Y.; Wang, J.; Huang, B.; Lin, Y.; Yang, J.; Cai, W.; Wang, X.; Cheng, J.; Chen, Z.; Sun, K.; Pan, W.; Zhan, Z.; Chen, L.; Ye, F. Development and Clinical Application of a Rapid IgM-IgG Combined Antibody Test for SARS-CoV-2 Infection Diagnosis. *J. Med. Virol.* **2020**, *92*, 1518.

(129) González, J. M.; Shelton, W. J.; Díaz-Vallejo, M.; RodriguezCastellanos, V. E.; Zuluaga, J. D. H.; Chamorro, D. F.; Arroyo-Ariza, D. Immunological Assays for SARS-CoV-2: An Analysis of Available Commercial Tests to Measure Antigen and Antibodies. *Open J. Immunol.* **2020**, *10*, 21.

(130) Lassaunière, R.; Frische, A.; Harboe, Z. B.; Nielsen, A. C.; Fomsgaard, A.; Krogfelt, K. A.; Jørgensen, C. S. Evaluation of Nine Commercial SARS-CoV-2 Immunoassays. *medRxiv* **2020**, 1.

(131) European Commission. *Current Performance of COVID-19 Test Methods and Devices and Proposed Performance Criteria*; 2020.

(132) Noh, J. Y.; Yoon, S. W.; Kim, Y.; Van Lo, T.; Ahn, M. J.; Jung, M. C.; Le, T. B.; Na, W.; Song, D.; Le, V. P.; Haam, S.; Jeong, D. G.; Kim, H. K. Pipetting-Based Immunoassay for Point-of-Care Testing: Application for Detection of the Influenza A Virus. *Sci. Rep.* **2019**, *9* (1), 1−9.

(133) Konstantinou, G. N. Enzyme-Linked Immunosorbent Assay (ELISA). *Methods Mol. Biol.* **2017**, *1592*, 79−94.

(134) Liu, W.; Liu, L.; Kou, G.; Zheng, Y.; Ding, Y.; Ni, W.; Wang, Q.; Tan, L.; Wu, W.; Tang, S.; Xiong, Z.; Zheng, S. Evaluation of Nucleocapsid and Spike Protein-Based ELISAs for Detecting Antibodies against SARS-CoV-2. *J. Clin. Microbiol.* **2020**, 1 DOI: 10.1128/JCM.00461-20.

(135) Adams, E. R.; Ainsworth, M.; Anand, R.; Andersson, M. I.; Auckland, K.; Baillie, J. K.; Barnes, E.; Beer, S.; Bell, J.; Berry, T.; Bibi, S.; Carroll, M.; Chinnakannan, S.; Clutterbuck, E.; Cornall, R. J.; Crook, D. W.; Silva, T. De; Dejnirattisai, W.; Dingle, K. E.; Dold, C.; Espinosa, A.; Eyre, D. W.; Farmer, H.; Mendoza, M. F.; Georgiou, D.; Hoosdally, S. J.; Hunter, A.; Jeffrey, K.; Klenerman, P.; Knight, J.; Knowles, C.; Kwok, A. J.; Leuschner, U.; Levin, R.; Liu, C.; Lopez-Camacho, C.; Garrido, J. C. M.; Matthews, P. C.; McGivern, H.; Mentzer, A. J.; Milton, J.; Mongkolsapaya, J.; Moore, S. C.; Oliveira, M. S.; Pereira, F.; Lopez, E. P.; Peto, T.; Ploeg, R. J.; Pollard, A.; Prince, T.; Roberts, D. J.; Rudkin, J. K.; Sanchez, V.; Scre, G. R.; Whitehouse, J. Antibody Testing for COVID-19: A Report from the National COVID Scientific Advisory Panel. *Wellcome Open Res.* **2020**, *5*, 139.

(136) Xiang, J.; Yan, M.; Li, H.; Liu, T.; Lin, C.; Huang, S.; Shen, C. Evaluation of Enzyme-Linked Immunoassay and Colloidal Gold-Immunochromatographic Assay Kit for Detection of Novel Coronavirus (SARS-Cov-2) Causing an Outbreak of Pneumonia (COVID-19). *medRxiv* **2020**, 1 DOI: 10.1101/2020.02.27.20028787.

(137) Wang, Q.; Du, Q.; Guo, B.; Mu, D.; Lu, X.; Ma, Q.; Guo, Y.; Fang, L.; Zhang, B.; Zhang, G.; Guo, X. A Method To Prevent SARS-CoV-2 IgM False Positives in Gold Immunochromatography and Enzyme-Linked Immunosorbent Assays. *J. Clin. Microbiol.* **2020**, *58* (6), 1−7.

(138) Aydin, S. A Short History, Principles, and Types of ELISA, and Our Laboratory Experience with Peptide/Protein Analyses Using ELISA. *Peptides* **2015**, *72*, 4−15.

(139) EUROIMMUN-US. *Anti-SARS-CoV-2 ELISA (IgG) - Instruction for Use*; 2020.

(140) Padoan, A.; Cosma, C.; Sciacovelli, L.; Faggian, D.; Plebani, M. Analytical Performances of a Chemiluminescence Immunoassay for SARS-CoV-2 IgM/IgG and Antibody Kinetics. *Clin. Chem. Lab. Med.* **2020**, *58*, 1081.

(141) Cinquanta, L.; Fontana, D. E.; Bizzaro, N. Chemiluminescent Immunoassay Technology: What Does It Change in Autoantibody Detection? *Autoimmun. Highlights* **2017**, *8* (1), 1 DOI: 10.1007/s13317-017-0097-2.

(142) Shahrajabian, M.; Hormozi-Nezhad, M. R. Design a New Strategy Based on Nanoparticle-Enhanced Chemiluminescence Sensor Array for Biothiols Discrimination. *Sci. Rep.* **2016**, *6*, 1 DOI: 10.1038/srep32160.

(143) Han, G. R.; Kim, M. G. Design, Synthesis, and Evaluation of Gold Nanoparticle-Antibody-Horseradish Peroxidase Conjugates for Highly Sensitive Chemiluminescence Immunoassay (Hs-CLIA). *Biotechnol. Bioprocess Eng.* **2019**, *24* (1), 206−214.

(144) Nirala, N. R.; Harel, Y.; Lellouche, J. P.; Shtenberg, G. Ultrasensitive Haptoglobin Biomarker Detection Based on Amplified Chemiluminescence of Magnetite Nanoparticles. *J. Nanobiotechnol.* **2020**, *18* (1), 1−10.

(145) Jiang, F.; Li, P.; Zong, C.; Yang, H. Surface-Plasmon-Coupled Chemiluminescence Amplification of Silver Nanoparticles Modified Immunosensor for High-Throughput Ultrasensitive Detection of Multiple Mycotoxins. *Anal. Chim. Acta* **2020**, *1114*, 58−65.

(146) Lin, Z.-y.; Fang, Y.-z.; Jin, H.-w.; Lin, H.-y.; Dai, Z.; Luo, Q.; Li, H.-w.; Lin, Y.-l.; Huang, S.-z.; Gao, L.; Xu, F.-h.; Zhang, Z.-y. Performance Evaluation of a Chemiluminescence Microparticle Immunoassay for CK-MB. *J. Clin. Lab. Anal.* **2018**, *32* (6), e22426.

(147) Tate, J.; Ward, G. Interferences in Immunoassay. *Clin. Biochem. Rev.* **2004**, *25* (6), 105−120.

(148) Caini, S.; Bellerba, F.; Corso, F.; Díaz-basabe, A.; Natoli, G.; Facciotti, F.; Raimondi, S.; Palli, D.; Mazzarella, L.; Pelicci, P. G. Meta-Analysis of Diagnostic Performance of Serological Tests for SARS-CoV-2 Antibodies and Public Health Implications. *medRxiv* **2020**, 1 DOI: 10.2807/1560-7917.ES.2020.25.23.2000980.

(149) Chen, D.; Zhang, Y.; Xu, Y.; Shen, T.; Cheng, G.; Huang, B.; Ruan, X.; Wang, C. Comparison of Chemiluminescence Immunoassay, Enzyme-Linked Immunosorbent Assay and Passive Agglutination for Diagnosis of Mycoplasma Pneumoniae Infection. *Ther. Clin. Risk Manage.* **2018**, *14*, 1091−1097.

(150) Soleimani, R.; Khourssaji, M.; Gruson, D.; Rodriguez-Villalobos, H.; Berghmans, M.; Belkhir, L.; Yombi, J. C.; Kabamba-Mukadi, B. Clinical Usefulness of Fully Automated Chemiluminescent Immunoassay for Quantitative Antibody Measurements in COVID-19 Patients. *J. Med. Virol.* **2020**, 1 DOI: 10.1002/jmv.26430.

(151) Mattioli, I. A.; Crespilho, F. N. Problems of Interpreting Diagnostic Tests for SARS-CoV-2: Analytical Chemistry Concerns. *An. Acad. Bras. Cienc.* **2020**, *92*, 1−3.

(152) Zhao, J.; Yuan, Q.; Wang, H.; Liu, W.; Liao, X.; Su, Y.; Wang, X.; Yuan, J.; Li, T.; Li, J.; Qian, S.; Hong, C.; Wang, F.; Liu, Y.; Wang, Z.; He, Q.; He, B.; Zhang, T.; Ge, S.; Liu, L.; Zhang, J.; Xia, N.; Zhang, Z. Antibody Responses to SARS-CoV-2 in Patients of Novel Coronavirus Disease 2019. *Clin. Infect. Dis.* **2020**, 1−22.

(153) Lou, B.; Li, T.; Zheng, S.; Su, Y.; Li, Z.; Liu, W.; Yu, F.; Ge, S.; Zou, Q.; Yuan, Q.; Lin, S.; Hong, C.; Yao, X.; Zhang, X.; Wu, D.; Zhou, G.; Hou, W.; Li, T.; Zhang, Y.; Zhang, S.; Fan, J.; Zhang, J.; Xia, N.; Chen, Y. Serology Characteristics of SARS-CoV-2 Infection since the Exposure and Post Symptoms Onset. *Eur. Respir. J.* **2020**, *56*, 2000763.

(154) Wang, Z.; Li, H.; Li, J.; Yang, C.; Guo, X.; Hu, Z.; Chen, Z.; Wang, S.; Liu, J. Elevated Serum IgM Levels Indicate Poor Outcome in Patients with Coronavirus Disease 2019 Pneumonia: A Retrospective Case-Control Study. *SSRN J.* **2020**, 1 DOI: 10.2139/ssrn.3557987.

(155) Long, Q.; Deng, H.; Chen, J.; Hu, J.; Liu, B.; Liao, P.; Lin, Y.; Yu, L.; Mo, Z.; Xu, Y.; Gong, F.; Wu, G.; Zhang, X.; Chen, Y.; Li, Z.; Wang, K.; Zhang, X.; Tian, W.; Niu, C.; Yang, Q.; Xiang, J.; Du, H.; Liu, H.; Lang, C.; Luo, X.; Wu, S.; Cui, X.; Zhou, Z.; Wang, J.; Xue, C.; Li, X.; Wang, L.; Tang, X.; Zhang, Y.; Qiu, J.; Liu, X.; Li, J.; Zhang, D.; Zhang, F.; Cai, X.; Wang, D.; Hu, Y.; Ren, J.; Tang, N.; Liu, P.; Li, Q.; Huang, A. Antibody Responses to SARS-CoV-2 in COVID-19 Patients: The Perspective Application of Serological Tests in Clinical Practice. *medRxiv* **2020**, 1 DOI: 10.1101/2020.03.18.20038018.

(156) Quesada-González, D.; Merkoçi, A. Nanoparticle-Based Lateral Flow Biosensors. *Biosens. Bioelectron.* **2015**, *73*, 47−63.

(157) De Puig, H.; Bosch, I.; Gehrke, L.; Hamad-schifferli, K. Challenges of the Nano-Bio Interface in Lateral Flow and Dipstick Immunoassays. *Trends Biotechnol.* **2017**, *35* (12), 1169−1180.

(158) Borse, V.; Srivastava, R. Process Parameter Optimization for Lateral Flow Immunosensing. *Mater. Sci. Energy Technol.* **2019**, *2* (3), 434−441.

(159) Zainol Rashid, Z.; Othman, S. N.; Abdul Samat, M. N.; Ali, U. K.; Wong, K. K. Diagnostic Performance of COVID-19 Serology Assays. *Malays. J. Pathol.* **2020**, *42* (1), 13−21.

(160) Whitman, J. D.; Hiatt, J.; Mowery, C. T.; Shy, B. R.; Yu, R.; Yamamoto, T. N.; Rathore, U.; Goldgof, G. M.; Whitty, C.; Woo, J. M.; Gallman, A. E.; Miller, T. E.; Levine, A. G.; Nguyen, D. N.; Bapat, S. P.; Balcerek, J.; Bylsma, S. A.; Lyons, A. M.; Li, S.; Wong, A. W.; Gillis-Buck, E. M.; Steinhart, Z. B.; Lee, Y.; Apathy, R.; Lipke, M. J.; Smith, J. A.; Zheng, T.; Boothby, I. C.; Isaza, E.; Chan, J.; II, D. D. A.; Lee, J.; Macrae, T. A.; Kyaw, T. S.; Wu, D.; Ng, D. L.; Gu, W.; York,

V. A.; Eskandarian, H. A.; Callaway, P. C.; Warrier, L.; Moreno, M. E.; Levan, J.; Torres, L.; Farrington, L. A.; Loudermilk, R.; Koshal, K.; Zorn, K. C.; Garcia-Beltran, W. F.; Yang, D.; Astudillo, M. G.; Bernstein, B. E.; Gelfand, J. A.; Ryan, E. T.; Charles, R. C.; Iafrate, A. J.; Lennerz, J. K.; Miller, S.; Chiu, C. Y.; Stramer, S. L.; Wilson, M. R.; Manglik, A.; Ye, C. J.; Krogan, N. J.; Anderson, M. S.; Cyster, J. G.; Ernst, J. D.; Wu, A. H. B.; Lynch, K. L.; Bern, C.; Hsu, P. D.; Marson, A. Test Performance Evaluation of SARS-CoV-2 Serological Assays. *medRxiv* **2020**, 1 DOI: 10.1101/2020.04.25.20074856.

(161) Qu, Z.; Wang, K.; Alfranca, G.; de la Fuente, J. M.; Cui, D. A Plasmonic Thermal Sensing Based Portable Device for Lateral Flow Assay Detection and Quantification. *Nanoscale Res. Lett.* **2020**, *15* (1), 1 DOI: 10.1186/s11671-019-3240-3.

(162) Tian, M.; Xie, W.; Zhang, T.; Liu, Y.; Lu, Z.; Li, C. M.; Liu, Y. A Sensitive Lateral FLow Immunochromatographic Strip with Prussian Blue Nanoparticles Mediated Signal Generation and Cascade Amplification. *Sens. Actuators, B* **2020**, *309*, 127728.

(163) Chen, Z.; Zhang, Z.; Zhai, X.; Li, Y.; Lin, L.; Zhao, H.; Bian, L.; Li, P.; Yu, L.; Wu, Y.; Lin, G. Rapid and Sensitive Detection of Anti-SARS-CoV-2 IgG Using Lanthanide-Doped Nanoparticles-Based Lateral Flow Immunoassay. *Anal. Chem.* **2020**, *92*, 7226.

(164) Huang, C.; Wen, T.; Shi, F.-J.; Zeng, X.-Y.; Jiao, Y.-J. Rapid Detection of IgM Antibodies against the SARS-CoV-2 Virus via Colloidal Gold Nanoparticle-Based Lateral-Flow Assay.Pdf. *ACS Omega* **2020**, *5*, 12550.

(165) Mohammadniaei, M.; Koyappayil, A.; Min, J.; Lee, M.-H.; Sun, Y. Electrochemical Detection of Multiple RNA Targets Using MXene/Duplex- Specific Nuclease: A Path towards Simultaneous Detection of SARS-CoV- 2 and H1N1 Influenza Virus. In *Biosensors for pandemics*; 2020; p 39.

(166) Mavrikou, S.; Moschopoulou, G.; Tsekouras, V.; Kintzios, S. A Rapid and Sensitive Bioelectrical Biosensor for the Detection of the SARS-CoV-2 S1 Spike Protein Based on Membrane-Engineered Cells. In *Biosensors for pandemics*; 2020; p 24.

(167) Hernandez, C. A.; Osma, J. F. Equivalent Electrical Model Circuit for COVID-19 Electrochemical Detection. In *Biosensors for pandemics*; 2020; p 33.

(168) Bouchiat, V.; Guerra, M.; Tripsky, A.; Bourrier, A.; Othmen, R. Graphene-on-Polymer Films for Low Cost Flexible & Disposable Biosensors. In *Biosensors for pandemics*; 2020; p 21.

(169) Iost, R. M.; Crespilho, F. N. Layer-by-Layer Self-Assembly and Electrochemistry: Applications in Biosensing and Bioelectronics. *Biosens. Bioelectron.* **2012**, *31* (1), 1−10.

(170) Iost, R. M.; Sales, F. C. P. F.; Martins, M. V. A.; Almeida, M. C.; Crespilho, F. N. Glucose Biochip Based on Flexible Carbon Fiber Electrodes: In Vivo Diabetes Evaluation in Rats. *ChemElectroChem* **2015**, *2* (4), 518−521.

(171) Kaya, S. I.; Karadurmus, L.; Ozcelikay, G.; Bakirhan, N. K.; Ozkan, S. A. Electrochemical Virus Detections with Nanobiosensors. In *Nanosensors for Smart Cities; INC*; 2020; pp 303−326. DOI: 10.1016/b978-0-12-819870-4.00017-7.

(172) Macedo, L. J. A.; Iost, R. M.; Hassan, A.; Balasubramanian, K.; Crespilho, F. N. Bioelectronics and Interfaces Using Monolayer Graphene. *ChemElectroChem* **2019**, *6* (1), 31−59.

(173) Macedo, L. J. A.; Lima, F. C. D. A.; Amorim, R. G.; Freitas, R. O.; Yadav, A.; Iost, R. M.; Balasubramanian, K.; Crespilho, F. N. Interplay of Non-Uniform Charge Distribution on the Electrochemical Modification of Graphene. *Nanoscale* **2018**, *10*, 15048−15057.

(174) Yadav, A.; Iost, R. M.; Neubert, T. J.; Baylan, S.; Schmid, T.; Balasubramanian, K. Selective Electrochemical Functionalization of the Graphene Edge. *Chem. Sci.* **2019**, *10* (3), 936−942.

(175) de Souza, J. C. P.; Iost, R. M.; Crespilho, F. N. Nitrated Carbon Nanoblisters for High-Performance Glucose Dehydrogenase Bioanodes. *Biosens. Bioelectron.* **2016**, *77*, 860−865.

(176) Luz, R. A. S.; Crespilho, F. N. Gold Nanoparticle-Mediated Electron Transfer of Cytochrome c on a Self-Assembled Surface. *RSC Adv.* **2016**, *6* (67), 62585−62593.

(177) Barman, S. C.; Zahed, M. A.; Sharifuzzaman, M.; Ko, S. G.; Yoon, H.; Nah, J. S.; Xuan, X.; Park, J. Y. Immunosensing Platforms: A Polyallylamine Anchored Amine-Rich Laser-Ablated Graphene Platform for Facile and Highly Selective Electrochemical IgG Biomarker Detection. *Adv. Funct. Mater.* **2020**, *30* (14), 2070093.

(178) Akbari Nakhjavani, S.; Afsharan, H.; Khalilzadeh, B.; Ghahremani, M. H.; Carrara, S.; Omidi, Y. Gold and Silver Bio/Nano-Hybrids-Based Electrochemical Immunosensor for Ultrasensitive Detection of Carcinoembryonic Antigen. *Biosens. Bioelectron.* **2019**, *141* (April), 111439.

(179) Mahari, S.; Roberts, A.; Shahdeo, D.; Gandhi, S. ECovSens-Ultrasensitive Novel In-House Built Printed Circuit Board Based Electrochemical Device for Rapid Detection of NCovid-19. *bioRxiv* **2020**, 1 DOI: 10.1101/2020.04.24.059204.

(180) Islam, S.; Shukla, S.; Bajpai, V. K.; Han, Y. K.; Huh, Y. S.; Kumar, A.; Ghosh, A.; Gandhi, S. A Smart Nanosensor for the Detection of Human Immunodeficiency Virus and Associated Cardiovascular and Arthritis Diseases Using Functionalized Graphene-Based Transistors. *Biosens. Bioelectron.* **2019**, *126*, 792−799.

(181) Fu, W.; Feng, L.; Panaitov, G.; Kireev, D.; Mayer, D.; Offenhäusser, A.; Krause, H. J. Biosensing near the Neutrality Point of Graphene. *Sci. Adv.* **2017**, *3* (10), e1701247.

(182) Seo, G.; Lee, G.; Kim, M. J.; Baek, S.-H.; Choi, M.; Ku, K. B.; Lee, C.-S.; Jun, S.; Park, D.; Kim, H. G.; Kim, S.-J.; Lee, J.-O.; Kim, B. T.; Park, E. C.; Kim, S. Il. Rapid Detection of COVID-19 Causative Virus (SARS-CoV-2) in Human Nasopharyngeal Swab Specimens Using Field-Effect Transistor-Based Biosensor. *ACS Nano* **2020**, *14*, 5135.

(183) Yang, M.; Jiang, T. J.; Wang, Y.; Liu, J. H.; Li, L. N.; Chen, X.; Huang, X. J. Enhanced Electrochemical Sensing Arsenic(III) with Excellent Anti-Interference Using Amino-Functionalized Graphene Oxide Decorated Gold Microelectrode: XPS and XANES Evidence. *Sens. Actuators, B* **2017**, *245*, 230−237.

(184) Ali, A.; Hu, C.; Jahan, S.; Yuan, B.; Saleh, M. S.; Ju, E.; Gao, S.-J.; Panat, R. Sensing of COVID-19 Antibodies in Seconds via Aerosol Jet Printed Three Dimensional Electrodes. *medRxiv* **2020**, 1−40, DOI: 10.1101/2020.09.13.20193722.

(185) Bhattacharjee, M.; Bandyopadhyay, D. Flexible Paper Touchpad for Parkinson's Hand Tremor Detection. *Sens. Actuators, A* **2019**, *294*, 164−172.

(186) Ratajczak, K.; Stobiecka, M. High-Performance Modified Cellulose Paper-Based Biosensors for Medical Diagnostics and Early Cancer Screening: A Concise Review. *Carbohydr. Polym.* **2020**, *229*, 115463.

(187) Iost, R. M.; Cantanhede, W.; Madurro, J. M.; Graci, A.; Madurro, B.; Franco, L.; Crespilho, F. N. Recent Advances in Nano-Based Electrochemical Biosensors: Application in Diagnosis and Monitoring of Diseases. *Front. Biosci., Elite Ed.* **2011**, 3, 663−689.

(188) Li, Y.; He, R.; Niu, Y.; Li, F. Paper-Based Electrochemical Biosensors for Point-of-Care Testing of Neurotransmitters. *J. Anal. Test.* **2019**, 3 (1), 19−36.

(189) Mandal, N.; Mitra, S.; Bandyopadhyay, Di. Paper-Sensors for Point-of-Care Monitoring of Drinking Water Quality. *IEEE Sens. J.* **2019**, *19* (18), 7936−7941.

(190) Tang, R. H.; Liu, L. N.; Zhang, S. F.; He, X. C.; Li, X. J.; Xu, F.; Ni, Y. H.; Li, F. A Review on Advances in Methods for Modification of Paper Supports for Use in Point-of-Care Testing. *Microchim. Acta* **2019**, *186* (8), 1 DOI: 10.1007/s00604-019-3626-z.

(191) Kong, F.; Hu, Y. F. Biomolecule Immobilization Techniques for Bioactive Paper Fabrication. *Anal. Bioanal. Chem.* **2012**, *403* (1), 7−13.

(192) Rusmini, F.; Zhong, Z.; Feijen, J. Protein Immobilization Strategies for Protein Biochips. *Biomacromolecules* **2007**, *8* (6), 1775−1789.

(193) Pereira, A. R.; Sedenho, G. C.; de Souza, J. C. P.; Crespilho, F. N. Advances in Enzyme Bioelectrochemistry. *An. Acad. Bras. Cienc.* **2018**, *90* (1), 825−857.

(194) Devarakonda, S.; Singh, R.; Bhardwaj, J.; Jang, J. Cost-Effective and Handmade Paper-Based Immunosensing Device for

Electrochemical Detection of Influenza Virus. *Sensors* **2017**, *17* (11), 2597.

(195) Liu, W.; Yang, H.; Ding, Y.; Ge, S.; Yu, J.; Yan, M.; Song, X. Paper-Based Colorimetric Immunosensor for Visual Detection of Carcinoembryonic Antigen Based on the High Peroxidase-like Catalytic Performance of ZnFe2O4-Multiwalled Carbon Nanotubes. *Analyst* **2014**, *139* (1), 251−258.

(196) Reboud, J.; Xu, G.; Garrett, A.; Adriko, M.; Yang, Z.; Tukahebwa, E. M.; Rowell, C.; Cooper, J. M. Paper-Based Microfluidics for DNA Diagnostics of Malaria in Low Resource Underserved Rural Communities. *Proc. Natl. Acad. Sci. U. S. A.* **2019**, *116* (11), 4834−4842.

(197) Imamura, A. H.; Segato, T. P.; de Oliveira, L. J. M.; Hassan, A.; Crespilho, F. N.; Carrilho, E. Monitoring Cellulose Oxidation for Protein Immobilization in Paper-Based Low-Cost Biosensors. *Microchim. Acta* **2020**, *187* (5), 1 DOI: 10.1007/s00604-020-04250-6.

(198) Sher, M.; Zhuang, R.; Demirci, U.; Asghar, W. Paper-Based Analytical Devices for Clinical Diagnosis: Recent Advances in the Fabrication Techniques and Sensing Mechanisms. *Expert Rev. Mol. Diagn.* **2017**, *17* (4), 351−366.

(199) Mejía-Salazar, J. R.; Oliveira, O. N. Plasmonic Biosensing. *Chem. Rev.* **2018**, *118* (20), 10617−10625.

(200) Wu, F.; Thomas, P. A.; Kravets, V. G.; Arola, H. O.; Soikkeli, M.; Iljin, K.; Kim, G.; Kim, M.; Shin, H. S.; Andreeva, D. V.; Neumann, C.; Küllmer, M.; Turchanin, A.; De Fazio, D.; Balci, O.; Babenko, V.; Luo, B.; Goykhman, I.; Hofmann, S.; Ferrari, A. C.; Novoselov, K. S.; Grigorenko, A. N. Layered Material Platform for Surface Plasmon Resonance Biosensing. *Sci. Rep.* **2019**, *9* (1), 1−10.

(201) Ferreira, J.; Santos, M. J. L.; Rahman, M. M.; Brolo, A. G.; Gordon, R.; Sinton, D.; Girotto, E. M. Attomolar Protein Detection Using In-Hole Surface Plasmon Resonance. *J. Am. Chem. Soc.* **2009**, *131* (2), 436−437.

(202) Zagorodko, O.; Spadavecchia, J.; Serrano, A. Y.; Larroulet, I.; Pesquera, A.; Zurutuza, A.; Boukherroub, R.; Szunerits, S. Highly Sensitive Detection of Dna Hybridization on Commercialized Graphene-Coated Surface Plasmon Resonance Interfaces. *Anal. Chem.* **2014**, *86* (22), 11211−11216.

(203) Lee, J. S.; Kim, S. W.; Jang, E. Y.; Kang, B. H.; Lee, S. W.; Sai-Anand, G.; Lee, S. H.; Kwon, D. H.; Kang, S. W. Rapid and Sensitive Detection of Lung Cancer Biomarker Using Nanoporous Biosensor Based on Localized Surface Plasmon Resonance Coupled with Interferometry. *J. Nanomater.* **2015**, *2015*, 1.

(204) Chang, C. Y.; Lin, H. T.; Lai, M. S.; Shieh, T. Y.; Peng, C. C.; Shih, M. H.; Tung, Y. C. Flexible Localized Surface Plasmon Resonance Sensor with Metal−Insulator−Metal Nanodisks on PDMS Substrate. *Sci. Rep.* **2018**, *8* (1), 1−8.

(205) Manzano, M.; Vizzini, P.; Jia, K.; Adam, P. M.; Ionescu, R. E. Development of Localized Surface Plasmon Resonance Biosensors for the Detection of Brettanomyces Bruxellensis in Wine. *Sens. Actuators, B* **2016**, *223*, 295−300.

(206) Ye, H.; Liu, Y.; Zhan, L.; Liu, Y.; Qin, Z. Signal Amplification and Quantification on Lateral Flow Assays by Laser Excitation of Plasmonic Nanomaterials. *Theranostics* **2020**, *10* (10), 4359−4373.

(207) Lung, J.; Lin, Y. S.; Yang, Y. H.; Chou, Y. L.; Shu, L. H.; Cheng, Y. C.; Liu, H. Te; Wu, C. Y. The Potential Chemical Structure of Anti-SARS-CoV-2 RNA-Dependent RNA Polymerase. *J. Med. Virol.* **2020**, *92*, 693.

(208) Patel, C. N.; Kumar, S. P.; Pandya, H. A.; Rakesh, M. Identification of Potential Binders of the SARS-Cov-2 Spike Protein via Molecular Docking, Dynamics Simulation and Binding Free Energy Calculation Identification of Potential Binders of the SARS-Cov-2 Spike Protein via Molecular Docking, Dynamics Simula. *ChemRxiv*, 12.05.2020.

(209) Liu, W.; Li, H. COVID-19: Attacks the 1-Beta Chain of Hemoglobin and Captures the Porphyrin to Inhibit Human Heme Metabolism. *ChemRxiv*, December 2019.

(210) Yu, R.; Chen, L.; Lan, R.; Shen, R.; Li, P. Computational Screening of Antagonist against the SARS-CoV-2 (COVID-19) Coronavirus by Molecular Docking. *Int. J. Antimicrob. Agents* **2020**, *56*, 106012.

(211) Mayer, K. M.; Hafner, J. H. Localized Surface Plasmon Resonance Sensors. *Chem. Rev.* **2011**, *111* (6), 3828−3857.

(212) Lee, J. H.; Cheglakov, Z.; Yi, J.; Cronin, T. M.; Gibson, K. J.; Tian, B.; Weizmann, Y. Plasmonic Photothermal Gold Bipyramid Nanoreactors for Ultrafast Real-Time Bioassays. *J. Am. Chem. Soc.* **2017**, *139* (24), 8054−8057.

(213) Jauffred, L.; Samadi, A.; Klingberg, H.; Bendix, P. M.; Oddershede, L. B. Plasmonic Heating of Nanostructures. *Chem. Rev.* **2019**, *119* (13), 8087−8130.

(214) Stehr, J.; Hrelescu, C.; Sperling, R. A.; Raschke, G.; Wunderlich, M.; Nichtl, A.; Heindl, D.; Kürzinger, K.; Parak, W. J.; Klar, T. A.; Feldmann, S. J. Gold NanoStoves for Microsecond DNA Melting Analysis. *Nano Lett.* **2008**, *8* (2), 619−623.

(215) Qiu, G.; Gai, Z.; Tao, Y.; Schmitt, J.; Kullak-Ublick, G. A.; Wang, J. Dual-Functional Plasmonic Photothermal Biosensors for Highly Accurate Severe Acute Respiratory Syndrome Coronavirus 2 Detection. *ACS Nano* **2020**, *14*, 5268.

(216) Rumbut, J.; Fang, H.; Wang, H.; Carreiro, S.; Smelson, D.; Chapman, B.; Boyer, E. Harmonizing Wearable Biosensor Data Streams to Test Polysubstance Detection. *2020 Int. Conf. Comput. Netw. Commun. ICNC* **2020**, *2020*, 445−449.

(217) Moon, G.; Choi, J.; Lee, C.; Oh, Y.; Hwan, K.; Kim, D. Machine Learning-Based Design of Meta-Plasmonic Biosensors with Negative Index Metamaterials. *Biosens. Bioelectron.* **2020**, *164*, 112335.

(218) Vashistha, R.; Dangi, A. K.; Kumar, A.; Chhabra, D.; Shukla, P. Futuristic Biosensors for Cardiac Health Care: An Artificial Intelligence Approach. *3 Biotech* **2018**, *8* (8), 1−11.

(219) Alimadadi, A.; Aryal, S.; Manandhar, I.; Munroe, P. B.; Joe, B.; Cheng, X. Artificial Intelligence and Machine Learning to Fight Covid-19. *Physiol. Genomics* **2020**, *52* (4), 200−202.

(220) Punn, N. S.; Sonbhadra, S. K.; Agarwal, S. COVID-19 Epidemic Analysis Using Machine Learning and Deep Learning Algorithms. *medRxiv* **2020**, 1 DOI: 10.1101/2020.04.08.20057679.

(221) Bai, L.; Yang, D.; Wang, X.; Tong, L.; Zhu, X.; Zhong, N.; Bai, C.; Powell, C. A.; Chen, R.; Zhou, J.; Song, Y.; Zhou, X.; Zhu, H.; Han, B.; Li, Q.; Shi, G.; Li, S.; Wang, C.; Qiu, Z.; Zhang, Y.; Xu, Y.; Liu, J.; Zhang, D.; Wu, C.; Li, J.; Yu, J.; Wang, J.; Dong, C.; Wang, Y.; Wang, Q.; Zhang, L.; Zhang, M.; Ma, X.; Zhao, L.; Yu, W.; Xu, T.; Jin, Y.; Wang, X.; Wang, Y.; Jiang, Y.; Chen, H.; Xiao, K.; Zhang, X.; Song, Z.; Zhang, Z.; Wu, X.; Sun, J.; Shen, Y.; Ye, M.; Tu, C.; Jiang, J.; Yu, H.; Tan, F. Chinese Experts' Consensus on the Internet of Things-Aided Diagnosis and Treatment of Coronavirus Disease 2019 (COVID-19). *Clin. eHealth* **2020**, *3*, 7−15.

(222) da Motta, O. J. R.; Silva, E.; Siqueira-Batista, R. Bioethical Aspects of Artificial Intelligence: COVID-19 & End of Life. *Rev. Assoc. Med. Bras.* **2020**, *66*, 5−6.

(223) Prasad, N.; Cheng, L. F.; Chivers, C.; Draugelis, M.; Engelhardt, B. E. A Reinforcement Learning Approach to Weaning of Mechanical Ventilation in Intensive Care Units. *arXiv [computer science]*; **2017**; 1704.06300.

(224) Vaishya, R.; Javaid, M.; Khan, I. H.; Haleem, A. Artificial Intelligence (AI) Applications for COVID-19 Pandemic. *Diabetes Metab. Syndr. Clin. Res. Rev.* **2020**, *14* (4), 337−339.

(225) Keshavarzi Arshadi, A.; Webb, J.; Salem, M.; Cruz, E.; Calad-Thomson, S.; Ghadirian, N.; Collins, J.; Diez-Cecilia, E.; Kelly, B.; Goodarzi, H.; Yuan, J. S. Artificial Intelligence for COVID-19 Drug Discovery and Vaccine Development. *Front. Artif. Intell.* **2020**, *3*, 1−13.

(226) Rodrigues, J. F.; Paulovich, F. V.; De Oliveira, M. C. F.; De Oliveira, O. N. On the Convergence of Nanotechnology and Big Data Analysis for Computer-Aided Diagnosis. *Nanomedicine* **2016**, *11* (8), 959−982.

(227) Oliveira, O. N.; Neves, T. T. A. T.; Paulovich, F. V.; De Oliveira, M. C. F. Where Chemical Sensors May Assist in Clinical Diagnosis Exploring "Big Data. *Chem. Lett.* **2014**, *43* (11), 1672−1679.

(228) Paulovich, F. V.; De Oliveira, M. C. F.; Oliveira, O. N. A Future with Ubiquitous Sensing and Intelligent Systems. *ACS Sensors* **2018**, *3* (8), 1433–1438.

CHAPTER II - Problems of Interpreting Diagnostic Tests for SARS-CoV-2: Analytical Chemistry Concerns

Author Contributions: Isabela A. Mattioli: conceived the project, performed bibliographic revision, endorsed discussion regarding the collected data, wrote and revised the manuscript; and Frank N. Crespilho: conceived the project, wrote, revised and corrected the manuscript.

In this article, a pertinent discussion on the most relevant analytical parameters that need to be analyzed for interpreting COVID-19 diagnostic tests was performed. This was made in order to clarify several misunderstandings between sensitivity, LOD, cut-off and other analytical parameters that are frequently employed in medical and clinical research carried out for developing COVID-19 detection methodologies. The principles discussed in this article were considered also of great importance for further analytical and bioanalytical studies in biosensing research field.

An Acad Bras Cienc (2020) 92(4): e20201208 DOI 10.1590/0001-3765202020201208
Anais da Academia Brasileira de Ciências | *Annals of the Brazilian Academy of Sciences*
Printed ISSN 0001-3765 I Online ISSN 1678-2690
www.scielo.br/aabc | www.fb.com/aabcjournal

LETTER TO THE EDITOR

Problems of Interpreting Diagnostic Tests for SARS-CoV-2: Analytical Chemistry Concerns

ISABELA A. MATTIOLI & FRANK N. CRESPILHO

Abstract: The COVID-19 pandemic outbreak made the development of reliable, sensitive, and reproducible testing methods crucial throughout the world. Without proper analytical validation, testing results can be misinterpreted, leading to a certain degree of misinformation in the clinical area. To accurately assess the methods, the determination of an analytical linear range of response of the assay is fundamental. Based on this curve, the evaluation of some parameters as sensitivity, limit of detection, and limit of quantification can be done, as well as the establishment of cut-off values. Statistical treatments of the collected data can be performed for reproducibility and reliability evaluations. In this context, there is a wide range of analytical concerns that should be in-depth discussed in medical, biomedical and chemical areas. This letter aims to briefly clarify some analytical chemistry concepts, as sensitivity, cut-off and limit of detection, and their application towards clinical diagnosis.

Key words: tests, COVID-19, Lateral Flow, SARS-CoV-2, diagnosis.

The COVID-19 pandemic outbreak highlighted one of the most relevant issues in analytical chemistry: the differences between the *testing technique* (TT) and *testing method* (TM) is a common misinterpreted concept in clinical area. TT consists of several procedures beyond the testing technique, such as the collection of specimens, its preservation, handling, transporting, labelling, and delivering. Patient pre-test preparation procedures are also part of the method (Fischbach & Dunning III 2015). These protocols, also known as preanalytical factors, were previously reported to be the main sources of testing errors in laboratories (Lippi et. al. 2020). While developing the TM, the most suitable TT for the TM must be validated for the detection of the target analyte, otherwise the analysis is executed within a wide range of analytical errors that lead to false results.

A successful validation comprises various factors: 1) characteristics of the samples to be analyzed (i.e., blood, serum, plasma, solid residues); 2) the need of a previous step concerning sample preparation; 3) the specimens to be quantified (i.e., genetic material or antibodies); 4) the determination of analytical parameters, such as the limit of detection (LOD), sensitivity and ultimately 5) the statistical treatment on the applicability of the TT in a suitable sample population. When a TT is validated for clinical purposes, sensitivity is a key factor to determine. It is defined as the slope of a calibration curve and is therefore relevant when a concentration range of detections is determined only. It provides information on the testing assay sensitivity to changes in the analyte concentration (Massart et. al. 1978, Mikkelsen & Cortón 2016). In many binary immunological assays, (*i.e.* those which gives a yes/no result) sensitivity is reported as a percentage quantity, related to the ability of the test in recognizing a positive result (Parikh et al. 2008). However, sensitivity is often misinterpreted as the LOD of an assay in several reports in the clinical area relates to COVID-19 diagnosis (Whitman et al. 2020). By definition, LOD is the minimum amount of an analyte that can be detected, generating a signal three times higher (in standard deviations magnitude) than the blank signal (Mikkelsen & Cortón 2016). It is possible for a TT to exhibit low sensitivity and low LOD, and *vice-versa* (Massart et. al. 1978). Reproducibility of TT should be correctly determined along with a proper statistical treatment, especially for COVID-19 diagnosis. To determine reproducibility, a large population of samples is necessary and a *t*-student test can be helpful to determine if the obtained results follow a normal distribution (De Winter 2013). Nonetheless, lack of reproducibility spoils the robustness of the TM.

One of the main side effects of the lack of robustness and reproducibility of TT is the occurrence of false positive and false negative results. Cut-off values that establish false negative-and positive results should be determined. Generally, cut-off values can be chosen as the correspondent signal to the LOD or LOQ (Limit of Quantification) of the assay (Mikkelsen & Cortón 2016). If the target analyte is present in a concentration lower than the cut-off value, and yet the technique indicates that it is present above this value, a false positive result occurs. Conversely, a false negative result occurs when the analyte is present in a concentration above the cut-off value, but the technique indicates that it is absent in the sample (Mikkelsen & Cortón 2016). It should be noticed that cut-off value is not related to the sensitivity of the assay and its TT (Mikkelsen & Cortón 2016).

Based on what has been pointed out in this letter and differently to what is being made in clinical literature (Sethuraman et. al. 2020), we strongly encourage that a proper discussion concerning TT for COVID-19 diagnosis and effectiveness of testing assays should include how these TTs are being validated and if the employed analytical concepts are being correctly interpreted (Figure 1).

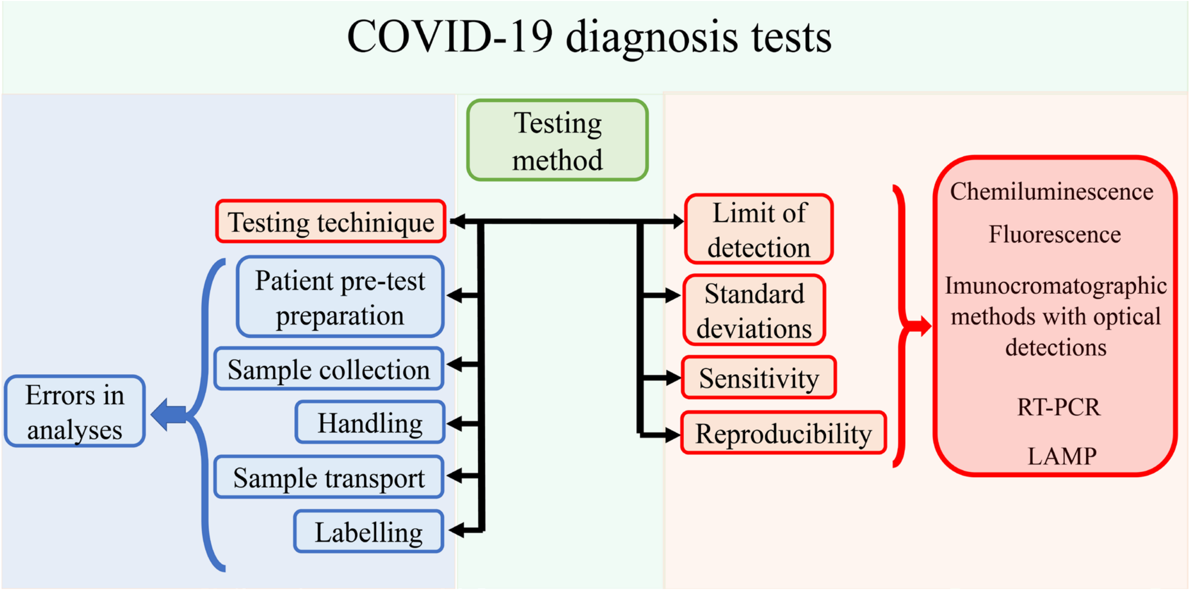

Figure 1. Steps involved in the development of a testing method for COVID-19 diagnosis. The TT to be employed is part of the entire method, although the main source of testing errors is not related to its execution. During the technique validation, it is fundamental to determine the assay reproducibility, sensitivity, LOD, and standard deviations through a statistical treatment of the results.

Acknowledgments

The authors gratefully acknowledge the Fundação de Amparo à Pesquisa do Estado de São Paulo (FAPESP) for the financial support of the research projects under the grant numbers: 18/11071-0, 19/15333-1, 19/12053-8 and 18/22214-6. Coordenação de Aperfeiçoamento de Pessoal de Nível Superior (CAPES), MeDiCo Network CAPES-Brazil grant number: 88881.504532/2020-01. Conselho Nacional de Desenvolvimento Científico e Tecnológico (CNPq) project number 305486/2019-5.

REFERENCES

DE WINTER JCF. 2013. Using the student's t-test with extremely small sample sizes. Pract Assess Res Evaluation 18: 1-12.

FISCHBACH F & DUNNING III MB. 2015. A Manual of Laboratory Diagnostic Tests. 9th ed., [s.l.] Wolters Kluwer Health, Lippincott Williams & Wilkins

LIPPI G, SIMUNDIC AM & PLEBANI M. 2020. Potential preanalytical and analytical vulnerabilities in the laboratory diagnosis of coronavirus disease 2019 (COVID-19). Clin Chem Lab Med 58(7): 1070-1076.

MASSART DL, DIJKSTRA A & KAUFMAN L. 1978. Sensitivity and Limit of Detection. In: Techniques and Instrumentation in Analytical Chemistry. [s.l.] Elsevier, p. 143-156.

MIKKELSEN SR & CORTÓN E. 2016. Bioanalytical Chemistry. 2nd ed., [s.l.] John Wiley & Sons.

PARIKH R ET AL. 2008. Understanding and using sensitivity, specificity and predictive values. Indian J Ophthalmol 56(4): 341.

SETHURAMAN N, JEREMIAH SS & RYO A. 2020. Interpreting Diagnostic Tests for SARS-CoV-2. JAMA 2019: 2019-2021.

WHITMAN JD ET AL. 2020. Test performance evaluation of SARS-CoV-2 serological assays. medRxiv, [s. l., s. n.].

How to cite

MATTIOLI IA & CRESPILHO FN. 2020. Problems of Interpreting Diagnostic Tests for SARS-CoV-2: Analytical Chemistry Concerns. An Acad Bras Cienc 92: e20201208. DOI 10.1590/0001-3765202020201208.

Manuscript received on July 29, 2020;
accepted for publication on August 31, 2020

ISABELA A. MATTIOLI
https://orcid.org/0000-0002-1646-3996

FRANK N. CRESPILHO
https://orcid.org/0000-0003-4830-652X

University of São Paulo, São Carlos Institute of Chemistry, Av. Trabalhador
São-Carlense, n° 400, Pq. Arnold-Schmidt, 13560-970 São Carlos, SP, Brazil

Correspondence to: **Frank Nelson Crespilho**
E-mail: frankcrespilho@iqsc.usp.br

Author Contributions

F.N.C and I.A.M conceived and discussed the main ideas of the manuscript. Bibliographic revision was carried out by I.A.M. This manuscript was prepared with equal contributions of all authors.

CHAPTER III - Highly sensitive interfaces of graphene electrical-electrochemical vertical devices for on drop atto-molar DNA detection

Author Contributions: Isabela A. Mattioli: conceived the project, manufactured the device, collected and analyzed the data, wrote and revised the manuscript; Ayaz Hassan: collected and analyzed the data, wrote and revised the manuscript; Natalia N. Sanches: manufactured the devices, analyzed the data, revised the manuscript; Nirton C. S. Vieira: collected and analyzed the data, revised the manuscript; and Frank N. Crespilho: conceived the project, wrote and revised the manuscript.

In this paper, it is reported for the first time a graphene-based device which working principles rely on electrochemical and electrical fundaments. The resulting device is named EEVD (Electrical Electrochemical Vertical Device). It is shown that electrical working features can be explored by the passage of current by graphene basal plane, as potential sweep is performed from working to counter terminals of the device, using a potenciostat. The potential readings are made in relation to the reference potenciostat terminal, and consequently, the device operation is hybrid (*i.e.* electrical and electrochemical). Further studies regarding the interface alterations that occur when the device is operated in hybrid electrical-electrochemical conditions were performed with a graphene-ferrocene van der Waals heterojunction. It was found that OCP of each interface can be read by the proposed methodology and is correlated to capacitive alterations of the interface. Moreover, it was demonstrated that OCP variations can be explored for biosensing purposes, in a proof-of-concept study with single-stranded DNA. In this experiment, a LOD of 5.3 10^{-21} mol L^{-1} was achieved, demonstrating the remarkable and promising features of EEVDs for biosensing.

Biosensors and Bioelectronics 175 (2021) 112851

Contents lists available at ScienceDirect

Biosensors and Bioelectronics

journal homepage: http://www.elsevier.com/locate/bios

Highly sensitive interfaces of graphene electrical-electrochemical vertical devices for on drop atto-molar DNA detection

Isabela A. Mattioli[a], Ayaz Hassan[a], Natalia M. Sanches[a], Nirton C.S. Vieira[b], Frank N. Crespilho[a,*]

[a] *São Carlos Institute of Chemistry, University of São Paulo, São Carlos, SP, 13560-970, Brazil*
[b] *Institute of Science and Technology, Federal University of São Paulo, 12231-280, São José dos Campos, SP, Brazil*

ARTICLE INFO

Keywords:
Van der waals surfaces
Short-circuit
Graphene electrochemical device
Zepto-molar detection
DNA biosensing

ABSTRACT

The development of novel high-sensitivity DNA-based biosensors is beneficial, as these devices have applications in the identification of genetic risk factors, medical diagnostics, and environmental monitoring. Herein, we report on the first robust device capable of detecting DNA on a microliter drop with a zepto-molar (10^{-21}) concentration. To accomplish this, we engineered an electrical-electrochemical vertical device (EEVD) that comprises a novel drain and source terminal in a short-circuited configuration, paired with an ideal non-polarizable reference electrode. Vertical electron transfer occurs perpendicularly to the graphene plane, while the electronic current flows through the graphene van der Waals (vdW) heterojunctions. Ferrocene adsorbed on graphene was strategically chosen as the vdW heterojunction redox component. Charge carrier insertion into the graphene makes the EEVD 10 times more sensitive than traditional graphene field-effect transistors. Interfacial potential changes were measured for single-stranded DNA detection with an unprecedented zepto-molar limit of detection.

1. Introduction

Graphene field-effect transistors (GFETs) are known to be highly sensitive biosensing devices and have potential applications in the development of portable and miniaturized sensors (Macedo et al., 2019). The effective sensing of a number of biologically relevant species using GFETs has already been reported in the literature for glucose (Kwak et al., 2012), HIV and related diseases (Islam et al., 2019b), carcinogenic embryonic antigen (Zhou et al., 2019), DNA nucleobases and single-stranded DNA (ssDNA) molecules (Dontschuk et al., 2015; Kim et al., 2019; Sun et al., 2019), to mention a few. Specifically, detection of single-stranded DNA is of particular importance for the diagnosis of genetic diseases, gene therapy, and development of healthcare methodologies (Cinti et al., 2018; Sun et al., 2019). Recently, the physiological response of cells owing to DNA damage could be better understood through ssDNA quantifications (Bantele et al., 2019), where ssDNA was used as a biomarker for identification and quantification of DNA damage, as ssDNA is frequently found at lesion sites of the genetic material due to damage processing (Bantele et al., 2019). Additionally, there is a wide range of emerging applications for ssDNA in studies involving aptamers, hybridization probes, and the elucidation of DNA recombination mechanisms for molecular biology (Damase et al., 2017; Yang and Ha, 2018).

In this context, many of the GFETs already reported for DNA-based molecule analytical quantifications are claimed to be ultrasensitive, and generally involve expensive lithographic procedures (Cai et al., 2014; Campos et al., 2019; Fu et al., 2017; Sun et al., 2019) and non-trivial methodologies for their preparation. However, only a few are capable of reaching the atto-molar (Campos et al., 2019) and zepto-molar (Hwang et al., 2020) limits of detection (LOD) through electrical and electrochemical techniques. Therefore, there remains a need to improve the sensitivity of graphene-based analytical devices to come one step closer to single-molecule detection.

Although many efforts have been made to employ pristine monolayer graphene toward the development and application of label-free sensitive GFETs, functionalization is still frequently used to improve LOD and reproducibility (Eissa et al., 2015; Macedo et al., 2018). To accomplish this, covalent functionalization with diazonium salts (Xia et al., 2016), benzoyl peroxides (Lonkar et al., 2015), and the production of reduced graphene oxide (Lei et al., 2017; Thakur et al., 2018) have

---

[*] Corresponding author.
E-mail address: frankcrespilho@iqsc.usp.br (F.N. Crespilho).

https://doi.org/10.1016/j.bios.2020.112851
Received 30 August 2020; Received in revised form 16 October 2020; Accepted 22 November 2020
Available online 24 November 2020

been some of the main strategies adopted. However, these methods frequently involve the rupture of sp^2 bonds on the graphene basal plane, which reduces the electronic conductivity of graphene (Macedo et al., 2018). An interesting alternative is the development of van der Waals (vdW) heterojunctions with ferrocene. As widely discussed in the literature (Gao et al., 2011; Nigar et al., 2019; Zribi et al., 2019), the adsorption of ferrocene on graphene by physisorption involves no hybridization or covalent bonding of the substrate and ferrocene molecules. Therefore, graphene and ferrocene interact by $\pi-\pi$ coupling resulting from weak vdW interactions. Consequently, the sp^2 lattice and the band structure of graphene are maintained intact after ferrocene adsorption (Nigar et al., 2019).

The development of the vdW interface with a graphene monolayer also improves the basal plane conductivity and charge carrier concentration, resulting in the enhancement of the sensitivity of the resulting heterojunction (Zribi et al., 2019). These phenomena have previously been monitored in terms of shifts in the charge neutrality point (CNP) of graphene using Raman spectroscopy (Van Den Beld et al., 2017). Few studies in the literature have used ferrocene for band-gap investigations in pristine graphene (Zribi et al., 2019) and biosensing applications (Rabti et al., 2016). The additional advantage of using this system is the possibility of observing the faradaic process at the interface due to the electron transfer at the active redox center of the ferrocene when irreversibly adsorbed on graphene. The occurrence of electron transfer at similar heterojunctions has already been demonstrated in some studies (Lima et al., 2014; Zribi et al., 2019) and can be used to observe, study, and develop analytical methods based on electrochemical features of graphene-based heterojunctions (Neubert et al., 2020). In addition to the abovementioned issues frequently faced in GFET applications, another problem related to their implementation as detection devices involves the frequent use of $Ag/AgCl_{sat}$ as a polarizable gate electrode for CNP monitoring. From an electrochemical viewpoint, this process is inadequate because of the non-polarizable characteristics of the reference electrodes, leading to imprecise and non-stable CNP potential measurements.

In this study, we propose a new device configuration, the electrical-electrochemical vertical device (EEVD). Our strategy combines a horizontally aligned graphene-ferrocene heterojunction, in which the device is connected in a “short-circuit” configuration, thus retaining the conventional three-electrode setup. We compared the EEVD performance with the traditional GFET configuration. EEVDs represent a lower-cost device than devices reported elsewhere (Islam et al., 2019a, 2019b), which is advantageous for the development of cost-effective biosensing strategies. We also monitored how faradaic contributions of adsorbed ferrocene influence EEVD behavior, as it is well-known that the presence of redox-active molecules in the analyte solution alters the charge distribution in graphene (Neubert et al., 2020).

2. Materials and methods

2.1. Apparatus

Electrical Ti contacts for the EEVDs were created using a BAK 600 evaporator (Balzers) with an 8 kV electron beam. Au contacts were deposited with an MED 020 Baltec evaporator (100 mA current and 1 nm s^{-1} deposition rate). Electrochemical experiments were carried out in a μAutolab-III potentiostat/galvanostat (Metrohm) with an FRA32 impedance module, managed by Nova 2.1.3 software using $Ag/AgCl_{sat}$ as the reference electrode and a Pt wire as the auxiliary electrode. Field-effect experiments were performed in a Keithley 2636 B source meter unit (Tektronix), using $Ag/AgCl_{sat}$ and a drop of 40 μL of electrolyte as the gate electrode. Raman spectroscopy data were acquired using LabSpec 6 software in a LabRAM HR Evolution spectrometer (Horiba Scientific). A HeNe 633 nm laser with 0.86 μm spot for 100x magnification was applied with an acquisition time of 1 s for 64 spectra.

2.2. Materials

Sulfuric acid (98%), ethanol, isopropanol, monobasic sodium phosphate, and dibasic sodium phosphate were acquired from Synth (Brazil). Acetone was purchased from Chemis (Brazil). Toluene, hydrochloric acid (37%, *v*/*v*), polystyrene (MW ~ 192,000 g mol^{-1}), ferrocene (98%), and potassium chloride were purchased from Sigma Aldrich. Hydrogen peroxide (30–32%, *v*/*v*) was acquired from Vetec (Brazil). For EEVD confection, chemical vapor deposition (CVD)-grown monolayer graphene on Cu foil was purchased from Graphenea (Spain) and *p*-doped Si/SiO_2 substrate material ($\varphi_{SiO2} = 90$ nm) was acquired from Graphene Supermarket (USA). Metallic targets of Ti and Au for electrical contact preparation were purchased from Electron Microscopy Sciences (USA). ssDNA (integrated DNA technology, USA) with the following genetic code was employed: 20^A (5-GTG AGC TAA CGT GTC AGT AC-3). All aqueous solutions were prepared using deionized water (>18 MΩ cm).

2.3. EEVD preparation

The EEVDs studied in this work and GFET platforms were prepared using CVD monolayer graphene transferred to a SiO_2/Si ($\varphi = 90$ nm) substrate with electrical contacts consisting of 10 nm of Ti and 20 nm of Au. Prior to the preparation, all SiO_2/Si chips were cleaned in a piranha solution (3 H_2SO_4: 1 H_2O_2), followed by rinsing with deionized water and isopropanol. Then, CVD monolayer graphene transfer was carried out as follows: approximately 10 μL of polystyrene in toluene was initially drop-casted onto the surface of a small piece of Cu-supported CVD-grown monolayer graphene and then dried at 70 °C in an oven for 10 min. The Cu was then removed through an etching solution (HCl and H_2O_2), leaving behind the graphene supported on polystyrene. The graphene was then transferred to a SiO_2/Si substrate and finally pre-annealed at 90 °C for 15 min. After cooling to room temperature, the polystyrene was dissolved from the chip using toluene and the chip was annealed at 585 °C for 1 min under an inert Ar atmosphere. Finally, any Cu residue remaining from the transfer procedure was removed by electrochemical etching in 0.10 mol L^{-1} HCl using cyclic voltammetry (Fig. S1, Section 1 of ESI) (Iost et al., 2014).

2.4. Short-circuit and electrochemical experiments

Short-circuit experiments were performed in a potentiostat/galvanostat (μ-Autolab-III, Metrohm). The drain terminal was connected to a counter-electrode (CE) terminal and the source terminal was connected to a working electrode WE terminal. An $Ag/AgCl_{sat}$ reference electrode and 40 μL of supporting electrolyte were used as the top-gated system. Electrochemical features were initially studied by cyclic voltammetry from −0.2 V to 0.6 V at 25 mV s^1 in phosphate buffer (0.10 mol L^{-1} pH 7.2) and KCl (0.10 mol L^{-1}). The EEVD vdW heterojunctions using graphene and ferrocene (graphene-fc) were constructed by drop casting, using ~30 μL of a ferrocene in ethanol solution (5.0 mg mL^{-1}). The excess ferrocene on the graphene surface was removed by cyclic voltammetry in 0.10 mol L^{-1} KCl. A schematic representation of the

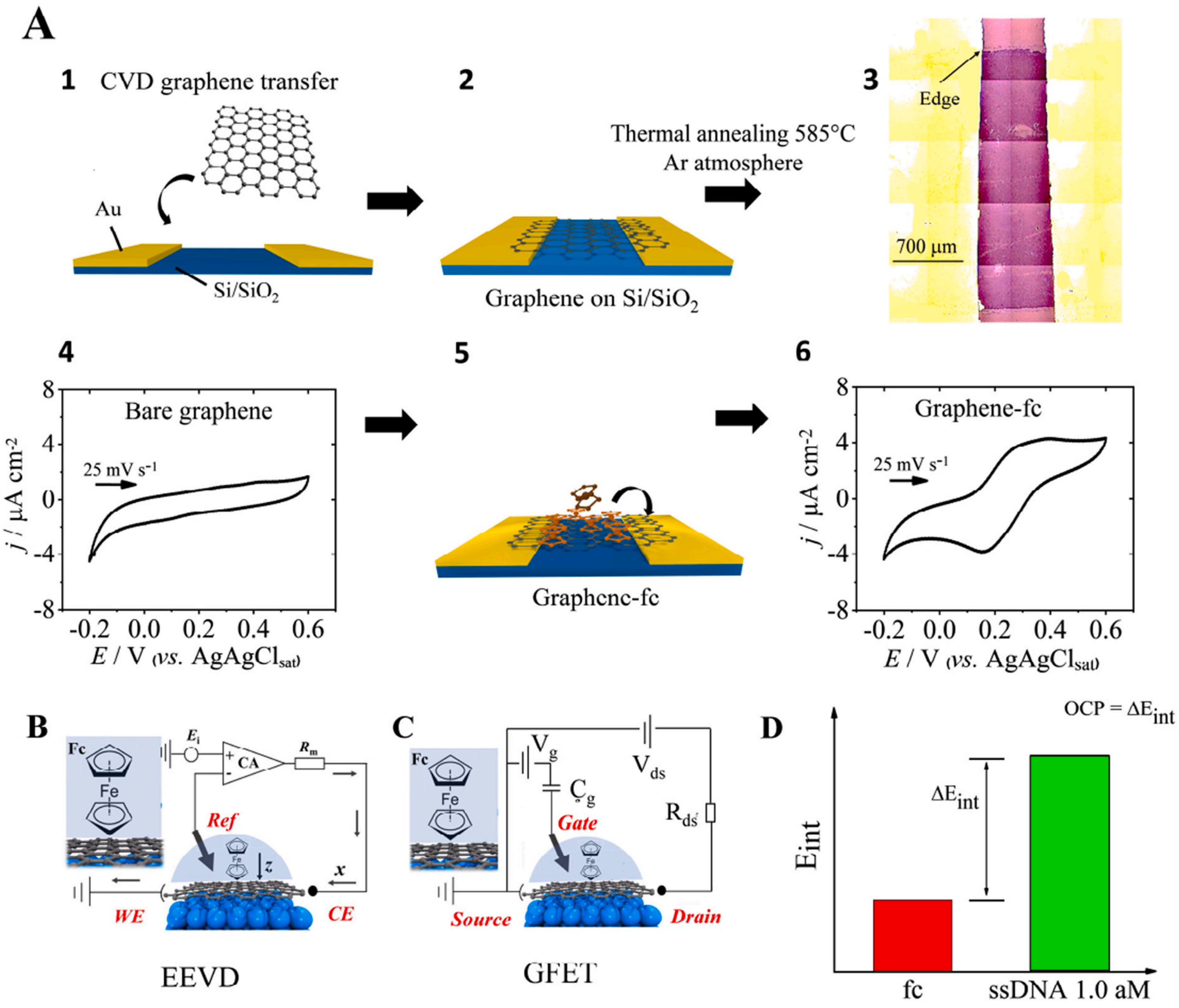

Fig. 1. EEVD preparation and operation schematics A) EEVD device preparation description. Steps 1 and 2 correspond to graphene wet transfer methodology. After subsequent thermal annealing for formation of graphene on the SiO_2/Si interface, Step 3 presents an optical micrograph of graphene on SiO_2/Si. Step 4 depicts a typical pristine graphene electrochemical response in a 0.10 mol L^{-1} phosphate buffer solution (pH 7.2). Step 5 illustrates ferrocene in ethanol (5.0 mg mL^{-1}) drop casting and adsorption on graphene, forming a graphene-fc vdW heterojunction. Step 6 illustrates a typical final cyclic voltammogram obtained for graphene-fc in a 0.10 mol L^{-1} phosphate buffer solution (pH 7.2) after removal of excess ferrocene. B) Schematic representation of the working principles of an EEVD with the proposed graphene-fc heterojunction. C) Schematic representation of a GFET's working principles for comparison purposes with Fig. 1B. D) Representation of ssDNA quantification with our EEVD graphene-fc devices through interfacial potential (E_{int}) variations.

production of the EEVDs is presented in Fig. 1A. Electrochemical impedance spectroscopy (EIS) was also carried out before and after ferrocene modifications from 100 kHz to 0.1 Hz by applying an open-circuit potential (OCP) with an amplitude of 5.0 mV to each electrode. Three spectra were obtained for each interface. ssDNA was adsorbed onto ferrocene-modified EEVDs by drop casting 40 µL of ssDNA solution in a phosphate buffer (0.10 mol L^{-1}, pH 7.2). An adsorption time of 5 min at room temperature was adopted as the standard methodology in this study, and experiments were conducted in the same phosphate buffer solution. For calibration curve experiments, a 40 µL droplet was added onto the graphene-fc surface for each concentration and washed off after the measurements were taken. The effects of ssDNA adsorption on interfacial features and on the electrochemical behavior of the EEVDs were monitored by EIS and cyclic voltammetry, respectively.

2.5. Raman spectroscopy

Raman spectroscopy analyses were carried out using the same monolayer graphene device supported on a Si/SiO_2 substrate. Spectra from 1000 cm^{-1} to 3000 cm^{-1} were acquired for pristine graphene using an HeNe (λ = 633 nm) excitation laser in a LabRAM HR Evolution spectrometer (Horiba Scientific). A drop of ~30 µL of ferrocene in ethanol was added onto the surface of the graphene and was electrochemically stabilized by cyclic voltammetry in KCl 0.1 mol L^{-1}, from −0.2 V to 0.6 V, at ν = 25 mV s^{-1}. For the ferrocene-modified samples, Raman spectra were acquired from 1000 cm^{-1} to 3000 cm^{-1}. Finally, a drop of 1.0 fmol L^{-1} ssDNA was added onto the graphene-fc device and spectra from 1000 cm^{-1} to 3000 cm^{-1} were also acquired after approximately 10 min. We chose low-concentrated ssDNA solutions to avoid any scattering effects or alterations in the spectra caused by surface saturation. Raman spectra of the edge and the basal plane of the graphene used in this work were also collected under the same conditions (Section 2 of ESI).

2.6. Atomic force microscopy characterizations

Atomic force microscopy (AFM) experiments were carried out by NMS to provide useful information regarding the monolayer nature of the graphene used in this study (see the results discussed in Section 2 of the ESI). AFM experiments were carried out in the LNLS laboratory (Brazilian Synchrotron Light Laboratory) at the National Center for

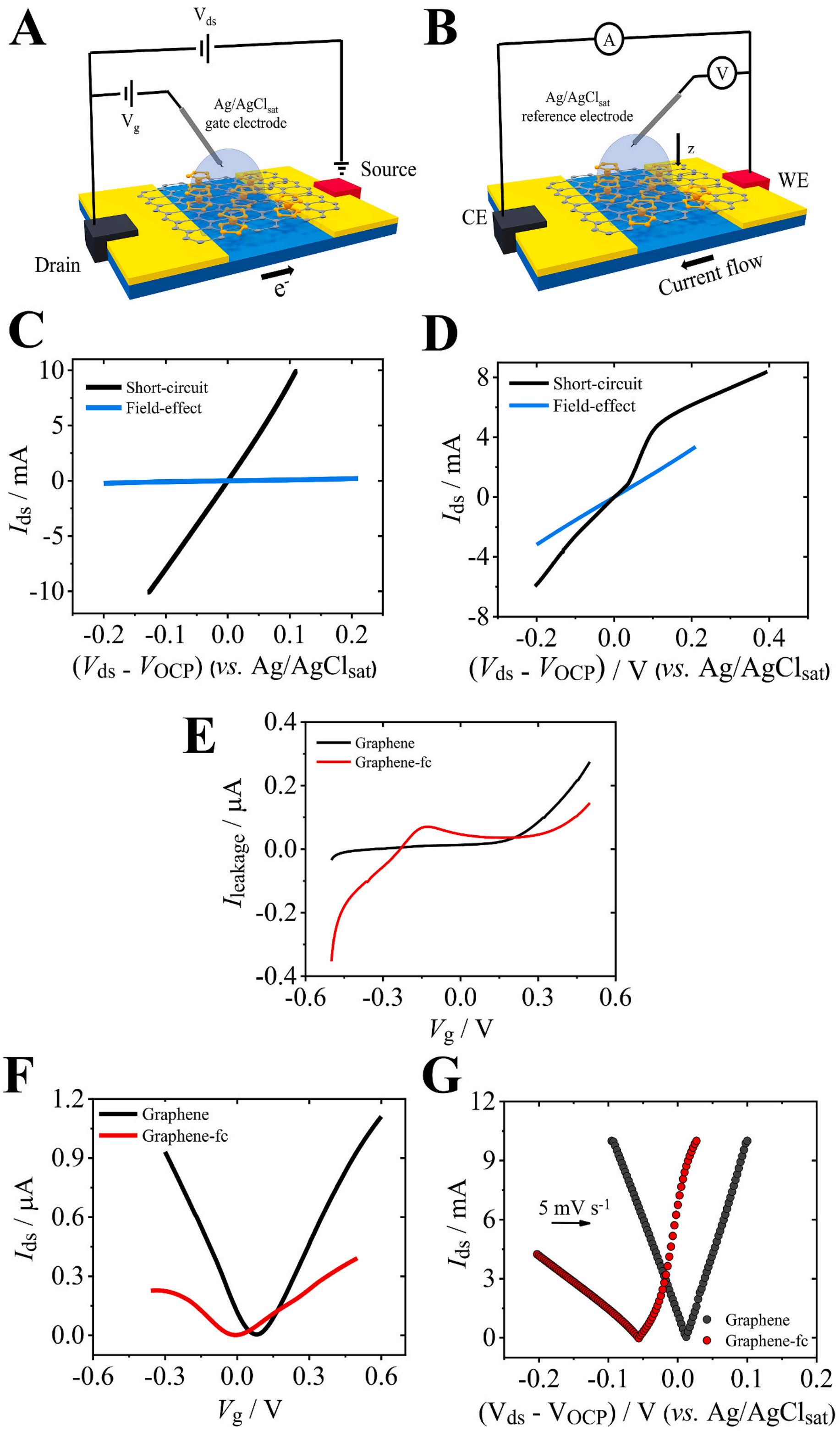

Fig. 2. EEVD electrical-electrochemical performance A) Schematic of GFET setup with graphene-fc interface. The represented setup is also valid for the bare graphene interface; B) Representative schematic of EEVD configuration with graphene-fc interface. This setup is also valid for the bare graphene interface; C) Output curves of bare graphene EEVDs in a 0.1 mol L^{-1} phosphate buffer solution (PBS) (pH 7.2) under (black) short-circuit conditions at 5 mV s^{-1} and (blue) field-effect conditions with $V_g = 0$ V (*vs.* Ag/AgCl$_{sat}$); D) Output curves of graphene-fc EEVDs in a 0.1 mol L^{-1} phosphate buffer (pH 7.2) under (black) short-circuit conditions at 5 mV s^{-1} and (blue) field-effect conditions with $V_g = 0$ V (*vs.* Ag/AgCl$_{sat}$); E) Leakage current plot for graphene (black) and graphene-fc (red) interfaces in 0.01 mol L^{-1} PBS (pH 7.4) under $V_{ds} = 0.01$ V using Ag/AgCl$_{sat}$ as the gate electrode; F) Transfer curves (under field-effect) obtained using graphene (black) and graphene-fc (red) in 0.01 mol L^{-1} PBS (pH 7.4). All experiments used $V_{ds} = 0.01$ V; G) Short-circuit profiles after direct inversion of current signals with bare graphene (black) and graphene-fc (red) heterojunctions in a 0.10 mol L^{-1} phosphate buffer solution (pH 7.2).

Energy and Materials Research (CNPEM, Campinas, Brazil). A NeaSNOM Microscope (Neaspec) located on the IR1 beamline was used.

2.7. Field-effect experiments

For the field-effect experiments, graphene and graphene-fc devices were used. A drop of 40 μL of 0.01 mol L^{-1} phosphate buffered saline solution (pH 7.4) was used as the electrolyte gate. A droplet of ferrocene was deposited onto the surface of the graphene, which was stabilized by cyclic voltammetry. I_{ds} *vs.* V_{ds} (I_{ds} = drain-source current; V_{ds} = drain-source voltage) experiments were carried out from −0.2 V to 0.2 V, and for the bare graphene interface, specifically, a narrower potential range was also investigated (from −0.05 to 0.05 V). The gate voltage (V_g) was swept from −0.3 V to 0.5 V (*vs.* Ag/AgCl$_{sat}$) for all I_{ds} *vs.* V_g experiments. For different evaluations using a bare graphene device, V_{ds} values of 0.01, 0.02, 0.03, 0.04, 0.05, 0.075, and 0.1 V were applied (Section 3 of ESI).

3. Results and discussions

3.1. EEVD working principles

Fig. 1B illustrates the working principles of our novel device in comparison to the conventional field-effect device (Fig. 1C). The EEVD is composed of two terminals: working and auxiliary electrodes. These two electrodes are in a short-circuit configuration and are analogous to the drain and source in a GFET device. However, by using a potentiostat, a controlled overpotential can be applied to the working electrode versus a reference electrode (Ag/AgCl$_{sat}$). When a negative potential is applied to the working electrode, current flows from the working electrode to the auxiliary electrode and flows in the opposite direction upon application of a positive potential. As the device is in a short-circuit configuration, current flows through the graphene's basal plane, thus connecting the working and auxiliary terminals. Under these conditions, current overload is expected during a potential sweep, especially because of the high basal plane conductivity of graphene. However, in an EEVD, graphene is supported on SiO_2/Si and its basal plane is connected electrochemically to the ferrocene and the supporting electrolyte. Therefore, a certain degree of loss in basal plane conduction is expected (Wang et al., 2012). In this configuration, working and auxiliary electrodes polarize the graphene surface that is in contact with the ferrocene and electrolyte in the vertical plane, and a new current type arises from the interface (the *z* current). Consequently, an additional charge is inserted into the graphene. This additional charge is added to the electric current generated by the movement of electrons and holes in the *xy* plane of the graphene, resulting in a significant increase in the total measured current. Because the *z* current originates from the electrolyte and the graphene-fc interface, its contribution primarily arises from the faradaic current of the ferrocene redox center and the capacitive current from the electrolyte/electrode double-layer. Therefore, monitoring faradaic redox footprints by ferrocene adsorption as well as other redox probes, should prove useful in improving selectivity in graphene-based 2D devices, as observed in a previous study (Neubert et al., 2020).

While ferrocene electron transfer can be monitored on the *z*-axis, we expect that some features related to the graphene-fc interface can be inferred through interfacial potential (E_{int}) measurements using the EEVD approach. From an electrochemical point of view, we propose that the total interfacial potential of these devices can be described as a function of the individual contributions of graphene (E^{gr}_{int}), ferrocene (i.e., the resulting graphene-fc heterojunction, E^{fc}_{int}), double-layer (E_{DL}), and reference electrode (E_{ref}) potentials, as described by Eq. (1).

$$E_{int} = E^{gr}_{int} + E^{fc}_{int} + E_{DL} + E_{ref} \quad (1)$$

As the electrolyte concentration used in these studies is sufficiently high (0.1 mol L^{-1}), issues related to ionic strength are not significant with respect to the graphene interface, and the double-layer capacitance contributions of the electrolyte remain constant. Reference electrode contributions also remain the same throughout the experiments. Therefore, we can expect that any E_{int} alterations in EEVDs are due to interactions between the graphene and graphene-fc with external media, as indicated in Eq. (2).

$$E_{int} = E^{gr}_{int} + E^{fc}_{int} + E^{0}_{constant} \quad (2)$$

To confirm the premises related to EEVD working features, experiments were performed using the EEVD configuration (Fig. 2A) and were compared with the results obtained using the GFET configuration (Fig. 2B). Initially, I_{ds} *vs.* V_{ds} curves were recorded by sweeping the potential of the reference electrode of the EEVD and comparing these with the I_{ds} *vs.* V_{ds} curves recorded under Ag/AgCl$_{sat}$ electrolyte-gating at 0 V (Fig. 2C). This V_g was chosen after investigating different V_g values (as presented in Section 3 of ESI, Fig. S3A).

A remarkably higher I_{ds} current was obtained in the short-circuit setup in comparison to the conventional field-effect I_{ds} configuration for the bare graphene interfaces. The main difference between these two experimental setups involves the use of Ag/AgCl$_{sat}$. In the conventional GFET experiments, Ag/AgCl$_{sat}$ acts as a polarized top-gate electrode through the application of a pre-determined V_g, while V_{ds} is swept. For GFETs operating in the linear region, the application of V_g controls the channel resistance, and I_{ds} should increase linearly with V_g (Misra and Öztürk, 2005). The application of this external electrical field modulates the channel conductivity. In the short-circuit configuration, Ag/AgCl$_{sat}$ is no longer polarized and in contrast to the GFET configuration, channel conductivity is no longer controlled. Therefore, the observed current does not include a field-effect contribution. The V_{ds} sweep is performed under potential control through a Ag/AgCl$_{sat}$ reference electrode, similar to electrochemical three-electrode conventional cells. Its contribution to the system potential is then its intrinsic electrochemical half-cell potential of ~0.197 V *vs.* a standard hydrogen electrode (Bard and Faulkner, 2001). In addition, the variation in the applied potential on a semiconductor is known to alter the surface charge carrier concentration (Batchelor and Hamnett, 1992). The graphene sheet resistivity (R_s) reached in each setup was also investigated. Differences in sheet resistivity between source and drain due to the lack of channel conductivity modulation are clearly observed when the expression $R_s = [(V_{ds}/j_{ds})\ (W/L)]$ (Kim and Frisbie, 2014) is applied to both I_{ds} *vs.* V_{ds} curves, such that $R_s = 0.34\ \Omega\ cm^{-2}$ while $R_s = 22.8\ \Omega\ cm^{-2}$ in the short-circuit and field-effect experiments, respectively. In addition, R_s can be described in terms of the contact resistance of the metal/graphene contacts ($R_{contact}$) and $1/ne\mu$, where n is the charge carrier concentration, e is the elementary charge, and μ is the charge carrier mobility (Kim and Frisbie, 2014). Therefore, the achieved charge carrier mobility in each setup plays an important role in the sheet resistance obtained. When the short-circuit channel conductivity without external modulation is explored, higher charge carrier mobility can be reached, justifying the higher I_{ds} values obtained using the proposed setup. Owing to the low resistivity of graphene-SiO_2 interfaces, the adsorption of extra layers onto the graphene is assumed to modulate its behavior in I_{ds} *vs.* V_{ds} curves.

After investigating channel resistance modifications, we proceeded to investigate the behavior of EEVDs using different scan rates (Fig. S5). The scan rate was varied and the short-circuit I_{ds} was recorded; however, a decrease in I_{ds} for a fixed V_{ds} value with increasing V_{ds} scan rate was observed. It was also observed that for $I_{ds} = 0$, V_{ds} reached the OCP value for all studied scan rates, as expected. OCP is a mixed potential that does not describe a thermodynamic equilibrium, and instead indicates the case in which the overall electrochemical current is zero (Lefrou et al., 2009). In semiconductor electrochemistry, OCP is also regarded as a condition in which the sum of the electron and hole currents (i_e, i_p) is zero (Zhang, 2005). However, changes in the OCP value with respect to the scan rate can be observed in Fig. S5 and are intriguing. To further understand this, the meaning of the applied V_{ds} in a semiconductor heterojunction needs to be clarified. In general, V_{ds} can be expressed in terms of the flatband potential, V_{fb}, and the potential drop in the space charge layer, V_s, by the expression $V_{ds} = V_{fb} + V_s$ (Zhang, 2005). V_{fb} is related to the condition in which the semiconductor does not present an excess charge or produce redox potentials at the band edges. The latter expression is still valid in the absence of external polarization, i.e., where V_{ds} = OCP. Thus, the OCP potential also depends on band bending and space charge layer characteristics (Zhang, 2005). Expanding this concept to EEVDs, we can confirm that both V_{fb} and V_s are inserted into the graphene (E_{int}^{gr}) and graphene-fc (E_{int}^{fc}) contributions to the total interfacial potential E_{int} of our system. This means that any change in V_s due to alterations in the surface charge layer width or capacitance will influence the OCP value. In fact, for semiconductors with an equivalent circuit containing a RC element, the dependence of space charge capacitance has been previously reported (Batchelor and Hamnett, 1992). This dependence was observed not only for potential sweep scan rates but also for any prepolarization to which the semiconductor electrode has been submitted (Batchelor and Hamnett, 1992). Thus, what is expected for electrochemically active surfaces is confirmed for graphene and graphene-fc heterojunctions. To obtain higher I_{ds} currents and minimize the mentioned charge effects (either by trapping or capacitance), we continued our studies using a fixed sweep rate of 5 mV s^{-1}.

The data obtained so far has provided information regarding the graphene monolayer interface and its behavior on non-electroactive media. To study the effect of the presence of a redox pair (i.e., faradaic processes) and its contributions to EEVD behavior, graphene was non-covalently modified with ferrocene. Although electron transfer processes from adsorbed species onto semiconductors are typically considered negligible (Zhang, 2005), ferrocene was chosen because of its well-known $\pi-\pi$ stacking with graphene, and its electronic coupling with graphene through charge carrier insertion (Zribi et al., 2019). A surface excess of 5.3×10^{-12} mol cm^{-2} was obtained by using the equation reported in the literature (Section 5 of ESI) after electrochemical stabilization of the graphene-fc interface in KCl (Section 6, Fig. S6A). Similar to the procedure adopted for bare graphene EEVDs, I_{ds} vs. V_{ds} curves were acquired for the graphene-fc interface under both field-effect and short-circuit conditions (Fig. 2D) after optimization of V_g (0 V) (Fig. S3B). Despite the increased current intensity, as observed with bare graphene devices, a voltammetric-like profile was observed for I_{ds} curves obtained under short-circuit conditions with an oxidation peak at approximately 0.14 V (*vs.* Ag/AgCl$_{sat}$). Toward more negative potentials, a reduction peak at 0.10 V (*vs.* Ag/AgCl$_{sat}$) was observed (Fig. S7). Three output curves were obtained in each potential direction, and the positions of the oxidation and reduction peaks remained stable. After comparison with cyclic voltammetry profiles obtained with the same graphene-fc interface (Fig. S6B), these peaks were attributed to ferrocene owing to its electron-transfer capability along the z-axis, which is absent in pure field-effect experiments. Additionally, the peak current intensities of the ferrocene/ferrocenium pair obtained in conventional cyclic voltammetry (Fig. S6B) and short-circuit approach (Fig. 2D) were compared, and a remarkable increase in current density under short-circuit conditions was obtained. This suggests that the coupling of a redox probe led to a Si/SiO$_2$-graphene-fc heterojunction with electron transfer along the z-axis, which can amplify the electrochemical responses. We also inferred that the intensity of these peaks and the shape of the I_{ds} *vs.* V_{ds} short-circuit curves depend strongly on the excess of ferrocene on the graphene surface. This is similar to what is observed in the I *vs.* V curves (voltammograms) of electroactive adsorbed layers (Eq. (S2)) (Bard and Faulkner, 2001). Sheet resistivity was also evaluated using the expression $R_s = [(V_{ds}/j_{ds})\ (W/L)]$ (Kim and Frisbie, 2014), where $R_s = 0.45\ \Omega\ cm^{-2}$ and $1.39\ \Omega\ cm^{-2}$ for current flow in the short-circuit and field-effect configurations, respectively. To ensure the occurrence of this redox phenomenon at the graphene-fc interface through the z current, we investigated the leakage current profile of graphene and graphene-fc interfaces as a function of gate potential sweeps with Ag/AgCl$_{sat}$ used as the gate electrode in the GFET configuration (Fig. 2E). In this setup, the leakage current is similar to the z current of the EEVD. This refers to the current flowing between the graphene drain terminal and the Ag/AgCl$_{sat}$ gate. As expected, a peak current was observed for graphene-fc, which was attributed to ferrocene oxidation. However, differences in peak potential were due to the different uses of Ag/AgCl$_{sat}$ as either the electrochemical reference electrode or gate electrode. Discrepancies in current intensities were also attributed to the application of different setups, as discussed above. These observations provided insights on how vertical electron transfer processes and interfacial features influence the basal plane graphene's properties. Therefore, unprecedented applications of short-circuit setups to study electrochemical processes are possible. By using pristine graphene EEVDs, the sluggish electron transfer kinetic characteristics can be overcome (Brownson et al., 2014; Macedo et al, 2018, 2019).

3.2. *Comparison of EEVDs and GFETs electrical behavior*

After confirming the redox and capacitive features of the graphene-fc heterojunctions under short-circuit conditions, we compared the EEVD and GFET transfer curve profiles obtained by each setup. We also evaluated the suitability of EEVDs as an alternative to GFETs. To accomplish this, field-effect I_{ds} *vs.* V_g transfer curves under gate voltage sweeps (Fig. 2F) and short-circuit curves (Fig. 2G) were obtained. In each case, different Ag/AgCl$_{sat}$ applications and potential sweep mechanisms were adopted, as shown in Fig. 2A and B. To clarify these alterations, signal modifications of the I_{ds} *vs.* V_{ds} plots as shown in Fig. 2G were taken and the resulting curves presented a profile quite similar to those obtained for the field-effect experiments (see Section 8 of ESI for original short-circuit curves). To fully understand and characterize the GFET platforms with graphene and graphene-fc interfaces, several relevant parameters such as gate capacitance (C_g), double-layer capacitance (C_{dl}), quantum capacitance (C_q) charge carrier mobility (μ), doping (n), and transconductance (g_m) were evaluated (see Section 9 of ESI, Table S1). Under typical field-effect conditions, a shift in the CNP (ΔV) due to the adsorption of ferrocene was observed, corresponding to a value of $\Delta V = -0.057$ V. The observed shift for more negative V_g potentials was attributed to n doping (Vieira et al., 2016), probably due to cyclopentadienyl ring electronic density donation to graphene during graphene and fc coupling. Interestingly, after comparing the GFET transfer curves to the EEVD short-circuit I_{ds} vs. V_{ds} transfer curves, a similar profile was obtained. In this case, OCP shifts were observed owing to space charge capacitance changes promoted by the adsorption of fc, which can be interpreted as surface states (Batchelor and Hamnett, 1992; Zhang, 2005). The magnitude of OCP displacement was $\Delta V = -0.065$ V after ferrocene modification. The obtained ΔV values were very similar for both GFETs and EEVDs, indicating that the proposed EEVD devices are suitable for doping and charge carrier-related studies. Because OCP and surface charge capacitance are related (Batchelor and Hamnett, 1992; Zhang, 2005), the reasons for ΔV deviations between the devices may occur because of local capacitive changes due to ferrocene adsorption on some active sites on graphene, although some capacitance parameters (e. g., C_{dl} and C_g) in Table S1 exhibit no relevant changes. This is, therefore, the objective of further studies to completely understand the capacitance changes under short-circuit conditions. The comparison of OCP shifts with those of CNP, however, requires further interpretation of the origin of OCP. It is known that CNP shifts are related to charge carrier insertion on graphene and can also be correlated to capacitive features (Reiner-Rozman et al., 2015; Vieira et al., 2016), as already discussed. Nonetheless, the theoretical treatment of CNP cannot be applied in our experiments because they were not realized under field-effect conditions, as evidenced by 1) the use of Ag/AgCl$_{sat}$ as a reference electrode and not a gate electrode; and 2)

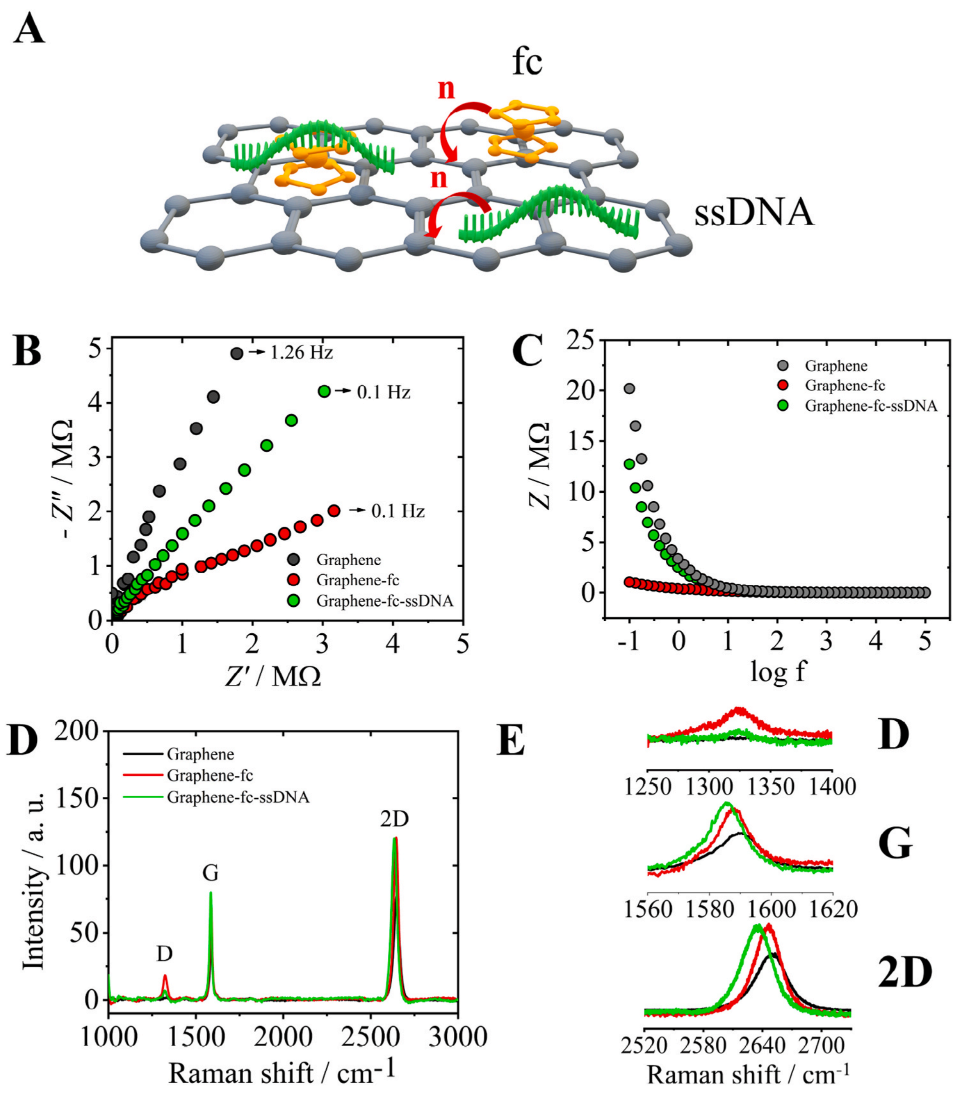

Fig. 3. ssDNA adsorption based on graphene-fc characterization A) Schematic representation of graphene-fc heterojunctions formed by van der Waals adsorption of ferrocene and ssDNA adsorption and its *n* doping on graphene; B) Nyquist plots for bare graphene (black), graphene-fc (red), graphene-fc-ssDNA (green) interfaces from 1.10^5 Hz to 0.1 Hz, under the OCP potential of each surface (OCP ~ 0.13 V), in a 0.10 mol L^{-1} phosphate buffer solution (pH 7.2) and potential amplitude of 0.005 V; C) Impedance modulus *vs.* applied frequency logarithm plot for bare graphene (black, onset frequency ~ 4.6 Hz), graphene-fc (red) and graphene-fc-ssDNA (green, onset frequency ~ 7.4 Hz); D) Raman spectra for graphene (black), graphene-fc (red), and graphene-fc-ssDNA (green) surfaces; E) Close-ups of D band; G band, and 2D band shifts obtained for each interface

potential sweeping from drain to source terminals and not on the gate electrode. However, charge carrier insertion and OCP potentials are frequently related by assuming a Schottky barrier junction formation in the context of semiconductors and Schottky heterojunctions for solar cells (Behura et al., 2013), which is clearly not the case here. In addition, the experiments were not performed under photovoltaic conditions, and therefore Schottky barrier formation can be overcome by vdW heterojunctions (Liu et al., 2016) using graphene-fc. Thus, the theoretical basis for graphene solar cells could not be applied to interpret these results. There is a need for further theoretical studies involving OCP, charge carriers, and capacitance changes under short-circuit conditions and without a photovoltaic experimental setup to correlate these experimental observations.

3.3. Characterization of graphene-fc and graphene-fc-ssDNA heterojunctions

Many of the observations discussed above rely on the redox behavior of the graphene-fc interface and its vertical electron transfer characteristics arising from the adsorption of the electroactive ferrocene layer. To prove these features of the heterojunction, further investigations were performed using EIS. We also demonstrated the occurrence of *n* doping by ferrocene on graphene through Raman spectroscopy, as also observed based on CNP shifts. In addition, the adsorption of ssDNA on the graphene-fc interface was investigated (Fig. 3A) to provide proof-of-concept and some analytical quantifications for EEVDs as an alternative to GFETs in biosensing technology.

We studied the electrochemical interfacial characteristics of graphene, graphene-fc, and graphene-fc heterojunction after adsorption of ssDNA (graphene-fc-ssDNA) through EIS. As ssDNA is a negatively charged biomolecule at pH 7.2 (Sherbet et al., 1983) and does not exhibit electron-transfer processes in pristine graphene-based electrodes, we inferred that its adsorption onto graphene-fc would lead only to capacitive changes. Our intent here is to confirm the redox behavior of the graphene-fc interface, as already mentioned, as well as to evaluate the capacitive features of the graphene-fc-ssDNA interface. The Nyquist plots (Fig. 3B) show that bare graphene exhibits pure capacitive behavior, with R_{ct} tending to infinity in the absence of an electroactive species (Barsoukov and Macdonald, 2005). The graphene-fc interface presented an incomplete semicircle whose diameter is related to the electron transfer resistance of the adsorbed ferrocene/ferrocenium redox pair. The observation of these electron-transfer phenomena confirmed the behavior of the graphene-fc interface as an electroactive vdW heterojunction on the *z*-axis (i.e., vertical electron transfer). As expected, the adsorption of ssDNA demonstrates purely capacitive effects on the graphene-fc-ssDNA interface based on experimental evidence based on the disappearance of the semicircle in the Nyquist plot recorded for fc adsorbed on graphene. Simulation using the most suitable equivalent circuit for graphene-fc and graphene-fc-ssDNA was performed considering previous modeling reported elsewhere (Bard and

Faulkner, 2001). From the most suitable circuit simulation, C_{dl} values could be evaluated (Section 10 of ESI). The C_{dl} values obtained for all interfaces studied are in agreement with the Helmholtz double-layer capacitance model applied to the electrochemical behavior of semiconductors (Zhang, 2005). This suggests that capacitance effects are indeed present on the graphene heterojunctions after adsorption of ssDNA. Therefore, the presence of capacitance contributions in each heterojunction becomes clearer when the total interfacial impedance modulus (Z) is plotted versus the frequency logarithm (Fig. 3C). While electron transfer resistance effects are notably pronounced in high-frequency regions of the impedance spectra, capacitive behavior is highlighted in low-frequency regions (Barsoukov and Macdonald, 2005). Graphene-fc curves do not exhibit a remarkable increase in the impedance modulus in lower frequency regions, indicating that double-layer capacitance effects may be negligible on this interface. However, non-electroactive interfaces such as bare graphene and graphene-fc-ssDNA presented a remarkable increase in the impedance modulus in lower frequency regions, corroborating their capacitive features. In addition, the latter heterojunctions presented similar values of onset frequencies in the impedance modulus curves, from which capacitive contributions become more evident and agree with previous data (reported in Section 9 of ESI) that were obtained through field-effect experiments using these interfaces). These data suggest that EEVDs can be successfully employed for the detection of ssDNA through adsorptive strategies and OCP shift monitoring, as these phenomena are reflected by the capacitive features of the interfaces.

Raman spectroscopy was then applied for graphene-fc and graphene-fc-ssDNA heterojunction characterization (Fig. 3D) as well as to obtain information regarding the occurrence of band-gap opening at these interfaces (see Section 11 of ESI). The bottom-line interface, graphene supported on SiO_2/Si, is automatically p-doped owing to the remaining atmospheric impurities and thermal annealing under Ar at high temperatures (Nourbakhsh et al., 2010; Wang et al., 2012). The adsorption of ferrocene on graphene leads to a band-gap opening resulting from doping, allowing the evaluation of Fermi levels (E_F) of the doped interfaces (Zribi et al., 2019). Values of E_F were evaluated from the Raman data of graphene-fc and graphene-fc-ssDNA using Eq. (3), where $\Delta(\omega)G$ is the difference between the G band frequencies of modified and pristine graphene (Wu et al., 2018). The charge carrier concentrations inserted by ferrocene and ssDNA were estimated using Eq. (4).

$$E_F = \frac{\Delta(\omega)G}{21} \tag{3}$$

$$E_F = \hbar\, v_F\, (\pi n)^{1/2} \tag{4}$$

The resulting parameters are listed in Table S2. From Fig. 3E, red-shifts of the G and 2D bands indicate the insertion of charge carriers in the heterojunction by ferrocene, leading to n-type doping. Although ferrocene is a neutral molecule with a Fe^{2+} metallic center, charge carriers were inserted by electronic donation of its cyclopentadienyl rings resulting from π−π stacking, as already mentioned. From the Raman data obtained after adsorption of 1.0 fmol L^{-1} ssDNA, it is apparent that charge carriers were also inserted, leading to n-type doping owing to the negative charge of ssDNA molecules and to π−π stacking, as expected (Husale et al., 2010; Zhang and Zhou, 2001). Further evidence of n-type doping with the addition of ferrocene and ssDNA layers was the decrease in the I_{2D}/I_G ratio, as previously reported in the literature (Wu et al., 2018). These data agree with the previous results obtained for both GFETs and our novel EEVDs. This indicates that the OCP shifts (i.e., E_{int}) obtained using the latter setup can also be interpreted as an indicator of doping occurrence in graphene-fc interfaces. It is important to mention that other than the pristine monolayer graphene experiments, no gate potential was applied during Raman experiments; thus, the observed charge carrier insertion occurs solely because of chemical doping. Therefore, the resulting heterojunctions are p-n for graphene-fc, and p-n-n for graphene-fc-ssDNA.

3.4. Proof-of-concept of EEVDs as biosensing devices

Next, we performed ssDNA detection using EEVDs based on the graphene-fc interface. In this case, a miniaturized setup with a 40 μL volume of electrolyte was employed (Fig. 4A and B). OCP variations were calculated as a function of ssDNA concentration according to Eq. (5).

$$\Delta_{OCP} = E_{int} = E_{int}^{fc-ssDNA} - E_{int}^{fc} \tag{5}$$

OCP variations (Δ_{OCP}) of the graphene-fc heterojunction regarding the adsorption of ssDNA were monitored over a wide range of sub-micromolar concentrations (Fig. 4C). We observed that ssDNA adsorption at 1.0 amol L^{-1} (atto-molar concentration) can alter the OCP

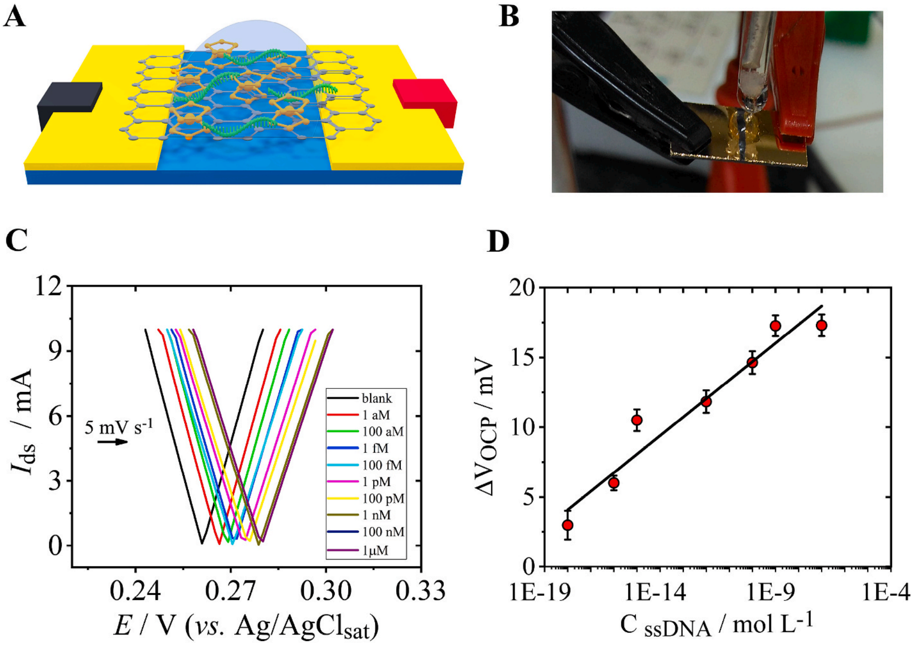

Fig. 4. ssDNA on drop detection A) Schematic representation of ssDNA adsorption onto EEVDs using a graphene-fc vdW heterojunction; B) Photograph of EEVD analysis on a drop setup during ssDNA detection; C) I_{ds} *vs.* V_{ds} plots of graphene-fc EEVDs under adsorption of ssDNA in a 1 amol L^{-1} – 1 μmol L^{-1} concentration range; D) Variation of OCP potential as a function of ssDNA adsorption in a 1.0 amol L^{-1} – 1 μmol L^{-1} concentration range (in 0.10 mol L^{-1} phosphate buffer solution: pH 7.2) for graphene-fc EEVD with n = 3.

potential, indicating the enhanced sensitivity of EEVDs.

By using graphene-fc EEVDs, an unprecedented LOD of 5.1×10^{-21} mol L^{-1} was reached for ssDNA detection at atto-molar concentrations. To obtain the LOD, the noise of the EEVDs was estimated and evaluations were made using the SD (Standard Deviation) of the lowest concentration measured. According to the literature, this approach relies on the signal-to-noise ratio of the device and proves the presence of analyte in the test sample with a probability greater than 99% (Brunetti B, 2015; Inczedy et al., 1998). Other reports in the literature also reached zepto-molar concentrations for LOD using graphene devices (Ganguli et al., 2020; Hwang et al., 2020). However, in these reports, specific DNA fragments were detected through DNA fragment amplification (Ganguli et al., 2020), and functionalization of graphene with specific DNA probes (Hwang et al., 2020). Although the methodology presented here can be considered simpler, robust, and more cost-effective than other approaches, it is important to consider that further studies to improve the selectivity and robustness of EEVDs are needed for analyses of real samples and development of reliable analytical methods. EEVDs exhibit an improved performance when compared to other non-graphene-based biosensors for ssDNA detection using electrochemical (Li et al., 2019) and electrical (Thangaraj et al., 2016) detection.

The sensitivity of graphene-fc EEVD for ssDNA biosensing was 1.3 mV/decade. This sensitivity is lower than that reported in the literature for other graphene-based devices (Campos et al., 2019). Low sensitivities were obtained for crumpled GFETs with respect to simple double-stranded DNA physisorption (~6 mV of potential shift for 12 decades, i.e., from 10^{-18} to 10^{-6} mol L^{-1}) (Ganguli et al., 2020). Based on the Ganguli study, low sensitivity values generally indicate that DNA-based molecules do not strongly adsorb onto the graphene-fc interface. Sensitivity would improve with further functionalization techniques or additional amplification steps.

In addition, the graphene-fc heterojunction also exhibited improved linearity in OCP variations with ssDNA concentration, with a dynamic range of up to 10^9. This range is five orders of magnitude greater than that achieved with the GFET system proposed by Campos (Campos et al., 2019). This suggests that an EEVD with the latter heterojunction may be more suitable for the development of a proper analytical methodology for future analytical quantifications.

The possibility of detecting atto-molar or sub-atto-molar concentrations using graphene monolayer interfaces has been scarcely explored in the literature. Most of the reports focus on graphene-based field-effect devices with structural modifications (Basu and Roychaudhuri, 2016; Hwang et al., 2020). The preliminary results using the proposed EEVDs are comparable to those obtained elsewhere using conventional GFETs (Campos et al., 2019; Hwang et al., 2020), which are known for their remarkable sensitivity. However, contrary to the aforementioned reports, the use of EEVDs in this work did not consider graphene modifications for enhanced selectivity, as reported by Campos and by Hwang (Campos et al., 2019; Hwang et al., 2020). To improve the selectivity in ssDNA detection, non-covalent functionalization of graphene-fc vdW heterojunctions is mandatory. Immobilization of a probe DNA strand onto graphene-fc is a simple strategy that can be performed (Hassan et al., 2020), and ssDNA quantification through in situ DNA hybridization can be successfully performed. Other successful strategies previously reported in the literature can be used as well. As an example, the immobilization of peptide nucleic bases onto graphene has proven successful (Cai et al, 2014, 2015). Immobilization of biotinylated DNA probes (Abad-Valle et al., 2007) onto graphene-fc heterojunctions can be considered as well, leading to the development of genosensors based on EEVD architectures. If properly validated, these devices can be applied for ssDNA detection in biological media containing proteins, whole cells, and other components of such complex matrices.

Therefore, by combining these selectivity strategies with an EEVD, it is possible to predict the successful development of unprecedented miniaturized robust electroanalytical methodologies for a wide range of samples using a limited volume, such as blood, serum, and plasma, with high sensitivity, selectivity, rapid analysis, low generation of residues, and cost-effectiveness. The increased drain-source current density obtained with EEVDs enables the monitoring of redox processes and label-free detection of biomolecules at extremely low concentrations. These findings open the way for the emergence of new electrochemical approaches toward more sensitive and stable graphene devices with electrical and electrochemical hybrid detection mechanisms.

4. Conclusions

In this study, we proposed a new short-circuit setup for hybrid electrochemical applications that provides basal plane current flow contributions, using a novel graphene-fc heterojunction. Contrary to field-effect experiments, Ag/$AgCl_{sat}$ is not polarized by potential sweeping, thus approximating our setup to that of a pure vertical electron transfer electrochemical process. Short-circuiting source and drain terminals allowed us to obtain remarkably higher currents through the basal plane graphene electron conductivity, which was not modulated by an external field (as would be the case in field-effect approaches). As expected, faradaic electron transfer processes could be successfully monitored in short-circuit setups owing to ferrocene adsorption, as evidenced by Nyquist EIS plots and the appearance of ferrocene oxidation and reduction peaks in short-circuit sweeps. This proved to be useful in the study of adsorbed redox molecules present in low excess quantities on a surface, as in the case of the graphene-fc interface. Furthermore, capacitance changes caused by ssDNA adsorption were also investigated, and we found that the OCP potential can be applied as a target parameter for monitoring some interfacial features of graphene-fc heterojunctions under short-circuit conditions. Using this novel setup, we were able to reach an LOD of 5×10^{-21} mol L^{-1} for ssDNA detection. Although in-depth discussions regarding the experimental observations were made, further theoretical developments will be necessary to fully understand EEVD behavior. Although ssDNA detection in real samples has not been performed in this study, studies regarding its applicability, reproducibility, and selectivity in complex media are of great importance and are being carried out.

CRediT authorship contribution statement

Isabela A. Mattioli: Conceptualization, Data curation, Formal analysis, Investigation, Methodology, Project administration, Validation, Visualization, Roles, Writing - original draft, Writing - review & editing. **Ayaz Hassan:** Data curation, Formal analysis, Investigation, Methodology, Visualization, Roles, Writing - original draft, Writing - review & editing. **Natalia M. Sanches:** Data curation, Formal analysis, Investigation, Methodology, Visualization, Roles, Writing - original draft, Writing - review & editing. **Nirton C.S. Vieira:** Formal analysis, Funding acquisition, Methodology, Resources, Supervision, Visualization, Roles, Writing - original draft, Writing - review & editing. **Frank N. Crespilho:** Conceptualization, Formal analysis, Funding acquisition, Investigation, Methodology, Project administration, Resources, Supervision, Validation, Visualization, Roles, Writing - original draft, Writing - review & editing.

Declaration of competing interest

The authors declare that they have no known competing financial interests or personal relationships that could have appeared to influence the work reported in this paper.

Acknowledgments

The authors appreciate the financial support from the São Paulo Research Foundation (FAPESP) (19/15333-1, 19/12053-8, 18/22214-6, 18/11071-0, 18/07508-3, and 17/20493-2), Coordinating Agency for

Advanced Training of Graduate Personnel (CAPES, Financial Code no 001, grant no 88887.358060/2019-00 of the PNPD program and MeDiCo Network CAPES Brazil, grant no.88881.504532/2020–01), and National Council of Scientific and Technological Development (CNPq grant no 305486/2019-5).

Abbreviations

EEVD	electrical-electrochemical vertical device
GFET	graphene field-effect transistor
ssDNA	single-stranded DNA
fc	ferrocene
CNP	charge neutrality point
OCP	open-circuit potential
EIS	electrochemical impedance spectroscopy
CVD	chemical vapor deposition; and vdW, van der Waals

Appendix A. Supplementary data

Supplementary data to this article can be found online at https://doi.org/10.1016/j.bios.2020.112851.

References

Abad-Valle, P., Fernández-Abedul, M.T., Costa-García, A., 2007. Biosens. Bioelectron. 22, 1642–1650. https://doi.org/10.1016/j.bios.2006.07.015.

Bantele, S.C.S., Lisby, M., Pfander, B., 2019. Nat. Commun. 10, 1–12. https://doi.org/10.1038/s41467-019-08889-5.

Bard, A.J., Faulkner, L.R., 2001, second ed. John Wiley & Sons, New York.

Barsoukov, E., Macdonald, J.R., 2005. John Wiley & Sons, Hoboken, New Jersey. https://doi.org/10.1002/0471716243.

Basu, J., Roychaudhuri, C., 2016. IEEE Electron. Device Lett. 37, 492–495. https://doi.org/10.1109/LED.2017.2655545.

Batchelor, R.A., Hamnett, A., 1992. In: Bockris, J.O., Conway, B.E., White, R.E. (Eds.), Appl. Phys. A Mater. Sci. Process., vol. 111. Springer Science & Business Media LLC, pp. 1159–1163. https://doi.org/10.1007/s00339-012-7335-2.

Behura, S.K., Mahala, P., Ray, A., Mukhopadhyay, I., Jani, O., 2013. Appl. Phys. A Mater. Sci. Process. 111, 1159–1163. https://doi.org/10.1007/s00339-012-7335-2.

Brownson, D.A.C., Varey, S.A., Hussain, F., Haigh, S.J., Banks, C.E., 2014. Nanoscale 6, 1607–1621. https://doi.org/10.1039/c3nr05643k.

Brunetti B, D.E., 2015. Pharm. Anal. Acta. https://doi.org/10.4172/2153-2435.1000355, 06.

Cai, B., Huang, L., Zhang, H., Sun, Z., Zhang, Z., Zhang, G.J., 2015. Biosens. Bioelectron. 74, 329–334. https://doi.org/10.1016/j.bios.2015.06.068.

Cai, B., Wang, S., Huang, L., Ning, Y., Zhang, Z., Zhang, G.J., 2014. ACS Nano 8, 2632–2638. https://doi.org/10.1021/nn4063424.

Campos, R., Borme, J., Guerreiro, J.R., Machado, G., Cerqueira, M.F., Petrovykh, D.Y., Alpuim, P., 2019. ACS Sensors. https://doi.org/10.1021/acssensors.8b00344.

Cinti, S., Proietti, E., Casotto, F., Moscone, D., Arduini, F., 2018. Anal. Chem. 90, 13680–13686. https://doi.org/10.1021/acs.analchem.8b04052.

Damase, T.R., Ellington, A.D., Allen, P.B., 2017. Bio Technol. 275–282. https://doi.org/10.2144/000114557.

Dontschuk, N., Stacey, A., Tadich, A., Rietwyk, K.J., Schenk, A., Edmonds, M.T., Shimoni, O., Pakes, C.I., Prawer, S., Cervenka, J., 2015. Nat. Commun. 6 https://doi.org/10.1038/ncomms7563.

Eissa, S., Jimenez, G.C., Mahvash, F., Guermoune, A., Tlili, C., Szkopek, T., Zourob, M., Siaj, M., 2015. Nano Res 8, 1698–1709. https://doi.org/10.1007/s12274-014-0671-0.

Fu, W., Feng, L., Panaitov, G., Kireev, D., Mayer, D., Offenhäusser, A., Krause, H.J., 2017. Sci. Adv. 3, 1–8. https://doi.org/10.1126/sciadv.1701247.

Ganguli, A., Faramarzi, V., Mostafa, A., Hwang, M.T., You, S., Bashir, R., 2020. Adv. Funct. Mater. 2001031, 1–9. https://doi.org/10.1002/adfm.202001031.

Gao, Y., Hu, G., Zhang, W., Ma, D., Bao, X., 2011. Dalton Trans. 40, 4542–4547. https://doi.org/10.1039/c0dt01392g.

Hassan, A., Macedo, L.J.A., Mattioli, I.A., Rubira, R.J.G., Constantino, C.J.L., Lima, F.C.D.A., Crespilho, F.N., 2020. chemRxiv 1–22.

Husale, B.S., Sahoo, S., Radenovic, A., Traversi, F., Annibale, P., Kis, A., 2010. Langmuir 26, 18078–18082. https://doi.org/10.1021/la102518t.

Hwang, M.T., Heiranian, M., Kim, Y., You, S., Leem, J., Taqieddin, A., Faramarzi, V., Jing, Y., Park, I., van der Zande, A.M., Nam, S., Aaluru, N.R., Bashir, R., 2020. Nat. Commun. 1543.

Inczedy, J., Lengyel, T., Ure, A.M., 1998. In: IUPAC Compendium on Analytical Nomenclature, Definitive Rules 1997. International Union of Pure and Applied Chemistry.

Iost, R.M., Crespilho, F.N., Zuccaro, L., Yu, H.K., Wodtke, A.M., Kern, K., Balasubramanian, K., 2014. ChemElectroChem 1, 2070–2074. https://doi.org/10.1002/celc.201402325.

Islam, S., Shukla, S., Bajpai, V.K., Han, Y.K., Huh, Y.S., Ghosh, A., Gandhi, S., 2019a. Sci. Rep. 9, 1–7. https://doi.org/10.1038/s41598-018-36746-w.

Islam, S., Shukla, S., Bajpai, V.K., Han, Y.K., Huh, Y.S., Kumar, A., Ghosh, A., Gandhi, S., 2019b. Biosens. Bioelectron. 126, 792–799. https://doi.org/10.1016/j.bios.2018.11.041.

Kim, C.H., Frisbie, C.D., 2014. J. Phys. Chem. C. https://doi.org/10.1021/jp505391u.

Kim, H.E., Schuck, A., Lee, J.H., Kim, Y.S., 2019. Sensor. Actuator. B Chem. 291, 96–101. https://doi.org/10.1016/j.snb.2019.03.080.

Kwak, Y.H., Choi, D.S., Kim, Y.N., Kim, H., Yoon, D.H., Ahn, S.S., Yang, J.W., Yang, W.S., Seo, S., 2012. Biosens. Bioelectron. 37, 82–87. https://doi.org/10.1016/j.bios.2012.04.042.

Lefrou, C., Fabry, P., Poignet, J.-C., 2009. Springer-Verlag Berlin Heidelberg.

Lei, Y.M., Xiao, M.M., Li, Y.T., Xu, L., Zhang, H., Zhang, Z.Y., Zhang, G.J., 2017. Biosens. Bioelectron. 91, 1–7. https://doi.org/10.1016/j.bios.2016.12.018.

Li, P.P., Liu, X.P., Mao, C.J., Jin, B.K., Zhu, J.J., 2019. Anal. Chim. Acta 1048, 42–49. https://doi.org/10.1016/j.aca.2018.09.063.

Lima, F.C.D.A., Calzolari, A., Caldas, M.J., Iost, R.M., Crespilho, F.N., Petrilli, H.M., 2014. J. Phys. Chem. C 118, 23111–23116. https://doi.org/10.1021/jp506425c.

Liu, Y., Stradins, P., Wei, S.H., 2016. Sci. Adv. 2, 1–7. https://doi.org/10.1126/sciadv.1600069.

Lonkar, S.P., Deshmukh, Y.S., Abdala, A.A., 2015. Nano Res 8, 1039–1074. https://doi.org/10.1007/s12274-014-0622-9.

Macedo, L.J.A., Iost, R.M., Hassan, A., Balasubramanian, K., Crespilho, F.N., 2019. ChemElectroChem 6, 31–59. https://doi.org/10.1002/celc.201800934.

Macedo, L.J.A., Lima, F.C.D.A., Amorim, R.G., Freitas, R.O., Yadav, A., Iost, R.M., Balasubramanian, K., Crespilho, F.N., 2018. Nanoscale 10, 15048–15057.

Misra, V., Öztürk, M.C., 2005, 109-126. https://doi.org/10.1016/B978-012170960-0/50012-8.

Neubert, T.J., Wehrhold, M., Kaya, N.S., Balasubramanian, K., 2020. Nanotechnology 31, 405201.

Nigar, S., Wang, H., Imtiaz, M., Yu, J., Zhou, Z., 2019. Appl. Surf. Sci. 481, 1466–1473. https://doi.org/10.1016/j.apsusc.2019.03.222.

Nourbakhsh, A., Cantoro, M., Klekachev, A., Clemente, F., Sorée, B., Van Der Veen, M.H., Vosch, T., Stesmans, A., Sels, B., De Gendt, S., 2010. J. Phys. Chem. C 114, 6894–6900. https://doi.org/10.1021/jp910085n.

Rabti, A., Mayorga-Martinez, C.C., Baptista-Pires, L., Raouafi, N., Merkoçi, A., 2016. Anal. Chim. Acta 926, 28–35. https://doi.org/10.1016/j.aca.2016.04.010.

Reiner-Rozman, C., Larisika, M., Nowak, C., Knoll, W., 2015. Biosens. Bioelectron. 70, 21–27. https://doi.org/10.1016/j.bios.2015.03.013.

Sherbet, G.V., Lakshmi, M.S., Cajone, F., 1983. Biophys. Struct. Mech. 10, 121–128. https://doi.org/10.1007/BF00537554.

Sun, J., Xie, X., Xie, K., Xu, S., Jiang, S., Ren, J., Zhao, Y., Xu, H., Wang, J., Yue, W., 2019. Nanoscale Res. Lett. 14, 1–8. https://doi.org/10.1186/s11671-019-3048-1.

Thakur, B., Zhou, G., Chang, J., Pu, H., Jin, B., Sui, X., Yuan, X., Yang, C.H., Magruder, M., Chen, J., 2018. Biosens. Bioelectron. 110, 16–22. https://doi.org/10.1016/j.bios.2018.03.014.

Thangaraj, V., Lepoitevin, M., Smietana, M., Balanzat, E., Bechelany, M., Janot, J.M., Vasseur, J.J., Subramanian, S., Balme, S., 2016. Microchim. Acta 183, 1011–1017. https://doi.org/10.1007/s00604-015-1706-2.

Van Den Beld, W.T.E., Odijk, M., Vervuurt, R.H.J., Weber, J.W., Bol, A.A., Van Den Berg, A., Eijkel, J.C.T., 2017. Sci. Rep. 7, 1–8. https://doi.org/10.1038/srep45080.

Vieira, N.C.S., Borme, J., Machado, G., Cerqueira, F., Freitas, P.P., Zucolotto, V., Peres, N.M.R., Alpuim, P., 2016. J. Phys. Condens. Matter 28. https://doi.org/10.1088/0953-8984/28/8/085302.

Wang, Q.H., Jin, Z., Kim, K.K., Hilmer, A.J., Paulus, G.L.C., Shih, C.J., Ham, M.H., Sanchez-Yamagishi, J.D., Watanabe, K., Taniguchi, T., Kong, J., Jarillo-Herrero, P., Strano, M.S., 2012. Nat. Chem. 4, 724–732. https://doi.org/10.1038/nchem.1421.

Wu, J. Bin, Lin, M.L., Cong, X., Liu, H.N., Tan, P.H., 2018. Chem. Soc. Rev. 47, 1822–1873. https://doi.org/10.1039/c6cs00915h.

Xia, Z., Leonardi, F., Gobbi, M., Liu, Y., Bellani, V., Liscio, A., Kovtun, A., Li, R., Feng, X., Orgiu, E., Samorì, P., Treossi, E., Palermo, V., 2016. ACS Nano 10, 7125–7134. https://doi.org/10.1021/acsnano.6b03278.

Yang, O., Ha, T., 2018. Elsevier Inc., pp. 463–477. https://doi.org/10.1016/bs.mie.2017.11.017

Zhang, X.G., 2005. https://doi.org/10.1007/0-306-47921-4_1.

Zhang, Y., Zhou, H., 2001. Biophys. J. 81, 1133–1143. https://doi.org/10.1016/S0006-3495(01)75770-0.

Zhou, L., Wang, K., Sun, H., Zhao, S., Chen, X., Qian, D., Mao, H., Zhao, J., 2019. Nano-Micro Lett. 11 https://doi.org/10.1007/s40820-019-0250-8.

Zribi, B., Haghiri-Gosnet, A.M., Bendounan, A., Ouerghi, A., Korri-Youssoufi, H., 2019. Carbon N. Y. 153, 557–564. https://doi.org/10.1016/j.carbon.2019.07.066.

Supporting information

Highly Sensitive Interfaces of Graphene Electrical-Electrochemical Vertical Devices for On Drop Atto-Molar DNA Detection

*Isabela A. Mattioli[1], Ayaz Hassan[1], Natalia M. Sanches[1], Nirton C. S. Vieira[2], and Frank N. Crespilho[1]**

[1]*São Carlos Institute of Chemistry, University of São Paulo, São Carlos, São Paulo 13560-970, Brazil*

[2]*Institute of Science and Technology, Federal University of São Paulo, 12231-280, São José dos Campos, SP, Brazil*

1. Electrochemical etching

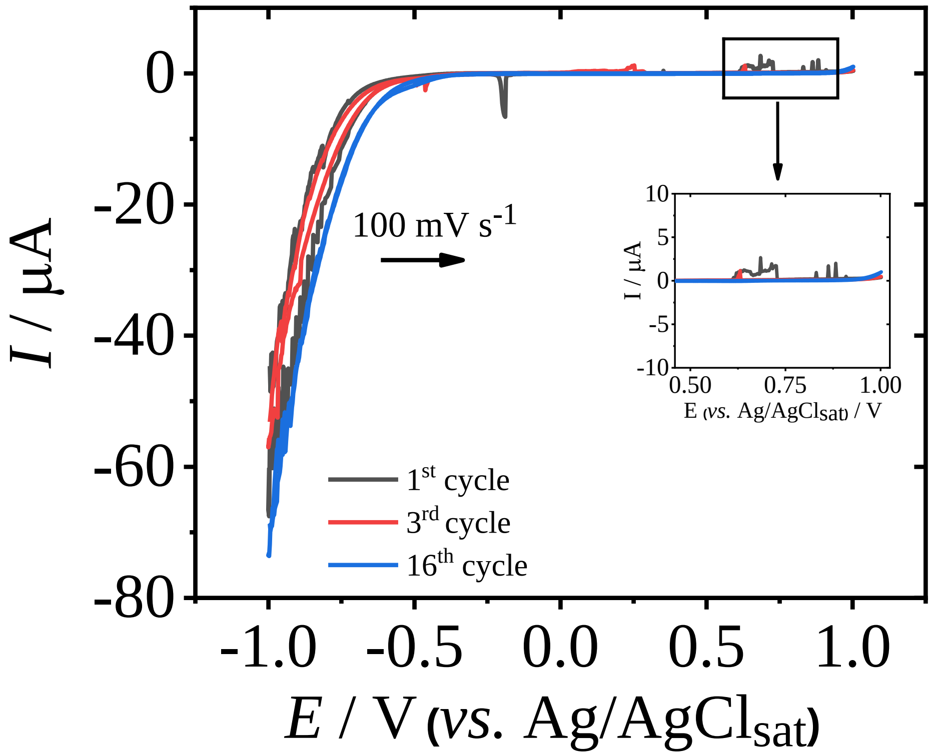

Figure S1. Cyclic voltammetry of bare graphene devices in 0.10 mol L^{-1} HCl for electrochemical removal of Cu residues at 1st cycle (black), 3rd cycle (red) and 16th cycle (blue). ν = 100 mV s^{-1}

2. Monolayer features of graphene

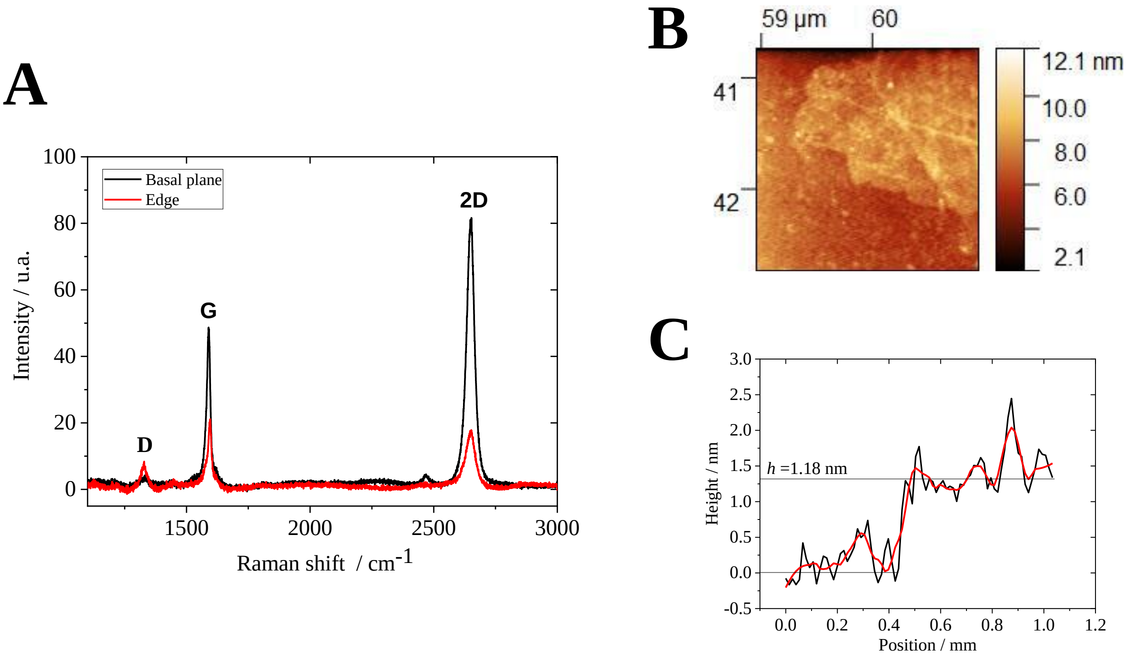

Figure S2 – A) Raman spectra for monolayer graphene on Si/SiO$_2$ after EEVD's confection collected at basal plane (black line) and edge (red line) of graphene; B) AFM micrograph obtained for graphene on Si/SiO$_2$ at its basal plane; C) graphene sheet thickness plot collected by AFM tip on contact mode operation

Figure S2A presents Raman spectra obtained for graphene on Si/SiO$_2$ after graphene transfer procedure. In both cases, it is noticeable the presence of typical graphene bands (Malard et al., 2009; Wu et al., 2018) as G band, in ~1588 cm^{-1} and 2D mode in ~ 2650 cm^{-1}. While 2D band appears in every graphite-derived material, G band is typical of graphene and is related to its sp^2 lattice and active phonons around the Brillouin symmetry point Γ**.** (Wu et al., 2018) The D mode, in ~1383 cm^{-1}, is frequently related to the presence of point defects on graphene sp^2 lattice and intervalley one-phonon processes. (Wu et al., 2018) The higher D mode, the higher the amount of point defects on the graphene sheet. Therefore, from Figure S2A, it is observable that D band intensity of graphene's edge is pronounced in comparison to the same band in the basal plane graphene spectrum. This is an indicative of a low number of defects of our graphene sheet.

Furthermore, 2D and G band intensities can be related to the number of layers of the analyzed material. If $I_{2D}/I_G = 2$, the studied graphene sheet is ideally presented in a single layer. (Hao et al., 2010; Wall, 2011) Based on basal plane spectra of Figure S2A, $I_{2D}/I_G = 1.7$, indicating that the graphene used in this work is monolayer.

AFM micrographs and graphene layer thickness plot (Figures S2B and S2C, respectively) also confirmed the monolayer nature of graphene. Figure S2B topology scale ranges 2 – 12 nm. Although the expected graphene width is approximately 1.0 nm, (Fei et al., 2011; Iost et al., 2016), the topological scale obtained in this work can be considered acceptable if unavoidable impurities adsorption during the EEVDs handling, insertion of point defects and sheet eventual deformations during transferring methodologies are taken into account.

Graphene thickness was measured from height *vs.* position of the tip plots in three different regions of graphene's basal plane. The average graphene thickness obtained was (1.1 ± 0.1) nm. Figure S2C presents one of these plots. Despite theoretical reports predicts a graphene thickness value of ~0.34 nm, literature considers that monolayer graphene sheets supported on Si/SiO_2 substrate presents a thickness of 1.0 nm. This value considers the adsorption of impurities, graphene sheet deformation due to transferring processes and the distance between Si/SiO_2 and graphene sheet due to their van der Waals interactions. (Fei et al., 2011; Iost et al., 2016)

3. Field-effect experiments with bare graphene and graphene-fc interfaces

Output curves were previously obtained in order to optimize V_{ds} to be applied in transfer curves (I_{ds} *vs.* V_g) and verify the linear region of response under field-effect conditions of each interface. The obtained results also indicate that all studied interfaces present ohmic behavior in the studied V_{ds} interval. No significant change was observed in these curves as a function of V_{ds} variation.

To evaluate *n*, a series of field-effect transfer curves experiments of bare monolayer graphene in SiO_2 were performed (Figures S3, S4), in which a $V_{CNP} \sim 0.075$ V (*vs*. $Ag/AgCl_{sat}$) was obtained. These data are similar to the results reported elsewhere in phosphate buffer pH ~7.4 media.(Ohno et al., 2009; Vieira et al., 2016) The expression $n = \eta . V_{CNP}$ was applied, in which *h* factor (2.4×10^{11} cm^{-2} V^{-1}) represents a parallel plate capacitor formed by monolayer graphene and 90 nm thick SiO_2. (Nourbakhsh et al., 2010) In sequence, Fermi energy could be evaluated by the classical formulation (Eq. 4 of the main text) in which v_F is Fermi velocity (1.1×10^8 cm s^{-1}), $\hbar$ is Planck constant and *n* is the charge carrier concentration (cm^{-2})(Wu et al., 2018).

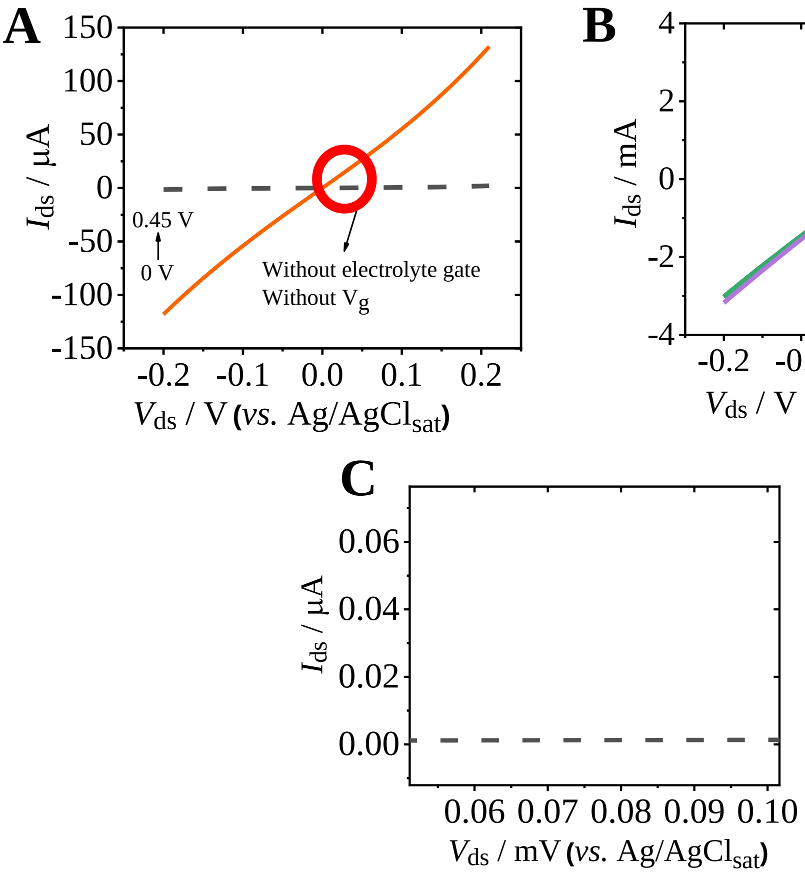

Figure S3. I_{ds} *vs.* V_{ds} plots for A) bare graphene, under V_g = 0, 0.1, 0.15, 0.2, 0.25, 0.3, 0.35, 0.4 and 0.45 V. Gray dashed line correspond to a no electrolyte and no gate voltage applied measurement; B) graphene-fc under V_g = -0.2, -0.1, 0, 0.1 and 0.2 V; C) Expanded red-circled region on Figure S2A for better observing I_{ds} variations as a function of different V_g. All voltages applied *vs.* Ag/AgCl$_{sat}$ as electrolyte-gated electrode. Experiments carried out in 0.01 mol L^{-1} phosphate buffer pH 7.4

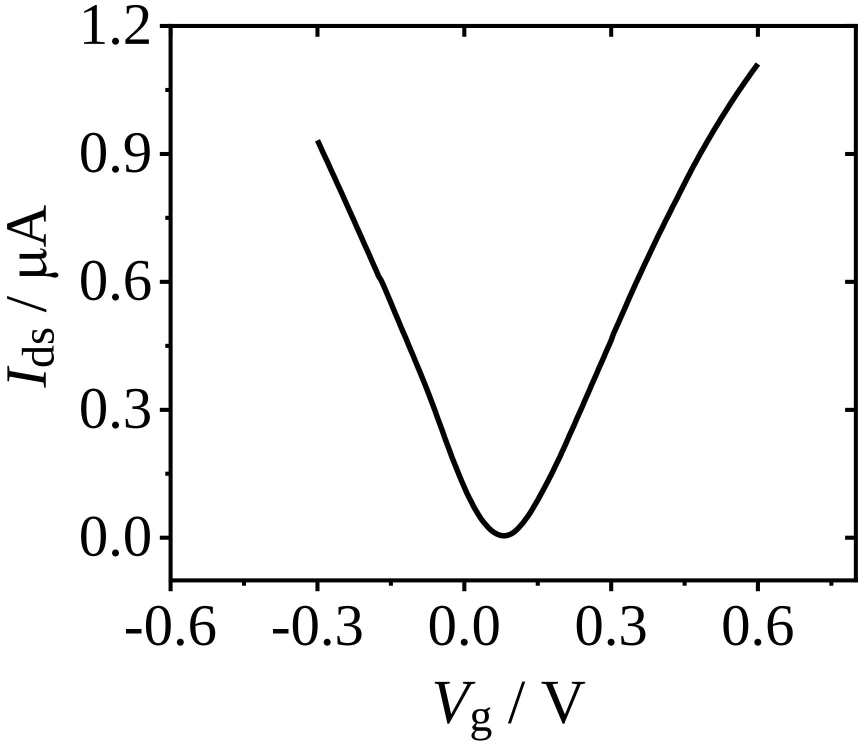

Figure S4. Bare graphene-SiO_2 transfer curve from -0.3 V to 0.5 V in 0.01 mol L^{-1} PBS under V_{ds} = 0.01 V

4. EEVD scan rate variation study

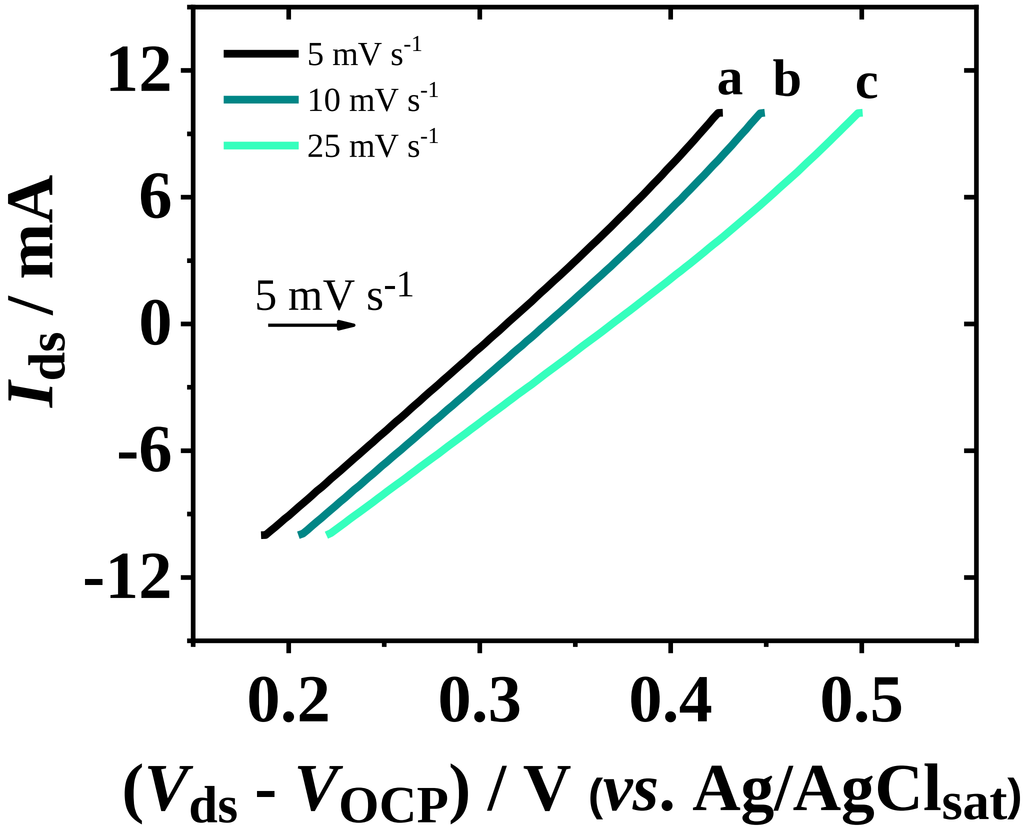

Figure S5. Output curves of bare graphene EEVDs in 0.1 mol L-1 phosphate buffer pH 7.2 taken in short circuit conditions with different scan rates: a) 5 mV s^{-1}; b) 10 mV s^{-1} and c) 25 mV s^{-1}.

5. Surface excess of adsorbed ferrocene onto graphene

$$\Gamma_0 = \frac{Q}{nFA} \tag{S1}$$

Where , *n* = number of electrons involved in Fe^{2+}/ Fe^{3+} redox pair, F = Faraday's constant = 96485 C mol^{-1}, A = geometric area of the electrode (in all devices, A ~ 0.01 cm^2) and Q = charge obtained by integration of peak current of graphene-fc cyclic voltammogram in 0.10 mol L^{-1} phosphate buffer pH 7.2 after subtraction of background current. (Bard and Faulkner, 2001)

6. Ferrocene cyclic voltammetry

Electrochemical behavior of graphene-fc interface was investigated in 0.1 mol L^{-1} phosphate buffer pH 7.2 by cyclic voltammetry. The adsorbed ferrocene onto graphene's surface acts as a redox probe, allowing us to observe faradaic processes using pristine graphene as a substrate. The graphene-fc interface presented a *quasi*-reversible profile, with a peak potential separation; ΔE_p value of ~ 159 mV and formal potential $E^{0'} = 0.239$ V (*vs.* Ag/AgCl$_{sat}$). As an adsorbed system, *i vs. E* curves (i.e, voltammograms) for graphene-fc interface can be described by Eq. S2, which depends on overpotential; $E\text{-}E^{0'}$ and adsorption rate ratio between oxidized (b_o) and reduced (b_R) forms of ferrocene, following Langmuir's adsorption model.(Bard and Faulkner, 2001)

$$i = \frac{n^2 \cdot F^2 \cdot \nu \cdot A \cdot \Gamma_0 \cdot \left({}^{b_O}/_{b_R}\right) \cdot e^{{}^{nF}/_{RT}\,(E-E^{0'})}}{RT \cdot \left[\, 1+\left({}^{b_O}/_{b_R}\right) \cdot e^{{}^{nF}/_{RT}\,(E-E^{0'})}\right]^2} \qquad \text{(S2)}$$

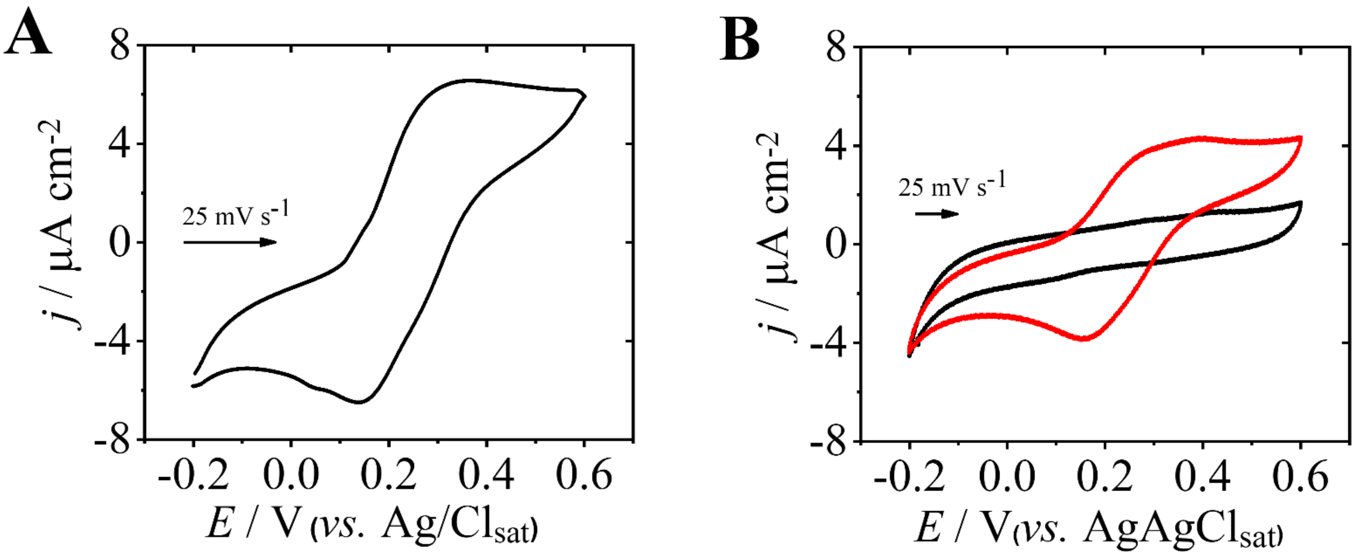

Figure S6. Cyclic voltammetry of adsorbed ferrocene onto graphene in A) 0.10 mol L^{-1} KCl (30th scan), scan rate = 25 mV s^{-1}; B) Cyclic voltammogram of bare graphene (black) and adsorbed ferrocene (red) 0.10 mol L^{-1} phosphate buffer pH 7.2, (3rd scan), ν = 25 mV s^{-1}

7. Ferrocene redox behavior in short-circuit EEVD approach

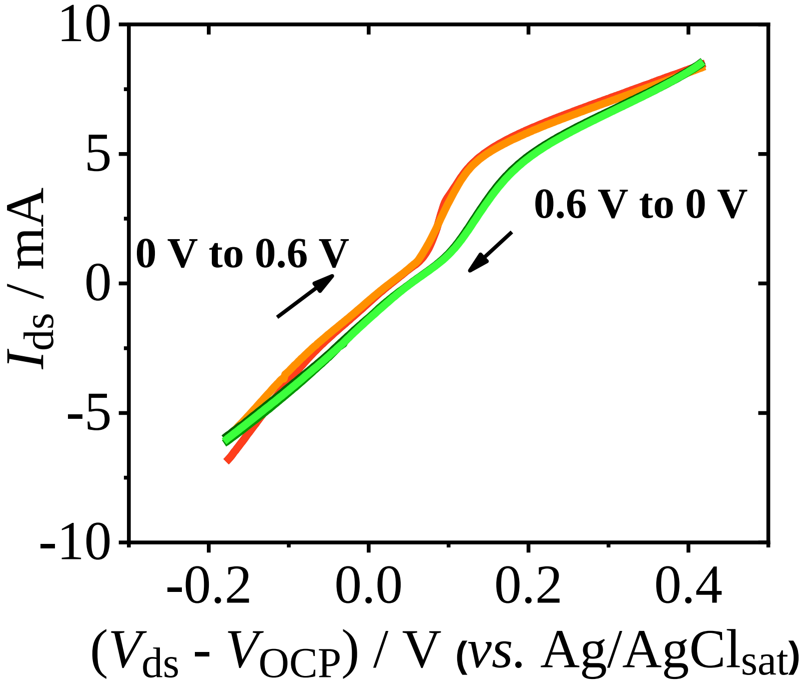

Figure S7. Short-circuit transfer curves for EEVD with graphene-fc interface in 0.10 mol L^{-1} phosphate buffer pH 7.2 from 0 to 0.6 V (*vs.* Ag/AgCl$_{sat}$) and from 0.6 V to 0 V (*vs.* Ag/AgCl$_{sat}$), at 5 mV s^{-1}

8. Output curves for graphene and graphene-fc in short-circuit conditions

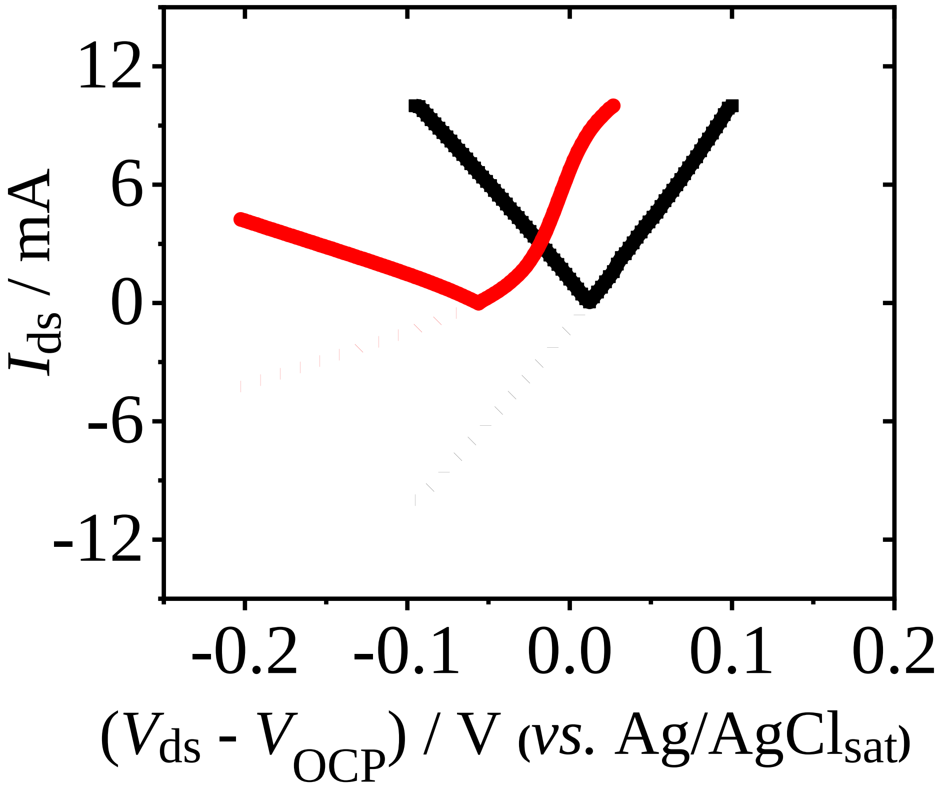

Figure S8. I_{ds} *vs.* V_{ds} curves In short-circuit conditions for bare graphene on SiO_2 (black; gray dots), graphene-fc (red; red dots). Dotted curves correspond to the non-modified ones while solid curves correspond to signal modified ones, as presented in Figure 2G of the main text.

9. Field-effect parameters evaluation of bare graphene, graphene-fc and graphene-fc-ssDNA heterojunctions

Firstly, double-layer capacitance, C_{dl}, was evaluated according to Eq. S3, (Ohno et al., 2009) in which ε_0 = vacuum permittivity, h = double-layer thickness (estimated by Debye-Length) ~ 1nm, ε_R = electrolyte dielectric constant (H_2O) ~ 80 and r = graphene radius without structural defects (assuming that it acts as a metal disk) ~ 799μm. In sequence, the number of charge carriers (n) inserted by ferrocene on graphene and the on graphene-fc heterojunction was estimated using Eq. S4. (Islam et al., 2019) For this we used C_{dl}, as usually advised for electrolyte-gated devices. (Vieira et al., 2016)

$$C_{dl} = \frac{2\pi\cdot\varepsilon_0\cdot(\varepsilon_R+1)}{\tan^{-1}\left[\frac{2h\cdot(\varepsilon_R+1)}{r\cdot\varepsilon_R}\right]} \tag{S3}$$

$$\Delta_n = \frac{C_{dl}}{e}\cdot(\Delta_{CNP}) \tag{S4}$$

In order to evaluate the total gate capacitance (C_{g}), we estimated the quantum capacitance of graphene, C_{q}, using Eq. S5, (Vieira et al., 2016) where: υ_F = Fermi velocity (1.10^8 cm s^{-1}) ħ = Planck's constant ($1.034\text{x}10^{-34}$ J.s) e = elementary charge n = number of charge carriers obtained from Eq S4. For pristine graphene interface, C_{q} was evaluated from charge carriers concentration due to graphene p doping obtained by n = $\eta.V_{\mathrm{CNP.}}$ (Nourbakhsh et al., 2010) Total gate capacitance C_{g} was then evaluated (Eq. S6) considering it as a series association of C_{dl} and C_{q} (Ohno et al., 2009; Vieira et al., 2016). Next, we obtained transconductance, g_{m}, for both electrons and holes linear regions as described by Eq. S7. With transconductance values, channel length L ~ 799 μm, channel width W ~1424 μm and V_{ds} = 0.01V, we estimated the charge carrier mobility (Eq. S8) using the transconductance model (Li et al., 2013) for electrons and holes in our graphene and graphene-fc devices. In this equation, L = channel length, W = channel width, t_{ox} =

thickness of substrate oxide (90 nm); ε_{ox} = SiO_2 dielectric constant (3.9). All results from these evaluations are presented in Table S1.

$$C_q = \frac{2e^2}{\pi} \cdot \frac{\sqrt{\pi n}}{\hbar \cdot \upsilon_F} \tag{S5}$$

$$C_g = \frac{C_{dl} \cdot C_q}{C_{dl} + C_q} \tag{S6}$$

$$g_m = \frac{dI_{ds}}{dV_{gs}} \tag{S7}$$

$$\mu = \frac{L}{W} \cdot \frac{t_{ox}}{\varepsilon_0 \cdot \varepsilon_{ox}} \cdot \frac{g_m}{V_{ds}} \tag{S8}$$

Table S1. Field effect parameters evaluated for bare graphene interface, graphene-fc and graphene-fc-ssDNA heterojunctions

Interface	**C_{dl} / μF cm^{-2}**	**C_q / μF cm^{-2}**	**C_g / μF cm^{-2}**	**Δn / cm^{-2}**	**g_m e^- / μS**	**g_m p^+ / μS**	**μ_e / cm^{-2} V s**	**μ_p / cm^{-2} V s**
Graphene	3.2	3.4	1.65	1.5×10^{12}	-2.76	2.86	4037.9	4184.2
Graphene-fc	3.2	2.93	1.53	1.14×10^{12}	-1.13	0.82	1653.2	1199.7
Graphene-fc-ssDNA	8.33	2.93	2.16	1.15×10^{12}	-1.58	1.23	2311.5	1799.5

10. Circuit simulation observations

For a suitable circuit simulation from Nyquist plots for graphene, graphene-fc and graphene-fc-ssDNA interfaces, both double-layer capacitance (C_{dl}) and adsorbed ferrocene layer capacitance (C_{ads}) were replaced by constant phase elements (CPE) due to non-ideal surface charge distributions, surface roughness and structural defects of both graphene monolayer and adsorbed ferrocene . (Barsoukov and Macdonald, 2005) Furthermore, C_{dl} can be interpreted as an association between diffuse layer capacitance (C_{diff}) and Helmholtz layer capacitance (C_H), $1/C_{dl} = 1/C_{diff} + 1/C_H$, and in higher ionic concentrations C_{diff} contributions are minimized. (Reiner-Rozman et al., 2015) For bare graphene interfaces, however, simulations were made considering a conventional $R_s[R_{ct}C_{dl}]$ circuit owing to the lack of an electroactive adsorbed layer. Considering the optimized circuit simulations, for bare graphene, $C_{dl} = (11.5 \pm 0.09)\ \mu F\ cm^{-2}$ was obtained and for graphene-fc, $R_{ct} = (30.6 \pm 2.3)\ k\Omega$ and $C_{dl} = (8.05 \pm 0.08)\ \mu F\ cm^{-2}$ were obtained Graphene-fc-ssDNA heterojunction presented capacitive profile without the appearance of semicircle in the high frequency regime corresponding to electron transfer resistance , similar to bare graphene interface, thus no R_{ct} could be obtained. A $C_{dl} = (3.7 \pm 0.09)\ \mu F\ cm^{-2}$ was obtained through the same circuit simulation. The value obtained for C_{dl} is significantly lower than those obtained for bare graphene and graphene-fc interfaces. These values are more coherent than the values obtained with field-effect experiments and previous estimative methods reported elsewhere. (Ohno et al., 2009) They are also in accordance to the Helmholtz electrochemical model for double-layer capacitance,(Bard and Faulkner, 2001) in which an increase in double layer length due to molecules adsorption leads to smaller C_{dl} values.

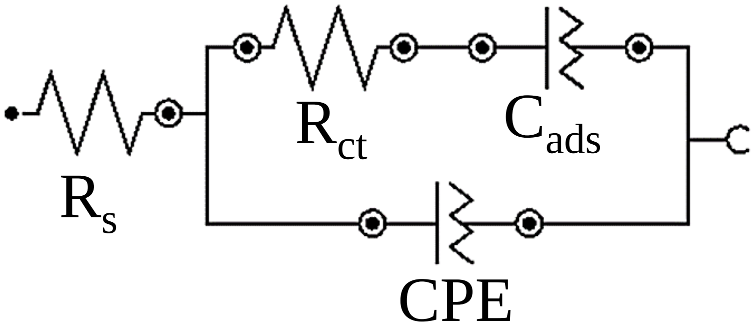

Figure S9. Equivalent circuit simulated for graphene-fc and graphene-fc-ssDNA heterojunctions

11. Raman Spectroscopy

The fabricated graphene devices were studied by Raman spectroscopy in order to obtain essential information about the bare monolayer graphene interface, such as density of defects (n_D), average distance between defects (L_D), and I_D/I_G ratios. Doping effects of ferrocene and ssDNA adsorption onto the graphene interface were also investigated by evaluating I_{2D}/I_G ratio, charge carrier concentrations, and Fermi levels, once the adsorption of ferrocene onto graphene by π–π stacking can open a band gap in the heterojunction. (Zribi et al., 2019) The studies concerning these three interfaces by Raman spectroscopy will serve as a guidance for our DNA biosensor based on our hybrid EEVDs with graphene-fc interface. Raman spectra obtained for bare graphene presented typical bands of graphene structure. The D mode in ~1324 cm^{-1} is associated to one-phonon intervalley processes and presence of point defects on graphene's basal plane. G band, typical in monolayer graphene sheets, in ~1588 cm^{-1} appears owning to active phonons around the Brillouin symmetry point Γ. 2D mode, in ~2650 cm^{-1}, associated to two-phonon intervalley processes which generally occurs in graphite structures. (Wu et al., 2018) We did nor observed typical ferrocene bands near 1000 cm^{-1} (Bodenheimer et al., 1969) for both graphene-fc and graphene-fc-ssDNA interfaces due to the significantly low concentration of adsorbed ferrocene (~10^{-10} mol L^{-1}). For a 0.1 cm^2 graphene sheet, we obtained an I_D/I_G ratio of 0.11 for pristine graphene, 0.37 for graphene-fc, and 0.25 for graphene-fc-ssDNA, indicating the presence of low number of defects on the basal plane. Using this data, for bare graphene we obtained a density of defects of 1.1×10^{10} cm^{-2} and an average distance between defects (L_D) value of 53 nm on the basal plane, according to Eqs. S9 and S10, respectively. (Cançado et al., 2011) Graphene-fc and graphene-fc-ssDNA presented values of 4.2×10^{10} and 2.8×10^{10} cm^{-2} defects, respectively.

These data were also in agreement to what is expected for low defect-density pristine graphene interfaces. (Young et al., 2019)

$$n_D(cm^{-2}) = \frac{1.8 \cdot 10^{22} \cdot I_D}{\lambda_L^4 \cdot I_G} \tag{S9}$$

$$L_D^2\ (nm^2) = \frac{1.8 \cdot 10^{-9} \cdot \lambda_L^4}{\frac{I_D}{I_G}} \tag{S10}$$

Table S2. Raman spectroscopy parameters obtained using a 633 nm laser for pristine graphene, graphene-fc and graphene-fc-ssDNA interfaces

	I_{2D}/I_G	E_F / eV	n / cm^{-2}
Graphene	1.676	+ 0.155	1.5 10^{12}
Graphene-fc	1.564	- 0.061	2.7 10^{11}
Graphene-fc-ssDNA	1.445	- 0.198	2.9 10^{12}

References

Bard, A.J., Faulkner, L.R., 2001. Second. ed. John Wiley & Sons, New York.

Barsoukov, E., Macdonald, J.R., 2005. John Wiley & Sons, Hoboken, New Jersey. https://doi.org/10.1002/0471716243

Bodenheimer, J., Loewenthal, E., Low, W., 1969. Chem. Phys. Lett. 3, 715–716. https://doi.org/10.1016/0009-2614(69)87018-1

Cançado, L.G., Jorio, A., Ferreira, E.H.M., Stavale, F., Achete, C.A., Capaz, R.B., Moutinho, M.V.O., Lombardo, A., Kulmala, T.S., Ferrari, A.C., 2011. Nano Lett. 11, 3190–3196. https://doi.org/10.1021/nl201432g

Fei, Z., Andreev, G.O., Bao, W., Zhang, L.M., S. McLeod, A., Wang, C., Stewart, M.K., Zhao, Z., Dominguez, G., Thiemens, M., Fogler, M.M., Tauber, M.J., Castro-Neto, A.H., Lau, C.N., Keilmann, F., Basov, D.N., 2011. Nano Lett. 11, 4701–4705. https://doi.org/10.1021/nl202362d

Hao, Y., Wang, Y., Wang, L., Ni, Z., Wang, Z., Wang, R., Koo, C.K., Shen, Z., Thong, J.T.L., 2010. Small 6, 195–200. https://doi.org/10.1002/smll.200901173

Iost, R.M., Crespilho, F.N., Kern, K., Balasubramanian, K., 2016. Nanotechnology 27. https://doi.org/10.1088/0957-4484/27/29/29LT01

Islam, S., Shukla, S., Bajpai, V.K., Han, Y.K., Huh, Y.S., Kumar, A., Ghosh, A., Gandhi, S., 2019. Biosens. Bioelectron. 126, 792–799. https://doi.org/10.1016/j.bios.2018.11.041

Li, B., Klekachev, A. V., Cantoro, M., Huyghebaert, C., Stesmans, A., Asselberghs, I., De Gendt, S., De Feyter, S., 2013. Nanoscale 5, 9640–9644. https://doi.org/10.1039/c3nr01255g

Malard, L.M., Pimenta, M.A., Dresselhaus, G., Dresselhaus, M.S., 2009. Phys. Rep. 473, 51–87. https://doi.org/10.1016/j.physrep.2009.02.003

Nourbakhsh, A., Cantoro, M., Klekachev, A., Clemente, F., Sorée, B., Van Der Veen, M.H., Vosch, T., Stesmans, A., Sels, B., De Gendt, S., 2010. J. Phys. Chem. C 114, 6894–6900. https://doi.org/10.1021/jp910085n

Ohno, Y., Maehashi, K., Yamashiro, Y., Matsumoto, K., 2009.. Nano Lett. 9, 3318–3322. https://doi.org/10.1021/nl901596m

Reiner-Rozman, C., Larisika, M., Nowak, C., Knoll, W., 2015. Biosens. Bioelectron. 70, 21–27. https://doi.org/10.1016/j.bios.2015.03.013

Vieira, N.C.S., Borme, J., Machado, G., Cerqueira, F., Freitas, P.P., Zucolotto, V., Peres, N.M.R., Alpuim, P., 2016. J. Phys. Condens. Matter 28. https://doi.org/10.1088/0953-8984/28/8/085302

Wall, M., 2011. Thermo Fischer Scientific.

Wu, J. Bin, Lin, M.L., Cong, X., Liu, H.N., Tan, P.H., 2018. Chem. Soc. Rev. 47, 1822–1873. https://doi.org/10.1039/c6cs00915h

Young, K.T., Phillips, S.S., Coley, J.T.T., Perini, C.J., Hitchcock, D.A., Serkiz, S.M., Vogel, E.M., 2019. Appl. Surf. Sci. 478, 959–968.

https://doi.org/10.1016/j.apsusc.2019.02.053

Zribi, B., Haghiri-Gosnet, A.M., Bendounan, A., Ouerghi, A., Korri-Youssoufi, H., 2019. Carbon N. Y. 153, 557–564. https://doi.org/10.1016/j.carbon.2019.07.066

CHAPTER IV - Graphene-based hybrid electrical-electrochemical point-of-care device for serologic COVID-19 diagnosis

Author Contributions: Isabela A. Mattioli: conceived the project, manufactured the device, collected and analyzed the data, wrote and revised the manuscript; Karla R Castro: manufactured the device, wrote and revised the manuscript; Lucyano J. A. Macedo: conceived the project, analyzed the data, revised the manuscript; Graziela C. Sedenho: collected and analyzed the data, revised the manuscript; Mona N. Oliveira: collected the samples, performed protein synhtesis; Iris Todeschini: collected the samples, performed protein synthesis, revised the manuscript; Phelipe M. Vitale: collected the samples, performed protein synthesis, revised the manuscript; Suzete C. Ferreira: collected and treated the human samples, revised the manuscript; Erika R. Manuli: collected and treated the human samples, revised the manuscript; Geovana M. Pereira: collected the samples, revised the manuscript, Ester C Sabino: collected the samples, revised the manuscript; and Frank N. Crespilho: conceived the project, wrote and revised the manuscript.

In this article, a graphene EEVD interface is presented for IgG detections produced in response for COVID-19 infections, aiming POC COVID-19 diagnosis in a rapid, easy-to-handle and highly sensitive assay. For this, a monolayer graphene interface was modified by subsequent non-covalent modifications. Initially, it was carried out an electropolimerization of a redox probe (poly-neutral red polymer, PNR). In sequence, antigen-antibody interactions established between IgG and RBD domain of S1 protein of SARS-CoV-2 was explored, by immobilization of a RBD bioconjugate with gold nanoparticles (AuNP). This strategy was adopted based on the affinity between AuNP-based species and PNR structure, which are capable of establishing van der Waals interactions. IgG detections were explored by employing the hybrid electrical-electrochemical detection methodology already developed in the previous work presented in Chapter III. In this sense, an LOD of 1.0 pg mL^{-1} for IgG was obtained, in a linear range of IgG concentrations varying from 10^{-12} to 10^{-7} mol L^{-1}. Finally, the device was applied for IgG detections in real human serum samples, with a positive/negative response based on the ΔV_{OCP} obtained. ELISA standard method for serologic detections was performed for validation of the obtained results.

Biosensors and Bioelectronics 199 (2022) 113866

Contents lists available at ScienceDirect

Biosensors and Bioelectronics

journal homepage: www.elsevier.com/locate/bios

Graphene-based hybrid electrical-electrochemical point-of-care device for serologic COVID-19 diagnosis

Isabela A. Mattioli [a], Karla R. Castro [a], Lucyano J.A. Macedo [a], Graziela C. Sedenho [a], Mona N. Oliveira [b], Iris Todeschini [b], Phelipe M. Vitale [b], Suzete Cleusa Ferreira [d,e], Erika R. Manuli [c,f], Geovana M. Pereira [c], Ester C. Sabino [c,f], Frank N. Crespilho [a,*]

[a] *São Carlos Institute of Chemistry, University of São Paulo, São Carlos, SP, 13560-970, Brazil*
[b] *Biolinker Synthetic Biology EIRELI, São Paulo, 05508-000, Brazil*
[c] *Institute of Tropical Medicine, Faculty of Medicine, University of São Paulo, 05403-000, Brazil*
[d] *Laboratory of Medical Investigation in Pathogenesis and Targeted Therapy in Onco-Immuno-Hematology (LIM-31), Department of Hematology, Clinical Hospital HCFMUSP, Faculty of Medicine, University of São Paulo, São Paulo, 01246903, Brazil*
[e] *Division of Research and Transfusion Medicine, São Paulo Hemocentre Pro-Blood Foundation, São Paulo, 05403000, Brazil*
[f] *LIM-46 HC-FMUSP – Laboratory of Medical Investigation, Clinical Hospital, Faculty of Medicine, University of São Paulo, 01246903, Brazil*

ARTICLE INFO

Keywords:
SARS-CoV-2
COVID-19
Serologic detections
Graphene
IgG
Biosensor

ABSTRACT

The outbreak of COVID-19 pandemics highlighted the need of sensitive, selective, and easy-to-handle biosensing devices. In the contemporary scenario, point-of-care devices for mass testing and infection mapping within a population have proven themselves as of primordial importance. Here, we introduce a graphene-based Electrical-Electrochemical Vertical Device (EEVD) point-of-care biosensor, strategically engineered for serologic COVID-19 diagnosis. EEVD uses serologic IgG quantifications on SARS-CoV-2 Receptor Binding Domain (RBD) bioconjugate immobilized onto device surface. EEVD combines graphene basal plane with high charge carrier mobility, high conductivity, low intrinsic resistance, and interfacial sensitivity to capacitance alterations. EEVD application was carried out in real human serum samples. Since EEVD is a miniaturized device, it requires just 40 μL of sample for a point-of-care COVID-19 infections detection. When compared to serologic assays such ELISA and other immunochromatographic methods, EEVD presents some advantages such as time of analyses (15 min), sample preparation, and a LOD of 1.0 pg mL^{-1}. We glimpse that EEVD meets the principles of robustness and accuracy, desirable analytic parameters for assays destined to pandemics control strategies.

1. Introduction

The outbreak of COVID-19 pandemics shocked all nations throughout the world due to the high transmittivity of its causative virus, SARS-CoV-2. It can be spread out through airborne, droplet, contact, fecal-oral, fomite and bloodborne, and once infected, a person can be either symptomatic or asymptomatic (Chaibun et al., 2021). The severeness of COVID-19 symptoms and high rate of hospitalizations and fatalities (Mattioli et al., 2020) concerned the World Health Organization (WHO), as well as leaderships of more than 200 countries to which SARS-CoV-2 migrated (WHO, 2020). A global mobilization has been established aiming the control of COVID-19 infections, by the adoption of mass immunization through vaccines, social distancing measurements, use of face masks, and mass testing (Raffle et al., 2020).

Understanding the SARS-CoV-2 structure and its functional proteins are of relevant importance to the development of vaccines, medication, and sensible tests for diagnosis. The Spike protein of SARS-CoV-2 (S protein), a structural protein responsible for interacting and invading external receptors, is one of the most studied SARS-CoV-2 encoded genes (Lan et al., 2020; Mattioli et al., 2020). The S protein is divided into two subunits, S1 and S2, and present a furin cleavage in the S1–S2 boundary that can improve its infection capacity in host cells (Lan et al., 2020). To interact with human receptor cells, interactions between S protein and ACE2 (Angiotensin Conversion Enzyme) are established (Lan et al., 2020). S protein uses its Receptor Binding Domain (RBD), localized in the S1 subunit, the main interaction site of SARS-CoV-2 virus (Mattioli et al., 2020). It is reported that RBD domain is used as a highly specific immunotarget of human antibodies produced in response to

---

* Corresponding author.
E-mail address: frankcrespilho@iqsc.usp.br (F.N. Crespilho).

https://doi.org/10.1016/j.bios.2021.113866
Received 16 June 2021; Received in revised form 27 August 2021; Accepted 3 December 2021

SARS-CoV-2 infection (Premkumar et al., 2020). The RBD structure has been used as a potential therapeutic target for immunization strategies, as vaccines (Chen et al., 2020; Yang et al., 2020), and protein target and/or immunogen for the development of methodologies aiming either viral or serologic detections (Li et al., 2020; Seo et al., 2020; Yakoh et al., 2021).

COVID-19 diagnoses have been proposed by using RBD as immobilized immunogen for serologic detections of human antibodies produced in response to SARS-CoV-2 infections (Li et al., 2020; Mattioli et al., 2020; Zeng et al., 2020). IgG antibodies are one of the most bioanalytes for the development of SARS-CoV-2 serologic detections, due to its higher stability (Liu and May 2012), higher specificity in comparison to other immunoglobulins (Charles A Janeway et al., 2001), and its long-term presence in human organism after the infection (Sun et al., 2020). Devices based on IgG detection by immunochromatographic methodologies are commonly used strategies for fast serologic detections of human antibody (Isho et al., 2020; Theel et al., 2020). Despite of the well-known advantages of immunochromatographic tests, as low-cost, rapidness of fabrication and easy-to-handle operation, immunochromatographic assays have been frequently associated with unsatisfactory limit of detection (LOD) (Zhang et al., 2020), low repeatability, and poor sensitivity (Ragavendar and Anmol, 2012). Functional nanomaterials are frequently employed as biodevice modifiers in order to improve the analytical features. For instance, gold nanoparticles (AuNP) are employed in biosensors due to size-dependent color, biocompatibility, and high extinction coefficients (Qing et al., 2020b). Due to its optical properties and relatively low cost, AuNP are extensively applied in colorimetric and serological detection devices (Qing et al., 2020a). Furthermore, AuNP use for biosensing and bioelectronics construction with integration between biological units expands its applications for different biosensing architectures, mainly the electrochemical ones (Guo and Wang, 2007; Pingarrón et al., 2008; Qing et al., 2020b). Recently, a large number of electrochemical biosensing devices relying on the application of AuNP as modifiers has been proposed (Akbari Nakhjavani et al., 2019; Filik and Aslıhan Avan, 2020; Prasad et al., 2020; Suresh et al., 2018).

Electrochemical devices have also been widely studied and applied for rapid and sensitive serologic detections through IgG quantifications (Kudr et al., 2021; Mattioli et al., 2020). There are different materials that can be used as a main constituent of these devices, as glassy carbon, screen printed carbon electrodes, pristine graphene, and graphene derivatives (e.g., oxidized graphene). Graphene has attracted much attention for biosensors design due to its high biocompatibility and chemical stability (Jiang et al., 2020; Roy et al., 2017) Graphene-based devices are promising and fit many of the biosensing requirements owing to its expressive sensitivity, ability to reach lower LODs, rapidness, simplicity of operation, and possibility to perform biofunctionalization to improve selectivity (Ali et al., 2021; Hashemi et al., 2021; Mattioli et al., 2021; Torrente-Rodríguez et al., 2020; Yakoh et al., 2021). For instance, serologic detections of IgG and IgM antibodies through RBD SARS-CoV-2 antigen, as well as other SARS-CoV-2 genes using graphene-based electrochemical devices have been reported (Torrente-Rodríguez et al., 2020). The so called "reduced graphene oxide" as a coating material for 3D electrodes aiming COVID-19 antibodies sensing in a microfluidic assay have also been reported (Ali et al., 2021). These devices frequently involve functionalization procedures, as pristine graphene present sluggish electron transfer kinetics (Brownson et al., 2014; Macedo et al., 2019). As a consequence, this leads to a long time of electrodes preparation, and with structures that are not well defined, as is the case of oxidized graphene (Zhu et al., 2010).

Applying pristine graphene in bioelectronics and electrochemical biosensing is interesting due to its high basal plane conductivity, high charge carrier mobility and low intrinsic resistivity (Jiang et al., 2020; Macedo et al., 2019). On the other hand, graphene in field-effect devices configuration (e.g., G-FET) involves not only functionalization procedures to improve selectivity, but also the use of a Ag/AgCl non-polarizable reference electrode as gate electrode for data collection (Reddy et al., 2012). The use of a reference electrode as a gate causes imprecision on potential values reading, affecting the reliability of the proposed detection method (Mattioli et al., 2021). Despite of these issues, graphene field-effect transistors for serological COVID-19 detections has not been reported in literature up to our knowledge.

Here, we propose the application of a Electrical Electrochemical Vertical Device (EEVD), a graphene-based device based on hybrid electrical and electrochemical working principles (Mattioli et al., 2021), for COVID-19 diagnosis through IgG detections. Unlike a conventional G-FET, EEVD uses the vertical electron transfer occurring perpendicularly to the graphene plane, while the electronic current flows through the graphene van der Waals (vdW) heterojunctions. Recent study reported that EEVD can be10 times more sensitive than traditional graphene field-effect transistors, reaching a degree of zepto-molar for the limit of detection (Mattioli et al., 2021). The detection signal is the variation of interfacial potential of the device's surface, obtained by open circuit potential (OCP) measurements. We performed IgG detections based on antigen-antibodies interactions through immobilized SARS-CoV-2 RBD bioconjugates onto a graphene-based van der Waals heterojunction capable of attaching RBD bioconjugates labels without damaging graphene sp^2 structure. This heterojunction was made by electrodeposition of poly-neutral red (PNR), leading to a graphene-PNR (G-PNR) surface. The variation of OCP signal is expected to be caused by the establishment of the specific antigen-antibody interactions.

2. Materials and methods

2.1. Reagents and materials

Sulfuric acid, ethanol, isopropanol, monobasic sodium phosphate (NaH_2PO_4) and potassium phosphate were acquired from Synth®, Brazil. Hydrochloric acid (37% *v/v*), toluene, polystyrene (MW ~192,000 g mol^{-1}), tetrachloroauric acid trihydrate, ethanolamine, Tween 20, potassium chloride, neutral red dye and bovine serum albumin protein were bought from Sigma Aldrich®. Acetone was purchased from Chemis®, Brazil, and hydrogen peroxide (30–32%, *v/v*) was acquired from Vetec®, Brazil. Monoclonal IgG human antibodies (IgG1 type) from SARS-CoV-2 (ab273073) were obtained from Abcam®, USA. Human IgM antibody was acquired from Rheabiotech, Brazil. Bilirubin oxidase was purchased from Amano, Japan. For graphene devices confection, *p*-doped Si/SiO$_2$ ($\Phi_{SiO_2} = 90$ nm) were purchased from Graphene Supermarket®, USA. CVD monolayer graphene was acquired from Graphenea®, Spain. Metallic spots for electrical contact films deposition of Ti and Pt were obtained from Electron Microscopy Sciences®, USA. All aqueous solutions were made using deionized water with resistivity >18 MΩ cm.

2.2. AuNP synthesis

Colloidal AuNP were synthetized through reduction of Au^{3+} by citrate ions, according to the Turkevich methodology (Turkevich et al., 1951). Briefly, 20 mL of $AuCl_3 \cdot 3H_2O$ (1.0 mmol L^{-1}) aqueous solution was heated to its boiling point under vigorous stirring. Then, 2.0 mL of sodium citrate (1.0%, *w/v*) was added to the boiling solution, and the mixture was kept under vigorous stirring at boiling point until to reach dark-red color. The resulting AuNP suspension was then rapidly cooled at ice bath under light protection. The final suspension was stored at 4 °C and protected from light to avoid nanoparticle agglomeration.

2.3. Bioconjugate synthesis

Bioconjugate of RBD with AuNP was strategically adopted in order to ensure an efficient modification of EEVD's G-PNR interface with RBD, as PNR and AuNP present a well-established adsorptive interaction (Mazar et al., 2017; Prakash et al., 2018). Therefore, AuNP based bioconjugates are expected to adsorb effectively on G-PNR EEVD interface. Prior to this, we expressed RBD of SARS-CoV-2 as follows. Firstly, we obtained the clones of the genes encoding for spike S1 RBD in the expression vector pET28a by chemical synthesis from Twist Bioscience (USA). RBD was produced by the *E. coli* expression system. The bacteria pellet was resuspended in lysis buffer (50 mM phosphate buffer pH 8.0, containing 200 mM NaCl, 1 mM DTT, and 1 mM PMSF and 1 mg mL^{-1} of egg lysozyme). RBD samples was subjected to chromatography and gel filtration on a Superdex 200 (16/600). RBD was then characterized by slot blot, UV–Vis, Micro-FTIR and circular dichroism. AuNP/RBD bioconjugates were prepared according to procedures reported elsewhere (de Oliveira et al., 2018; Li et al., 2020). For this, 10 μL of RBD (1.0 mg mL^{-1}) was added to 1.1 mL of colloidal AuNP, prior containing 100 μL of borate buffer (0.1 mol L^{-1}, pH 8.5). After incubation during 20 min, 100 μL of BSA (5%) in deionized water was added, and kept under incubation for 20 min. The resulting mixture was homogenized and centrifuged at 10,000 rpm and 4 °C for 20 min. After discarding the supernatant, a washing step with PBS (0.01 mol L^{-1}) and Tween 20 was performed. The final mixture was also centrifuged at 10,000 rpm and 4 °C during 20 min and resuspended in BSA (3%) solution in PBS (0.01 mol L^{-1}).

2.4. UV–Vis analyses

All proteinaceous samples were diluted 50 × from the original solutions used in bioconjugate synthesis. Final bioconjugate AuNP/RBD samples were diluted 10 ×. All spectra were presented with normalized absorbance values from 0 to 1 for maximum absorbance to clarify the data analysis.

2.5. Transmission electron microscopy (TEM)

TEM images were obtained for diluted AuNP and AuNP/RBD suspensions using a JEOL JEM-2100 microscope with a 200 kV electron beam. Diluted samples were sonicated for 30 min and drop cast onto a copper grid with thin carbon film (200 mesh, Electron Microscope Sciences, USA) and let to dry in vacuum at room temperature.

2.6. EEVDs

The Si/SiO_2 chips were cleaned with piranha solution (3 H_2SO_4: 1 H_2O_2) prior to the electrical contacts deposition. For this, Ti and Pt thin films of 10 and 20 nm, respectively, were subsequently deposited at Si/SiO_2 substrates through sputtering deposition at Brazilian Nanotechnology National Laboratory (LNNano) at the Brazilian Center for Research in Energy and Materials (CNPEM). For CVD monolayer graphene transfer to Si/SiO_2 chips, the polymer-mediated graphene transferring process was adopted (Hassan et al., 2021; Macedo et al., 2018). Briefly, a drop of polystyrene in toluene was deposited onto small-area pieces of CVD monolayer graphene on Cu foil and let under 70 °C for ~10 min. Then, the Cu foil was removed by etching in an aqueous solution containing HCl and H_2O_2 (1.4 and 0.5 mol L^{-1}, respectively). After graphene transfer onto Si/SiO_2 EEVDs substrates, a pre-annealing step in air at 90 °C was adopted. Next, the polystyrene layer was removed though toluene washing steps, and a thermal annealing under Ar atmosphere at 585 °C was finally performed. The success of this procedure was evaluated by optical images collected for each EEVD. Figure S1 present a schematic representation of these steps.

2.7. EEVD modification and characterization

Prior to EEVDs use, an electrochemical etching in HCl (0.1 mol L^{-1}) procedure (Figure S3) was performed for removing Cu traces remaining from EEVDs confection (Iost et al., 2014). Pristine graphene EEVDs were modified with poly-neutral red (PNR) by electropolymerization by cyclic voltammetry, as is further described in "Electrochemical experiments" session. The modification of G-PNR EEVDs with AuNP/RBD bioconjugate was performed by drop-casting of 20 μL of the final suspension. AuNP/RBD was let to adsorb on G-PNR interface for 30 min. Next, 10 μL of ethanolamine (5.0 mmol L^{-1}) aqueous solution (pH 8.0) was employed for blockage of extra RBD sites of AuNP/RBD (Raoof et al., 2013). This step was adopted in order to avoid non-specific interactions between these biomolecules and any other matrix component.

2.8. Micro-FTIR experiments

Micro-FTIR characterizations were performed in a Vertex 70v Fourier transform infrared spectrometer coupled to an IR microscope Hyperion 3000 (Bruker). Chemical 2D and 3D images of PNR and AuNP/RBD bioconjugates deposited onto graphene interfaces were obtained using a liquid nitrogen-cooled 64 × 64 Focal Plane Array (FPA) detector. To provide enough reflectivity for the IR beam (Brunner et al., 1997) experiments were performed in a thin Au layer substrate instead of conventional Si/SiO_2 substrates. Images were collected over a 200 × 200 μm^2 area. Experiments were performed at room temperature and room atmosphere, with 128 scans acquisition at 8 cm^{-1} resolutions. 2D and 3D chemical map of AuNP/RBD bioconjugate onto G-PNR surface was made according to amide I (1648 cm^{-1}) and amide II (1540 cm^{-1}) bands integration. All 3D contour plots have absorbance intensity in *z*-axis.

2.9. Raman spectroscopy

Raman spectra were acquired for bare graphene and G-PNR EEVD surfaces (for the latter surface, after electropolymerization and water evaporation in room temperature), from 1000 to 3000 cm^{-1} under air atmosphere and room temperature by a LabRAM HR Evolution spectrometer (Horiba Scientific) with an HeNe laser of 633 nm wavelength with an acquisition of 64 spectra and an aquisition time of 4s.

2.10. Electrochemical experiments

Electrochemical measurements of all EEVDs were acquired by a PGSTAT 128N potentiostat/galvanostat (Metrohm). Cyclic voltammetry of all electrodes which were performed in PBS (0.01 mol L^{-1}) were made from −1.0 to 1.0 V (*vs.* $Ag/AgCl_{sat}$), at scan rate (ν) 50 mV s^{-1}. Electropolymerization of PNR at pristine graphene EEVDs interfaces were performed by cyclic voltammetry from −1.0 to 1.2 V (*vs.* $Ag/AgCl_{sat}$) at $\nu = 50$ mV s^{-1} for 2 scans, and from −1.0 to 0.5 V (*vs.* $Ag/AgCl_{sat}$), $\nu = 50$ mV s^{-1} for 15 scans (Pauliukaite et al., 2007; Pauliukaite and Brett, 2008). Electrochemical impedance spectroscopy (EIS) experiments of graphene, G-PNR, G-PNR-AuNP/RBD and G-PNR-AuNP/RBD after IgG interaction were performed. All plots were obtained from 1×10^5 to 0.1 Hz, DC_{pot} (direct current potential) equals to OCP (open-circuit potential) of each interface with an amplitude of 5 mV s^{-1} in PBS (0.01 mol L^{-1}, pH 7.4).

2.11. Electrical-electrochemical experiments

Hybrid Electrical-Electrochemical (EE) experiments of all electrodes were performed in a PGSTAT 128N potentiostat/galvanostat (Metrohm). An $Ag/AgCl_{sat}$ electrode was applied as reference electrode, connected to potentiostat RE terminal. Both WE and CE terminals were connected to Ti/Pt electrical contacts in a short-circuit-like configuration. The applied potential range for each EE experiment was defined after the determination of the OCP of each interface. All experiments were performed in a drop of ~40 μL of PBS (0.01 mol L^{-1}) supporting electrolyte. IgG and RBD interactions experiments were performed by the drop-casting of 20 μL IgG (1.0 μg mL^{-1}) in PBS (0.01 mol L^{-1}, pH 7.4) target analyte in a G-PNR-AuNP/RBD EEVD. All curves were obtained in PBS (0.01 mol L^{-1}, pH 7.4); ν = 5 mV s^{-1}. Further details on EEVDs fabrication, theory and working principles can be find elsewhere (Mattioli et al., 2021; Mattioli and Crespilho, 2020)

2.12. Analytical quantifications by EEVDs

For detection studies, calibration curves for IgG detections by G-PNR-AuNP/RBD EEVDs were obtained by hybrid I_{ds} *vs.* V_{ds} electrical-electrochemical experiments, being I_{ds} = CE to WE terminals current and V_{ds} = CE to WE terminals potential. The LOD of the studied EEVD was evaluated considering the standard deviation (SD) of the lowest concentration sample that could be detected, relying on signal-to-noise ratio approaches recommended by IUPAC (Brunetti B, 2015; Inczedy et al., 1998). The collection and use of human sera was approved by the Ethical Committee number 30178220.3.000.0068 of diagnostic proposal analysis at Brazilian platform CNEP (National Council of Ethical and Clinical Research). The diagnosis of SARS-CoV-2 were PCR-based, Roche and Abbott diagnostic kit. The sera from uninfected humans were taken before June 2019 (Pro-blood foundation, Brazil).

2.13. ELISA Comparative method for IgG positive human sera samples

In house plates were immobilized with RBD (10 μg mL^{-1}) in carbonate buffer (0.1 mol L^{-1}, pH 9.4) overnight incubation at 4 °C. The plates were empty and dried at 37 °C. The patient serum sample were diluted 1:10 in PBS containing BSA (0.05%) and milk casein (2%) for titration across the plate to a final volume of 100 μL/well. The plates were incubated for 30 min, 1 h at 37 °C. At the end of the incubation period, the plates were washed with PBS-T and incubated with 100 μL/well of commercial anti-IgG secondary (RheaBiotech, Brazil) for 30 min and 1 h at 37 °C. The unbound conjugate will be removed by washing with PBS-T. The enzymatic activity by addition of TMB (3,3',5,5'-tetramethylbenzidine, Scienco, Brazil) ready to use was measured after incubating each well with 100 μL of TMB solution. After 15 min at 25 °C the reaction was stopped by adding 100 μL of HCl (1.0 mol L^{-1}) to each well. The absorbance was read at 450 nm in a TECAN sunrise conventional ELISA reader.

3. Results and discussions

3.1. PNR-modified graphene EEVDs studies

After EEVDs confection (Fig. 1A), the monolayer features of our transferred pristine graphene onto EEVD Si/SiO$_2$ chips were evaluated by Raman spectroscopy (Fig. 1B). As expected, the obtained Raman spectra presented only D, G, and 2D bands, typical of monolayer graphene structures (Malard et al., 2009), at 1327, 1583, and 2631 cm^{-1}, respectively. I_D/I_G ratio is usually interpreted as an indicative of sp^2 integrity along the monolayer graphene sheet, for which a value equal to 0 refers to an ideal non-defective graphene (Liu et al., 2013). For our monolayer graphene, a I_D/I_G ratio of 0.35 was obtained and found adequate for considering its features as of a low-defective graphene, taking into account the inevitable defects formation during wet transfer steps (Bleu et al., 2019). Moreover, I_{2D}/I_G ratio is used to obtain insights on the number of layers for graphene-based materials with acceptable accuracy (Bleu et al., 2019). I_{2D}/I_G ratios equal to 2 are obtained for ideal non-defective monolayer graphene. However, there is an agreement in literature for considering monolayer graphene characteristics with ratios ranging from 1.3 up to 2 (Bleu et al., 2019). As our graphene presented an I_{2D}/I_G ratio of 1.5, we inferred that in fact most of its monolayer pristine graphene features could be preserved during transferring procedures.

Sequentially, electropolymerization of PNR onto graphene was performed by cyclic voltammetry (Fig. 3C). It was firstly studied in a large-area graphene electrode (Figure S4A), under inert atmosphere, according to an electrochemical methodology described elsewhere (Pauliukaite et al., 2007; Pauliukaite and Brett, 2008). PNR was chosen due to its ability to adsorb on gold nanoparticles-based bioconjugates with high

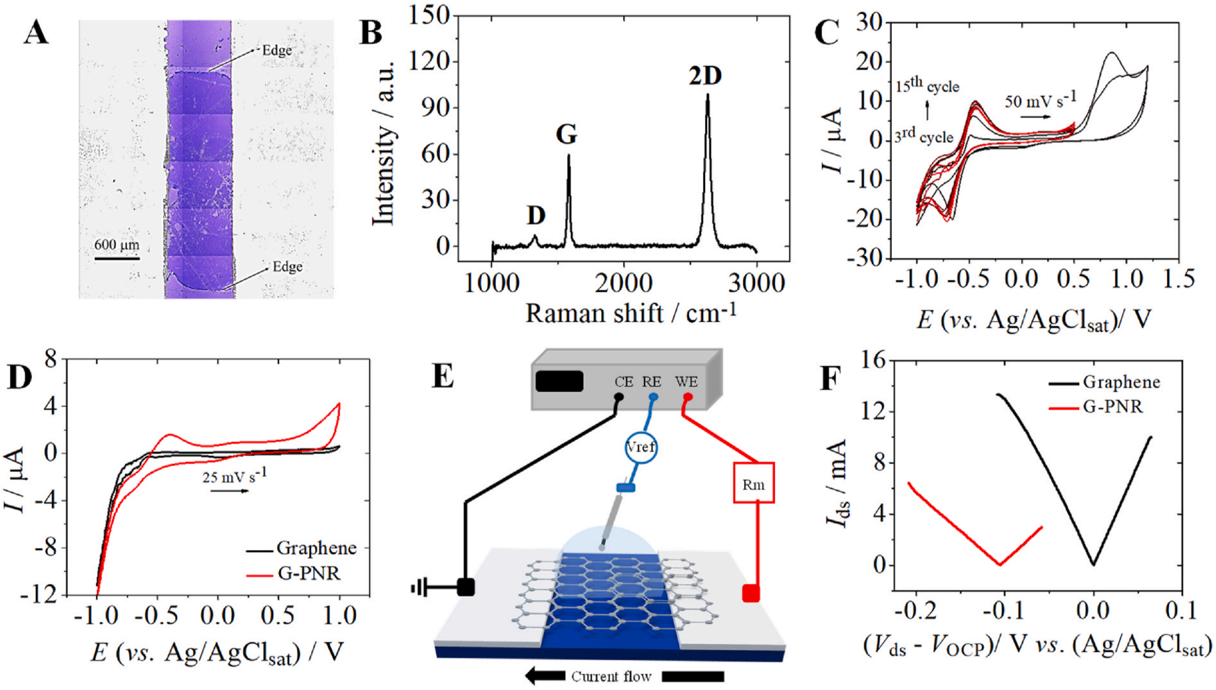

Fig. 1. G-PNR EEVDs. A) Optical image of a pristine graphene EEVD after confection; B) Raman spectrum for pristine graphene EEVD (graphene on Si/SiO$_2$); C) Cyclic voltammograms of PNR electropolymerization under Ar atmosphere in a graphene large area (~0.1 cm^2) 2D electrode in PBS (0.01 mol L^{-1}, pH 7.4), KNO$_3$ (0.5 mol L^{-1}), and neutral red monomer (2.0 mmol L^{-1}), from – 1.0 V to +1.0 V (*vs.* Ag/AgCl$_{sat}$) for 2 scans and from – 1.0 V to +0.5 V (*vs.* Ag/AgCl$_{sat}$) for 15 scans; ν = 50 mV s^{-1}; D) Cyclic voltammograms of graphene interface in bare PBS (0.01 mol L^{-1}, pH 7.4) before PNR functionalization (black) and after PNR functionalization (red), leading to G-PNR interface; E) Schematic representation of hybrid EE experiments with graphene-based EEVDs; F) Pristine graphene (black) and G-PNR (red) EE I_{ds} *vs.* V_{ds} curves in PBS (0.01 mol L^{-1}, pH 7.4). (For interpretation of the references to color in this figure legend, the reader is referred to the Web version of this article.)

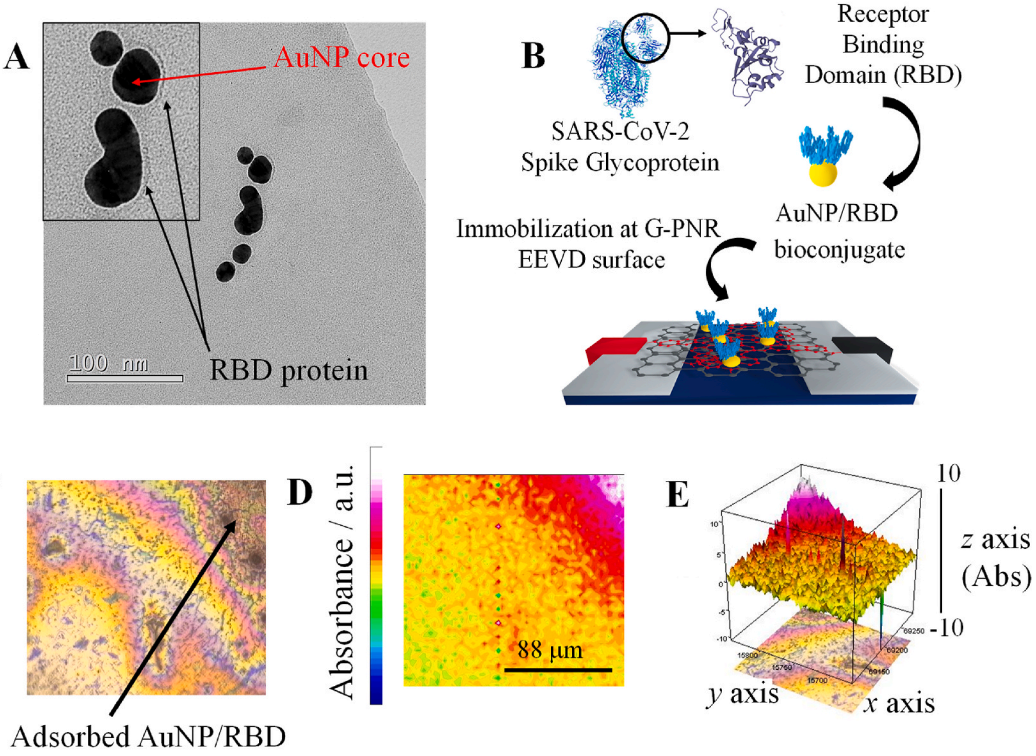

Fig. 2. AuNP/RBD characterization and adsorption onto G-PNR. A) TEM micrograph of AuNP/RBD bioconjugate; B) Schematic representation on AuNP/RBD immobilization methodology onto G-PNR; C) Optical image of G-PNR-AuNP/RBD surface in thin layer Au substrate; D) 2D chemical mapping of AuNP/RBD distribution onto G-PNR by proteinaceous RBD amide-I band monitoring. Scales in Fig. 2C and D are the same; E) The respective 3D chemical mapping.

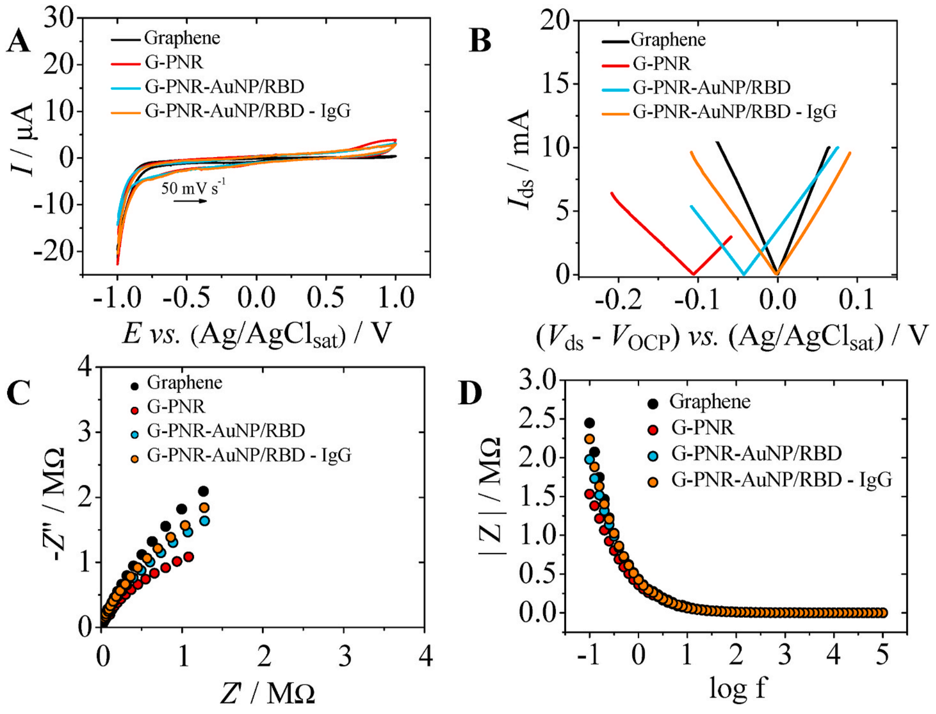

Fig. 3. Electrochemical and EE studies for IgG interaction with G-PNR-AuNP/RBD surface. A) Cyclic voltammograms for bare graphene (black), G-PNR (red), G-PNR-AuNP/RBD (cyan) and G-PNR-AuNP/RBD after interaction with human IgG (1.0 μg mL^{-1}) (orange) in PBS (0.01 mol L^{-1}, pH 7.4), ν = 50 mV s^{-1}; B) Hybrid I_{ds} *vs.* V_{ds} EE curves for bare graphene (black), G-PNR (red), G-PNR-AuNP/RBD (cyan) and G-PNR-AuNP/RBD after interaction with human IgG (1.0 μg mL^{-1}) (orange) in PBS (0.01 mol L^{-1}, pH 7.4), ν = 5 mV s^{-1}; C) Nyquist plots for bare graphene (black), G-PNR (red), G-PNR-AuNP/RBD (cyan) and G-PNR-AuNP/RBD after interaction with human IgG (1.0 μg mL^{-1}) (orange) interfaces in PBS (0.01 mol L^{-1}, pH 7.4), from 1 × 10^{5} to 0.1 Hz, amplitude = 5 mV and DC$_{pot}$ = OCP of each interface; D) Respective impedance modulus plots for each interface of item C). (For interpretation of the references to color in this figure legend, the reader is referred to the Web version of this article.)

affinity, useful for our next analytical studies (Mazar et al., 2017; Prakash et al., 2018). Typical redox peaks are observed due to irreversible monomer oxidation at +0.86 V (*vs.* Ag/AgCl$_{sat}$) and the redox pair interconversion neutral red – *leuco*-neutral red at −0.585 V (*vs.* Ag/AgCl$_{sat}$) (Pauliukaite et al., 2007). After this procedure, the formation of G-PNR interface (Figure S4B) and its stability is electrochemically observed in Fig. 3D. Although the reversibility of neutral red – *leuco*-neutral red redox pair is affected, the presence of oxidation peak concerning this redox pair at *c.a.* + 0.6 V is interpreted as indicative of a successful and stable electropolymerization.

Then, hybrid EE I_{ds} *vs.* V_{ds} curves were obtained for graphene and G-PNR interfaces (Fig. 1E and F). For this, CE and WE terminals are directly connected through G-PNR basal plane, allowing current flow with high charge carrier mobility and low intrinsic resistivity (Vieira et al., 2016; Wang et al., 2012). Moreover, in this configuration, it is possible to monitor interfacial OCP displacements (ΔV_{OCP}) depending on the modification of the graphene interface (Mattioli et al., 2021). The OCP shifts are correlated to capacitive alterations of the EEVD interface and they are observed at more negative potentials due to PNR adsorption. As, EE experiments are performed in a potential range without the occurrence of PNR faradaic processes, we expected that only capacitive alterations would be manifested in G-PNR interfaces during these studies. As already discussed in our previous work (Mattioli et al., 2021), this shift is also an indicative of charge carrier insertion onto graphene, resulting in *n*-doping. This occurs probably due to the establishment of weak van der Waals interactions between graphene sp^2 lattice and neutral red sp^2 electronic density (Georgakilas et al., 2016) and nitrogen atoms of PNR structure. This coupling can be confirmed by G band displacements in Raman spectroscopy data (Figure S5). Despite this, our Raman spectroscopy characterizations of G-PNR could not be useful to corroborate hybrid EE doping insights, as expected due to the creation of some point defects during voltammetric cycling. (See Section 4 of SI for further discussion). Further interfacial capacitive features of graphene and G-PNR EEVDs interfaces were also investigated and confirmed by EIS measurements. A detailed discussion is presented in Section 5 of SI. Therefore, we conclude that G-PNR interfaces would not present any faradaic process, but only capacitive features to be considered during further bioanalytical IgG quantifications by EE studies.

3.2. AuNP/RBD and G-PNR-AuNP/RBD EEVDs surface characterization

G-PNR EEVDs was modified with RBD protein by non-covalent functionalization with AuNP-based bioconjugates, aiming IgG detections through antigen-antibody interaction. It is known that AuNP-based bioconjugates with proteins are established through electrostatic interactions by chemisorption mechanisms (Busch et al., 2019). UV-Vis spectra were collected after each step of the procedure (Figure S8). Transmission electron microscopy (TEM) images of AuNP/RBD bioconjugate are in accordance with UV–Vis results (See Section S7 for further information). As shown in Fig. 2A, the coating material on AuNP characterizes RBD protein, indicating that the protein effectively interacts with AuNP (Busch et al., 2019). AuNP/RBD bioconjugate was drop-casted onto G-PNR EEVDs as illustrated in Fig. 2B. The distribution of AuNP/RBD onto G-PNR was evaluated by micro-FTIR 2D and 3D chemical mapping of AuNP/RBD spatial distribution.

Optical image of G-PNR-AuNP/RBD interface onto Au substrate shown in Fig. 2C indicates that most of AuNP/RBD proteinaceous bioconjugate have a tendency to accumulate on G-PNR edges while aqueous solvent is dried due to coffee-ring effects, typical in protein-based coatings (Devineau et al., 2016; Sedenho et al., 2021). From 2D and 3D special distribution of AuNP/RBD (Fig. 2D and E, respectively), it is observed that the homogeneity of AuNP/RBD distribution is associated to the homogeneity of PNR electropolymerization onto graphene. Fresh solution containing the precursors of electropolymerization was always used. In order to ensure a homogeneous AuNP/RBD immobilization over G-PNR surface, solvent evaporation in drop-casting procedures should be carried out at room temperature, to avoid extensive coffee-ring formation.

3.3. G-PNR-AuNP/RBD interaction with IgG

To understand the expected capacitance alterations at G-PNR-AuNP/RBD interface due to IgG interaction with immobilized RBD sites, EE and electrochemical experiments of the specific antigen-antibody interaction with IgG (1.0 μg mL^{-1}) as target were carried out. Electrochemical behavior of G-PNR-AuNP/RBD was first investigated by cyclic voltammetry (Fig. 3A). Neither the adsorption of AuNP/RBD bioconjugate nor its interaction with human IgG (1.0 μg mL^{-1}) interferes on PNR redox behavior and only capacitive changes are observed. This was already expected, as both bioconjugates do not present redox-active sites (from −1.0V to 1.0V). Therefore, EE I_{ds} *vs.* V_{ds} curves for these interfaces were obtained within a potential range with no faradaic process occurring (Fig. 3B). The immobilization of AuNP/RBD bioconjugate onto G-PNR leads to OCP value shifts to more positive values in relation to G-PNR interface OCP potential value, probably due to G-PNR sp^2 electronic density displacement towards AuNP/protein bioconjugate. These shifts occasioned by charge insertion/removal and electronic density variations in EEVDs are correlated to capacitive changes that lead to OCP potential displacements (Mattioli et al., 2021). Similar to what is observed for Graphene Field-Effect Transistors (GFET), these OCP shifts can be interpreted in a similar way as it is done for the charge neutrality point (CNP). The interaction of IgG with G-PNR-AuNP/RBD interface could be monitored by ΔV_{OCP} shifts, and in this case, the specific RBD-IgG interaction led to $\Delta V_{OCP} = 0.0437$ V compared to the G-PNR-AuNP/RBD initial potential. The shift of OCP potential to more positive values (*p*-doping) due to specific IgG interaction is coherent to the presence of a positive net charge, as the type of the human IgG antibody (IgG1) used in this work present an isoelectric point (pI) that mainly ranges from 7.9 to 8.6 (Yang et al., 2019). Based on these results, it was concluded that G-PNR-AuNP/RBD EEVDs interface can be sensitive to IgG interaction and detections through ΔV_{OCP} potential displacements.

In order to confirm the capacitive nature of the above-mentioned interfaces and the IgG interaction, EIS data were collected in a non-electroactive electrolyte medium (Fig. 3C and D). Capacitive alterations in accordance to EE data in Fig. 3B can be also seen due to each subsequent modification of EEVD interface based on Nyquist plots inclination changes. The inclination of G-PNR-AuNP/RBD Nyquist plot in Fig. 3C is close to the bare graphene one, indicating that the employed subsequent modifications led to an increase in total interfacial capacitance of the EEVD (Fig. 3D), until it reaches values similar to the bare graphene one (Mattioli et al., 2021). The predominance of capacitive features G-PNR-AuNP/RBD interface can be confirmed. It was also possible to fit a best circuit to describe G-PNR-AuNP-RBD impedance features, which was the same obtained for G-PNR (Figure S7B). These insights can be corroborated by the impedance modulus plots of Fig. 3D as well, based on the absence of peaks through the entire swept frequency range. EIS data corroborated to all ΔV_{OCP} potential displacements occurred due to capacitive alterations at each EEVD interface and, therefore, IgG detections in different concentrations may be performed based on these principles.

3.4. COVID-19 diagnosis through IgG quantifications by G-PNR-AuNP/RBD EEVDs

We proceeded with the development of an analytical quantification method for serological diagnosis related to COVID-19 disease, based on total interfacial capacitance alterations on the EEVD interface due to specific RBD-IgG interaction (Fig. 4A). For this, ΔV_{OCP} were monitored as a function of IgG concentration, as indicated in Equation (1).

$$\Delta V_{OCP} = E_{int} = E_{int}^{(PNR-AuNP/RBD)-IgG} - E_{int}^{(PNR-AuNP/RBD)} \tag{1}$$

In this Equation, $E_{int}^{(PNR-AuNP/RBD)-IgG}$ corresponds to the interfacial OCP potential of G-PNR-AuNP/RBD interface after adsorption and interaction with IgG and $E_{int}^{(PNR-AuNP/RBD)}$ corresponds to the G-PNR-AuNP/RBD interfacial OCP potential before interaction with IgG. All detections were performed in a miniaturized configuration by using a drop of 40 μL of electrolyte as reactional medium. A calibration curve shows an unprecedent wide linear range of IgG concentrations, from 10^{-12} up to 10^{-7} mol L^{-1}. Despite of the absence of COVID-19-related IgG detections by GFETs, the extent of this dynamic linear range is wider than the obtained for IgG COVID-19 diagnosis through electrochemical methods

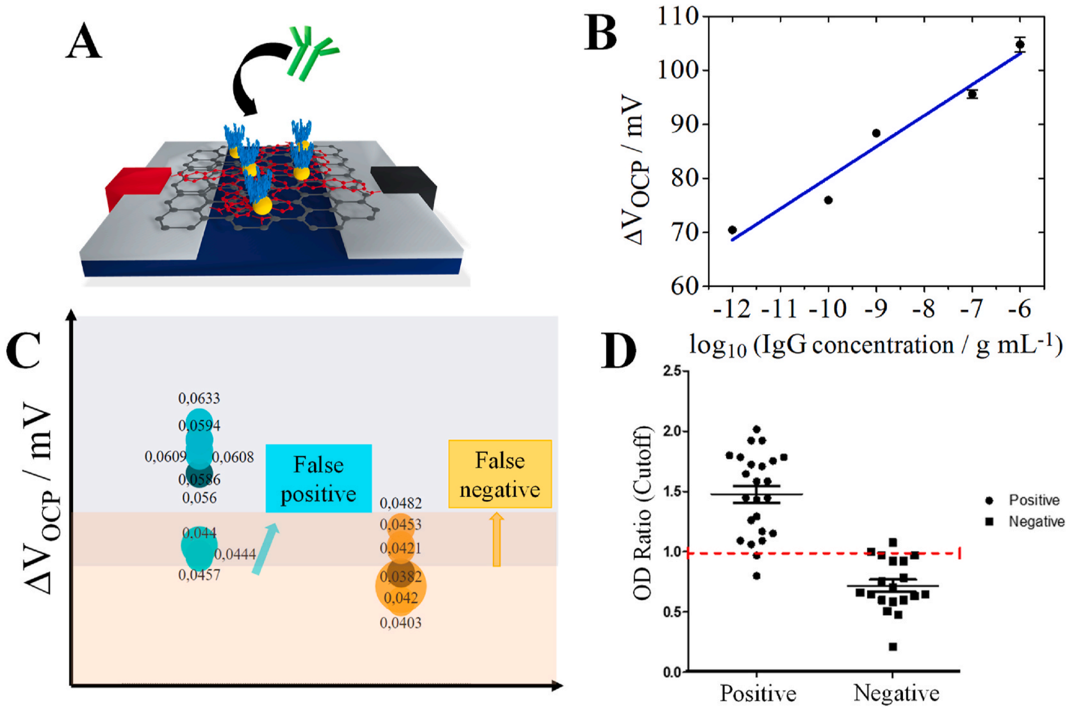

Fig. 4. IgG detections for COVID-19 diagnosis through EEVD. A) Schematic representation of G-PNR-AuNP/RBD interface detecting IgG antibodies; B) Calibration curve for IgG detections from 1.0 pg mL^{-1} to 1.0 μg mL^{-1} concentrations in PBS (0.01 mol L^{-1}, pH 7.4) as support electrolyte by hybrid I_{ds} *vs.* V_{ds} EE experiments at 5 mV s^{-1}; C) Distribution of OCP displacement values for n = 9 for positive and negative IgG detections in diluted patient serum samples by G-PNR-AuNP/RBD EEVD; D) Analysis via ELISA dimerized intact RBD in samples from 20 positive and negative patients.

reported elsewhere (Torrente-Rodríguez et al., 2020). The EEVD sensitivity obtained for IgG quantifications based on the slope of calibration curve was of 5.8 mV/decade. A LOD of 1.0 pg mL^{-1} was obtained. The LOD was evaluated according to IUPAC recommendations, by using the standard deviation of the lowest concentration sample to estimate the signal-to-noise ratio of our device, with 99% of confidence level (Brunetti B, 2015; Inczedy et al., 1998). Interestingly, to the best of our knowledge, there has, so far, one of the lowest LODs already reported in literature, where EEVD performance is compared to other serological assays presented in Table 1. This can be related to the high sensitivity of the EEVD interface to its chemical environment and to the EE detection method through interfacial capacitive alterations. Due to the similarities of the EEVDs to GFETs, a comparison between these two kinds of devices is of relevant interest. However, no FET or GFET was reported in literature for RBD-based IgG detections. The reached LOD value by G-PNR-AuNP/RBD, as well as its sensitivity were compared to the values obtained for general immunoglobulin detections by FETs. For example, G-PNR-AuNP/RBD LOD was comparable to the obtained by Vu and co-authors using a GFET (1.0 pg mL^{-1}) (Vu et al., 2021), and remarkably lower than the reached by Minamiki and co-authors applying an OFET (0.62 μg mL^{-1}) (Minamiki et al., 2014). The sensitivity of G-PNR-AuNP/RBD obtained by the slope of the calibration curve could not be compared to the values reported by different serological assays due to incompatibility of units.

Although the EEVDs reported here for the diagnosis of COVID-19 have a great positive impact in the area of biosensors using graphene monolayers, it is necessary to emphasize that other works using GFETs sensors for different proteins achieved remarkable sensitivity. Just to exemplify among several studies, Danielson and collaborators reached 14 mV/decade for streptavidin (Danielson et al., 2020). Our value of 5.8 mV/decade can be correlated to the low sensitivity of G-PNR interface to the IgG-AuNP/RBD complex formation due to the establishment of antigen-antibody interaction. This value may improve replacing PNR by other non-covalent modifier, capable of stronger interactions with graphene basal plane through more effective heterojunction formation, as, for example, ferrocene derivatives or PBASE for direct IgG immobilization. Consequently, stronger capacitive alterations would be observed with the addition of each target analyte concentration. Despite of this, IgG detections by G-PNR-AuNP/RBD could be performed in a short time of analyses. Each EE experimental run can be performed within 5 min.

Table 1
Comparison of several serological detection methods of IgG antibodies produced in response to SARS-CoV-2 infection.

Detection method	Device components	LOD	Sensitivity	Accuracy/κ coefficient	Reference
LFIA	Paper strip/colloidal AuNP	Not informed	69.1%	κ = 0.612	Wen et al. (2020)
ELISA	NovaLisa SARS-CoV-2 test	0.18 a.u.	94.9%	Not informed	Tré-Hardy et al. (2020)
Electrochemical	COVID-19 ePAD/SWV	0.96 ng mL^{-1}	100%	κ = 0.881	Yakoh et al. (2021)
SERS/LFIA	SERS-based LFIA/Ag@SiO$_2$	1.0 pg mL^{-1}	Not informed	100%	Liu et al. (2021)
Electrochemical	3D nanoprinted electrodes/rGO, Spike S1 subunit	2.8 × 10^{-15} mol L^{-1}	1.0 × 10^{-12} mol L^{-1}	Not informed	Ali et al. (2021)
LFIA	Paper strip/Selenium NPs bioconjugate	5.0 ng mL^{-1}	93.33%	Not informed	Wang et al. (2020)
LISA	N protein	0.4 pg mL^{-1}	71%	Not informed	Liang et al. (2021)
Colorimetric	Epitope functionalized AuNPs	3.2 nmol L^{-1}	83%	Not informed	Lew et al. (2021)
Hybrid EE detections	G-PNR-AuNP/RBD EEVDs	1.0 pg mL^{-1}	5.8 mV/decade	61.1%	This work

ePAD = electrochemical paper based analytical device; SWV = Square Wave Voltammetry; rGO = reduced graphene oxide; LFIA = Lateral Flow Immunochromatographic Assay; SERS = Surface Enhanced Raman Scattering; LISA = Luciferase Immunosorbent Assay.

This feature is considerably advantageous especially in relation to LFIAs and ELISA assays reported in Table 1, which experimental runs usually take more than 15–20 min. Furthermore, other assays reported in this table require extensive device preparations with nanoparticles functionalization and expensive electrode printings, making the proposed methodologies less suitable for fast and simple serologic COVID-19 mass-testing of a population.

To further evaluate the analytical performance of our G-PNR-AuNP/RBD EEVD, IgG detections were performed in human sera with n = 9 replicates, for proof-of-concept purposes (Fig. 4C). Mean ΔV_{OCP} potential shifts for positive and negative IgG detections were, respectively, 0.056 ± 0.009 V and 0.042 ± 0.003 V. We used the value of OCP potential displacements that was possible to discriminate the healthy from the infected patient with COVID-19 as cut-off values. The estimated SARS-CoV-2 IgG cut-off was 40 mV. Nonetheless, some quantifications could not be differentiated between a positive or negative result according to the obtained ΔV value. A false-positive region and a false-negative region of ΔV range between 43 and 48 mV could be estimated by our results, probably due to bioconjugates removal during washing steps and EEVD surface harm. Consequently, from a total of 9 samples studied for positive results, 3 of them appeared in the false-positive region. From all 9 samples studied for negative results, 4 of them appeared in the false-negative region. These problems can be overcome by increasing the population size of samples to be analyzed by our EEVD. Despite these issues and the relatively small population size, the obtained results indicated that the proposed EEVD can be a suitable device for point-of-care serologic diagnosis.

Lastly, we estimated possible interferents for IgG detections by G-PNR-AuNP/RBD in human sera. We evaluated human IgM, BSA and bilirubin oxidase enzyme (Mattioli et al., 2020). Experiments in 0.01 mol L^{-1} PBS pH 7.4 were performed and ΔV_{OCP} shifts obtained for each studied biomolecule (1.0 μg mL^{-1} concentration) was compared to the ΔV_{OCP} shift presented by the detection of 1.0 μg mL^{-1} IgG. The obtained results are illustrated in Figure S10. It is noticeable that human IgM presented the higher interference, as bilirubin oxidase and BSA did not interfere significantly. This tendency was expected as human IgM also has immunogenic activity against SARS-CoV-2 viral infections and can bind to RBD through antigen-antibody interactions. As BSA and bilirubin oxidase does not bind to RBD through this mechanism, low interference from these proteins was already expected. Despite of the interference for the proposed IgG detection method, these results gave us insights on future improvements, by considering IgM as another target analyte for total antibody serologic detections aiming COVID-19 diagnosis. This strategy is similar to what is already used by a number of immunoassays in literature (Carter et al., 2020; Imai et al., 2020; Montesinos et al., 2020; Wang et al., 2020).

Positive and negative tests with EEVD were compared with ELISA, based on RBD and human IgG specific interactions. (Fig. 4D). Nine replicates (n = 9) already evaluated by EEVDs were added in a n = 20 population, in order to minimize relative errors and measurement uncertainty (Biswas and Kumar Saha, 2015). Likewise, ELISA quantifications also presented false results, indicating that this may be originated from non-specific interactions that still happen in extra RBD active sites. Apart from this, all human sera samples with true-positive results (6 from a total of 9 samples) by EEVD recovered positive results by ELISA. True-negative COVID-19 diagnosis returned by IgG detections (5 of a total of 9 samples) by EEVDs also presented negative results by ELISA. Based on these results and validation methodologies from Brazilian Society of Laboratorial Medicine, Brazilian Society of Clinical Analyzes and Brazilian Society of Clinical Pathology (ABRAMED, 2021), it was possible to estimate a accuracy of 61.1% and sensitivity of 66.7% by considering a division of true positive and true negative samples by total of analyzed samples. The sensitivity obtained for our serological evaluation in real samples is lower than the values reported in literature, as presented in Table 1. However, it is expected that both sensitivity and accuracy values can be improved for analyses with larger populations. (Mattioli and Crespilho, 2020) Although false-positive and false-negative results were presented in both assays, it is possible to infer that a satisfactory accuracy could be achieved by employing EEVD in our proof-of-concept studies in real human serum samples.

4. Conclusions

A graphene-based EEVD was developed aiming serologic COVID-19 diagnosis applications. For EEVD fabrication, non-covalent functionalization with PNR was adopted in order to allow AuNP/RBD bioconjugate proper adsorption onto the device interface, without harming graphene sp^2 lattice. EEVD working principles relied on the current passage through graphene basal plane with high charge carrier mobility. Monitoring interfacial potential (*i.e.,* OCP) displacement with the adsorption of each EEVD modifier was made similarly to the procedures usually adopted in GFETs studies. The specific interaction of adsorbed RBD with IgG showed to be dependent on the IgG concentration, and therefore, an analytical calibration curve could be obtained. A LOD of 1.0 pg mL^{-1} was reached with a sensitivity of 5.8 mV per decade, within a wide linear dynamic range of IgG concentrations varying from 10^{-12} to 10^{-7} g mL^{-1}. These results give us insights on the possibility of using our proposed devices for trace IgG detections, combined with their miniaturized features for rapid point-of-care purposes. Human blood serum samples were evaluated for positive and negative diagnosis of COVID-19 infection based on IgG quantifications, as a proof-of-concept of our device performance in real samples analyses. Although false-positive and false-negative results were obtained, our results showed a satisfactory accuracy of 61.1%, and a sensitivity of 66.7%. EEVD can be considered as promising alternative for COVID-19 serologic detections in large populations, since the device showed good sensitivity, low LOD, rapidness of analyses, robustness and accuracy. All these are desirable analytic parameters for assays destined to pandemics control strategies.

Author contributions

FNC and IAM conceived the original project. FNC, IAM, KRC, LJAM, GCS and MNO designed the experimental procedures. MNO, IT, PMV, SCF, ERM and GMP prepared human real samples. IAM, KRC, LJAM, GCS, MNO, IT, PMV, SCF, ERM and GMP collected the data. IAM, KRC, LJAM, GCS, MNO, IT, PMV, SCF, ERM, GMP, ECS and FNC analyzed the data. This manuscript was written and revised with contributions by all authors.

Declaration of competing interest

The authors declare that they have no known competing financial interests or personal relationships that could have appeared to influence the work reported in this paper.

Acknowledgments

The authors gratefully acknowledge the funding agencies: Sao Paulo Research Foundation (FAPESP) for all the financial support under the grants: 17/20493-2 (L.J.A.M.), 18/11071-0 (I.A.M.), 20/04796-8 (G.C.S.), 20/06752-8 and 20/05030-1 (M.N.O.) and 18/22214-6; 19/15333-1 e 19/12053-8 (F.N.C.); Coordinating Agency for Advanced Training of Graduate Personnel (CAPES), Metabolomics and Diagnostic Research Network of Covid-19 (MeDiCo Network), CAPES-Brazil grant number: 88881.504532/2020-01 and for the fellowship grant 88887.511448/2020-00 (K.R.C.); and National Council of Scientific and Technological Development (CNPq). Authors are grateful for Professor Edson Leite's immeasurable effort to Brazilian science during the pandemic, and thankful to Rui Murer for all electrical contacts deposition at LNNano, and CNPEM-Brazil for their facilities.

Appendix A. Supplementary data

Supplementary data to this article can be found online at https://doi.org/10.1016/j.bios.2021.113866.

Abbreviations

EEVD	electrical-electrochemical vertical device
IgG	Immunoglobulin G
GFET	graphene field-effect transistor
EE	Electrical-Electrochemical
PNR	poly-neutral red
CNP	charge neutrality point
OCP	open-circuit potential
EIS	electrochemical impedance spectroscopy
CVD	carbon vapor deposition
RBD	receptor binding domain
LOD	limit of detection

References

Abramed, Sbac, Cbdl, Sbpc/Ml, 2021.

Akbari Nakhjavani, S., Afsharan, H., Khalilzadeh, B., Ghahremani, M.H., Carrara, S., Omidi, Y., 2019. Biosens. Bioelectron. 141, 111439.

Ali, M.A., Hu, C., Jahan, S., Yuan, B., Saleh, M.S., Ju, E., Gao, S.J., Panat, R., 2021. Adv. Mater. 33, 1–15.

Biswas, S., Kumar Saha, M., 2015. Immunochem. Immunopathol. 1–5, 01.

Bleu, Y., Bourquard, F., Loir, A.S., Barnier, V., Garrelie, F., Donnet, C., 2019. J. Raman Spectrosc. 50, 1630–1641.

Brownson, D.A.C., Varey, S.A., Hussain, F., Haigh, S.J., Banks, C.E., 2014. Nanoscale 6, 1607–1621.

Brunetti B, D.E., 2015. Pharm. Anal. Acta, 06.

Brunner, H., Mayer, U., Hoffmann, H., 1997. Appl. Spectrosc. 51, 209–217.

Busch, R.T., Karim, F., Weis, J., Sun, Y., Zhao, C., Vasquez, E.S., 2019. ACS Omega 4, 15269–15279.

Carter, L.J., Garner, L.V., Smoot, J.W., Li, Y., Zhou, Q., Saveson, C.J., Sasso, J.M., Gregg, A.C., Soares, D.J., Beskid, T.R., Jervey, S.R., Liu, C., 2020. ACS Cent. Sci. 6, 591–605.

Chaibun, T., Puenpa, J., Ngamdee, T., Boonapatcharoen, N., Athamanolap, P., O'Mullane, A.P., Vongpunsawad, S., Poovorawan, Y., Lee, S.Y., Lertanantawong, B., 2021. Nat. Commun. 12, 1–10.

Charles A Janeway, J., Travers, P., Walport, M., Shlomchik, M.J., 2001. Immunobiol. Immune Syst. Heal. Dis. 1–9.

Chen, W.H., Hotez, P.J., Bottazzi, M.E., 2020. Hum. Vaccines Immunother. 16, 1239–1242.

Danielson, E., Sontakke, V.A., Porkovich, A.J., Wang, Z., Kumar, P., Ziadi, Z., Yokobayashi, Y., Sowwan, M., 2020. Sensor. Actuator. B Chem. 320, 128432.

de Oliveira, T.R., Martucci, D.H., Faria, R.C., 2018. Sensor. Actuator. B Chem. 255, 684–691.

Devineau, S., Anyfantakis, M., Marichal, L., Kiger, L., Morel, M., Rudiuk, S., Baigl, D., 2016. J. Am. Chem. Soc. 138, 11623–11632.

Filik, H., Aslıhan Avan, A., 2020. Microchem. J. 158, 105242.

Georgakilas, V., Tiwari, J.N., Kemp, K.C., Perman, J.A., Bourlinos, A.B., Kim, K.S., Zboril, R., 2016. Chem. Rev. 116, 5464–5519.

Guo, S., Wang, E., 2007. Anal. Chim. Acta 598, 181–192.

Hashemi, S.A., Bahrani, S., Mousavi, S.M., Omidifar, N., Behbahan, N.G.G., Arjmand, M., Ramakrishna, S., Lankarani, K.B., Moghadami, M., Shokripour, M., Firoozsani, M., Chiang, W.-H., 2021. J. Electroanal. Chem. 894, 115341.

Hassan, A., Macedo, L.J.A., Mattioli, I.A., Rubira, R.J.G., Constantino, C.J.L., Amorim, R. G., Lima, F.C.D.A., Crespilho, F.N., 2021. Electrochim. Acta 376, 138025.

Imai, K., Tabata, S., Ikeda, M., Noguchi, S., Kitagawa, Y., Matuoka, M., Miyoshi, K., Tarumoto, N., Sakai, J., Ito, T., Maesaki, S., Tamura, K., Maeda, T., 2020. J. Clin. Virol. 128, 104393.

Inczedy, J., Lengyel, T., Ure, A.M., 1998. International Union of Pure and Applied Chemistry.

Iost, R.M., Crespilho, F.N., Zuccaro, L., Yu, H.K., Wodtke, A.M., Kern, K., Balasubramanian, K., 2014. ChemElectroChem 1, 2070–2074.

Isho, B., Abe, K.T., Zuo, M., Jamal, A.J., Rathod, B., Wang, J.H., Li, Z., Chao, G., Rojas, O. L., Bang, Y.M., Pu, A., Christie-Holmes, N., Gervais, C., Ceccarelli, D., Samavarchi-Tehrani, P., Guvenc, F., Budylowski, P., Li, A., Paterson, A., Yun, Y.F., Marin, L.M., Caldwell, L., Wrana, J.L., Colwill, K., Sicheri, F., Mubareka, S., Gray-Owen, S.D., Drews, S.J., Siqueira, W.L., Barrios-Rodiles, M., Ostrowski, M., Rini, J.M., Durocher, Y., McGeer, A.J., Gommerman, J.L., Gingras, A.C., 2020. Sci. Immunol. 5, 1–14.

Jiang, Z., Feng, B., Xu, J., Qing, T., Zhang, P., Qing, Z., 2020. Biosens. Bioelectron. 166, 112471.

Kudr, J., Michalek, P., Ilieva, L., Adam, V., Zitka, O., 2021. TrAC Trends Anal. Chem. (Reference Ed.) 136, 116192.

Lan, J., Ge, J., Yu, J., Shan, S., Zhou, H., Fan, S., Zhang, Q., Shi, X., Wang, Q., Zhang, L., Wang, X., 2020. Nature.

Lew, T.T.S., Aung, K.M.M., Ow, S.Y., Amrun, S.N., Sutarlie, L., Ng, L.F.P., Su, X., 2021. ACS Nano.

Li, Z., Yi, Y., Luo, X., Xiong, N., Liu, Y., Li, S., Sun, R., Wang, Y., Hu, B., Chen, W., Zhang, Y., Wang, J., Huang, B., Lin, Y., Yang, J., Cai, W., Wang, X., Cheng, J., Chen, Z., Sun, K., Pan, W., Zhan, Z., Chen, L., Ye, F., 2020. J. Med. Virol.

Liang, Y., Yan, H., Huang, L., Zhao, J., Wang, H., Kang, M., Wan, Z., Shui, J., Tang, S., 2021. J. Virol. Methods 292, 114141.

Liu, H., Dai, E., Xiao, R., Zhou, Z., Zhang, M., Bai, Z., Shao, Y., Qi, K., Tu, J., Wang, C., Wang, S., 2021. Sensor. Actuator. B Chem. 329, 129196.

Liu, H., May, K., 2012. mAbs 4, 17–23.

Liu, J., Li, Q., Zou, Y., Qian, Q., Jin, Y., Li, G., Jiang, K., Fan, S., 2013. Nano Lett. 13, 6170–6175.

Macedo, L.J.A., Iost, R.M., Hassan, A., Balasubramanian, K., Crespilho, F.N., 2019. ChemElectroChem 6, 31–59.

Macedo, L.J.A., Lima, F.C.D.A., Amorim, R.G., Freitas, R.O., Yadav, A., Iost, R.M., Balasubramanian, K., Crespilho, F.N., 2018. Nanoscale 10, 15048–15057.

Malard, L.M., Pimenta, M.A., Dresselhaus, G., Dresselhaus, M.S., 2009. Phys. Rep. 473, 51–87.

Mattioli, Isabela A., Crespilho, F.N., 2020. CC-PI-2020–0101.

Mattioli, Isabela Alteia, Crespilho, F.N., 2020. An. Acad. Bras. Cienc. 1–3.

Mattioli, I.A., Hassan, A., Oliveira, O.N., Crespilho, F.N., 2020. ACS Sens.

Mattioli, I.A., Hassan, A., Sanches, N.M., Vieira, N.C.S., Crespilho, F.N., 2021. Biosens. Bioelectron. 175, 112851.

Mazar, F.M., Alijanianzadeh, M., Molaeirad, A., Heydari, P., 2017. Process Biochem. 56, 71–80.

Minamiki, T., Minami, T., Kurita, R., Niwa, O., Wakida, S.I., Fukuda, K., Kumaki, D., Tokito, S., 2014. Materials (Basel) 6, 6843–6852.

Montesinos, I., Gruson, D., Kabamba, B., Dahma, H., Wijngaert, S. Van Den, Reza, S., Carbone, V., Vandenberg, O., Gulbis, B., Wolff, F., Rodriguez-Villalobos, H., 2020. J. Clin. Virol. 128, 104413.

Pauliukaite, R., Brett, C.M.A., 2008. Electroanalysis 20, 1275–1285.

Pauliukaite, R., Ghica, M.E., Barsan, M., Brett, C.M.A., 2007. J. Solid State Electrochem. 11, 899–908.

Pingarrón, J.M., Yáñez-Sedeño, P., González-Cortés, A., 2008. Electrochim. Acta 53, 5848–5866.

Prakash, A., Pathrose, B.P., Mathew, S., Nampoori, V.P.N., Radhakrishnan, P., Mujeeb, A., 2018. Opt. Mater. (Amst). 79, 237–242.

Prasad, K.S., Cao, X., Gao, N., Jin, Q., Sanjay, S.T., Henao-Pabon, G., Li, X.J., 2020. Sensor. Actuator. B Chem. 305, 127516.

Premkumar, L., Segovia-Chumbez, B., Jadi, R., Martinez, D.R., Raut, R., Markmann, A.J., Cornaby, C., Bartelt, L., Weiss, S., Park, Y., Edwards, C.E., Weimer, E., Scherer, E.M., Rouphael, N., Edupuganti, S., Weiskopf, D., Tse, L.V., Hou, Y.J., Margolis, D., Sette, A., Collins, M.H., Schmitz, J., Baric, R.S., de Silva, A.M., 2020. Sci. Immunol. 5, 1–10.

Qing, Z., Li, Yacheng, Li, Younan, Luo, G., Hu, J., Zou, Z., Lei, Y., Liu, J., Yang, R., 2020a. Microchim. Acta 187.

Qing, Z., Luo, G., Xing, S., Zou, Z., Lei, Y., Liu, J., Yang, R., 2020b. Angew. Chem. Int. Ed. 59, 14044–14048.

Raffle, A.E., Pollock, A.M., Harding-edgar, L., 2020. BMJ 10–11.

Ragavendar, M.S., Anmol, C.M., 2012. Proc. Annu. Int. Conf. IEEE Eng. Med. Biol. Soc. EMBS 2408–2411.

Raoof, M., Jans, K., Bryce, G., Ebrahim, S., Lagae, L., Witvrouw, A., 2013. Microelectron. Eng. 111, 421–424.

Reddy, D., Register, L.F., Carpenter, G.D., Banerjee, S.K., 2012. J. Phys. D. Appl. Phys. 45.

Roy, E., Patra, S., Tiwari, A., Madhuri, R., Sharma, P.K., 2017. Biosens. Bioelectron. 89, 234–248.

Sedenho, G.C., Hassan, A., Macedo, L.J.A., Crespilho, F.N., 2021. J. Power Sources 482, 229035.

Seo, G., Lee, G., Kim, M.J., Baek, S.-H., Choi, M., Ku, K.B., Lee, C.-S., Jun, S., Park, D., Kim, H.G., Kim, S.-J., Lee, J.-O., Kim, B.T., Park, E.C., Kim, S. Il, 2020. ACS Nano.

Sun, B., Feng, Y., Mo, X., Zheng, P., Wang, Q., Li, P., Peng, P., Liu, X., Chen, Z., Huang, H., Zhang, Fan, Luo, W., Niu, X., Hu, P., Wang, L., Peng, H., Huang, Z., Feng, L., Li, Feng, Zhang, Fuchun, Li, Fang, Zhong, N., Chen, L., 2020. Emerg. Microb. Infect. 1–36, 0.

Suresh, L., Brahman, P.K., Reddy, K.R., Bondili, J.S., 2018. Enzym. Microb. Technol. 112, 43–51.

Theel, E.S., Harring, J., Hilgart, H., Granger, D., 2020. J. Clin. Microbiol. 58.

Torrente-Rodríguez, R.M., Lukas, H., Tu, J., Min, J., Yang, Y., Xu, C., Rossiter, H.B., Gao, W., 2020. Matter 3, 1981–1998.

Tré-Hardy, M., Wilmet, A., Beukinga, I., Favresse, J., Dogné, J.M., Douxfils, J., Blairon, L., 2020. J. Med. Virol. 93, 803–811.

Turkevich, J., Stevenson, P.C., Hillier, J., 1951. Discuss. Faraday Soc. 55, 55–75.

Vieira, N.C.S., Borme, J., Machado, G., Cerqueira, F., Freitas, P.P., Zucolotto, V., Peres, N. M.R., Alpuim, P., 2016. J. Phys. Condens. Matter 28.

Vu, C.A., Pan, P.H., Yang, Y.S., Chan, H.W.H., Kumada, Y., Chen, W.Y., 2021. Sensors (Switzerland) 21, 1–12.

Wang, Q.H., Jin, Z., Kim, K.K., Hilmer, A.J., Paulus, G.L.C., Shih, C.J., Ham, M.H., Sanchez-Yamagishi, J.D., Watanabe, K., Taniguchi, T., Kong, J., Jarillo-Herrero, P., Strano, M.S., 2012. Nat. Chem. 4, 724–732.

Wang, Z., Zheng, Z., Hu, H., Zhou, Q., Liu, W., Li, X., Liu, Z., Wang, Y., Ma, Y., 2020. Lab Chip 20, 4255–4261.

Wen, T., Huang, C., Shi, F.J., Zeng, X.Y., Lu, T., Ding, S.N., Jiao, Y.J., 2020. Analyst 145, 5345–5352.

Who, 2020. Situation by WHO Region.

Yakoh, A., Pimpitak, U., Rengpipat, S., Hirankarn, N., Chailapakul, O., Chaiyo, S., 2021. Biosens. Bioelectron. 176, 11912.

Yang, D., Kroe-Barrett, R., Singh, S., Laue, T., 2019. Antibodies 8, 24.

Yang, Jingyun, Wang, W., Chen, Z., Lu, S., Yang, F., Bi, Z., Bao, L., Mo, F., Li, X., Huang, Y., Hong, W., Yang, Y., Zhao, Y., Ye, F., Lin, S., Deng, W., Chen, H., Lei, H., Zhang, Z., Luo, M., Gao, H., Zheng, Y., Gong, Y., Jiang, X., Xu, Y., Lv, Q., Li, D., Wang, M., Li, F., Wang, S., Wang, Guanpeng, Yu, P., Qu, Y., Yang, L., Deng, H., Tong, A., Li, J., Wang, Z., Yang, Jinliang, Shen, G., Zhao, Z., Li, Y., Luo, J., Liu, H., Yu, W., Yang, M., Xu, J., Wang, J., Li, H., Wang, H., Kuang, D., Lin, P., Hu, Z., Guo, W., Cheng, W., He, Y., Song, X., Chen, C., Xue, Z., Yao, S., Chen, L., Ma, X., Chen, S., Gou, M., Huang, W., Wang, Y., Fan, C., Tian, Z., Shi, M., Wang, F.S., Dai, L., Wu, M., Li, G., Wang, Guangyu, Peng, Y., Qian, Z., Huang, C., Lau, J.Y.N., Yang, Z., Wei, Y., Cen, X., Peng, X., Qin, C., Zhang, K., Lu, G., Wei, X., 2020. Nature 586, 572–577.

Zeng, L., Li, Y., Liu, J., Guo, L., Wang, Z., Xu, X., Song, S., Hao, C., Liu, L., Xin, M., Xu, C., 2020. Mater. Chem. Front.

Zhang, Y., Liu, X., Wang, L., Yang, H., Zhang, X., Zhu, C., Wang, W., Yan, L., Li, B., 2020. Sci. Rep. 10, 9604.

Zhu, Y., Murali, S., Cai, W., Li, X., Suk, J.W., Potts, J.R., Ruoff, R.S., 2010. Adv. Mater. 22, 3906–3924.

Supporting information

Graphene-Based Hybrid Electrical-Electrochemical Point-of-Care Device for Serologic COVID-19 Diagnosis

*Isabela A. Mattioli[1], Karla R. Castro[1], Lucyano J. A. Macedo[1]; Graziela C. Sedenho[1] Mona N Oliveira[2], Iris Todeschini[2], Phelipe M. Vitale[2], Suzete C. Ferreira[4,5], Erika R. Manuli[3,6], Geovana M. Pereira[3], Ester C. Sabino [3,6] and Frank N. Crespilho[1]**

[1]São Carlos Institute of Chemistry, University of São Paulo, São Carlos, SP 13560-970, Brazil
[2] Biolinker Synthetic Biology EIRELI, São Paulo, 05508-000, Brazil
[3] Institute of Tropical Medicine, Faculty of Medicine, University of São Paulo, 05403-000, Brazil
[4] Laboratory of Medical Investigation in Pathogenesis and Targeted Therapy in Onco-Immuno-Hematology (LIM-31), Department of Hematology, Clinical Hospital HCFMUSP, Faculty of Medicine, University of São Paulo, São Paulo, 01246903, Brazil
[5] Division of Research and Transfusion Medicine, São Paulo Hemocentre Pro-Blood Foundation, São Paulo, 05403000, Brazil
[6] LIM-46 HC-FMUSP – Laboratory of Medical Investigation, Clinical Hospital, Faculty of Medicine, University of São Paulo, 01246903, Brazil

Keywords: SARS-CoV-2, COVID-19, serologic detections, graphene, IgG, biosensor

1. EEVD preparation

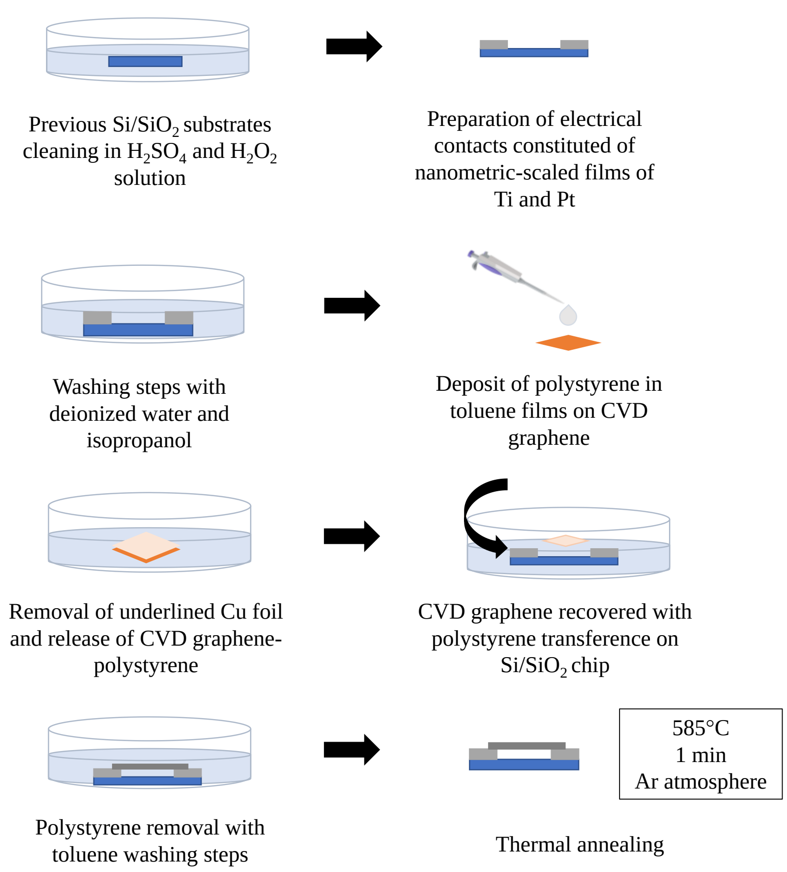

Figure S1 - Pristine graphene EEVD confection. Schematic representation of the steps involved on the monolayer graphene EEVD confection by wet graphene transfer procedure, mediated by polystyrene polymer.

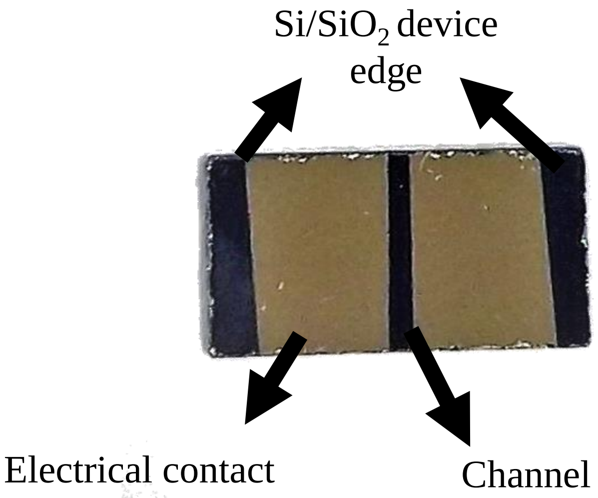

Figure S2 - Pristine graphene EEVD. Photograph of pristine graphene EEVD ready-to-use.

2. Electrochemical etching

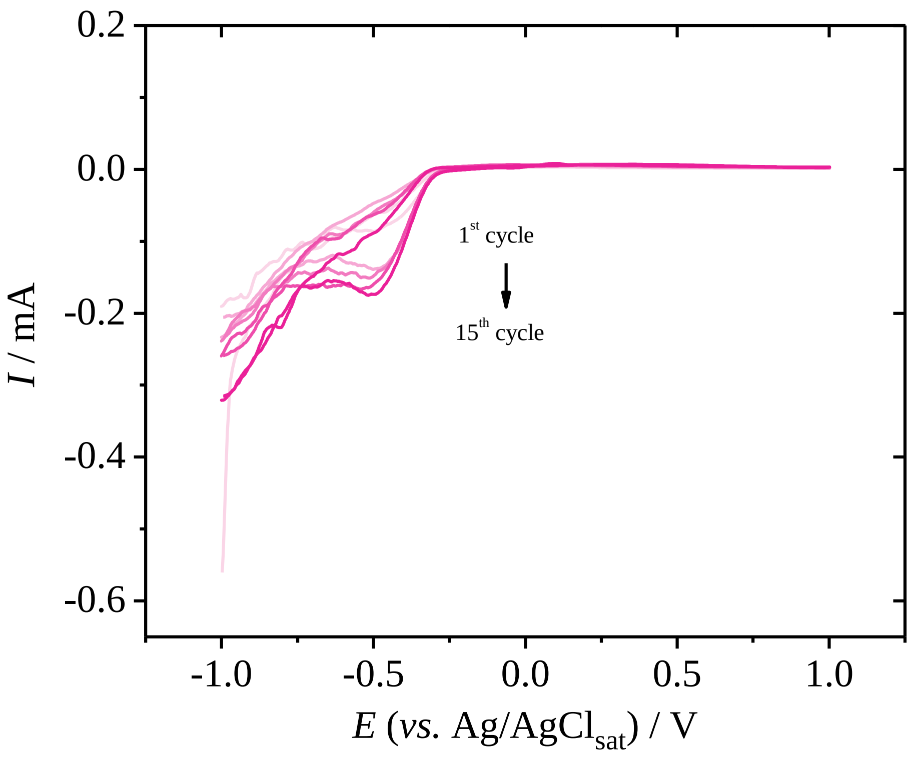

Figure S3 - E-etching of Cu residues. Cyclic voltammograms of Cu residues removal of EEVD graphene surface after wet transfer procedure in 0.1 mol L^{-1} HCl, ν = 100 mV s^{-1}. The color scale varies from clearer pink to darker pink, between 1st, 3rd, 5th, 10th and 15th scans.

3. PNR Electropolymerization

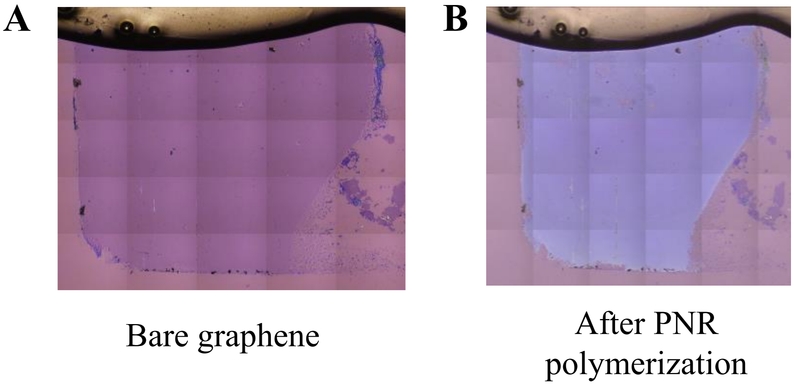

Bare graphene

After PNR polymerization

Figure S4 – Optical images of PNR polymerization. Optical image of large area pristine graphene 2D electrode (A) before and (B) after PNR electropolymerization.

The electropolymerization coating of the graphene sheet is also observed by the color contrast in the optical micrographies, where the PNR-coated graphene sheet becomes much less translucid on Si/SiO_2 substrate.

4. Raman Spectroscopy for G-PNR interface

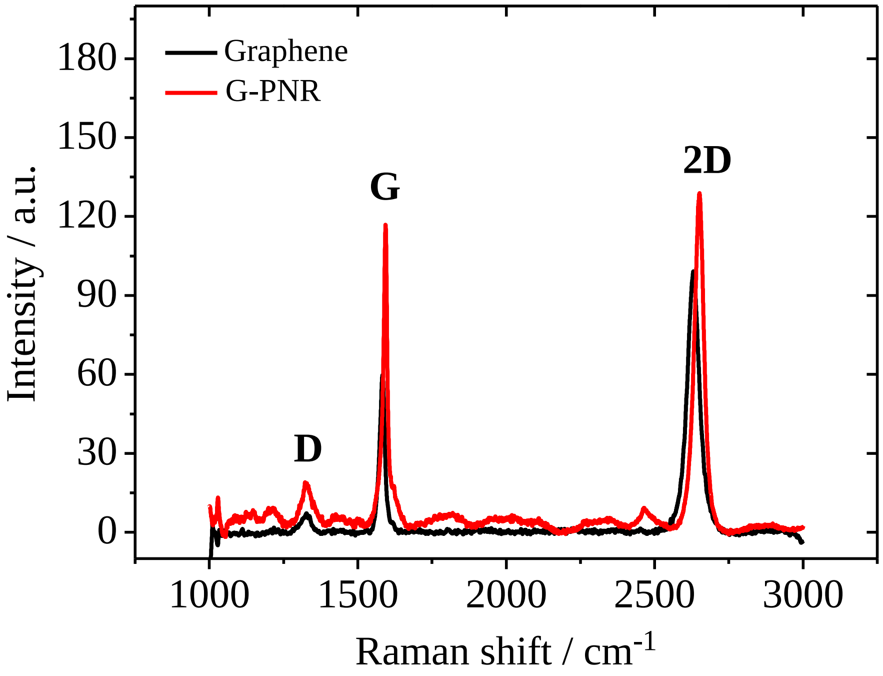

Figure S5 - Raman spectra of graphene and G-PNR electrode surfaces. Comparison between graphene and G-PNR after PNR electropolymerization.

The adsorption of electropolymerized PNR led to the occurrence on *n*-doping onto graphene, according to EEVDs I_{ds} *vs.* V_{ds} results. According to literature, tendencies on *n* or *p*-doping can also be inferred by Raman Spectroscopy, by evaluating G and 2D modes wavenumber shifts.(Wu et al., 2018) However, Raman spectra obtained for both graphene and G-PNR interfaces presented subtle blueshifts of both G and 2D modes, controversially indicating *p*-doping. In fact, evidences of *p*-doping can appear due to sp^3-like defects creation by oxidation of some parts of graphene lattice during electropolymerization by cyclic voltammetry, similarly to what is observed for GO.(Wu et al., 2018) This is corroborated by the increase in D band, generally correlated to point defects on graphene lattice.(Malard et al., 2009) The formation of graphene-polymer composites can also involve stress and strain of graphene lattice and, for this reason, blueshifts are also expected.(Wu et al., 2018)

5. G-PNR Electrochemical Impedance Spectroscopy studies

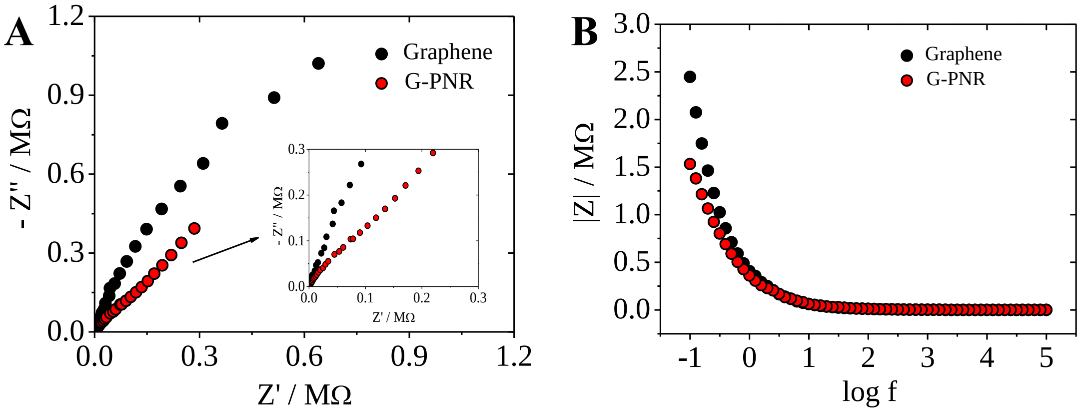

Figure S6 - EIS G-PNR characterization. A) Nyquist plots obtained by EIS for bare graphene (black) and G-PNR (red) EEVD interfaces in a non-electroactive reaction medium (0.01 mol L^{-1} PBS pH 7.4), from 1×10^5 to 0.1 Hz under DC_{pot} = each interface OCP potential, variating with 5 mV of amplitude. B) Impedance modulus curves for graphene (black) and G-PNR (red) interfaces in 0.01 mol L^{-1} PBS pH 7.4, from 1×10^5 to 0.1 Hz, amplitude = 5 mV and DC_{pot} = OCP of each interface

Nyquist plots (Figure S6A) were obtained under OCP potential polarization in a non-electroactive electrolyte, no R_{ct} semicircle was clearly observed, due to the absence of charge transfer processes. For G-PNR, however, a tendency to a semicircle formation can be noticed owing to the faradaic features of electroactive PNR layer. Differences in the plots inclination are generally attributed to capacitive alterations, (Barsoukov and Macdonald, 2013) and in this context, it was possible to infer that PNR modifications decreased the total interfacial capacitance (Figure S6B). This is coherent to the Helmholtz double-layer capacitance model, in which the double-layer capacitance (C_{dl}) is inversely proportional to the double-layer width.(Bard and Faulkner, 2001) This was corroborated by C_{dl} values obtained after best electrochemical circuit fitting (Figure S7): 99.5 ± 5.8 μF cm^{-2} for bare graphene and 84.6 ± 14.1 μF cm^{-2} for G-PNR. Both circuits were simulated based on a typical Randles circuit for electrochemical interfaces. However, ideal double-plate capacitance was replaced by a Constant Phase Element (CPE) in order to take into account interfacial imperfections as roughness, non-homogeneous surface charge distributions, and structural defects.(Barsoukov and Macdonald, 2013) The adsorbed PNR electroactive layer was also considered on equivalent circuit in Figure S7 by adding an extra CPE_{ads} in series to R_{ct}.(Bard and Faulkner, 2001)

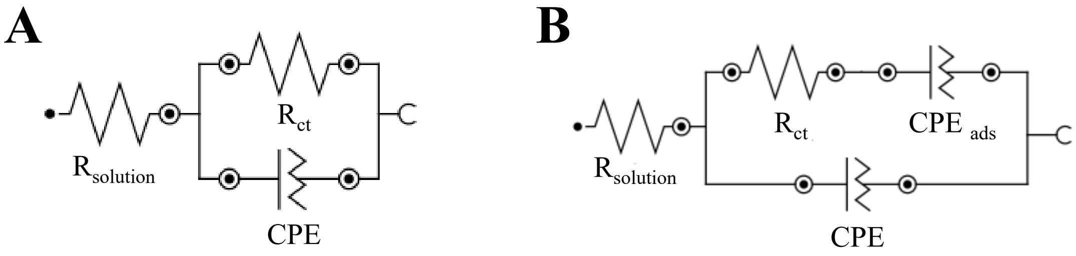

Figure S7 - Equivalent circuits. Equivalent circuits for A) graphene and B) G-PNR interfaces after best electrochemical circuit fitting on NOVA software.

6. UV-Vis for AuNP/RBD bioconjugate

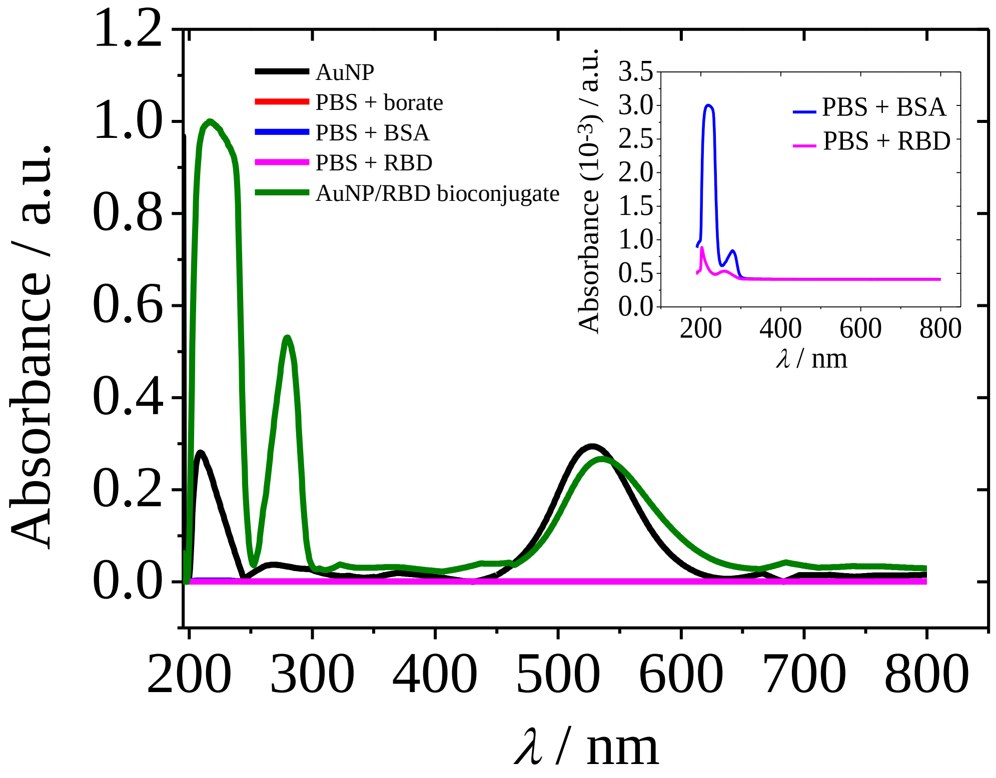

Figure S8 – Bioconjugates UV-Vis spectra. UV-Vis spectra for individual steps of BSA and protein additions for A) AuNP/RBD bioconjugates for the following involved reagents: AuNP (—), PBS + borate buffer (—), PBS + BSA protein (—), PBS + RBD protein (—) and the final AuNP/RBD bioconjugate (—).

All spectra were obtaining considering the spectrum of an aqueous 0.01 mol L^{-1} PBS pH 8 solution as baseline. As expected, AuNP spectrum presented its typical absorption band in 525 nm for AuNP, indicating that insignificant nanoparticles aggregation occurred and the used AuNP may present a diameter value between 15-20 nm.(Cervini et al., 2019) RBD individual spectrum in 0.01 mol L^{-1} PBS pH 8 presented an absorption band in 280 nm, expected due to its proteinaceous nature and the predicted presence of some chromophore residues, as Trp and Tyr.(Nelson and Cox, 2005) This was also valid for individual BSA spectra. Finally, AuNP/RBD spectrum presented a shift in AuNP-525 nm absorption band to higher wavenumbers (537 nm). This redshift is expected for AuNP-based bioconjugates formation and is associated with alterations in the dielectric constant of the electrostatically bonded proteins.(Kozlowski et al., 2018) This is an indicative of interaction establishment between AuNP and RBD and can be used to conclude that the bioconjugate synthesis was successful.

7. TEM characterization for AuNP

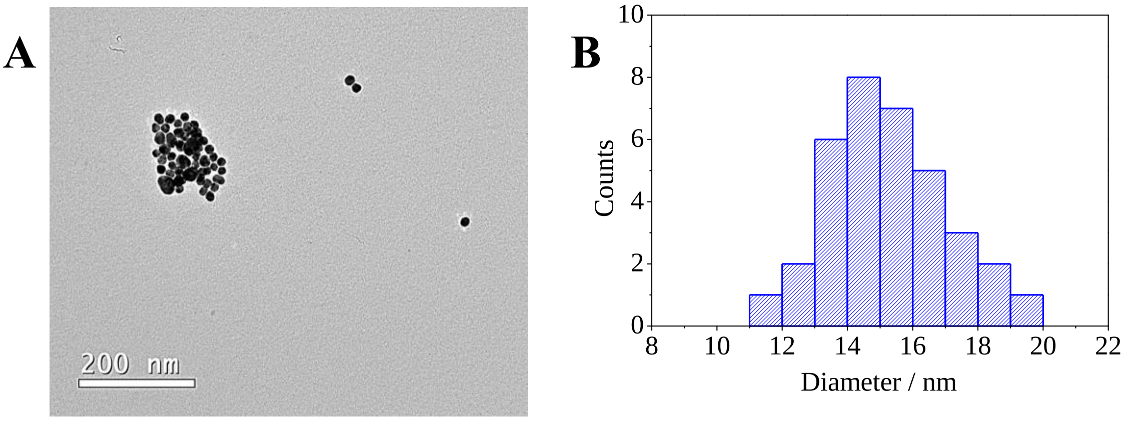

Figure S9 – TEM micrograph for bare AuNP. A) TEM micrograph for bare AuNP colloidal suspension; B) AuNP diameter distribution obtained from TEM micrograph in A), average diameter of (15.3 ± 1.9) nm.

8. Interferents tests

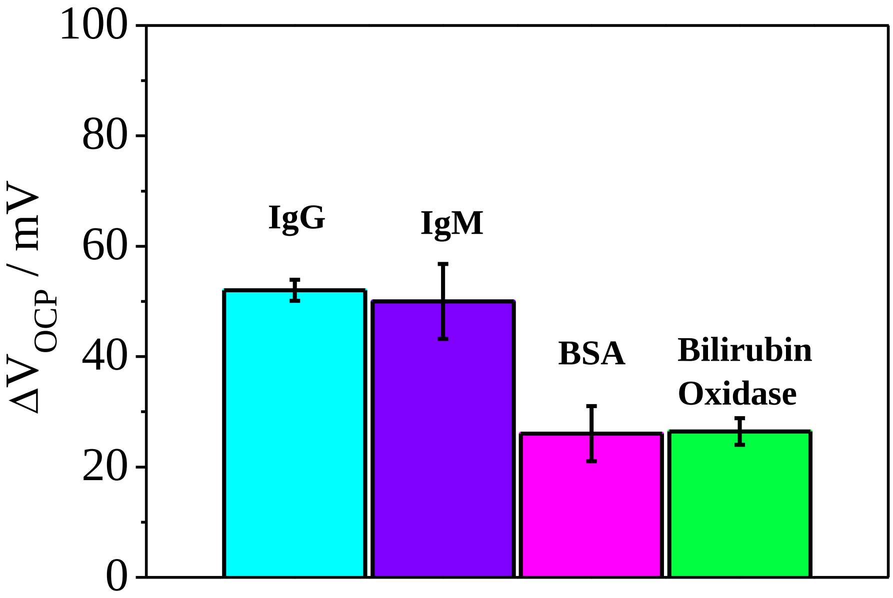

Figure S10 – Possible interferents in IgG detection in human sera samples. Experiments were performed in 0.01 mol L^{-1} PBS pH 7.4 as support electrolyte with 1.0 μg mL^{-1} human IgM, BSA and bilirubin oxidase, respectively.

References

Bard, A.J., Faulkner, L.R., 2001. Electrochemical methods, fundamentals and applications, 2nd ed, John Wiley & Sons, Inc. New York.

Barsoukov, E., Macdonald, J.R., 2013. Impedance Spectroscopy - Theory, Experiment, and Applications. John Wiley & Sons, Inc., Hoboken.

Cervini, P., Mattioli, I.A., Cavalheiro, E.T.G., 2019. RSC Adv. 9, 42306–42315.

Kozlowski, R., Ragupathi, A., Dyer, R.B., 2018. Bioconjug. Chem. 29, 2691–2700.

Malard, L.M., Pimenta, M.A., Dresselhaus, G., Dresselhaus, M.S., 2009. Phys. Rep. 473, 51–87.

Nelson, D.L., Cox, M.M., 2005. Lehninger principles of biochemistry. W. H. Freeman & Company, New York.

Wu, J. Bin, Lin, M.L., Cong, X., Liu, H.N., Tan, P.H., 2018. Chem. Soc. Rev. 47, 1822–1873.

CHAPTER V - Interfacial SARS-CoV-2 RBD femtomolar detections through graphene electrical-electrochemical vertical devices in serum and saliva

In this original work, two different detection devices were developed for COVID-19 diagnosis though serological and viral quantification strategies. For this, the same G-PNR interface employed in the work presented in the Chapter IV was used. A similar strategy in which AuNP-bioconjugates were employed for immobilized probes was adopted, however, with AuNP/IgG species, capable of attaching RBD through antigen-antibody interactions. Further studies on the G-PNR interface were carried out by Micro-Raman mapping, in order to understand the extension of defects generation by PNR electropolymerization. After AuNP/IgG immobilization by drop-casting, Micro-FTIR images were collected to check the distribution of the bioconjugate throughout the surface. Hybrid EE experiments also proved that OCP variations can be used for monitoring RBD interfacial interaction with G-PNR-AuNP/IgG device by the establishment of specific antigen-antibody bondings. Moreover, these OCP shifts were showed to follow a linear relationship as a function of detected RBD. These results were already expected based on the reports of our EEVDs behavior in the previous chapters. A remarkably low LOD of 2.86 fmol L^{-1} with a sensitivity of 6.1 mV/decade was obtained for RBD detections in a wide linear range (from 10^{-12} to 10^{-7} mol L^{-1}), showing the promising sensitivity of the device for early-stage viral diagnosis of COVID-19. Studies on synthetic saliva and bovine fetal serum showed that the device can maintain its sensitivity in more complex matrixes and differentiate positive than negative infected samples in a rapid, easy-to-handle and miniaturized assay.

1. INTRODUCTION

One of the most effective strategies for controlling COVID-19 pandemics and SARS-CoV-2 rapid spread throughout the global communities is performing rapid detections of active viral infections in early stage. (SHAO *et al.*, 2021) Several strategies have been presented with these purposes, mainly relying on antigen and genetic detections. (BAKER *et al.*, 2020; CORMAN *et al.*, 2020; LEE *et al.*, 2021; ROH; JO, 2011; SHAO *et al.*, 2021; TORRENTE-RODRÍGUEZ *et al.*, 2020; ZHANG, Xiaoyan *et al.*, 2020) Among them, antigen detection strategies are attractive because they are inexpensive, with a short turnaround time and high specificity if adequate probes are used. (SHAO *et al.*, 2021) Recently, Lateral Flow Devices (LFD) and POC antigen SARS-CoV-2 for rapid detections have been massively employed due to its high specificity, low cost, facility of operation and rapidness of the analyses. However, their low sensitivity frequently claimed in literature make LFD's reliability and robustness dubious for early stage diagnosis.(MOYSE, 2021; SHAO *et al.*, 2021) Furthermore, its high false negative rates are also disadvantages for patients social isolation maintenance. (MOYSE, 2021) On the other hand, when compared to genetic detections, mainly performed by RT-PCR (Reverse Transcription Polymerase Chain Reaction), antigen detections do not require expensive and specific primers, dedicated laboratory facilities, and highly-skilled operators. (BAKER *et al.*, 2020; MATTIOLI *et al.*, 2020; SHAO *et al.*, 2021) Therefore, these issues related to antigen detections by LFD and genetic detections by RT-PCR are challenges to be overcame in diagnosis research area.

For antigen detections, an antigen domain must be chosen as target for assay development. SARS-CoV-2 Spike (S) protein is one of the most employed encoded genes, due to its primordial importance for infection establishment, cells invasion, and immunity induction through vaccines. (WALLS *et al.*, 2020; YANG *et al.*, 2020) S protein is divided into two subunits, S1 and S2. Its main binding site, the Receptor Binding Domain (RBD), located at S1 subunit, is capable of binding to host cells and allowing cell invasion, specially through interactions with Angiotensin Conversion Enzyme (ACE2). (MATTIOLI *et al.*, 2020) In addition, RBD is a highly specific and dominant target for antibodies response and infection combat in a infected patient. (PREMKUMAR *et al.*, 2020) In this context, literature present several methodologies described for SARS-CoV-2 antigen detection based on optical, (PINALS *et al.*, 2021) electrochemical, (AYDIN; AYDIN; SEZGINTÜRK, 2021; MOJSOSKA *et al.*, 2021), and electrical detections, (SEO *et al.*, 2020; SHAO *et al.*, 2021) as well as immunochromatographic (BAKER *et al.*, 2020) and ELISA (BARLEV-GROSS *et al.*, 2021) assays.

Among these, electrical detections are advantageous due to its rapidness of analyses, high sensitivity and possibility of miniaturization, and delivering POC assays for COVID-19 large-scale infection mapping. Graphene detection devices, by its turn, are promising for application in bioelectronics due to its unique intrinsic properties, as high charge carrier mobility, high electrical conductivity, chemical stability and biocompatibility, being a suitable 2D platform for biomolecules immobilization. (SAN ROMAN; GARG; COHEN-KARNI, 2020) In this sense, for a proper electrical detection by a graphene device with maximum exploration of its high basal plane conductivity, charge carrier mobility, and low basal plane resistivity, the graphene sp^2 carbon lattice must be preserved. (MACEDO *et al.*, 2019; MATTIOLI *et al.*, 2021; SUN; SUN; XIE, 2017) Simultaneously, for improving some analytical features of these devices, as Limit of Detection (LOD), specificity and sensitivity, functionalization is often required. In order to overcome these challenges without harming graphene carbon lattice and decreasing its electrical performance, non-covalent functionalization is the most suitable strategy to be adopted. (SHOWN; GANGULY, 2016) In some cases, the adsorption of compounds onto graphene by $\pi-\pi$ stacking can lead to interesting graphene-based heterojunctions with redox behavior, enabling the application of a hybrid electrical-electrochemical detection methodology.(MATTIOLI *et al.*, 2021) Moreover, by choosing a suitable modifier, these heterojunctions can act as efficient biosensing platform for anchoring proteins and other biomolecules without the need of extensive reactions and covalent modifications.

2. OBJECTIVES

In this work, a miniaturized graphene device modified with COVID-19 monoclonal IgG antibodies was developed for highly sensitive early-stage SARS-CoV-2 detections by specific interactions with RBD domain of S protein. To the best of our knowledge, there are few reports on SARS-CoV-2 viral detections through Spike/RBD antigen targeting using graphene-based electrical devices [7,16] and further studies for analytical performance improvements are needed. For this, a gold nanoparticle (AuNP)-based bioconjugate was employed as immobilized probes for RBD protein, similar to that demonstrated in our previous work. (MATTIOLI *et al.*, 2021) The detection is based on interfacial potential variations due to specific antigen-antibody interactions, similarly to field-effect transistors Dirac's point shifts monitoring, (DONNELLY *et al.*, 2018; MATTIOLI *et al.*, 2021) enabling detections with high sensitivity, device stability, and rapidness. Moreover, the miniaturized features of this working device required only 40 μL of sample in an *on-drop* configuration. This allowed in-field POC detections with the use of miniaturized potentiostat equipment for mass COVID-19.

3. METHODS

3.1. Reagents and materials

Ethanol, isopropanol, monobasic sodium phosphate, potassium phosphate and sulfuric acid were purchased from Synth®, Brazil. Neutral red dye, hydrochloric acid (37% *v/v*), toluene, polystyrene (MM ~192.000 g mol^{-1}), tetrachloroauric acid trihydrate, potassium chloride, lactic acid (85% *v/v*), ethanolamine, Tween 20, bovine fetal serum (BS) and bovine serum albumin (BSA) protein were acquired from Sigma Aldrich®. Hydrogen peroxide (30-32%, *v/v*) was purchased from Vetec®, Brazil, and acetone was obtained from Chemis®, Brazil. Monoclonal IgG human antibodies from SARS-CoV-2 (ab273073) were acquired from Abcam®, (USA). Recombinant SARS-CoV-2 S1-RBD with His tag (MW ~35 kDa) was obtained from Biolinker®, (Brazil). *p*-doped Si/SiO_2 (ϕ_{SiO2} = 90 nm) substrates were acquired from Graphene Supermarket®, USA. CVD (Chemical Vapor Deposition) monolayer graphene was purchased from Graphenea®, Spain. Electrical contact films were made through deposition of Ti and Pt metallic spots obtained from Electron Microscopy Sciences®, USA. All aqueous solutions were prepared with deionized water with resistivity > 18 MΩ cm.

3.2. Samples preparation

BS (Bovine Serum) was used as matrix for RBD detections. Spiked RBD positive samples were prepared according to the literature, (STAMATATOS *et al.*, 2021) by diluting 0.2 mg mL^{-1} RBD in BS matrix (1:500, *v/v*). The negative ones concerned bare BS matrix. Synthetic saliva samples were prepared according to Bao and collaborators. (BAO; KAUR; KIM, 2019) Briefly, 12 μL of lactic acid (85%), NaCl (13.2 mg). KCl (96.5 mg), $CaCl_2$ (17.2 mg), urea (20.4 mg), KH_2PO_4 (65 mg) and carboxymethylcelullose (5 mg) were added to 100 mL of deionized water. Positive saliva samples were spiked with RBD in the 1:500 (*v/v*) proportion.

3.3. AuNP synthesis

Colloidal AuNP was synthetized according to previous literature methods. (TURKEVICH; STEVENSON; HILLIER, 1951) For this, 20 mL of 1.0 mmol L^{-1} $AuCl_3{\cdot}3H_2O$ aqueous solution were heated until it reached boiling point under vigorous stirring. Next, 2.0 mL of 1.0 % (*m/v*) sodium citrate was added and the resulting mixture was kept under vigorous stirring at boiling point until reaching a dark-red color. The resulting AuNP colloidal suspension was cooled at ice bath under light protection. The final suspension was stored at 4 °C and kept protected from light.

3.4. Bioconjugates synthesis

AuNP/IgG bioconjugates were prepared according to a previous reported procedure.(TAGHIPOUR; KHARRAZI; AMINI, 2018) Briefly, 1.5 mL of colloidal AuNP was mixed with 60 µL of 0.1 mol L^{-1} NaOH and 0.6 µL of monoclonal IgG antibody. After incubation at room temperature for 30 min under stirring, 25 µL of 0.4 mg mL^{-1} BSA in deionized water was added, and the resulting mixture was again incubated for 30 minutes at room temperature. Finally, it was centrifuged at 10,000 rpm and 4 °C for 20 minutes, then the AuNP/IgG bioconjugate was resuspended into deionized water, in order to keep the pH between 5.5-6.0, close to the IgG isoelectric point.(TAGHIPOUR; KHARRAZI; AMINI, 2018)

3.5. Micro-FTIR measurements

Micro-FTIR (Fourier Transformed Infrared Spectroscopy) characterizations were performed in a Vertex 70v Fourier Transform Infrared Spectrometer coupled to an Infrared microscope Hyperion 3000 (Bruker). Chemical 2D and 3D images of PNR and AuNP/IgG deposited onto graphene interfaces were obtained using a liquid nitrogen-cooled 64×64 Focal Plane Array (FPA) detector over a 200 × 200 μm^2 area. The measurements were performed in a thin Au layer substrate at room temperature and room atmosphere, with 128 scans acquisition at 8 cm^{-1} resolution. 2D and 3D chemical map of AuNP/IgG bioconjugate onto G-PNR (Graphene modified with PNR after electrodeposition) surface was made according to amide I (1652 cm^{-1}) and amide II (1570 cm^{-1}) bands integration.

3.6. UV-Vis measurements

UV-Vis measurements were carried out in JASCO V-670 UV-Vis spectrophotometer, using an halogen-tungsten light source ranging from 800 to 190 nm, with scan speed of 200nm min^{-1}. Dilutions of 50× from the original stock solutions were performed for all samples containing proteins (IgG, BSA) used in bioconjugate synthesis. Final bioconjugate samples were diluted 10×. All spectra were presented with normalized absorbance values from 0 to 1 for maximum absorbance.

3.7. Dynamic light scattering measurements (DLS)

These measurements were performed in a Zetasizer Nano ZS Nanoseries equipment (Malvern). AuNP and AuNP/IgG bioconjugate samples were diluted in in water at 1:8 proportion prior to analyzes. The used parameters were: refraction index of 1.33; temperature of 25°C, viscosity of 0.8872 cP and material absorption index of 3.320. All experiments carried out in triplicate.

3.8. EEVDs confection

Initially, EEVD (Electrical Electrochemical Vertical Devices) electric contacts were made by deposition of thin films of 10 nm Ti and 20 nm of Pt at Si/SiO_2 substrates by sputtering at Brazilian Nanotechnology National Laboratory (LNNano) at the Brazilian Center for Research in Energy and Materials (CNPEM). Then, CVD monolayer graphene was transferred to Si/SiO_2 chips by polymer-mediated graphene process.(HASSAN *et al.*, 2021; MACEDO *et al.*, 2018) For this, a drop of polystyrene dissolved in toluene was deposited onto small-area pieces of CVD monolayer graphene on Cu foil and let to dry at 70 °C. The Cu foil was subsequently removed by etching in an aqueous oxidizing solution containing HCl and H_2O_2 (3:1, *v/v*). After this, substrates with monolayer graphene already transferred were kept at 90 °C for 15 min. Then, the polystyrene layer was dissolved in toluene. A thermal annealing under Ar atmosphere at 585 °C was finally performed.

3.9. EEVD modification

The pristine graphene surfaces of EEVDs were modified with poly-neutral red (PNR) by electropolymerization. For this, cyclic voltammetry was performed in 2 mmol L^{-1} PNR in 0.5 mol L^{-1} KNO_3 solution from -1.0 to 1.2 V (*vs.* $Ag/AgCl_{sat}$) at ν = 50 mV s^{-1} for 2 scans, and from -1.0 to 0.5 V (*vs.* $Ag/AgCl_{sat}$), ν = 50 mV s^{-1} for 15 scans. (PAULIUKAITE *et al.*, 2007; PAULIUKAITE; BRETT, 2008) The immobilization of AuNP/IgG bioconjugate was made by drop-casting with adsorption time of 30 minutes. Then, 10 μL of 3% BSA in PBS (0.01 mol L^{-1} pH 7.4) were used for blockage purposes of AuNP/IgG extra active sites.(DE OLIVEIRA; MARTUCCI; FARIA, 2018) This step was adopted in order to avoid non-specific interactions between these biomolecules and any other matrix component.

3.10. Raman Spectroscopy

Raman spectra of graphene, G-PNR and G-PNR-AuNP/IgG will be collected using an HeNe laser (λ = 633 nm) in a LabRAM HR Evolution Spectrophotometer (Horiba Scientific), from 1100 to 2800 cm^{-1} with 2 spectra acquisition per second, using 40× objective lens. Raman mapping of graphene, G-PNR and G-PNR-AuNP/IgG surfaces were obtained in a 55 × 60 μm^2 area, in the same conditions detailed above.

3.11. Electrical-Electrochemical experiments

All Electrical-Electrochemical (EE) experiments were performed in a PGSTAT 128N potentiostat/galvanostat (Metrohm), with an $Ag/AgCl_{sat}$ electrode as reference electrode, connected to potentiostat RE (Reference) terminal. WE and CE terminals (Working and Counter Electrode, respectively) were directly connected to the graphene's basal plane through Pt electrical contacts of the EEVD. The applied potential range for each EE experiment was defined after obtaining the OCP potential of each interface. The V-shaped curve was obtained after applying mathematical modulus of the obtained current using OCP as inflexion point. All experiments were performed in a drop of ~40 μL of 0.01 mol L^{-1} phosphate buffered saline (PBS) as supporting electrolyte medium. For IgG and RBD interactions experiments, 20 μL 1.0 μg mL^{-1} RBD in 0.01 mol L^{-1} PBS pH 7.4 were dropped onto the G-PNR-AuNP/IgG EEVD. let to interact for 10 minutes. The resulting surface was rinsed with 10 μL of PBS prior to the experiment. All curves were obtained in 0.01 mol L^{-1} PBS pH 7.4; $\nu = 5$ mV s^{-1}.

3.12. Analytical quantifications by EEVDs

Calibration curves for RBD detections by G-PNR-AuNP/IgG EEVDs were obtained by hybrid I_{ds} *vs.* V_{ds} electrical-electrochemical experiments. The LOD of EEVDs was evaluated considering the standard deviation (SD) of the lowest concentration sample that could be detected, relying on signal-to-noise ratio approaches recommended by IUPAC.(BRUNETTI B, 2015; INCZEDY; LENGYEL; URE, 1998) Positive or negative analyzes of spiked bovine fetal serum and synthetic saliva samples were carried out by the obtention of OCP shift for each aliquot compared to the G-PNR-AuNP-IgG interface in bare 0.01 mol L^{-1} PBS electrolyte.

4. RESULTS AND DISCUSSION

4.1 Graphene EEVD working features

Prior to any experiment, a final electrochemical etching by cyclic voltammetry was performed in 0.1 mol L^{-1} HCl, from -1.0 V to 1.0 V (*vs.* $Ag/AgCl_{sat}$), ν = 100 mV s^{-1} (Figure 1), where ν = scan rate. This procedure is needed for cleansing and removing of the remaining Cu traces from the graphene surface. (IOST *et al.*, 2014) Then, the success of graphene wet transferring procedure was evaluated by optical images collected for each EEVD (Figure 2A).

Figure 1 – Successive cyclic voltammograms obtained for pristine monolayer graphene cycling in 0.1 mol L^{-1} HCl, from -1.0 to 1.0 V (*vs.* $Ag/AgCl_{sat}$), 16 scans, ν = 100 mV s^{-1}

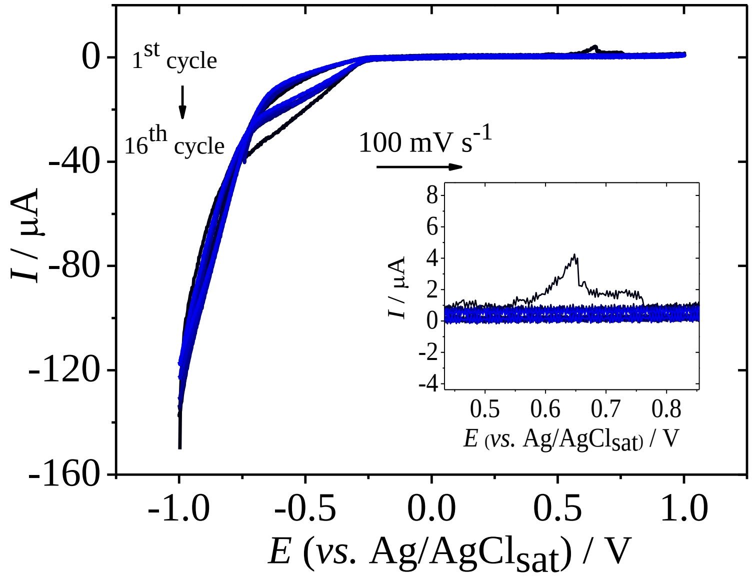

Source: own author.

The proposed graphene-based EEVD devices for viral detections through RBD quantifications are constituted of a monolayer graphene supported on Si/SiO_2 substrate, with an intrinsic resistivity R_s, given by $1/ne\mu$, where n is number of charge carriers, e is elementary charge and μ is charge carrier mobility. (KIM, Chang Hyun; FRISBIE, 2014; WANG *et al.*, 2012) It is strongly dependent on the pristine features of the deposited CVD graphene after the wet transferring procedure. In this case, structural features of monolayer CVD graphene can be investigated by Raman Spectroscopy by monitoring its D, G and 2D typical bands. G band (1595 cm^{-1}) is typical of graphene and correlated to the presence of active phonons around Brillouin symmetry Γ point and its sp^2 lattice. (WU *et al.*, 2018) D band (1328 cm^{-1}) is frequently related to the presence of point defects on sp^2 lattice, and is generated from intravalley one-phonon processes. (WU *et al.*, 2018) 2D band (2652 cm^{-1}), by its turn, is typical of graphite-derived materials. Moreover, I_D/I_G ratio can be used to analyze how defective the graphene sheet is. The closer to zero the I_D/I_G ratio is, the higher the integrity of sp^2 graphene lattice. (BLEU *et al.*, 2019; LIU *et al.*, 2013)

Figure 2 – A) Optical image of monolayer graphene deposited onto EEVD channel on Si/SiO_2 substrate; B) Raman spectrum of monolayer graphene device showed in Figure 1A presenting typical graphene bands at 1328 (D band), 1595 (G band) and 2652 cm^{-1} (2D band); C) Schematic representation of EEVD's hybrid electrical-electrochemical working principles and Equations 1 and 2 representation

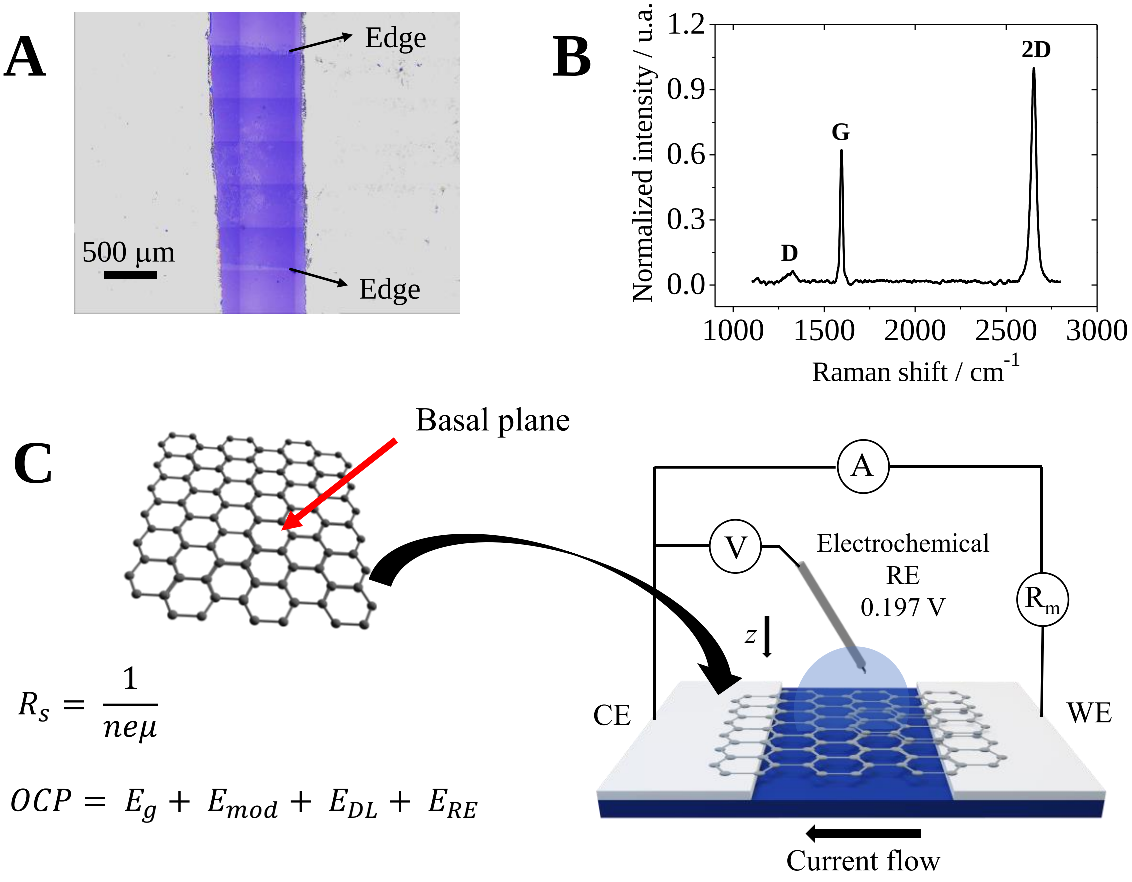

Source: own author.

For Raman spectrum showed in Figure 2B, an I_D/I_G ratio of 0.10 was obtained, indicating that the graphene in the produced devices present a highly intact basal plane sp^2 lattice. I_{2D}/I_G ratio is another parameter employed to obtain a confirmation of the graphene monolayer features by estimating a number of layers.(BLEU *et al.*, 2019) In this case, an I_{2D}/I_G ratio of 1.61 was obtained. As a value ranging between 1.3 and 2.0 is considered of pristine monolayer graphene in literature,(BLEU *et al.*, 2019) we inferred that in fact a monolayer sheet was employed for manufacturing the devices.

As elucidated in our previous work (MATTIOLI *et al.*, 2021), a hybrid electrical electrochemical detection methodology is possible by the direct connection of working (WE) and counter (CE) terminals of the device, similarly to the direct connection of drain and source terminals in Graphene Field-Effect Transistors (GFETs), exploring the direct current passage from these terminals through graphene basal plane. The success of this strategy is based on the intrinsic resistivity when the device is supported on Si/SiO_2, avoiding harmful short-circuit risks, and graphene's intrinsic high basal plane conductivity when kept with pristine features. (MATTIOLI *et al.*, 2021) As WE and CE are directly connected, an $Ag/AgCl_{sat}$ reference electrode (RE) is vertically positioned and electrolyte-gated with graphene interface (Figure 2C). This allows the application of an intrinsic potential of ~0.197 V (*vs.* standard hydrogen electrode) on graphene interface for electrical field modulation, as it is made in GFETs with gate electrodes. (BARD; FAULKNER, 2001; VIEIRA *et al.*, 2016) Moreover, the applied potential between WE and CE is made in relation to RE. The main advantage of using a reference electrode instead of a gate electrode is the possibility of modulating and reading the interfacial potential of the device without the external polarization of an ideally non-polarizable electrode. (BARD; FAULKNER, 2001)

Therefore, the measurable signal in EEVDs concerns the interfacial potential of the device (Figure 2C). In this case, the open circuit potential (OCP) reflects the interfacial potential with individual contributions of each interface component. These contributions are related to capacitive alterations of the interface due to charge accumulation, existence of redox potentials, and surface charge layer alterations in the absence of external polarization, *i.e.*, in OCP conditions, for semiconductor materials, as graphene. (BATCHELOR; HAMNETT, 1992; ZHANG, Xiaoge Gregory, 2005) The measured OCP reflects individual potential contributions of bare graphene (E_g), electrical double-layer (E_{DL}), reference electrode (E_{RE}) and possible adsorbed modifiers onto graphene interface (E_{mod}), as described in Equation 1. As E_{DL} and E_{RE} are constant, Equation 1 can be reduced only to the individual potential contributions from graphene and modifier components, as shown in Equation 2. (MATTIOLI *et al.*, 2021)

$$\mathrm{OCP} = E_{\mathrm{g}} + E_{\mathrm{mod}} + E_{\mathrm{DL}} + E_{\mathrm{RE}} \qquad (1)$$

$$\mathrm{OCP} = E_{\mathrm{g}} + E_{\mathrm{mod}} + \mathrm{E}_{\mathrm{constant}} \qquad (2)$$

4.2 Non-covalent modification of EEVD interface with PNR and AuNP/IgG bioconjugate

As our device working principles rely on the passage of current through graphene's basal plane while a potential (*vs.* Ag/AgCl$_{sat}$) is swept between WE and CE terminals, the integrity of graphene sp^2 lattice is of great importance for the performance of the EEVD. Because of that, non-covalent functionalization by electrodeposition was performed, instead of covalent modification. PNR was chosen as modifier due to its redox behavior and chemical structure, capable of interact with graphene sp^2 lattice by $\pi-\pi$ stacking. PNR electrodeposition was conducted according to previous reports in literature, (PAULIUKAITE *et al.*, 2007; PAULIUKAITE; BRETT, 2008), leading to G-PNR surface (Figure 3A). The success of G-PNR modification with a resulting stable surface is indicated by the prevalence of PNR redox peaks in the cyclic voltammogram of G-PNR obtained in 0.01 mol L^{-1} PBS (pH 7.4) showed in Figure 3B. The redox behavior of G-PNR surface was investigated by electrochemical impedance spectroscopy (EIS) (Figure 3C). As no semi-circle related to charge transfer resistance was observed and only imaginary Z" component alterations occurred, it was inferred that only capacitive changes would be present under these conditions.

Figure 3 – A) Cyclic voltammograms obtained during the PNR electrodeposition from -1.0 to 1.2 V (*vs.* Ag/AgCl$_{sat}$), 2 scans and from -1.0 to 0.5 V, 15 scans, ν = 50 mV s^{-1}; B) Cyclic voltammograms for bare graphene surface (black) and G-PNR surface after electrodeposition (red) in 0.01 mol L^{-1} PBS pH 7.4; C) Nyquist plots for bare graphene surface (black) and G-PNR surface after electrodeposition (red) in 0.01 mol L^{-1} PBS, pH 7.4, obtained from 1×10^5 to 0.1 Hz, DC$_{pot}$ = OCP with 5.0 mV amplitude, with the resultant equivalent circuit for G-PNR in the inset figure. D) Best electrochemical circuit fit for EEVD's bare graphene surface using NOVA software.

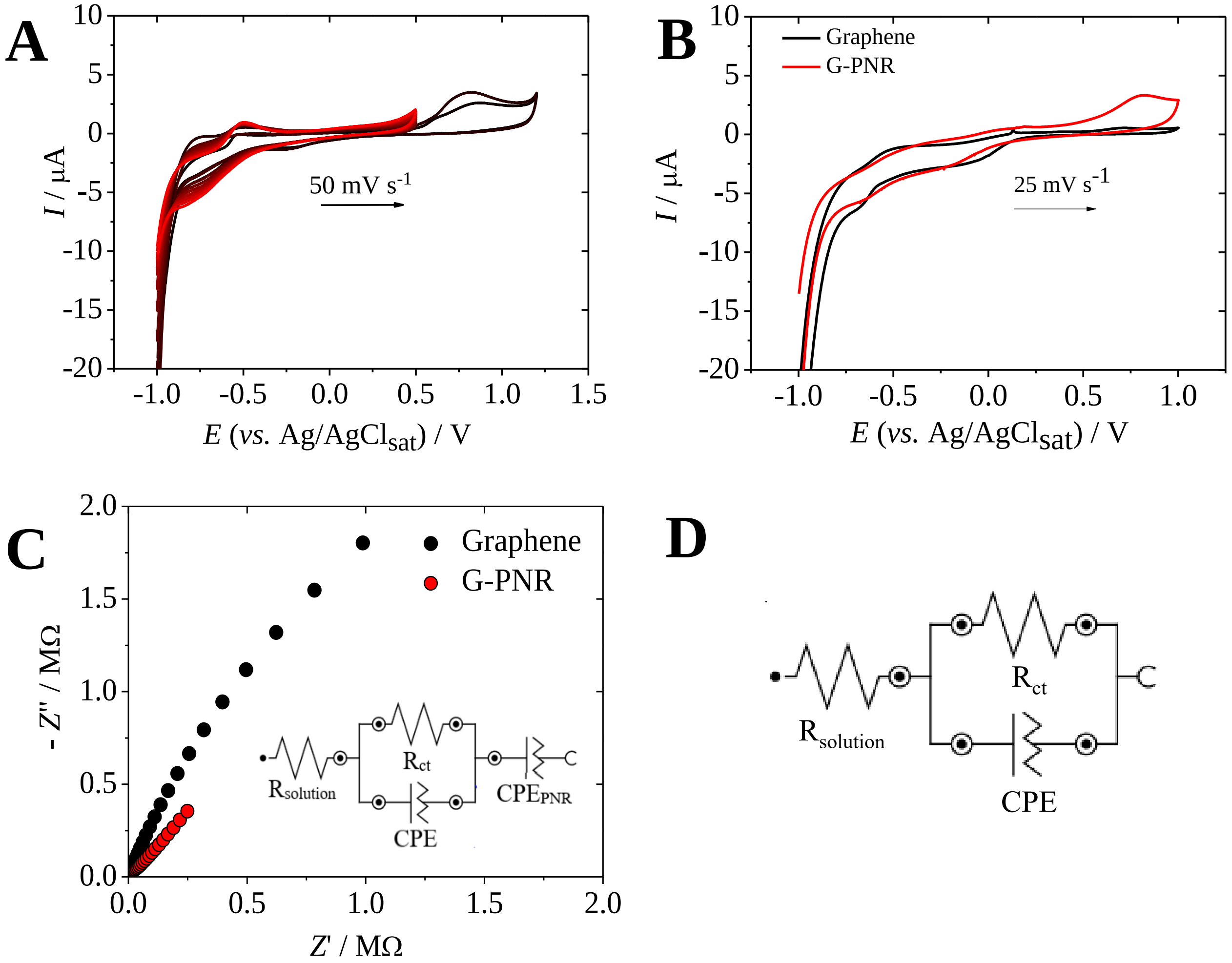

Source: own author.

To properly attach human IgG on G-PNR surface as probe for further RBD detection, AuNP-based bioconjugate was employed. The resulting AuNP/IgG bioconjugate is established by electrostatic interactions between AuNP and IgG, which is evidenced by the shift of the AuNP main band in the UV-Vis spectra (Figure 4A), from the typical wavelength at 525 nm (AuNP + NaOH, *i.e.* AuNP in NaOH adjusted electrolyte medium) (CERVINI; MATTIOLI; CAVALHEIRO, 2019) to 532 nm after interaction with IgG. This shift for higher wavelength is expected for electrostatic interactions between AuNP and proteinaceous species and reflects alterations in the dielectric constant values due to the bioconjugate formation. (KOZLOWSKI; RAGUPATHI; DYER, 2018) Proteinaceous band at 280 nm is observed in the spectrum of bare IgG in PBS buffer (Figure 5), which is related to the presence of Tyr and Trp residues. (NELSON; COX, 2006) In addition, as the bioconjugate formation is also indicated by the presence of both AuNP and IgG bands in the spectrum of AuNP/IgG spectrum (green line, Figure 4A).

Figure 4 – A) UV-Vis spectra obtained for each step of AuNP/IgG bioconjugate synthesis; B) Schematic representation of AuNP/IgG immobilization onto G-PNR EEVD

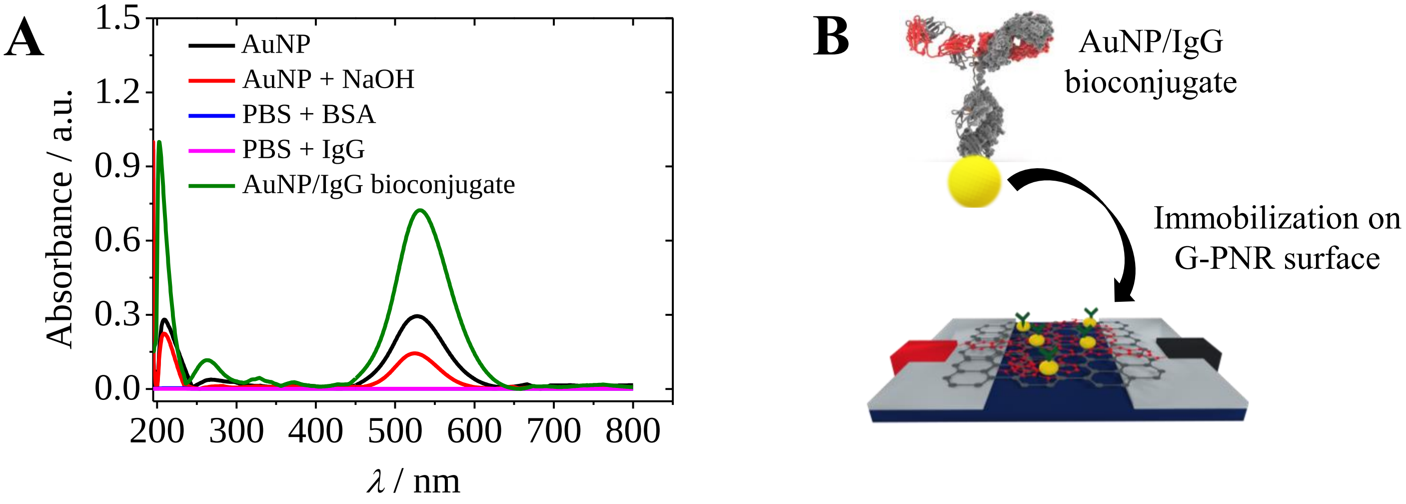

Source: own author.

Figure 5 – UV-Vis IgG spectrum in 0.01 mol L^{-1} PBS pH 8.

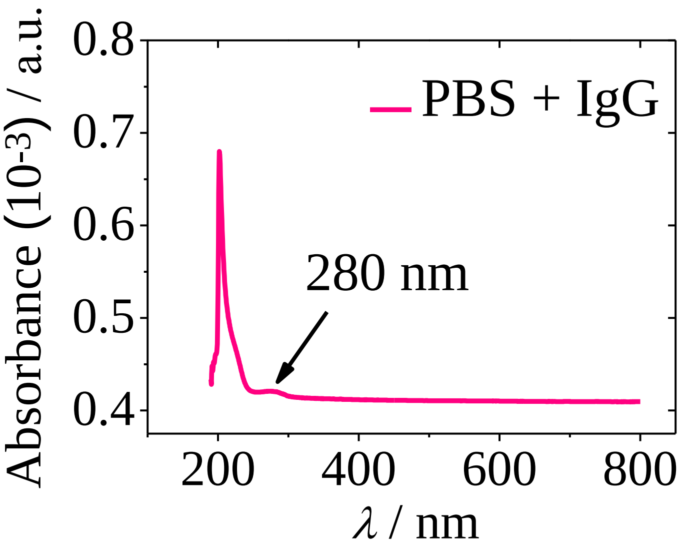

Source: own author.

The bioconjugate formation is also evidenced by the difference in the hydrodynamic radius (R_H) of bare AuNP and AuNP/IgG obtained by DLS (Figure 6). AuNP/IgG showed a R_H equal to 32.7 ± 1.3 nm, whereas AuNP R_H is 22.2 ± 0.3 nm. This increase of 10.5 nm in the R_H of the bioconjugate compared to bare AuNP is attributed to the IgG attaching in AuNP by electrostatic interactions, corroborating with UV-Vis results. Therefore, we inferred that the proposed bioconjugate was successfully synthetized and is suitable for immobilization on G-PNR surface.

Figure 6 – DLS size distribution by intensity of A) AuNP; B) AuNP/IgG bioconjugate.

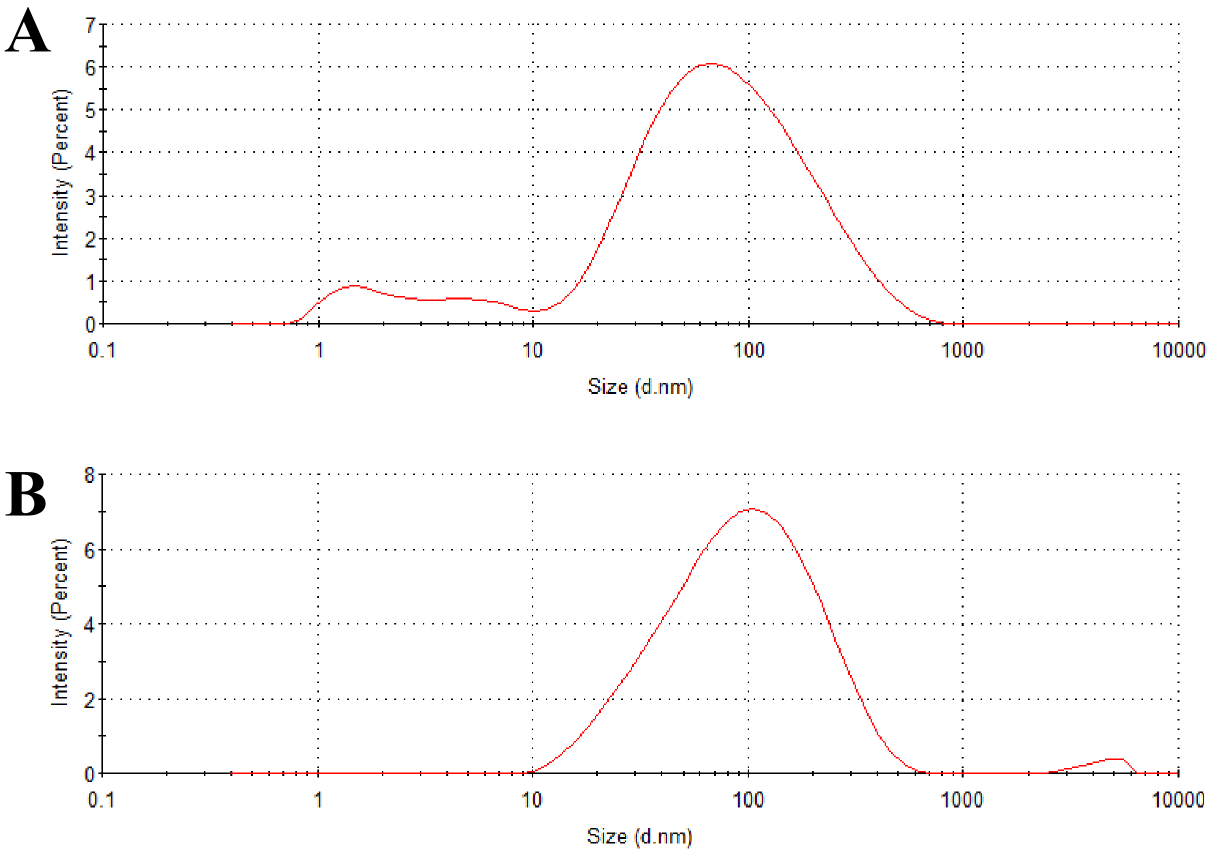

Source: own author.

The distribution of AuNP/IgG bioconjugate onto G-PNR after the immobilization process was investigated by Micro-FTIR imaging. Before AuNP/IgG immobilization, G-PNR surface was also analyzed by Micro-FTIR in order to differentiate AuNP/IgG bands from PNR ones (Figure 7). Optical image of AuNP/IgG adsorbed on G-PNR in an Au substrate in Figure 8A indicate the region where the FTIR spectra were collected to generate the chemical map of Figure 2D. Despite of the presence of few and small agglomerates, a quite homogeneous distribution of the bioconjugate can be observed. It is important to mention that this homogeneity is dependent on the solvent evaporation rate after a careful immobilization of the AuNP/IgG bioconjugate is performed by drop-casting. Consequently, these are important aspects to be controlled for obtaining an homogeneous final G-PNR-AuNP/IgG surface.

Figure 7 – A) Optical image of G-PNR surface onto Au substrate; B) 2D chemical mapping showing the distribution of PNR typical bands (SEELAJAROEN *et al.*, 2019).

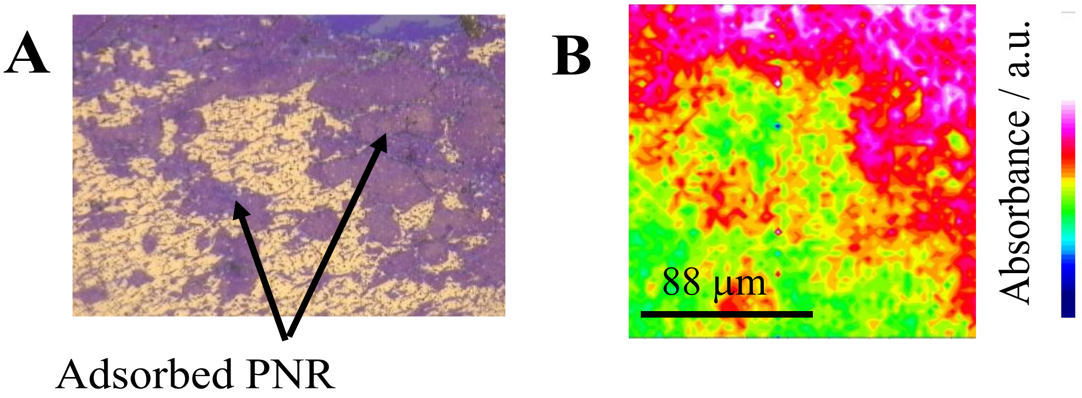

Source: own author.

Figure 8 – A) Optical image of G-PNR interface with immobilized AuNP/IgG bioconjugate in an Au substrate; B) 2D and C) 3D chemical map of immobilized AuNP/IgG onto G-PNR based on amide I (1652 cm^{-1}) and amide II (1570 cm^{-1}) bands of the antibody.

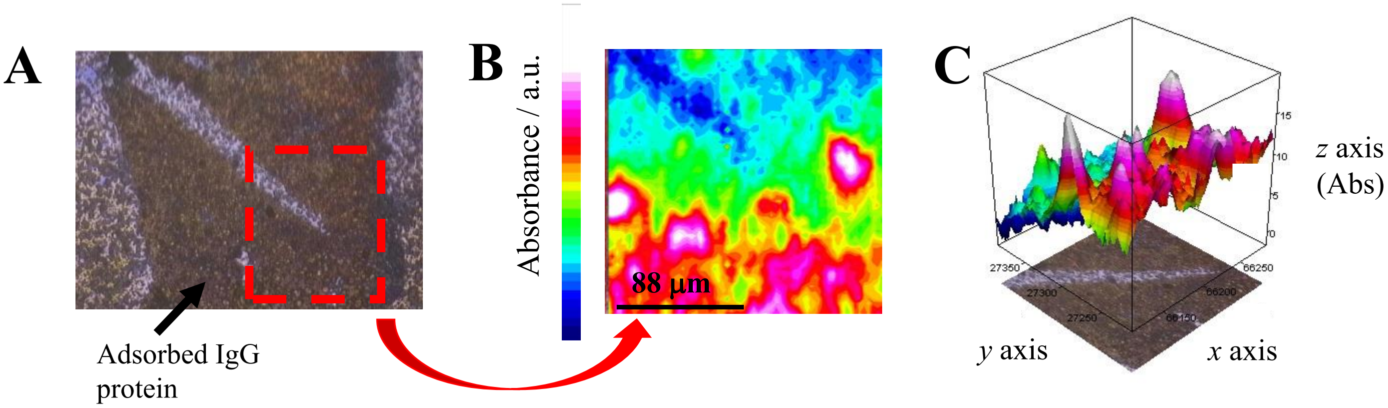

Source: own author.

The physical adsorption of AuNP/IgG species onto PNR film is expected to occur through non-covalent interaction between PNR and AuNP through PNR nitrogen atoms, based on the affinity of Au and N. (MATTIOLI *et al.*, 2019; MAZAR *et al.*, 2017) However, PNR electropolymerization is not free from creating structural defects on graphene, but expected to do it in a smaller extent in comparison to covalent modifications. Therefore, the insertion of few defects on graphene lattice are likely to happen based on the adopted modification strategy. To ensure this, Raman mapping of graphene, G-PNR and G-PNR-AuNP/IgG surfaces were carried out by monitoring both D- and G- typical bands of graphene. Prior to Raman mapping, optical images were collected for each analyzed surface, as presented in Figure 9, to obtain information on the visual integrity of the device after each preparation step until G-PNR-AuNP/IgG was reached and for mapping guidance.

Figure 9 – Optical images collected for each surface analyzed by Raman mapping: A) bare graphene, B) G-PNR and C) G-PNR-AuNP/IgG

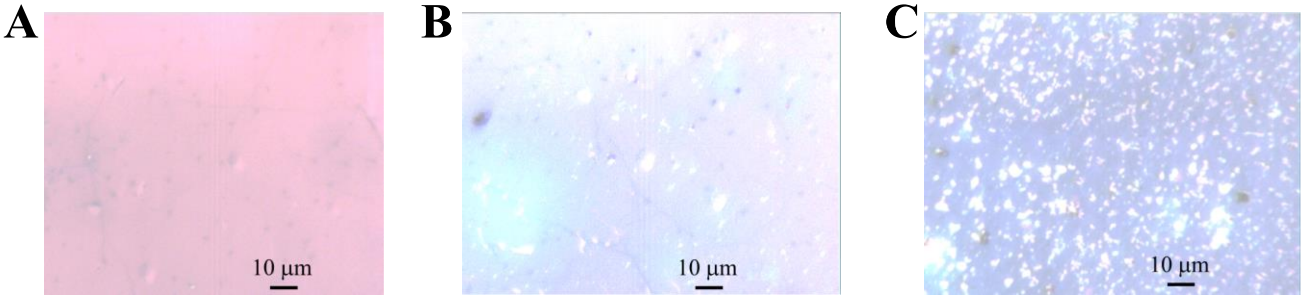

Source: own author.

Figure 10 present the resulting Raman mappings for bare graphene, G-PNR and G-PNR-AuNP/IgG surfaces. We observed in Figures 10A, 10B and 10C the predominance of G graphene bands in bare graphene surface in comparison to D band. This result was expected based on its punctual Raman spectrum presented in Figure 2B and bare graphene I_D/I_G ratio, indicating major pristine features of the sp^2 lattice. After PNR electrodeposition, G band 3D mapping (Figure 10E) still present a homogeneous distribution of this band intensity, indicating little alteration in this mode. A small increase in D band normalized intensity is observed in Figure 10F, indicating the generation of some point defects on graphene sp^2 lattice. This result agrees to previous studies reporting the occurrence of stress and strain of graphene lattice by the formation of a graphene-polymer, which by their turn lead to the generation of some point defects. (MATTIOLI *et al.*, 2022; WU *et al.*, 2018) The immobilization of AuNP/IgG bioconjugate onto G-PNR surface led to an increase in D and G graphene bands. Literature reports on human sera Raman spectra with IgG, IgM and other related compounds describe the probable presence of some IgG intrinsic Raman contributions in 1518 and 1656 cm^{-1} by a careful resulting scores analyzes. (GOULART *et al.*, 2021) Moreover, a typical IgG spectrum show Raman contributions of different modes between ~1557 – 1674 cm^{-1}. (ETTAH; ASHTON, 2018) The proximity of wavenumbers from these bands to G graphene band can lead to some band convolution during Raman mapping. Likewise, D graphene band (1328 cm^{-1}) is near to typical amide III antibody band region (~1230 – 1340 cm^{-1}) and can also convolute, leading to an increase in D band intensity in Raman mapping. (ETTAH; ASHTON, 2018; GOULART *et al.*, 2021) This information corroborates to the homogeneous increase in D and G bands in AuNP/IgG in 3D Raman mapping of G-PNR-AuNP/IgG interface (Figures 10H, 10I).

Figure 10 – 2D and 3D Raman mapping by D (Red color) and G (Green color) graphene bands integration for A), B) and C) bare graphene surface; D), E) and F) G-PNR and G), H) and I) G-PNR-AuNP/IgG surface. All 3D plots are normalized by highest band intensity of each surface

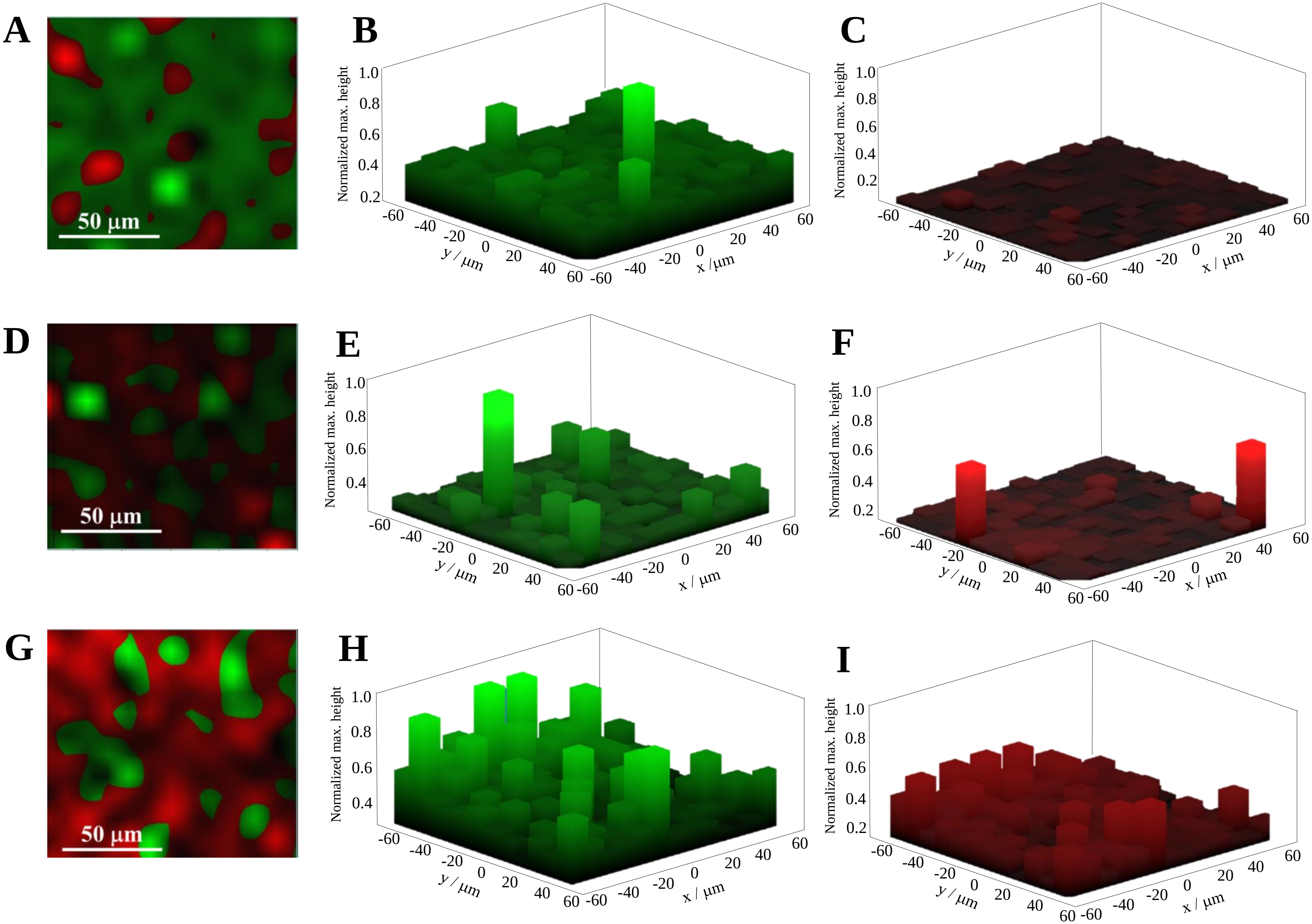

Source: own author.

4.3 Hybrid electrical electrochemical studies

Hybrid EE studies were performed with G-PNR-AuNP/IgG and G-PNR-AuNP/IgG after incubation in 1.0 µg mL^{-1} RBD target for 10 minutes. Figure 11A presents hybrid EE results for bare graphene and G-PNR-AuNP/IgG interface before (green curve) and after (pink curve) interaction with RBD. Here, I_{DS} represent the WE-to-CE current, as drain-to-source GFET current. Similarly, V_{DS} represent WE-to-CE potential, however, in our experiments, the swept potential is normalized by bare graphene OCP voltage (V_{OCP}) to produce a symmetrical curve and set graphene OCP as "zero". An OCP shift (ΔV_{OCP}) of G-PNR-AuNP/IgG for more positive potential after the incubation in RBD solution, $\Delta V_{OCP} = 0.0243$ V, was observed and can be attributed to the specific antigen-antibody bonding onto the EEVD surface. This positive shift can be interpreted as an indicative of *p*-doping of graphene caused by RBD interaction, as it structure present an overall positive net charge. (PAWŁOWSKI, 2021) Moreover, the ΔV_{OCP} observed for AuNP/IgG modification, as well as RBD adsorption are caused by capacitance alterations on EEVD interface due to surface charge layer width alterations and presence of charge excess on band edges. (MATTIOLI *et al.*, 2021; ZHANG, Xiaoge Gregory, 2005) The capacitive nature of OCP changes is confirmed by EIS measurements (Figure 11B) obtained at the OCP of each interface. The absence of charge-transfer semicircles and visualization of a *quasi*-vertical Nyquist profile (BARD; FAULKNER, 2001; BARSOUKOV; MACDONALD, 2013) confirm the above-mentioned interpretations.

Figure 11 – A) Hybrid EE I_{ds} vs. ($V_{ds} - V_{OCP}$) curves for graphene (black), G-PNR-AuNP/IgG (green) and G-PNR-AuNP/IgG (pink) after interaction with 1.0 µg mL^{-1} RBD for 10 minutes and B) EIS Nyquist plots for graphene (black), G-PNR-AuNP/IgG (green) and G-PNR-AuNP/IgG (pink) after interaction with 1.0 µg mL^{-1} RBD for 10 minutes collected from 1×10^5 Hz to 0.1 Hz with direct-current potential, DC$_{pot}$, equal to OCP, amplitude of 5 mV. All plots obtained in 0.01 mol L^{-1} PBS, pH 7.4

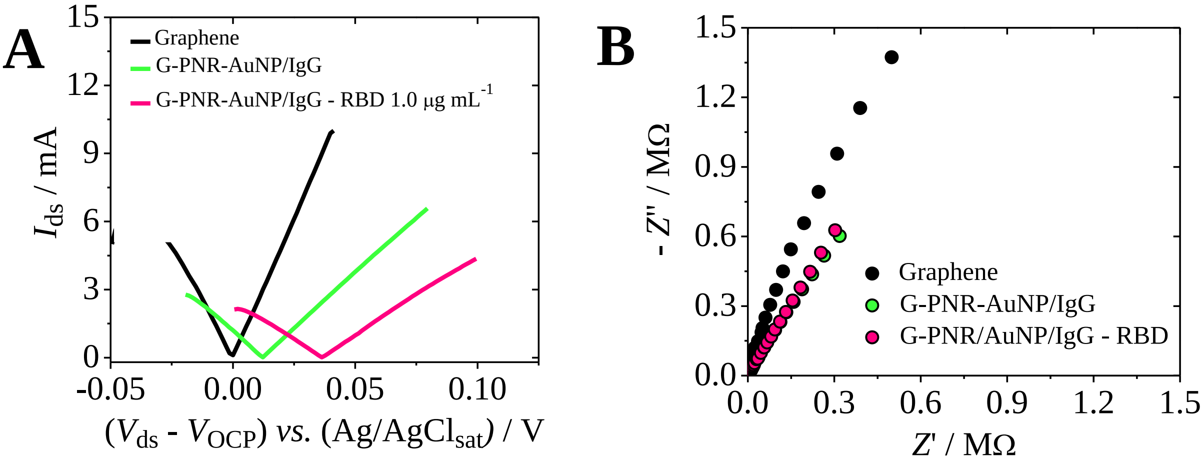

Source: own author.

Moreover, this capacitive phenomena behind ΔV_{OCP} were confirmed by cyclic voltammetry for each EEVD surface (bare graphene, G-PNR, G-PNR-AuNP/IgG). The absence of redox processes in the voltammograms of Figure 12, except the oxidation peak at *c.a.* 0.81 V (*vs.* Ag/AgCl$_{sat}$) of G-PNR attributed to the irreversible oxidation of some NR sites (PAULIUKAITE *et al.*, 2007), confirm our insights on the origins for the observed OCP shifts. Besides, as no electroactive co-factor is presented in RBD structure, it was inferred that this target protein only led to capacitance changes onto the interface where it is adsorbed. Therefore, these results demonstrate that RBD and IgG interaction can be monitored by an electrical-electrochemical experimental setup based on interfacial changes of the EEVDs.

Figure 12 - Cyclic voltammogram of graphene (black), G-PNR (red) and G-PNR-AuNP/IgG (green) obtained from -1.0 to 1.0 V (*vs.* Ag/AgCl$_{sat}$), ν = 50 mV s^{-1}, in 0.01 mol L^{-1} PBS, pH 7.4.

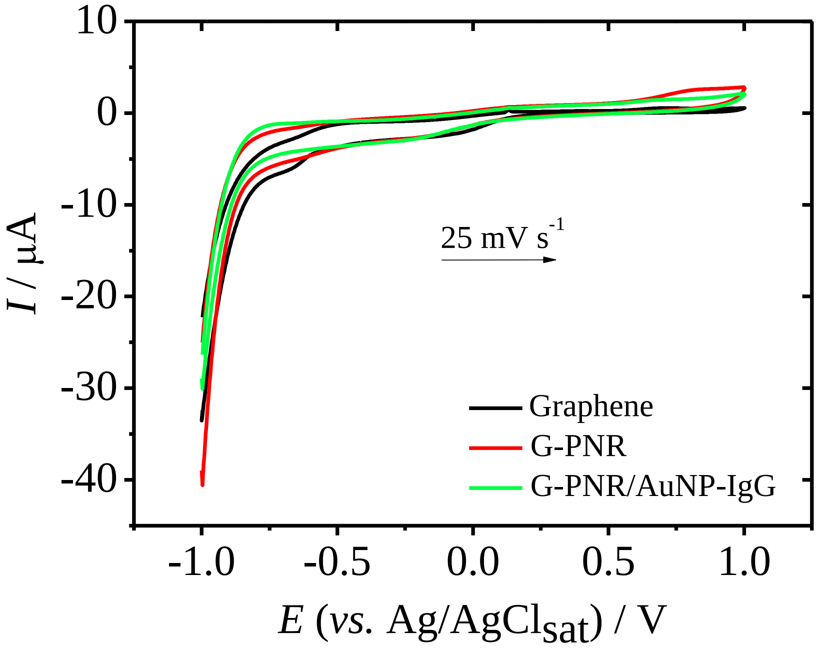

Source: own author.

4.4 Viral detections through RBD quantifications

The results indicate that RBD and IgG interaction can be studied by EE experiments through the monitoring of ΔV_{OCP}. As detailed in previous works (MATTIOLI *et al.*, 2021), ΔV_{OCP} were observed to be proportional to the adsorbed analyte concentration, and can be monitored by the difference between interfacial OCP values of G-PNR-AuNP/IgG after RBD interaction ($E_{int}^{(G-PNR/AuNP-IgG)-RBD}$) and before the interaction ($E_{int}^{(G-PNR/AuNP-IgG)}$), as indicated in Equation 3.

$$\Delta_{OCP} = E_{int} = E_{int}^{(G-PNR/AuNP-IgG)-RBD} - E_{int}^{(G-PNR/AuNP-IgG)} \tag{3}$$

In this sense, a calibration curve was constructed based on several "*on drop*" interfacial RBD detections. For this, G-PNR-AuNP/IgG EEVD surface was incubated in different RBD concentrations, ranging from 10^{-12} to 10^{-7} g mL^{-1} (Figures 13A, 13B). It is noticed a well-defined linear OCP response with increasing concentrations, with low standard deviation in each curve point, indicating satisfactory precision and repeatability of the analyzes, within a wide linear range of response. The sensitivity of the device was calculated to be 6.1 mV/decade and represents the slope of the calibration curve. Although this value is lower than other sensitivity values reported elsewhere by GFETs for several biomolecules (KIM, Duck Jin *et al.*, 2013; PAPAMATTHAIOU; ESTRELA; MOSCHOU, 2021; PICCININI *et al.*, 2017), it is higher than the previous sensitivity obtained for EEVDs without specific probes functionalization onto its surface. (MATTIOLI *et al.*, 2021) Despite other field-effect devices have been developed for RBD and/or Spike protein detections, (KE *et al.*, 2021; SEO *et al.*, 2020; SHAO *et al.*, 2021) the sensitivity of the present hybrid electrical-electrochemical device cannot be compared to them, as frequently LOD is misinterpreted as sensitivity. (MATTIOLI; CRESPILHO, 2020) Additionally, a LOD of 0.1 pg mL^{-1} (or approximately 2.86 fmol L^{-1}) was obtained with G-PNR-AuNP/IgG EEVDs for RBD hybrid EE detection, considered advantageous in relation to other lower LOD values reported in literature for RBD/Spike protein detections by different methodologies. (EL-SAID; AL-BOGAMI; ALSHITARI, 2020; MOJSOSKA *et al.*, 2021) Although some reports show lower LODs for RBD detection, (AYDIN; AYDIN; SEZGINTÜRK, 2021; KE *et al.*, 2021), this is the first hybrid detection methodology proposed for the development of detection technologies related to COVID-19.

Figure 13 – A) Schematic representation of RBD detection in a 40 µL drop by interaction with IgG in G-PNR-AuNP/IgG surface by hybrid EE methodology; B) Calibration curve for RBD detections from 10^{-12} to 10^{-7} g mL^{-1} concentrations (n = 3) in 0.01 mol L^{-1} PBS, pH 7,4; C) Positive (green) and negative (red) RBD detections in spiked bovine fetal serum (left, n = 20); and positive (blue) and negative (pink) RBD detections for spiked synthetic saliva (right, n = 30)

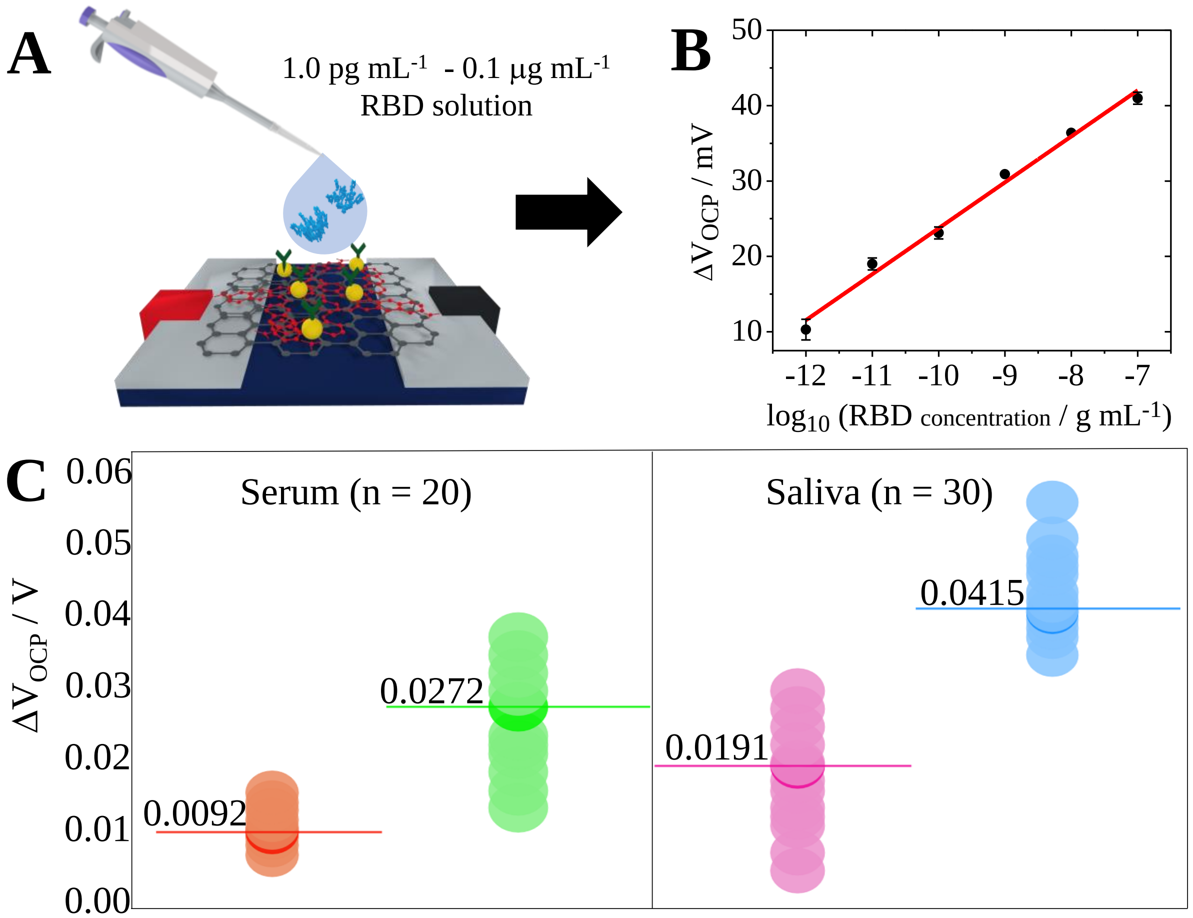

Source: own author.

The above-mentioned analytical parameters of G-PNR-AuNP/IgG EEVD proved that it can be a suitable alternative device for RBD detection aiming early stage COVID-19 diagnosis, by the return of an OCP value that can be interpreted as a binary positive or negative diagnosis response in a rapid and easy-to-handle miniaturized assay. Then, to establish a proof-of-concept of its applicability, spiked bovine fetal serum and synthetic saliva samples were analyzed for positive RBD diagnosis, and this same studied matrixes without RBD were employed as negative samples (See Section 3.2 for sample preparation details). Bovine fetal serum analyzes were performed with a replicate of 20 positive and 20 negative samples, whereas 30 positive and 30 negative saliva samples were analyzed. This matrix was chosen for proof-of-concept studies to evaluate the device performance in a matrix of such complexity. The results of ΔV_{OCP} shifts obtained with G-PNR-AuNP/IgG EEVDs are presented in Figure 13C. The average ΔV_{OCP} for positive spiked serum samples is 0.027 ± 0.007 V, whereas negative serum samples presented a ΔV_{OCP} of (0.009 ± 0.002) V. Likewise, saliva positive samples present a ΔV_{OCP} shift of 0.041 ± 0.005 V, whereas as negative samples show a ΔV_{OCP} shift of 0.019 ± 0.008 V. It can be noticed that no false-positive or false-negative result was obtained in the synthetic saliva samples, as no positive and negative samples showed same ΔV_{OCP} value. This can be facilitated by the low complexity of this matrix and absence of other biomolecules. However, for bovine fetal serum samples a poorer separation from positive and negative diagnosis is observed, which can be attributed to the higher matrix complexity and to the smaller population size analyzed. Despite that, it can be assumed that ΔV_{OCP} values of approximately 0.009 V or smaller can be inferred as a true negative result for COVID-19 diagnosis. Similarly, ΔV_{OCP} values of approximately 0.020 V or higher can be interpreted as true positive result for COVID-19 diagnosis in serum samples. However, to better endorse the application of our G-PNR-AuNP/IgG EEVDs for COVID-19 diagnosis in real human fluid samples with high precision, further studies on real human serum, human saliva and nasal fluid need to be carried out in a sample population higher than n = 50. After all these analytical studies, a concise comparison between the present hybrid EE device with different techniques reported in literature is presented in Table 1.

Table 1 – Comparison between different detection methodologies for RBD/Spike S1 protein quantification aiming COVID-19 diagnosis

Detection method	Device components	LOD	Sensitivity	Reference
Electrochemical	Sandwich Immunosensor with MUA@GNPs	0.577 fg mL^{-1}	0.238 kΩ pg mL^{-1} cm^{-2}	(AYDIN; AYDIN; SEZGINTÜRK, 2021)
Duplex Digital ELISA	Magnetic beads encoding technology	20.6 fg mL^{-1}	Not informed	(CAI *et al.*, 2021)
Immunochromatography	LFIA-AuNP/monoclonal antibodies	62.5 ng mL^{-1}	Not informed	(LI, Ge *et al.*, 2021)
Sandwich ELISA with time resolved flurorescence	Europium lanthanides	S/N ratio = 1.7	66%	(BARLEV-GROSS *et al.*, 2021)
Near-Infrared	SWCNTs functionalized with ACE2	12.6 nmol L^{-1}	Not informed	(PINALS *et al.*, 2021)
Electrochemical	Graphene electrode coupled to anti-spike antibodies	20 µg mL^{-1}	Not informed	(MOJSOSKA *et al.*, 2021)
SERS coupled to Square Wave Voltammetry	ITO electrode / GNPs@reduced porous graphene	39.5 fmol L^{-1}	6.23 µA cm^{-2} L $pmol^{-1}$	(EL-SAID; AL-BOGAMI; ALSHITARI, 2020)
Hybrid EE detections	G-PNR-AuNP/IgG EEVDs	0.1 pg mL^{-1} or 2.86 fmol L^{-1}	6.1 mV/decade	This work

LFIA = Lateral Flow Immunoassay; **MUA** = 11-mercaptoundecanoid acid; **GNPs** = gold nanoparticles; **SWCNTs** = Single-Walled Carbon Nanotubes; **ACE2** = Angiotensin Conversion Enzyme; **ITO** = Indium Tin Oxide; **SERS** = Surface-Enhanced Raman Scattering.

5. CONCLUSIONS

In this work, a hybrid electrical electrochemical detection methodology was developed for rapid COVID-19 early-stage diagnosis. For this, an EEVD based on G-PNR heterojunction was successfully manufactured and modified with AuNP/IgG bioconjugate, which acts as detection probes. The bioconjugate was based on human monoclonal antibodies produced in response to COVID-19 infection, providing high specificity and sensitivity to the proposed detection methodology. As a result, the EEVD showed a wide linear range of interfacial ΔV_{OCP} response in relation to RBD concentrations, varying from 10^{-12} to 10^{-7} g mL^{-1}, and sensitivity equals to 6.1 mV/decade. Moreover, the remarkably low LOD obtained with this device in femtomolar order of magnitude (2.86 10^{-15} mol L^{-1} or 0.1 pg mL^{-1}) evidenced that G-PNR-AuNP/IgG device can be a suitable alternative for viral detections in early stage of COVID-19 infections. The miniaturized *on drop* assay configuration, in which less than 40 µL of sample/support electrolyte are needed for analyzes, allows the application of the proposed devices for on-site mass testing. Finally, a proof-of-concept of device applicability was demonstrated in samples of RBD-spiked bovine fetal serum and synthetic saliva. Satisfactory discrepancy between ΔV_{OCP} values of the positive and negative samples led to small percentage of false-positive or false-negative results, making this analytical approach suitable for early stage detection of COVID-19 infections.

6. REFERENCES

AYDIN, E. B.; AYDIN, M.; SEZGINTÜRK, M. K. Highly selective and sensitive sandwich immunosensor platform modified with MUA-capped GNPs for detection of spike receptor binding domain protein: a precious marker of COVID 19 infection. **Sensors and Actuators B:** chemical, Amsterdam, v. 345, p. 130355, 2021.

BAKER, A. N.; RICHARDS, S. J.; GUY, C. S.; CONGDON, T. R. ; HASAN, M.; ZWETSLOOT, A. J.; GALLO, A.; LEWANDOWSKI, J. R.; STANSFELD, P. J. STRAUBE, A.; WALKER, M.; CHESSA, S.; PERGOLIZZI, G.; DEDOLA, S.; FIELD, R.A.; GIBSON, M. The sars-cov-2 spike protein binds sialic acids and enables rapid detection in a lateral flow point of care diagnostic device. **ACS Central Science**, Washington, v. 6, n. 11, p. 2046–2052, 2020.

BAO, C.; KAUR, M.; KIM, W. S. Toward a highly selective artificial saliva sensor using printed hybrid field effect transistors. **Sensors and Actuators, B:** chemical, Amsterdam, v. 285, p. 186–192, 2019.

BARD, A. J.; FAULKNER, L. R. **Electrochemical methods:** fundamentals and applications. 2. ed. Hoboken: John Wiley, 2001. 833p.

GROSS, M. B.; WEISS, S.; SHMUEL, A. B.; SITTNER, A.; EDEN, K.; MAZUZ, N.; GLINERT, I.; BAR-DAVID, E.; PUNI, R.; AMIT, S.; KRIGER, O.; SCHUSTER, O.; ALCALAY, R.; MAKDASI, E.; EPSTEIN, E.; NOV-PORAT, T.; ROSENFELD, R.; ACHDOUT, H.; MAZOR, O.; ISRAELY, T.; LEVY, H. MECHALY, A. Spike vs nucleocapsid SARS-CoV-2 antigen detection: application in nasopharyngeal swab specimens. **Analytical and Bioanalytical Chemistry**, Berlin, v. 413, n. 13, p. 3501–3510, 2021.

BARSOUKOV, E.; MACDONALD, J. R. **Impedance spectroscopy**: theory, experiment, and applications. Hoboken: John Wiley, 2005. 595p.

BATCHELOR, R. A.; HAMNETT, A. Surface states on semiconductors. *In:* BOCKRIS, J. O.; CONWAY, B. E.; WHITE, R. E. (ed.). **Modern aspects of electrochemistry**. New York: Springer Science, 1992. v. 22.

BLEU, Y.; BOURQUARD, F.; LOIR, A. S.; BARNIER, V.; GARRELIE, F. ; DONNET, C. Raman study of the substrate influence on graphene synthesis using a solid carbon source via rapid thermal annealing. **Journal of Raman Spectroscopy**, Hoboken, v. 50, n. 11, p. 1630–1641, 2019.

BRUNETTI B, D. E. About estimating the limit of detection by the signal to noise approach. **Pharmaceutica Analytica Acta**, London, v. 6, n. 4, 2015.

CAI, Q.; MU, J.; LEI, Y.; , GE, J.; ARYEE, A. A.; ZHANG, X.; LI, Z. Simultaneous detection of the spike and nucleocapsid proteins from SARS-CoV-2 based on ultrasensitive single molecule assays. **Analytical and Bioanalytical Chemistry**, Berlin, v. 413, n. 18, p. 4645–4654, 2021.

CERVINI, P.; MATTIOLI, I. A.; CAVALHEIRO, E. T. G. Developing a screen-printed graphite-polyurethane composite electrode modified with gold nanoparticles for the voltammetric determination of dopamine. **RSC Advances**, London, v. 9, p. 42306–42315, 2019.

CORMAN, V. M.; LANDT, O.; KAISER, M.; MOLENKAMP, R.; MEIJER, A.; CHU, D. K.; DROSTEN, C. Detection of 2019 novel coronavirus (2019-nCoV) by real-time RT-PCR. **Eurosurveillance**, Stockholm, v. 25, n. 3, p. 1–8, 2020.

DE OLIVEIRA, T. R.; MARTUCCI, D. H.; FARIA, R. C. Simple disposable microfluidic device for Salmonella typhimurium detection by magneto-immunoassay. **Sensors and Actuators, B:** chemical, Amsterdam, v. 255, p. 684–691, 2018.

DONNELLY, M.; MAO, D.; PARK, J.; XU, G. Graphene field-effect transistors: the road to bioelectronics. **Journal of Physics D:** applied physics, London, v. 51, n. 49, 16 p. 2018.

EL-SAID, W. A.; AL-BOGAMI, A. S.; ALSHITARI, W. Synthesis of gold nanoparticles@reduced porous graphene-modified ITO electrode for spectroelectrochemical detection of SARS-CoV-2 spike protein. **Spectrochimica Acta Part A:** molecular and biomolecular spectroscopy, Amsterdam, v. 264, p. 120237, 2020.

ETTAH, I.; ASHTON, L. Engaging with raman spectroscopy to investigate antibody aggregation. **Antibodies**, Basel, v. 7, n. 3, p. 24, 2018.

CASTRO GOULART, A. C.; ZANGARO, R. A.; CARVALHO, H. C.; SILVEIRA JR., L. Diagnosing COVID-19 in human sera with detected immunoglobulins IgM and IgG by means of raman spectroscopy. **Journal of Raman Spectroscopy**, Hoboken, v.52, n.12, p. 2671, 2021.

HASSAN, A.; MACEDO, L.; MATTIOLI, I. A.; RUBIRA, R. J. G.; CONSTANTINO, C. J. L.; AMORIM, R. G.; LIMA, F.; CRESPILHO, F. N. A three component-based van der Waals surface vertically designed for biomolecular recognition enhancement. **Electrochimica Acta**, Amsterdam, v. 376, p. 138025, 2021.

INCZEDY, J.; LENGYEL, T.; URE, A. M. Detection and quantification capabilities. In: **IUPAC Compendium on Analytical Nomenclature, Definitive Rules 1997**. 3 ed. Research Triangle Park: International Union of Pure and Applied Chemistry, 1998.

IOST, R. M.; CRESPILHO, F. N.; ZUCCARO, L.; YU, H. K.; WODTKE, A. M.; KERN, K.; BALASUBRAMANIAN, K. Enhancing the electrochemical and electronic performance of cvd-grown graphene by minimizing trace metal impurities. **ChemElectroChem**, Weinheim, v. 1, n. 12, p. 2070–2074, 2014.

KE, G.; SU, D.; LI, Y.; ZHAO, Y.; WANG, H.; LIU, W.; LI, M.; YANG, Z.; XIAO, F.; YUAN, Y.; HUANG, F.; MO, F.; WANG, P.; GUO, X. An accurate, high-speed, portable bifunctional electrical detector for COVID-19. **Science China Materials**, New York, v. 64, n. 3, p. 739–747, 2021.

KIM, C. H.; FRISBIE, C. D. Determination of quantum capacitance and band filling potential in graphene transistors with dual electrochemical and field-effect gates.

Journal of Physical Chemistry C, Washington, v. 118, n. 36, p. 21160–21169, 2014.

KIM, D. J.; PARK, H. C.; SOHN, I. Y.; JUNG, J. H.; YOON, O. J.; PARK, J.S.; YOON, M. Y.; LEE, N. E. Electrical graphene aptasensor for ultra-sensitive detection of anthrax toxin with amplified signal transduction. **Small**, Weinheim, v. 9, n. 19, p. 3352–3360, 2013.

KOZLOWSKI, R.; RAGUPATHI, A.; DYER, R. B. Characterizing the surface coverage of protein-gold nanoparticle bioconjugates. **Bioconjugate Chemistry**, Washington, v. 29, n. 8, p. 2691–2700, 2018.

LEE, J. H.; CHOI, M.; JUNG, Y.; LEE, S. Y.; LEE, C. S.; KIM, J.; KIM, J.; KIM, N. H.; KIM, B. T.; KIM, H. G. A novel rapid detection for SARS-CoV-2 spike 1 antigens using human angiotensin converting enzyme 2 (ACE2). **Biosensors and Bioelectronics**, Amsterdam, v. 171, p. 112715, 2021.

LI, G.; WANG, A.; CHEN, Y.; SUN, Y.; DU, Y.; WANG, X.; ZHANG, G. Development of a colloidal immunochromatographic strip for rapid detection of severe acute respiratory syndrome coronavirus 2 spike protein. **Frontiers in Immunology**, Lausanne, v. 12, p. 1–8, 2021.

LI, J.; WU, D.; YU, Y.; LI, T.; LI, K.; XIAO, M. M.; ZHANG, G. J. Rapid and unamplified identification of COVID-19 with morpholino-modified graphene field-effect transistor nanosensor. **Biosensors and Bioelectronics**, Amsterdam, v. 183, p. 113206, 2021.

LIU, J.; LI, Q.; ZOU, Y.; QIAN, Q.; JIN, Y.; LI, G.; FAN, S. The dependence of graphene raman d-band on carrier density. **Nano Letters**, Washington, v. 13, n. 12, p. 6170–6175, 2013.

MACEDO, L. J. A.; LIMA, F. C. D. A.; AMORIM, R. G.; FREITAS, R. O.; YADAV, A.; IOST, R. M.; BALASUBRAMANIAN, K.; CRESPILHO, F. N. Interplay of non-uniform charge distribution on the electrochemical modification of graphene. **Nanoscale**, London, v. 10, n. 31, p. 15048–15057, 2018.

MACEDO, L. J.; IOST, R. M.; HASSAN, A.; BALASUBRAMANIAN, K.; CRESPILHO, F. N. Bioelectronics and interfaces using monolayer graphene. **ChemElectroChem**, Weinheim, v. 6, n. 1, p. 31–59, 2019.

MATTIOLI, I. A.; BACCARIN, M.; CERVINI, P.; CAVALHEIRO, E. T. G. Electrochemical investigation of a graphite-polyurethane composite electrode modified with electrodeposited gold nanoparticles in the voltammetric determination of tryptophan. **Journal of Electroanalytical Chemistry**, Amsterdam, v. 835, p. 212–219, 2019.

MATTIOLI, I. A. ; HASSAN, A. ; OLIVEIRA JUNIOR, O. N. ; CRESPILHO, F. N. On the challenges for the diagnosis of sars-cov-2 based on a review of current methodologies. **ACS Sensors**, Washington, v. 5, n. 12, p. 3655–3677, 2020.

MATTIOLI, I. A.; HASSAN, A. ; SANCHES, N. M.; VIEIRA, N. C. S.; CRESPILHO, F. N. Highly sensitive interfaces of graphene electrical-electrochemical vertical devices for on drop atto-molar DNA detection. **Biosensors and Bioelectronics**, Amsterdam, v. 175, p. 112851, 2021.

MATTIOLI, I. A.; CASTRO, K. R.; MACEDO, L. J.; SEDENHO, G. C.; OLIVEIRA, M. N. ; TODESCHINI, I.; CRESPILHO, F. N. Graphene-based hybrid electrical-electrochemical point-of-care device for serologic covid-19 diagnosis. **Biosensors and Bioelectronics**, Amsterdam, v. 199, p. 113866, 2022.

MATTIOLI, I. A.; CRESPILHO, F. N. Problems of interpreting diagnostic tests for SARS-CoV-2: analytical chemistry concerns. **Anais da Academia Brasileira de Ciencias**, Rio de Janeiro, v. 92, n. 4, p. 1–3, 2020.

MAZAR, F. M.; ALIJANIANZADEH, M., MOLAEIRAD, A. ; HEYDARI, P. Development of novel glucose oxidase immobilization on graphene/gold nanoparticles/poly neutral red modified electrode. **Process Biochemistry**, Amsterdam, v. 56, p. 71–80, 2017.

MOJSOSKA, B.; LARSEN, S.; OLSEN, D. A.; MADSEN, J. S.; BRANDSLUND, I. ; ALATRAKTCHI, F. A. Rapid SARS-CoV-2 detection using electrochemical immunosensor. **Sensors**, Basel, v. 21, n. 2, p. 1–11, 2021.

MOYSE, K. A. Lateral flow tests need low false positives for antibodies and low false negatives for virus. **The BMJ**, London, v. 372, p. 33277265, 2021.

NELSON, D. L.; COX, M. M. **Lehninger principles of biochemistry**. 4 ed. New York: W. H. Freeman, 2006, 1119p.

PAPAMATTHAIOU, S.; ESTRELA, P.; MOSCHOU, D. Printable graphene BioFETs for DNA quantification in Lab-on-PCB microsystems. **Scientific Reports**, London, v. 11, n. 1, p. 1–9, 2021.

PAULIUKAITE, R.; GHICA, M. E.; BARSAN, M.; BRETT, C. M. Characterisation of poly(neutral red) modified carbon film electrodes; application as a redox mediator for biosensors. **Journal of Solid State Electrochemistry**, New York, v. 11, n. 7, p. 899–908, 2007.

PAULIUKAITE, R.; BRETT, C. M. A. Poly(neutral red): electrosynthesis, characterization, and application as a redox mediator. **Electroanalysis**, Weinheim, v. 20, n. 12, p. 1275–1285, 2008.

PAWŁOWSKI, P. H. Charged amino acids may promote coronavirus SARS-CoV-2 fusion with the host cell. **AIMS Biophysics**, Springfield, v. 8, n. 1, p. 111–120, 2021.

PICCININI, E.; BLIEM, C.; REINER-ROZMAN, C.; BATTAGLINI, F.; AZZARONI, O.; KNOLL, W. Enzyme-polyelectrolyte multilayer assemblies on reduced graphene oxide field-effect transistors for biosensing applications. **Biosensors and Bioelectronics**, Amsterdam, v. 92, p. 661–667, 2017.

PINALS, R. L.; LEDESMA, F.; YANG, D.; NAVARRO, N.; JEONG, S.; PAK, J. E.; KUO, L.; CHUANG, U. C.; CHENG, Y. W.; SUN, H. S.; LANDRY, M. P. Rapid sars-cov-2 spike protein detection by carbon nanotube-based near-infrared nanosensors.

Nano Letters, Washington, v. 21, n. 5, p. 2272–2280, 2021.

PREMKUMAR, L.; SEGOVIA-CHUMBEZ, B., JADI, R.; MARTINEZ, D. R.; RAUT, R.; MARKMANN, A. J.; DE SILVA, A. M. The receptor-binding domain of the viral spike protein is an immunodominant and highly specific target of antibodies in SARS-CoV-2 patients. **Science Immunology**, Washington, v. 5, n. 48, p. 1–10, 2020.

ROH, C.; JO, S. K. Quantitative and sensitive detection of SARS coronavirus nucleocapsid protein using quantum dots-conjugated RNA aptamer on chip. **Journal of Chemical Technology and Biotechnology**. London, v. 86, p. 1475-1479, 2011.

SAN ROMAN, D.; GARG, R.; COHEN-KARNI, T. Bioelectronics with graphene nanostructures. **APL Materials**, College Park, v. 8, n. 10, 2020.

SEELAJAROEN, H.; HABERBAUER, M.; HEMMELMAIR, C.; ALJABOUR, A.; DUMITRU, L. M.; HASSEL, A. W.; SARICIFTCI, N. S. Enhanced bio-electrochemical reduction of carbon dioxide by using neutral red as a redox mediator. **ChemBioChem**, Weinheim, v. 20, n. 9, p. 1196–1205, 2019.

SEO. G.; LEE, G.; KIM, M. J.; BAEK, S. H.; CHOI, M.; KU, K. B.; LEE, C. S.; JUN, S.; PARK, D.; KIM, H. G.; KIM, S. J.; KIM, J. O.; PARK, E. C.; KIM, S. II. Rapid detection of covid-19 causative virus (sars-cov-2) in human nasopharyngeal swab specimens using field-effect transistor-based biosensor. **ACS Nano**, Washington v.14, n. 4, p. 5135-5142, 2020.

SHAO, W.; SHURIN, M.E.; WHEELER, S. E.; HE, X.; STAR, A. Rapid detection of sars-cov-2 antigens using high-purity semiconducting single-walled carbon nanotube-based field-effect transistors. **ACS Applied Materials & Interfaces**, Washington, v. 13, n. 8, p.10321-10327, 2021.

SHOWN, I.; GANGULY, A. Non-covalent functionalization of CVD-grown graphene with Au nanoparticles for electrochemical sensing application. **Journal of Nanostructure in Chemistry**, New York, v. 6, n. 4, p. 281–288, 2016.

STAMATATOS, L.; CZARTOSKI, J.; WAN, Y. H.; HOMAD, L. J.; RUBIN, V.; GLANTZ, H.; MCGUIRE, A. T. mRNA vaccination boosts cross-variant neutralizing antibodies elicited by SARS-CoV-2 infection. **Science**, Washington, v. 372, n. 6549, p. 1413–1418, 2021.

SUN, Y.; SUN, M.; XIE, D. Graphene electronic devices. *In:* ZHU, H. (ed.) **Graphene**: fabrication, characterizations, properties and applications. Amsterdam: Elsevier , 2017, p. 103-155.

TAGHIPOUR, Y. D.; KHARRAZI, S.; AMINI, S. M. Antibody conjugated gold nanoparticles for detection of small amounts of antigen based on surface plasmon resonance (SPR) spectra. **Nanomedicine Research Journal**, Tehran, v. 3, n. 2, p. 102–108, 2018.

TORRENTE-RODRÍGUEZ, R. M.; LUKAS, H.; TU, J.; MIN, J.; YANG, Y.; XU, C.; GAO, W. SARS-CoV-2 rapidplex: a graphene-based multiplexed telemedicine platform for rapid and low-cost covid-19 diagnosis and monitoring. **Matter**, Cambridge, v. 3, n.

6, p. 1981–1998, 2020.

TURKEVICH, J.; STEVENSON, P. C.; HILLIER, J. A study of the nucleation and growth processes in the synthesis of colloidal gold. **Discussions of the Faraday Society**, London, v. 55, n. c, p. 55–75, 1951.

VIEIRA, N. C. S.; BORME, J.; MACHADO JUNIOR, G.; CERQUEIRA, F.; FREITAS, P. P.; ZUCOLOTTO, V.; ALPUIM, P. Graphene field-effect transistor array with integrated electrolytic gates scaled to 200 mm. **Journal of Physics:** condensed matter, Bristol,v. 28, n. 8, p. 085302-1-085302-9, 2016.

WALLS, A. C.; PARK, Y. J.; TORTORICI, M. A.; WALL, A.; MCGUIRE, A. T.; VEESLER, D. Structure, function, and antigenicity of the sars-cov-2 spike glycoprotein. **Cell**, Cambridge, v. 181, n. 2, p. 281- 292, 2020.

WANG, Q. H.; JIN, Z.; KIM, K. K.; HILMER, A. J. ; PAULUS, G. L. C.; SHIH, C. J.; HAM, M. H.; YAMAGISHI, J. D. S.; WATANABE, K.; TANIGUCHI, T.; KONG, J.; HERRERO, P. J. ; STRANO, M. Understanding and controlling the substrate effect on graphene electron-transfer chemistry via reactivity imprint lithography. **Nature Chemistry**, London, v. 4, n. 9, p. 724–732, 2012.

WU, J. B.; LIN, M. L.; CONG, X.; LIU, H. N.; TAN, P. H. Raman spectroscopy of graphene: based materials and its applications in related devices. **Chemical Society Reviews**, Washington, v. 47, n. 5, p. 1822–1873, 2018.

YANG, J.; WANG, W.; ZIMIN, C.; LU, S.; YANG, F.; BI, Z.; BAO, L.; MO, F.; LI, X.; HUANG, Y.; HONG, W.; YANG, Y.; ZHAO, Y.; YE, F.; LIN, S.; DENG, W.; CHEN, H.; HONG, L.; ZHANG, Z.; LUO, M.; GAO, H.; ZHENG, Y.; GONG, Y.; JIANG, X.; XU, Y.; LV, Q; LI, D.; WANG, M; LI, F.; WANG, S.; WANG, G.; YU, P; QU, Y.; YANG, L.; DENG, H.; TONG, A.; LI, J.; WANG, Z.; YANG, J.; SHEN, G.; ZHAO, Z.; LI, Y.; LUO, J.; LIU, H.; YU, W.; YANG, M.; XU, J.; LI, H.; WANG, H.; KUANG, D.; LIN, P.; HU, Z.; GUO, W.; CHENG, W.; HE, Y.; SONG, X.; CHEN, C.; XUE, Z.; YAO, S.; CHEN, L.; MA, X.; CHEN, S.; GOU, M.; HUANG, W.; WANG, Y.; FAN, C.; TIAN, Z.; SHI, M.; W, F. S.; DAI, L.; WU, M; LI, G.; WANG, G.; PENG, Y.; QIAN, Z.; HUANG, C.; LAY, J. Y-N.; YANG, Z.; WEI, Y.; CEN, X.; PENG, X.; QIN, C.; ZHANG, K.; LU, G.; WEI, X. A vaccine targeting the RBD of the S protein of SARS-CoV-2 induces protective immunity. **Nature**, London, v. 586, n. 7830, p. 572–577, 2020.

ZHANG, X.; QI, Q.; JING, Q.; AO, S.; ZHANG, Z.; DING, M.; FU, W. Electrical probing of COVID-19 spike protein receptor binding domain via a graphene field-effect transistor. **arXiv**, Ithaca, p. 1–20, 2020.

ZHANG, X. G. Basic theories of semiconductor electrochemistry. *In:* ZHANG, X. G. (ed.). **Electrochemistry of silicon and its oxide**. New York: Kluwer, 2001, p. 1-43.

REFERENCES

AJAMI, S.; TEIMOURI, F. Features and application of wearable biosensors in medical care. **Journal of Research in Medical Sciences**, Isfahan, v. 20, n. 12, p. 1208–1215, 2015.

ANDRADE, C. A.; OLIVEIRA, M. D.; FAULIN, T. E.; HERING, V. R. ; ABDALLA, D. S. Biosensors for detection of low-density lipoprotein and its modified forms. *In:* SERRA, P. A. (ed.) **Biosensors for Health, Environment and Biosecurity**, Intech Open, 2011, 554 p.

AYDIN, E. B.; AYDIN, M.; SEZGINTÜRK, M. K. Highly selective and sensitive sandwich immunosensor platform modified with MUA-capped GNPs for detection of spike receptor binding domain protein: a precious marker of covid 19 infection. **Sensors and Actuators B:** chemical, Amsterdam, v. 345, p. 130355, 2021.

BAKER, A. N.; RICHARDS, S. J.; GUY, C. S.; CONGDON, T. R.; HASAN, M.; ZWETSLOOT, A. J. ; STRAUBE, A. ; WALKER, M.; CHESSA, S.; PERGOLIZZI, G.; DEDOLA, S.; FIELD, R.; GIBSON, M. The sars-cov-2 spike protein binds sialic acids and enables rapid detection in a lateral flow point of care diagnostic device. **ACS Central Science**, Washingtion, v. 6, n. 11, p. 2046–2052, 2020.

BARD, A. J.; FAULKNER, L. R. **Electrochemical methods, fundamentals and applications**. 2. ed. Hoboken: John Wiley, 2001.

BENVIDI, A.; SAUCEDO, N. M.; RAMNANI, P.; VILLARREAL, C.; MULCHANDANI, A.; TEZERJANI, M. D.; JAHANBANI, S. Electro-oxidized monolayer cvd graphene film transducer for ultrasensitive impedimetric DNA biosensor. **Electroanalysis**, Weinheim, v. 30, n. 8, p. 1783–1792, 2018.

CHAIBUN, T.; PUENPA, J.; NGAMDEE, T.; BOONAPATCHAROEN, N.; ATHAMANOLAP, P.; O'MULLANE, A. P.; LERTANANTAWONG, B. Rapid electrochemical detection of coronavirus SARS-CoV-2. **Nature Communications**, Berlin, v. 12, n. 1, p. 1–10, 2021.

CHEN, Z.; ZHANG, Z.; ZHAI, X.; LI, Y.; LIN, L.; ZHAO, H.; LIN, G. Rapid and sensitive detection of anti-SARS-CoV-2 IgG using lanthanide-doped nanoparticles-based lateral flow immunoassay. **Analytical Chemistry**, Washington**,** v. 92, n.10, p. 7226-7231, 2020.

CHOWDHURY, A. D.; AKEMURA, K..; LI, T. C.; SUZUKI, T.; PARK, E. Y. Electrical pulse-induced electrochemical biosensor for hepatitis E virus detection. **Nature Communications**, Berlin, v. 10, n. 1, p. 4–7, 2019.

DEVARAKONDA,S.; SINGH, R., J.; JANG, J. Cost-effective and handmade paper-based immunosensing device for electrochemical detection of influenza virus. **Sensors**, Basel, v. 17, n. 11, 2017.

EHSAN, M. A.; KHAN, S. A.; REHMAN, A. Screen-printed graphene/carbon electrodes on paper substrates as impedance sensors for detection of coronavirus in nasopharyngeal fluid samples. **Diagnostics**, Basel, v. 11, n. 6, 2021.

EISSA, S.; JIMENEZ, G. C.; MAHVASH, F.; GUERMOUNE, A.; TLILI, C.; SZKOPEK, T. ; SIAJ, M. Functionalized CVD monolayer graphene for label-free impedimetric biosensing. **Nano Research**, New York, v. 8, n. 5, p. 1698–1709, 2015.

HAMMOND, J. L.; FORMISANO, N.; ESTRELA, P.; CARRARA, S. ; TKAC, J. Electrochemical biosensors and nanobiosensors. **Essays in Biochemistry**, London, v. 60, n. 1, p. 69–80, 2016.

JIANG, F. LI, P.; ZONG, C.; YANG, H. Surface-plasmon-coupled chemiluminescence amplification of silver nanoparticles modified immunosensor for high-throughput ultrasensitive detection of multiple mycotoxins. **Analytica Chimica Acta**, Amsterdam, v. 1114, p. 58–65, 2020a.

JIANG, Z.; FENG, B.; XU, J.; QING, T.; ZHANG, P.; QING, Z. Graphene biosensors for bacterial and viral pathogens. **Biosensors and Bioelectronics**, Amsterdam, v. 166, p. 112471, 2020.

KICHLOO, A.; ALBOSTA, M.; DETTLOFF, K.; WANI, F.; EL-AMIR, Z.; SINGH, J.; CHUGH, S. Telemedicine, the current COVID-19 pandemic and the future: a narrative review and perspectives moving forward in the USA. **Family Medicine and Community Health**, London, v. 8, n. 3, p. 1–9, 2020.

KIM, C. H.; FRISBIE, C. D. Determination of quantum capacitance and band filling potential in graphene transistors with dual electrochemical and field-effect gates. **Journal of Physical Chemistry C**, Washington, v. 118, n. 36, p. 21160–21169, 2014.

LEE, J. S.; KIM, S. W.; JANG, E.Y.; KANG, B. H. ; LEE, S. W.; SAI-ANAND, G.; LEE, S. H.; KWON, D. H.; KANG, S. W. Rapid and sensitive detection of lung cancer biomarker using nanoporous biosensor based on localized surface plasmon resonance coupled with interferometry. **Journal of Nanomaterials**, London, v. 2015, p. 1-11, 2015.

LEE, J. S. ; KIM, S. W.; Jang, E. Y.; KANG, B. H.; LEE, S. W.; SAI-ANAND, G.; LEE, S. H.; KWON, D. H.; KANG, S. W. Detection of heart failure-related biomarker in whole blood with graphene field effect transistor biosensor. **Biosensors and Bioelectronics**, Amsterdam, v. 91, p. 1–7, 2017.

LI, J.; WU, D.; YU, Y.; LI, T.; LI, K.; XIAO, M. M.; ZHANG, G. J. Rapid and unamplified identification of COVID-19 with morpholino-modified graphene field-effect transistor nanosensor. **Biosensors and Bioelectronics**, Amsterdam, v. 183, p. 113206, 2021.

LIU, H.; LIU, Y.; ZHU, D. Chemical doping of graphene. **Journal of Materials Chemistry**, London, v. 21, n. 10, p. 3335–3345, 2011.

LUKAS, H.; XU, C.; YU, Y.; GAO, W. Emerging telemedicine tools for remote covid-19 diagnosis, monitoring, and management. **ACS Nano**, Washington, v. 14, n. 12, p. 16180–16193, 2020.

MARTÍNEZ-DOMINGO, C.; CONTI, S.; DE LA ESCOSURA-MUÑIZ, A.; TERÉS, L.; MERKOÇI, A. ; RAMON, E. Organic-based field effect transistors for protein detection fabricated by inkjet-printing. **Organic Electronics**, Amsterdam, v. 84, p. 1–9, 2020.

MATTIOLI, I. A.; HASSAN, A.; SANCHES, N. M.; VIEIRA, N. C. S.; CRESPILHO, F. N. Highly sensitive interfaces of graphene electrical-electrochemical vertical devices for on drop atto-molar DNA detection. **Biosensors and Bioelectronics**, Amsterdam, v. 175, p. 112851, 2021.

MOJSOSKA, B.; LARSEN, S.; OLSEN, D. A.; MADSEN, J. S.; BRANDSLUND, I.; ALATRAKTCHI, F. A. Rapid SARS-CoV-2 detection using electrochemical immunosensor. **Sensors**, Basel, v. 21, n. 2, p. 1–11, 2021.

NIRALA, N. R.; HAREL,Y.; LELLOUCHE, J. P.; SHTENBERG, G. Ultrasensitive haptoglobin biomarker detection based on amplified chemiluminescence of magnetite nanoparticles. **Journal of Nanobiotechnology**, New York, v. 18, n. 1, p. 1–10, 2020.

NOVOSELOV, K. S.; GEIM, A. K. ; MOROZOV, S. V.; JIANG, D. E.; ZHANG, Y.; DUBONOS, S. V.; FIRSOV, A. A. Electric field effect in atomically thin carbon films. **Science**, Washington, v. 5, n. 1, p. 1–12, 2004.

OLIVEIRA JUNIOR, O. N.; IOST, R. M.; SIQUEIRA JUNIOR, J. R.; CRESPILHO, F. N.; CASELI, L. Nanomaterials for diagnosis: challenges and applications in smart devices based on molecular recognition. **ACS Applied Materials and Interfaces**, Washington, v. 6, n. 17, p. 14745–14766, 2014.

PARK, D.; KIM, J. H.; KIM, H. J.; LEE, D.; LEE, D. S.; YOON, D. S. ; HWANG, K. S. Multiplexed femtomolar detection of alzheimer’s disease biomarkers in biofluids using a reduced graphene oxide field-effect transistor. **Biosensors and Bioelectronics**, Amsterdam, v. 167, p. 112505, 2020.

QIU, G.; GAI, Z.; TAO, Y.; SCHMITT, J.; KULLAK-UBLICK, G. A.; WANG, J. Dual-functional plasmonic photothermal biosensors for highly accurate severe acute respiratory syndrome coronavirus 2 detection. **ACS Nano**, Washington, v. 14, n. 5, p. 5268-5277, 2020.

REDDY, D.; REGISTER, L. F.; CARPENTER, G. D.; BANERJEE, S. K. Graphene field-effect transistors. **Journal of Physics D:** applied physics, Bristol, v. 44, n. 31, p. 313001, 2012.

SHAO, W.; SHURIN, M. E.; WHEELER, S. E.; HE, X.; STAR, A. Rapid detection of sars-cov-2 antigens using high-purity semiconducting single-walled carbon nanotube-based field-effect transistors. **ACS Applied Materials & Interfaces**, Washington, v. 13, n. 8, p.10321-10327, 2021.

SIQUEIRA JUNIOR, J. R. ; FERNANDES, E. G. R.; OLIVEIRA JUNIOR, O. N.; ZUCOLOTTO, V. Biosensors based on field-effect devices. *In*: CRESPILHO, F. N. (ed.). **Nanobioelectrochemistry:** from implantable biosensors to green power generation. Berlin: Springer-Verlag, 2013. p. 137.

VIGNESHVAR, S.; SUDHAKUMARI, C. C.; SENTHILKUMARAN, B.; PRAKASH,

H. Recent advances in biosensor technology for potential applications : an overview. **Frontiers in Bioengineering and Biotechnology**, Lausanne, v. 4, p. 1–9, 2016.

WANG, O. H.; JIN, Z.; KIM, K. K.; HILMER, A. J.; PAULUS, G. L.; SHIH, C. J.; HAM, M. H.; SANCHEZ-YAMAGISHI, J.; WATANABE, K.; TANIGUCHI, T.; KONG, J.; JARILLO-HERRERO, P.; STRANO, M. S. Understanding and controlling the substrate effect on graphene electron-transfer chemistry via reactivity imprint lithography. **Nature Chemistry**, London, v. 4, n. 9, p. 724–732, 2012.

ZHAN, X.; HU, G.; WAGBERG, T.; ZHAN, S.; XU, H. Electrochemical aptasensor for tetracycline using a screen-printed carbon electrode modified with an alginate film containing reduced graphene oxide and magnetite (Fe3O4) nanoparticles. **Microchimica Acta**, New York, v. 183, n. 2, p. 723–729, 2016.

ZHANG, X. G. Basic theories of semiconductor electrochemistry. *In:* ZHANG, X. G. **Electrochemistry of silicon and its oxide**. New York: Kluwer Academic Publishers, 2001, p. 1-43.

ZHAO, H.; LIU, F.; XIE, W.; ZHOU, T. C.; YANG, J. O.; JIN, L.; LI, L.; ZHAO, C. H.; ZHANG, L.; WEI, J.; ZHANG, Y. P.; PENG, C. Ultrasensitive supersandwich-type electrochemical sensor for SARS-CoV-2 from the infected COVID-19 patients using a smartphone. **Sensors and Actuators. B,** chemical, Amsterdam, v. 327, p. 128899, 2021.

APPENDIX

DESCRIPTION AND DISCUSSION OF EEVDs WORKING PRINCIPLES

The EEVDs working principles are based on the novel hybrid electrical-electrochemical methodology developed in this Thesis. As explained, EEVDs are devices consisting of a graphene monolayer deposited onto a Si/SiO_2 substrate with two metallic electrical contacts separated by a non-metallic covered region of pure Si/SiO_2, as illustrated in Figure 1.

Figure 1 – A) Schematic representation of an EEVD; B) Optical image of EEVD channel with monolayer graphene deposited onto Si/SiO_2

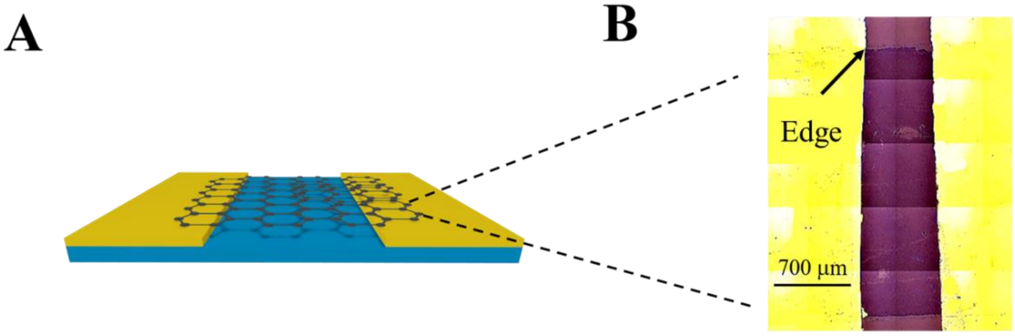

Source: own author

It is known from literature that graphene present exceptional electrical conductivity and near-to-zero intrinsic resistance (NOVOSELOV et al., 2004). However, when deposited onto Si/SiO_2, it is reported an increase in graphene's resistivity sheet R_s, as a function of charge carrier mobility, μ, number of charge carriers n and elementary charge e, as shown in Equation 1. (WANG et al., 2012; KIM; FRISBIE, 2014)

$$R_s = \frac{1}{ne\mu} \tag{1}$$

This property is of particular interest when the EEVD hybrid electrical-electrochemical working principles are discussed. They consist, initially, of connecting each of metallic contacts of the device to WE (Working Electrode) and CE (Counter Electrode) terminals of a potentiostat. In this system, it is possible to observe current flow from WE to CE terminals (in relation to a reference electrode connected in RE terminal) through graphene's basal plane, similar to a short-cut configuration. At this point, the presence of an intrinsic resistivity avoids the occurrence of accidents and overload of the entire EEVD system. Consequently, it is possible to evaluate graphene sheet resistance in an EEVD by experimental data, using Equation 2 based on 2nd Ohm's law, taking into account the geometric parameters W (Width) and L (Length) of monolayer graphene and, WE to CE current and potential (I_{DS}, V_{DS}, respectively).

$$R_S = \frac{W}{L} \cdot \frac{V_{DS}}{I_{DS}} \qquad (2)$$

Besides, the passage of current through graphene's basal plane allow the exploration of some of its most promising electrical properties, as high charge carrier mobility and high basal plane conductivity, giving the "electrical" feature to the EEVDs and electrical-electrochemical detection methodology.

The electrochemical approach arises from the use of an $Ag/AgCl_{sat}$ electrode as a pure non-polarizable reference electrode, connected to RE terminal of a potentiostat. This application of reference electrodes in this electrical-based device was chosen in order to avoid dubious robustness of Dirac potential readings due to instabilities in internal chemical equilibrium of such electrodes. (MATTIOLI et al., 2021) This is a typical problematic thar can be found when they are applied as gate electrodes as in graphene field effect transistors (GFETs). In this sense, every potential reading from WE to CE terminals was made *versus* $Ag/AgCl_{sat}$ reference electrode, as in a conventional electrochemical cell. The electrochemical features were corroborated in one of the works presented in this Thesis in which the hybrid electrical-electrochemical characteristic of the proposed device allowed the observation of faradaic peaks of an EEVD with adsorbed ferrocene. (MATTIOLI et al., 2021) The use of this electrode as a pure reference one also gives to the entire system a potential contribution of ~ 0.197 V (*vs* SHE), in non-polarizable conditions. Therefore, the application of this external voltage vertically to the current flow plane also led to some field effect in the EEVD.

Another interesting aspect of EEVDs regards the possibility of monitoring the variation of interfacial potential E_{int} of the employed device based on the adsorbed analytes onto graphene surface or any non-covalent heterojunction formed with an adsorbed redox modifier. This is possible once E_{int} is obtained by the individual contributions of each interfacial component of the entire electrical-electrochemical system, as described in Equation 3, where E_{DL} is the double-layer potential, E_{ref} is the reference electrode intrinsic potential (these both are constant and can turn into a single

E^0 component, as described in Equation 4), $E_{\text{int}}{}^{\text{gr}}$ is the graphene individual contribution and $E_{\text{int}}{}^{\text{mod}}$ is the adsorbed modifier individual contribution.

$$E_{\text{int}} = E_{\text{DL}} + E_{\text{ref}} + E_{\text{int}}{}^{\text{gr}} + E_{\text{int}}{}^{\text{mod}} \qquad (3)$$

$$E_{\text{int}} = E^0 + E_{\text{int}}{}^{\text{gr}} + E_{\text{int}}{}^{\text{mod}} \qquad (4)$$

Interestingly, it was observed that the EEVD Open Circuit Potential (OCP) shifted as the scan rate of potential sweepings of hybrid electrical-electrochemical I_{DS} vs. V_{DS} varied. Moreover, when the adsorption of an analyte onto graphene occurred, OCP shifts were also observed. (MATTIOLI et al., 2021) OCP is simply the V_{DS} potential between WE and CE EEVD terminals read in a condition of zero current. This alteration can be associated with total interfacial capacitance changes, by a correlation of interfacial potential E_{int} with some semiconductor electrochemical features that graphene can manifest, due to its semiconducting characteristics when deposited on Si/SiO$_2$. To better understand this, it is necessary to interpret OCP not only as a mixed potential that indicates a condition of overall current equals to zero, but also a potential in which the sum of electron and holes charge carrier types currents (i_{e}, i_{p}, respectively) is also equals to zero. (ZHANG, 2005; MATTIOLI et al., 2021) On the other hand, V_{DS} can be seen as a sum of individual contributions of flatband potential V_{fb} and potential drop in space charge layer V_{s}. (Equation 5).

$$\text{OCP} = V_{\text{DS}} = V_{\text{fb}} + V_{\text{s}} \qquad (5)$$

These potentials are correlated to the absence of charge excess and band edge, band bending and space charge layer features (as width) which are, by their turn, deeply correlated to capacitance variations. (ZHANG, 2005) It is also possible to interpret V_{fb} and V_{s} as part of the individual $E_{\text{int}}{}^{\text{gr}}$ and $E_{\text{int}}{}^{\text{mod}}$ contributions once they depend on intrinsic characteristics of graphene and modifier materials. Therefore, the observed OCP variations in EEVD experiments were assumed as interfacial E_{int} alterations, and then, it was possible to conclude that EEVD hybrid electrical-electrochemical methodology are capable of observing interfacial capacitance alterations of the studied surface (*i.e.* bare graphene, or modified graphene through non-covalent functionalization) by the adsorption of an analyte of interest. (MATTIOLI et al., 2021)

Another interesting behavior observed in graphene EEVDs concerns the variation of OCP as a consequence of the adsorbed analyte onto the device surface. It was observed that OCP follows a similar tendency in comparison to Dirac point for GFETs. (MATTIOLI et al., 2021) It means that depending on the residual charge of the adsorbed analyte, a *n*-or-*p*-type doping can be observed. For *n*-doping, OCP displaces towards more negative potentials while for *p*-doping, a displacement towards more positive potentials occurred. (LIU; LIU; ZHU, 2011; MATTIOLI et al., 2021)This hypothesis was confirmed by Raman Spectroscopy experiment, evaluating the G band shifts as a function of the adsorption of ferrocene and ssDNA in the work presented in Chapter III of this Thesis. (MATTIOLI et al., 2021) With the performed experiments, it became noticeable that as chemical doping of graphene by insertion of *n* or *p* charge carriers on graphene altered its band structure near its K point of first Brillouin zone. (LIU; LIU; ZHU, 2011) In this sense, it can be considered that OCP potential shifts can be used as an indicative of doping, evidencing another interesting feature of EEVDs provided by the hybrid electrical-electrochemical features.

ANNEX

CCC RightsLink®

Home | Help | Email Support | Isabela Mattioli

ACS Publications
Most Trusted. Most Cited. Most Read.

On the Challenges for the Diagnosis of SARS-CoV-2 Based on a Review of Current Methodologies

Author: Isabela A. Mattioli, Ayaz Hassan, Osvaldo N. Oliveira, et al

Publication: ACS Sensors

Publisher: American Chemical Society

Date: Dec 1, 2020

PERMISSION/LICENSE IS GRANTED FOR YOUR ORDER AT NO CHARGE

This type of permission/license, instead of the standard Terms and Conditions, is sent to you because no fee is being charged for your order. Please note the following:

- Permission is granted for your request in both print and electronic formats, and translations.
- If figures and/or tables were requested, they may be adapted or used in part.
- Please print this page for your records and send a copy of it to your publisher/graduate school.
- Appropriate credit for the requested material should be given as follows: "Reprinted (adapted) with permission from {COMPLETE REFERENCE CITATION}. Copyright {YEAR} American Chemical Society." Insert appropriate information in place of the capitalized words.
- One-time permission is granted only for the use specified in your RightsLink request. No additional uses are granted (such as derivative works or other editions). For any uses, please submit a new request.

If credit is given to another source for the material you requested from RightsLink, permission must be obtained from that source.

BACK CLOSE WINDOW

License for reusing article

2 messages

Isabela Alteia Mattioli <isabela.mattioli@usp.br> Sat, Jan 8, 2022 at 12:10 PM
To: aabc@abc.org.br

Good morning,

I am the author of a manuscript published in AABC, of DOI https://doi.org/10.1590/0001-3765202020201208.

I need to reprint this full manuscript in my Doctorate Thesis. How can I obtain the license for granting this permission?

I look forward to hearing from you.

Thank you

Isabela

--
Isabela Alteia Mattioli
Universidade de São Paulo

Daniel Lopes Lima Sant Anna <dlopes@abc.org.br> Mon, Jan 10, 2022 at 8:44 AM
To: Isabela Alteia Mattioli <isabela.mattioli@usp.br>

Prezada,

Obrigado por sua mensagem.

De acordo com as políticas de acesso aberto, desde que a senhora cite e referencie corretamente o artigo, o mesmo pode ser reproduzido livremente.

Fico à disposição.

Atenciosamente,

Daniel Lopes Lima Sant'Anna

Assistente Editorial

Anais da Academia Brasileira de Ciências

Rua Araujo Porto Alegre, 64, 5º andar, RJ

www.scielo.br/aabc

https://mc04.manuscriptcentral.com/aabc-scielo

CCC RightsLink®

Home | Help | Email Support | Isabela Mattioli

Highly sensitive interfaces of graphene electrical-electrochemical vertical devices for on drop atto-molar DNA detection

Author: Isabela A. Mattioli,Ayaz Hassan,Natalia M. Sanches,Nirton C.S. Vieira,Frank N. Crespilho

Publication: Biosensors and Bioelectronics

Publisher: Elsevier

Date: 1 March 2021

Journal Author Rights

Please note that, as the author of this Elsevier article, you retain the right to include it in a thesis or dissertation, provided it is not published commercially. Permission is not required, but please ensure that you reference the journal as the original source. For more information on this and on your other retained rights, please visit: https://www.elsevier.com/about/our-business/policies/copyright#Author-rights

BACK CLOSE WINDOW

Home | Help | Email Support | Isabela Mattioli

Graphene-based hybrid electrical-electrochemical point-of-care device for serologic COVID-19 diagnosis

Author:
Isabela A. Mattioli,Karla R. Castro,Lucyano J.A. Macedo,Graziela C. Sedenho,Mona N. Oliveira,Iris Todeschini,Phelipe M. Vitale,Suzete Cleusa Ferreira,Erika R. Manuli,Geovana M. Pereira,Ester C. Sabino,Frank N. Crespilho

Publication: Biosensors and Bioelectronics

Publisher: Elsevier

Date: 1 March 2022

Journal Author Rights

Please note that, as the author of this Elsevier article, you retain the right to include it in a thesis or dissertation, provided it is not published commercially. Permission is not required, but please ensure that you reference the journal as the original source. For more information on this and on your other retained rights, please visit: https://www.elsevier.com/about/our-business/policies/copyright#Author-rights

BACK CLOSE WINDOW

Home | Help | Email Support | Sign in | Create Account

Nanomaterials for Diagnosis: Challenges and Applications in Smart Devices Based on Molecular Recognition

Author: Osvaldo N. Oliveira, Rodrigo M. Iost, José R. Siqueira, et al

Publication: Applied Materials

Publisher: American Chemical Society

Date: Sep 1, 2014

PERMISSION/LICENSE IS GRANTED FOR YOUR ORDER AT NO CHARGE

This type of permission/license, instead of the standard Terms and Conditions, is sent to you because no fee is being charged for your order. Please note the following:

- Permission is granted for your request in both print and electronic formats, and translations.
- If figures and/or tables were requested, they may be adapted or used in part.
- Please print this page for your records and send a copy of it to your publisher/graduate school.
- Appropriate credit for the requested material should be given as follows: "Reprinted (adapted) with permission from {COMPLETE REFERENCE CITATION}. Copyright {YEAR} American Chemical Society." Insert appropriate information in place of the capitalized words.
- One-time permission is granted only for the use specified in your RightsLink request. No additional uses are granted (such as derivative works or other editions). For any uses, please submit a new request.

If credit is given to another source for the material you requested from RightsLink, permission must be obtained from that source.

BACK CLOSE WINDOW